Numerical study of ultrashort laser-induced periodic nanostructure formation in dielectric materials

Anton Rudenko

N° d'ordre NNT : 2017LYSES020

THESE de DOCTORAT DE L'UNIVERSITE DE LYON

opérée au sein de

Université Jean Monnet - Saint-Etienne

Ecole Doctorale N° 488
Sciences Ingénierie et Santé

Spécialité de doctorat :
Optique, photonique et hyperfréquences

Soutenue le 11/07/2017, par:

Anton Rudenko

Numerical study of ultrashort laser induced periodic nanostructure formation in dielectric materials

Étude numérique de la formation des nanostructures périodiques induites par laser ultrabref dans les matériaux diélectriques

---

Devant le jury composé de :

Stoian, Razvan	Directeur de Recherche au CNRS UJM St-Etienne	Président
Sentis, Marc	Directeur de Recherche au CNRS Marseille	Rapporteur
Hallo, Ludovic	Ingénieur de recherche CEA CESTA Bordeaux	Rapporteur
Bonse, Jörn	Dr. rer. nat. BAM, Berlin	Examinateur
Skupin, Stefan	Chargé de recherche au CNRS Univ. Lyon 1	Examinateur
Itina, Tatiana	Directrice de Recherche au CNRS UJM St-Etienne	Directrice de thèse
Colombier, Jean-Philippe	Maître de conférences UJM St-Etienne	Co-directeur de thèse

Université Jean-Monnet - Saint-Étienne

École doctorale "Sciences, Ingénierie, Santé"

Étude numérique de la formation des nanostructures périodiques induites par laser ultrabref dans les matériaux diélectriques

par

Anton Rudenko

Thèse présentée pour obtenir le grade de Docteur en Sciences
en spécialité Optique, photonique et hyperfréquences

Soutenue le 11 Juillet, 2017 devant le jury composé de:

M. Sentis Directeur de Recherche au CNRS	Laboratoire LP3, UMR 6182 CNRS, Université de la Méditerranée, Marseille, France	Rapporteur
L. Hallo Ingénieur de recherche au CEA CESTA, HdR	CEA CESTA, Bordeaux, France	Rapporteur
R. Stoian Directeur de Recherche au CNRS	Laboratoire Hubert Curien, UJM/CNRS UMR 5516, Saint-Étienne, France	Examinateur
J. Bonse Dr. rer. nat.	Bundesanstalt für Materialforschung und -prüfung (BAM), Berlin, Germany	Examinateur
S. Skupin Chargé de recherche au CNRS	Université Claude Bernard Lyon 1, Lyon, France	Examinateur
J.-P. Colombier Maître de Conférences, HdR	Laboratoire Hubert Curien, UJM/CNRS UMR 5516, Saint-Étienne, France	Co-Directeur
T. E. Itina Directrice de Recherche au CNRS	Laboratoire Hubert Curien, UJM/CNRS UMR 5516, Saint-Étienne, France	Directrice

Jean Monnet University - Saint-Étienne

Numerical study of ultrashort laser-induced periodic nanostructure formation in dielectric materials

by

Anton Rudenko

Thesis presented in partial fulfillment of the requirements
for the degree of Doctor of Philosophy
in the subject of Optics, photonics and hyperfrequencies

Defended on July 11, 2017 before the committee:

M. Sentis Directeur de Recherche au CNRS	Laboratoire LP3, UMR 6182 CNRS, Université de la Méditerranée, Marseille, France	Rapporteur
L. Hallo Ingénieur de recherche au CEA CESTA, HdR	CEA CESTA, Bordeaux, France	Rapporteur
R. Stoian Directeur de Recherche au CNRS	Laboratoire Hubert Curien, UJM/CNRS UMR 5516, Saint-Étienne, France	Examinateur
J. Bonse Dr. rer. nat.	Bundesanstalt für Materialforschung und -prüfung (BAM), Berlin, Germany	Examinateur
S. Skupin Chargé de recherche au CNRS	Université Claude Bernard Lyon 1, Lyon, France	Examinateur
J.-P. Colombier Maître de Conférences, HdR	Laboratoire Hubert Curien, UJM/CNRS UMR 5516, Saint-Étienne, France	Co-Directeur
T. E. Itina Directrice de Recherche au CNRS	Laboratoire Hubert Curien, UJM/CNRS UMR 5516, Saint-Étienne, France	Directrice

Résumé

Cette thèse se concentre sur l'étude numérique de l'interaction laser ultrabref avec les diélectriques transparents. En particulier, le phénomène d'auto-organisation des nanoréseaux dans la silice est discuté et un modèle multiphysique est proposé pour expliquer le mécanisme de leur formation. Les nanoréseaux en volume sont des nanostructures périodiques de périodicité sub-longueur d'onde, qui consistent en un matériau moins dense et sont générés par une irradiation laser multi-impulsionnelle femtoseconde dans certains verres, cristaux et semiconducteurs. Leur origine physique ainsi que les conditions d'irradiation laser pour leur formation et leur effacement sont investiguées dans ce travail théorique.

Pour simuler la propagation nonlinéaire dans les verres, les équations de Maxwell sont couplées avec l'équation d'évolution de la densité électronique. Il est démontré que les nanoplasmas périodiques 3D sont formés pendant l'interaction laser ultrabref avec les inhomogénéités de la silice fondue. Les nanopores induits par laser sont supposés jouer le rôle de centres inhomogènes de diffusion. La périodicité sub-longueur d'onde et l'orientation des nanoplasmas dependante de la polarization, révélées dans cette thèse, font d'eux un excellent candidat pour expliquer la formation des nanoréseaux en volume. En plus, il est demontré que les nano-ripples sur la surface de silice fondue et les nanoréseaux en volume ont des mécanismes de formation similaires.

Pour justifier la présence de nanopores dans la silice fondue irradiée par laser, les processus de décomposition du verre sont étudiés. Premièrement, les profils de température sont calculés sur la base d'un modèle électron-ion. Ensuite, à partir des températures calculées, des critères de cavitation et de nucléation dans le verre ainsi que des équations hydrodynamiques de Rayleigh-Plesset, les conditions pour la formation des nanopores et la survie des nanoréseaux en volume sont élucidées.

Pour établir les dependences des paramètres du laser de formation et d'effacement des nanoréseaux en volume, l'approche multiphysique est developpée comprenant la propagation du laser ultrabref dans le verre, les processus d'excitation/relaxation électroniques et le modèle à deux températures. Les résultats numériques fournissent les paramètres du laser en fonction de l'énergie de l'impulsion, sa durée et le taux de répétition pour induire des nanoréseaux en volume, en bon accord avec les expériences nombreuses et indépendantes de la littérature.

Le travail réalisé a non seulement permis de déterminer les mécanismes de formation des nanostructures périodiques mais améliore également notre connaissance du contrôle optimal des paramètres du laser sur la réponse ultrarapide du matériau, en ouvrant des nouvelles opportunités de traitement des diélectriques par laser ultrabref.

Abstract

This thesis is focused on the numerical modeling of ultrashort laser interaction with transparent dielectrics. More particularly, the phenomenon of self-organized volume nanogratings in fused silica bulk is discussed and a multiphysical model is proposed to explain the mechanism of their formation. Volume nanogratings are sub-wavelength periodic nanostructures, consisting of less dense material, which are commonly induced by multipulse femtosecond laser irradiation in some glasses, crystals and indirect semiconductors. Their physical origin as well as the laser irradiation conditions for their formation and erasure are investigated in this theoretical work.

To model the nonlinear propagation inside glass, Maxwell's equations are coupled with rate equation. It is shown that three-dimensional periodic nanoplasmas are formed during ultrashort laser interaction with fused silica inhomogeneities. Laser-induced nanopores are proposed to play the role of inhomogeneous scattering centers. Subwavelength periodicity and polarization-dependent orientation of the nanoplasmas, revealed in this thesis, make them a strong candidate for explaining volume nanogratings formation. Additionally, it is demonstrated that the nanoripples on fused silica surface and volume nanogratings have similar formation mechanisms.

To justify the presence of nanopores in laser-irradiated fused silica bulk, glass decomposition processes are investigated. Firstly, the temperature profiles are found by incorporating the electron-ion temperature model. Then, based on the calculated temperatures, criteria for cavitation and nucleation in glass and also hydrodynamic Rayleigh-Plesset equation, the conditions for nanopores formation and for volume nanogratings survival are elucidated.

To define the laser parameter dependencies on the volume nanogratings formation/erasure, a self-consistent multiphysical approach is developed including ultrafast laser propagation in glass, multiple rate equation to take into account excitation/relaxation processes and two-temperature model. The numerical results provide a laser parameter window as a function of laser pulse energy, laser pulse duration and repetition rate for volume nanogratings consistent with numerous independent experiments.

The performed work not only provides new insights into the formation mechanisms of periodic nanostructures but also improves our knowledge of the optimal laser parameter control over ultrafast material response, opening new opportunities in ultrashort laser processing of dielectrics.

Contents

Acknowledgments

First, I would like to thank Prof. Florence Garrelie and Prof. Florent Pigeon, Directors of Laboratoire Hubert Curien during my PhD thesis, for providing me the excellent working environment and all necessary facilities to carry out this work.

I would like to acknowledge the financial support by the NANODIELEC project, LABEX MANUTECH SISE (ANR-10-LABEX-0075) of Université de Lyon, within the program "'Investissements d'Avenir"' (ANR-11-IDEX-0007) operated by the French National Research Agency (ANR) and thank their representatives, for instance, Pr. Christophe Donnet. I equally acknowledge the support of Jean-Monnet University for proposing interesting useful courses/cultural events that I have attended.

I am very grateful to my thesis rapporteurs, Marc Sentis and Ludovic Hallo for their rigorous analysis of the manuscript, as well as useful advices and comments in order to improve its quality. I am also thankful to examinators Stefan Skupin, Razvan Stoian and Jörn Bonse for taking time to attend my defense and asking interesting questions.

My sincere thanks go to my advisers, Dr. Tatiana E. Itina and Pr. Jean-Philippe Colombier, for infinite number of original ideas and useful advices during my thesis and beyond this research work, for teaching me the way to write publications and opening new opportunities in the world research area. Additionally, I am grateful to all the co-authors, including Guanghua Cheng, Ciro D'Amico, Razvan Stoian, Jörn Bonse and others for their contribution.

I would like to thank particularly Pr. Stéphan Mottin and Pr. Alexandre V. Tishchenko, as well as Dr. Vytautas Jukna and Ma Hongfeng for stimulating discussions within our LASERMODE group during my research work.

Many special thanks should be addressed to all those who have made my stay memorable, colorful and enjoyable in the lab and outside the lab and who helped me along the long way to obtain this degree: Andrey Voloshko, Emile Bévillon, Serena Rizzolo, Adriana Morana, Ciro d'Amico, Diego di Francesca, Antonino Alessi, Chiara Cangialosi, Gaetano Li Vecchi, Marie Vangheluwe, Elena Silaeva, Olga Shavdina, Ayoub Ladaci, Imène Reghioua, Valentina Zantedeschi, Giorgio Baraldi, Said Bakhti, Florent Bourquard, Vytautas Jukna, Maxime Bichotte, Joyce Ibrahim, Maxime Royon, Camille Sabatier, Teddy Tite, Isabelle Planes, Anthony Abou Saleh, Alberto Aguilar, Brisbane Ovilla, Sedao, Nipun Sharma, Rahul Mourya, Bobin Varghese, Chiru Maddi, Ma Hongfeng, Madhura Somayaji, Zeming Liu, Praveen Kumar Velpula, Manoj Kumar Bhuyan, Carlos Arango, Angela Guttila, Mohamed Elawady, Erika Koussi, Dat Nguyen, Mariana Moriño and many others.

I would like to thank also permanent staff from our lab: Ciro d'Amico, Cyril Mauclair, Youcef Ouerdane, Emmanuel Marin, Aziz Boukenter, Sylvain Girard, Nathalie Destouches, Nadège Ollier, François Royer, Jean-Jacques Rousseau, Nicolas Fauré, Léonor Becerra, as well as visiting professors Guanghua Cheng, Konstantin Khishchenko, Marco Cannas, Simonpietro Agnello, Luciano Mescia for supplementary support and participation.

Additional thanks go to scientific researchers with whom I had useful discussions during my PhD thesis on the conferences: Saulius Juodkazis, Sergey Makarov, Jörn Bonse, Javier Solis, Jan Siegel, Thibault Derrien, Rüdiger Grunwald, Sergey Kudryashov, Vadim Veiko, Vitaly Gruzdev, Yves Bellouard, P. G. Kazansky, François Courvoisier, Olivier Uteza, Ya Cheng, Yang Liao, Bärbel Rethfeld, Vladimir Zhukov, Nadezhda Bulgakova, Jeremy Gulley, Laurent Gallais, Jörgen Reif, and many others.

Finally, I would like to thank my family members, especially, my parents for their unconditional support, understanding and encouragement to do PhD in France.

Table 1: Electromagnetic symbols

$(x, y, z)/(r, \theta, \varphi)$	Cartesian/Spherical coordinates	(m, m, m)/(m, -, -)
Δt	Time step	s
Δx	Space step	m
$\vec{E}$	Electric field	V/m
$\vec{B}$	Magnetic field	N/(m·A)
$\vec{H}$	Magnetizing field	A/m
$\vec{D}$	Displacement current	A·s/m^2
$\vec{J}$ ($\vec{J_D}$, $\vec{J_L}$, $\vec{J_{pi}}$, $\vec{J_{Kerr}}$, $\vec{J_{PM}}$)	Electric current density (due to heating, photoionization depletion, Kerr effect, ponderomotive force)	V/m
$\vec{P}$	Polarization current	A·s/m^2
I	Laser intensity	W/m^2
θ	Pulse duration	s
φ	Time delay	s
ϵ, ϵ_∞	Material permittivity (at infinite frequency)	without unity
ω	Frequency	s^{-1}
k	Wave number	m^{-1}
ω_p	Plasma frequency	s^{-1}
R	Repetition rate	s^{-1}
N	Number of pulses	without unity
Σ	Laser pulse energy	J
F	Laser fluence	J/m^2
λ (λ_1)	Laser wavelength (in the media)	m
ω_0	Beam waist	m
z_R	Rayleigh range	m
ζ	Gouy phase shift	without unity
G_j	Oscillator strength	without unity
γ_j	Damping factor	s^{-1}
q	Size parameter	without unity
B_1^e	First order electric moment	V·m^2
B_1^m	First order magnetic moment	V·m
n_e	Electron density	m^{-3}
n_{cr}, n_a	Critical/saturation electron density	m^{-3}
m^*	Effective mass	kg
ν_e	Electron collision frequency	s^{-1}
χ	Susceptibility	without unity
χ_3	Third-order material susceptibility	m^2/V^2
χ_{PM}	Ponderomotive force susceptibility	m^2/V^2
n	Refractive index	without unity
α_{abs}, l_{abs}	Absorption coefficient/Average absorption depth	without unity
k	Extinction coefficient	without unity
E_g	Electron band gap	eV
n_{Kerr}	Kerr nonlinear refractive index	m^2/W
τ_{rec}	Electron recombination time	s
w_{pi}	Photo-ionization rate	m^{-3}s^{-1}
σ_6	Six-photon ionization coefficient	m^{9}W^{-6}s^{-1}
σ_3	Three-photon ionization coefficient	m^{3}W^{-3}s^{-1}
W_{av}	Avalanche ionization rate	m^{-3}s^{-1}
α	Avalanche ionization coefficient	m^2/(W·s)
$\bar{\alpha}$	Avalanche parameter	s^{-1}

Table 2: Thermo-mechanical symbols

C_e	Electron heat capacity	$\mathrm{J{\cdot}K^{-1}m^{-3}}$
k_e	Electron thermal conductivity	$\mathrm{W/(m{\cdot}K)}$
D	Diffusion coefficient	$\mathrm{m^2/s}$
V	Thermal velocity	$\mathrm{m/s}$
μ	Electron mobility	$\mathrm{m^2/(V{\cdot}s)}$
C_i	Lattice heat capacity	$\mathrm{J/(kg{\cdot}K)}$
k_i	Lattice thermal conductivity	$\mathrm{W/(m{\cdot}K)}$
T_e	Electron temperature	K
T_i	Lattice temperature	K
T_{anneal}, T_{melt}, T_{cr}	Annealing/softening/critical temperatures	K
γ_{ei}	Electron-lattice coupling factor	$\mathrm{W{\cdot}K^{-1}m^{-2}}$
$\vec{u}$	Displacement vector	m
ρ	Material density	$\mathrm{kg/m^3}$
η	Viscosity	Pa·s
τ_M	Maxwell's relaxation time	s
σ	Surface tension	N/m
ζ	Strain rate	$\mathrm{s^{-1}}$
P_{dyn}	Dynamic tensile strength	Pa
R	Characteristic radius	m
r_{cr}	Critical radius of nucleus	m
W	Free energy	J
ΔP	Difference in free energy per unit volume	Pa
M	Molar mass	kg/mole
β	Thermal expansion coefficient	$\mathrm{K^{-1}}$
Y	Young's modulus	Pa
B	Bulk modulus	Pa
G	Shear modulus	Pa
C_L	Longitudinal sound velocity	m/s
ν	Poisson ratio	without unity
σ_{ij}	Stress tensor	Pa
σ_{tens}	Tensile strength	Pa
p_{ij}	Photo-elastic coefficients	without unity
α, ξ	Accumulation rates	without unity

Table 3: Physical universal constants

μ_0	Permeability in free space	$4\pi \cdot 10^7$ $\mathrm{N{\cdot}A^{-2}}$
ϵ_0	Permittivity in free space	$8.854 \cdot 10^{-12}$ $\mathrm{s^4A^2m^{-3}kg^{-1}}$
$\hbar$	Reduced Plank constant	$1.055 \cdot 10^{-34}$ J·s
c	Speed velocity	$3 \cdot 10^8$ m/s
m_e	Electron mass	$9.1 \cdot 10^{-31}$ kg
e	Electron charge	$1.6 \cdot 10^{-19}$ A·s
N_a	Avogadro number	$6.022 \cdot 10^{23}$
k_B	Boltzmann constant	$1.38 \cdot 10^{-23}$ $\mathrm{m^2kg{\cdot}K^{-1}s^{-2}}$

Table 4: Acronyms

VNG	Volume nanogratings
LFNG	Low-frequency nanogratings
HFNG	High-frequency nanogratings
LIPSS	Laser-induced periodic surface structures
LSFL	Low spatial frequency LIPSS
HSFL	High spatial frequency LIPSS
FDTD	Finite-difference Time-domain
ADE	Auxiliary differential equation
ABS	Absorbing boundary conditions
PML	Perfect matched layers
UPML	Uniaxial perfect matched layers
CFS	Complex-frequency-shifted
CPML	CFS perfect matched layers
FWHM	Full width at half maximum
MPI	Message passing interface
GPU	Graphics-processing-units
NLSE	Nonlinear Schrödinger equation
CNT	Classical nucleation theory
NA	Numerical aperture
SEM	Secondary electron image

Chapter 1

Introduction

Femtosecond laser interactions have attracted increasing interest due to new possibilities for the efficient nanostructuring of different materials [1]. Nano- and microprocessing of transparent dielectrics are particularly promising since they enable writing optical waveguides, nanovoid arrays, polarization-dependent periodic surface structures and volume nanogratings [2,3].

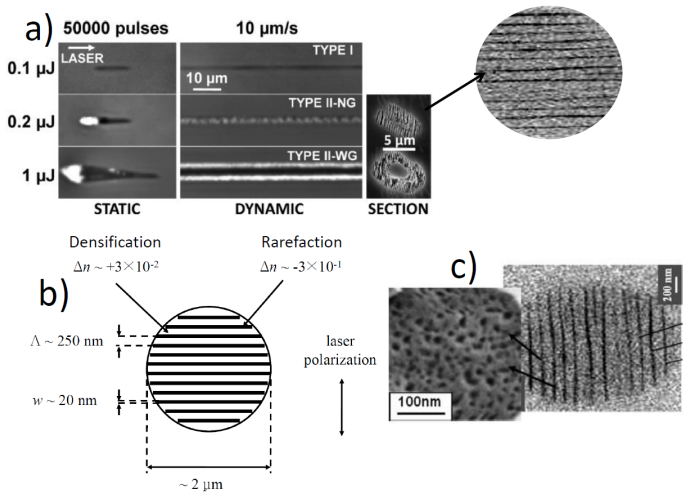

Figure 1.1: a) Ultrashort laser-induced modifications in fused silica taken from Refs. [4,5]. b) Composition of self-organized nanogratings (illustration from Ref. [6]). c) [taken from Ref. [7]] shows nanogratings consisting of nanopores.

The progress in ultrashort laser processing and the ability to control over the laser-induced modifications have already paved the way towards a wide range of applications in three-dimensional nanofabrication, biomedicine, data storage and development of polarization-sensitive and optofluidic devices [1,8]. Depending on the laser irradiation conditions, different types of permanent material modification could be induced in glasses by ultrashort laser pulses. Thus, single pulse irradiation is known to lead either to smooth modification characterized by positive index change or more dense material (often referred to as type I) or to void-like rarefaction regions characterized by negative index change (type II) [2,9–11]. The densification was attributed either to defect-assisted structural changes in glass (bond breaking) or to pressure compaction mechanisms [5], whereas the rarefaction was related to glass decomposition processes, i. e. mechanically induced cavitation or thermally induced phase explosion [12]. In addition, self-organized nanogratings were found to be formed as a result of multi-pulse laser irradiation of fused silica glass [4,13–18], few other glasses [7,19–23], and several indirect bandgap semiconductors [24–26]. Fig. 1.1(a) shows the ultrashort laser-induced modifications induced by applying $N = 50000$ number of pulses with focusing conditions $NA = 0.4$ and for laser irradiation wavelength $\lambda = 800$ nm in fused silica. For low laser pulse energy $\Sigma = 0.1\mu J$, the modification is characterized by positive refractive index change indicated by black color (densification, type-I). For higher laser pulse energies, nanogratings are formed in the regions of negative refractive index change indicated by white color (void, type-II).

Fig. 1.1(b) demonstrates that the modification consists of more dense layers of ≈ 250 nm, associated with nanogratings period, and ≈ 20 nm of less dense layers associated with nanogratings thickness. Fig. 1.1(c) shows that the void-like layers consist of nanometric pores of radius $r = 10 - 20$ nm.

To control over the laser-induced processing, the resulting modifications were experimentally investigated as a function of laser pulse energy [10, 13, 27–30], pulse duration [13, 15, 31, 32], numerical aperture [10], laser wavelength [10, 16], polarization [5, 10, 20, 33, 34], repetition rate [16, 23, 35–37], and number of applied pulses [5, 16, 18]. In particular, it was shown that by varying pulse energy, focusing conditions or temporal pulse envelope, completely different types of modifications from positive index change to negative can be induced in fused silica glass [2, 10, 11, 27, 28]. Pulse duration is also found to be a crucial parameter in the formation of self-organized nanogratings, influencing laser pulse energy conditions for their formation [13], periodicity (spacing decreases with the increasing pulse duration) [15], and refractive index contrast of the nanostructures [38]. Furthermore, a choice of the convenient repetition rate allows a better control over the heat accumulation effects playing an important role in the multi-pulse laser irradiation [16, 23, 35]. A better understanding of the differences between the distinct laser-irradiation regimes and the resulting laser-induced modifications is still lacking.

Volume nanogratings formation regime is of particular interest, because of numerous unique applications illustrated in Fig. 1.2, including highly survivable and long lifetime rewritable data storage [39–41](a, b), recent development of phase elements for polarization control and computer-generated holography [5, 42] (c, d), as well as fabrication of nanofluidic channels for biomedicine and DNA molecular analysis [39, 43](e, f). These applications became realizable owing to several unique features of the nanogratings revealed by experimental investigations.

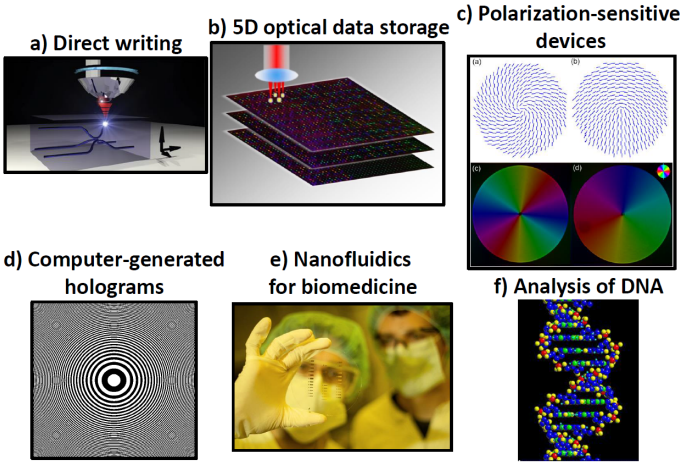

Figure 1.2: Examples of potential applications of VNGs.

First observed in 2003 by using a tightly focused femtosecond laser beam [4], these nanoplanes were found to be oriented perpendicular to the laser polarization. In particular, it was revealed that the orientation of the nanostructures depended on the local laser polarization [33, 44] (see Fig. 1.3(c, d)). For instance, it is possible to rotate the nanoplanes imprinted in fused silica bulk in space [45] and to inscribe the nanogratings and the nanoripples of the designable spatial structure [46]. Up to now, several experimental works have been devoted to reveal nanostructures created by radial and azimuthal polarizations [33, 47], circular polarization [46, 48], and even spiral polarization [49–51].

Remarkably, nowadays, the VNGs are still considered to be the smallest embedded structures ever created by light. Liao et al. reported that a single grating with transverse width as small as 40 nm could be inscribed in fused silica [18], opening the opportunities for nanofluidics (Fig. 1.2(e)).

The nanoplanes are typically spaced by the half of the wavelength in the medium [16, 20, 44]. However, the period was shown to decrease continuously with the number of the applied pulses [4, 16, 19, 52–54] as shown in Fig. 1.3(e). It was also demonstrated that the periodicity could be controlled by changing the temporal pulse envelope in Fig. 1.3(f), where the period decreases with the increasing pulse duration [15]. The dependence of the laser pulse energy on the nanoplanes spacing is controversially discussed in the literature [4, 44, 55–57]. Firstly, it was proposed by Shimotsuma et

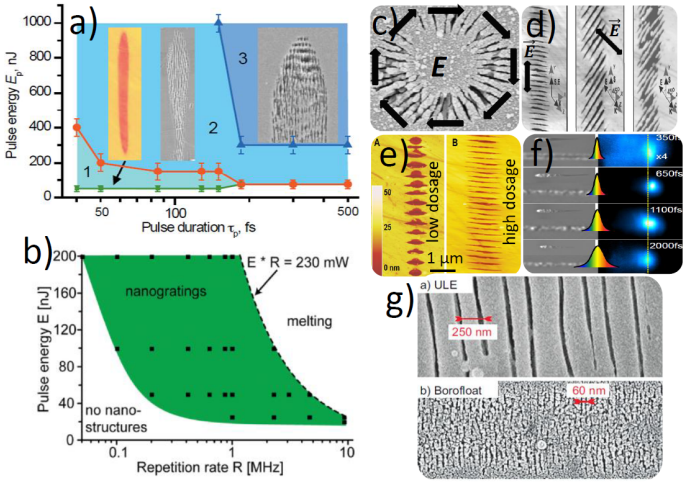

Figure 1.3: a) Laser parameter window as a function of laser pulse energy and laser pulse duration defined by Taylor et al. [39]. b) Laser parameter window as a function of laser pulse energy and repetition rate defined by Richter et al. [16]. c) Nanogratings inscribed by radial polarization [33]. d) Nanogratings inscribed by different angle orientation to laser polarization [44]. e) Control of nanogratings period and size by changing the number of applied pulses [39]. f) Control of nanogratings period by changing the temporal pulse envelope [15]. g) Nanogratings observed in ULE and borofloat glasses [38].

al. that the periodicity would increase with the deposited laser pulse energy. However, Bhardwaj et al. demonstrated that it didn't considerably change for large pulse energy interval from $\Sigma = 200$ nJ to $\Sigma = 1\mu J$ and different laser polarizations. The decreasing trend of the nanogratings spacing with the increasing pulse energy deposition for different number of applied pulses was also reported [55]. Liang et al. emphasized that the spacing decreased not with the increasing pulse nergy, but with the increasing laser pulse fluence [56]. In contrast, Ahsan et al. found that the periodicity increased with the increasing laser pulse energy and fixed pulse duration and also with the increasing laser pulse duration but fixed laser pulse energy [57].

Several experimental studies revealed an existence of a laser parameter window required for nanostructure formation and erasure. Among these parameters, the major ones are laser pulse energy, pulse duration and repetition rate [10,11,13,16]. A rigorous study of the phenomenon was performed by Taylor et al., where three regimes of femtosecond laser dielectric modification at different laser conditions were underlined [39]: (i) smooth modification, (ii) birefringent modification enabling nanogratings self-organization and (iii) disruptive modification at higher pulse energy and longer pulse duration (Fig. 1.3(a)). Furthermore, the role of the local temperature and heat accumulation in the multi-pulse ultrashort laser irradiation has been recently demonstrated leading to nanogratings in the case of low repetition rates and to melted disrupted regions at high repetition rates [23,58] (Fig. 1.3(b)).

Apart from the direct observations of the final laser-induced modifications, a rigorous experimental works were devoted to analyze the temporal dynamics of the laser-affected zone.

The electron dynamics was investigated in different laser irradiation regimes in order to define the average values of laser-induced electron densities as well as the lifetime of plasma in fused silica and borosilicate glasses [2,28,59,60]. It was found that the electrons have sub-picosecond trapping time in the regimes of low laser pulse energies and sub-picosecond pulse durations in fused silica [61,62] and up to hundreds of picoseconds in borosilicate and soda-lime glasses [60,62]. In the regimes of higher laser pulse energies, picosecond pulse durations and the electron densities approaching to the critical value, the electron plasma was shown to survive up to nanoseconds [2,59,60].

The temperature dynamics was also investigated in few recent works in case of a single pulse irradiation [29] and multipulse irradiation [37], indicating the temperatures exceeding the melting point. The time-resolved measurements revealed the launch of pressure waves on nanosecond timescales in different glasses [2,17,63–65], as well as the void formation on nanosecond/microsecond timescales [66].

Several studies were devoted to the multi-physical analysis of laser-induced modifications in glass.

Rigorous calculations were performed to investigate ultrafast free-electron dynamics in dielectrics

by nonlinear Schrödinger (NLSE), Boltzmann and Maxwell's equations [67–73]. On one side, the NLSE, being an asymptotic parabolic approximation of Maxwell's equations, requires the unidirectionality of the light beam and cannot describe cases where dense electron plasma is generated causing light scattering to large angles [74, 75]. On the other side, NLSE is advantageous as the solution for the electromagnetic propagation on microscale distances significantly larger than the laser irradiation wavelength, on which solving Maxwell's equations coupled with the rate equation is the problem requiring enormous computer time and memory resources. A quantum-kinetic approach based on Boltzmann equations is an alternative way to investigate the electron dynamics during ultrashort laser propagation and is the method which avoids the application of phenomenological models such as Drude model for electron heating and takes into account a wide range of non-equilibrium processes in the laser interactions [73]. The main disadvantage of this method is its numerical complexity. The mentioned approaches were used to investigate the competition between nonlinear processes in dielectrics, such as Kerr effect, photoionization and impact ionization [71, 73] and connect the laser irradiation conditions with the resulting electron density spatial distributions [69–71]. Note, that the mentioned approaches treated the material as a homogeneous media and, therefore, took account for a single pulse irradiation, whereas in case of multipulse irradiation the propagation and, therefore, the electron density distribution is influenced by already created inhomogeneous modification. In order to consider the ultrashort laser interaction with inhomogeneities, Maxwell's equations coupled with rate equation seem to be the most appropriate as this approach treats the propagation of media with the given three-dimensional spatial discretization.

Initially, numerical approaches based on Maxwell's equations were developed to study the electromagnetic interaction of ultrashort laser irradiation with a rough surface [76–79]. It was suggested that the interference patterns left by the inhomogeneous absorption of linear polarized laser radiation below a rough surface corresponded to the localized surface ripples which could be organized within single laser shot [76]. The simulations based on the developed approaches supported the conclusions drawn by previously proposed analytical solution for electromagnetic propagation through rough interface between two media, often referred to as Sipe theory [80]. According to this theory, the light interaction with dielectric rough surface results in the formation of the interference patterns preferentially oriented parallel to laser polarization and spaced by laser wavelength in media, whereas the light interaction with metallic rough surface induces radiation remnants preferentially perpendicular to laser polarization and spaced by laser wavelength. In fact, the orientation and the spacing were found consistent with the experimentally observed classical low spatial frequency ripples on the surface of dielectrics, semiconductors and metals [76]. Skolski et al. proposed then that high spatial frequency ripples with sub-wavelength periodicity could be also explained by the electromagnetic approach [77]. The method was further expanded to take into account the interpulse positive and negative feedback mechanisms to explain the formation of grooves with spacing larger than laser wavelength, low spatial frequency parallel oriented ripples on metals with typical laser in wavelength spacing [77,79,81]. Moreover, Maxwell's equations were coupled with electron density equation to investigate the dynamics of the interaction with randomly distributed inhomogeneities in fused silica glass to explain the self-organization of nanogratings which require multiple pulse evolution related to multiphoton ionization memory feedback [82]. Buschlinger et al. demonstrated that the irradiation of randomly distributed inhomogeneities could also lead to quasi-periodic organization of polarization-dependent nanoplasmas [82]. Despite numerous previous studies, the sub-wavelength periodicity of the nanostructures has not been clearly explained.

Thermo-elastoplastic wave equations were further incorporated to study the mechanisms of refractive index change [31, 75, 83]. The propagation of the pressure wave as well as stress-induced compaction and rarefaction were explained by the combined approaches [31, 60]. The final modification structure was found to be imprinted in fused silica on sub-nanosecond scales [75]. The influence of laser irradiation parameters on the transient refractive changes was also investigated [83].

A comprehensive thermo-mechanical modeling was performed for CO_2 laser heating [84, 85] and laser-induced structural relaxation of glass [86]. The approaches were also developed for femtosecond laser interaction with fused silica, where the nonlinear propagation equations were coupled with two-temperature model [83, 87, 88]. Romanova et al. proposed that type-I modification (more dense

material) took place, where the glass transition temperature was exceeded based on the numerical calculations [87]. Doualle et al. predicted the depth of the crater after CO_2 irradiation of fused silica surface [85]. The ablation threshold of fused silica surface ultrashort irradiation were also derived taking into account the air ionization [88].

Hydrodynamic simulations based on the equation of state were also done to investigate the cavity formation under tight focusing laser irradiation conditions [89,90]. The calculated size of the void-like modification was found in a good agreement with the experimental results.

Heat accumulation in glass was studied by models based on the heat equation [23, 35–37]. In multipulse picosecond irradiation regime, Sun et al. proposed that the thermal damage took place when the melting temperature $T = 1051$ K was exceeded, whereas the electronic damage, referred to a certain electron density threshold above which the electronic accumulation plays a crucial role in plasma generation and expansion by consequent pulses, required the temperatures greater than $T \approx 3600$ K for borosilicate glass [35]. Caulier et al. derived that the permanent modification in soda-lime glass took place, when the annealing temperature $T \approx 800$ K was exceeded [36].

Note, that in most cases, ultrafast propagation and thermo-mechanical processes were not coupled and, therefore, the results do not connect directly the laser parameters with final modifications. Different electron density and temperature criteria were used for defining numerically laser-induced modifications, however, none of them are sufficiently general to be applied as the thresholds for various laser irradiation conditions. The mechanisms of void-like modification remain to be investigated.

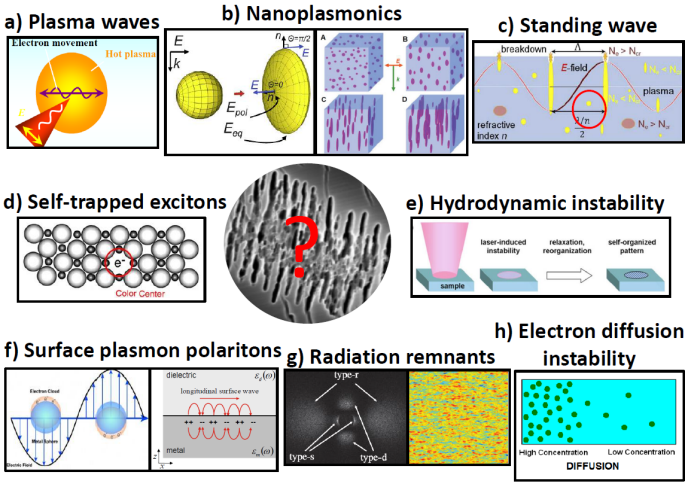

Figure 1.4: Alternative scenarios of nanogratings formation.

Several scenarios were proposed to explain the organization of periodic structures illustrated in Fig. 1.4. The first model for nanogratings formation was proposed by Shimotsuma et al. [4] based on the interference of the laser field with the laser-induced plasma waves (Fig. 1.4(a)). In this model, the nanogratings period depends on the optical properties of the plasma and on the local electron temperatures. This approach becomes invalid at a high plasma density and does not agree with the experimental observations denying the strong pulse energy and nonlinear wavelength dependencies of the nanogratings period. The values of the electron temperatures as high as $T_e \approx 1-5\cdot10^7$ K required for the established nanometric grating periodicity are put in doubt by several research groups [7,44]. Another scenario was proposed by Taylor et al. [39], describing the evolution of spherically-shaped nanoplasmas from the hot-spots organized inhomogeneously around defects or color centers, leading to anisotropic multiphoton ionization illustrated in Fig. 1.4(b). The periodicity is defined by the lowest order optical mode of multiple nanoplasmas, which behave like planar metallic waveguides [44]. Buividas et al. proposed that nanoplanes were pinned to the smallest possible standing wave cavity inside material [91] (Fig. 1.4(c)). Despite the predicted grating period of half the wavelength in the media agrees with experimental results, the dependency of the period on the number of laser pulses deviates from the above prediction. In fact, this dependency cannot be explained by corresponding changes of the refractive index [92], which could increase not more than by $\approx 30\%$ even for overcritical electron densities [93]. It was also reported that longitudinal periodicity of nanogratings could be

explained by interference of short-living exciton polaritons [94,95] (Fig. 1.4(d)). In contrast to plasma wave [4] and nanoplasmonic models [39,44], this approach requires low electron densities, as at higher densities $n_e > 10^{27}$ m^{-3} the exciton-polariton interaction is heavily screened by the electron plasma when the plasma begins to efficiently absorb laser energy [96]. Furthermore, the self-trapped excitons are commonly created in the regime of lower laser pulse energies for waveguides fabrication (type I) [2,11]. In this regime, the nanogratings have not been revealed yet [39].

VNGs have similarities with femtosecond laser-induced ripples on the surface, sharing sub-wavelength periodicity, polarization, wavelength and number of pulses dependencies. Additionally, the transition between the surface ripples and the volume nanogratings was experimentally observed [97]. A closer examination revealed that the periodically arranged nanoplanes were preferentially formed at the interface between the regions affected and unaffected by the femtosecond laser irradiation [18]. Therefore, it was proposed that the mechanisms of the nanostructure formation could be related [98]. Thus, the generally accepted mechanisms of surface ripples formation such as the interference between the incident light and the electromagnatic waves scattered at the rough surface with possible excitation of surface plasmon polaritons [76] (Fig. 1.4(f,g)), hydrodynamic instability [99] (Fig. 1.4(h)) and second harmonic generation [100], are worth mentioning. On one hand, Liao et al. and Makin et al. suggested that excitation of standing plasma waves at the interfaces between modified and unmodified areas played a crucial role in promoting the growth of periodic nanogratings [18, 101]. On the other hand, it was further underlined that the evidence of the defect-assisted local field rearrangement excluded the scenario that the nanograting was a result of interference between the writing beam and the surface plasma waves [102]. The surface plasmon excitation on the unexcited glass/metallic glass or void/metallic glass requires the condition $Re(\epsilon) < -n^2$ to be fulfilled, where ϵ is the permittivity of the modified material and n is the refractive index of the unexcited glass or air/void. The possibility of plasmonic scenario for excited dielectrics has been controversially discussed in the literature [18, 76, 79, 103]. Alternatively, a non-plasmonic scenario based on so-called radiation remnants or non-propagating electronic modes close to the rough surface was proposed to explain the formation of ripples [76, 79, 80].

Furthermore, the following scenarios have been recently discussed: ionization scattering instabilities [74, 75, 104], a space-charge built from ponderomotive force [105] and Weibel instability [106], and electron diffusion-induced instability [107].

One can note, that most of the proposed scenarios have an electromagnetic nature. This is justified by the experimental observation of strong dependence of the electric field polarization and wavelength on the nanostructures three-dimensional orientation and spacing [16, 33, 44]. Furthermore, the inhomogeneities or the instabilities playing a key role of scattering centers are likely to be involved in the initiation of nanoplasma formation [23, 39, 74, 76, 82]. Experimental investigation of nanogratings evolution evidenced that pre-distributed nanogrooves and laser-induced defects strongly affected local field arrangement [18, 54, 102, 108]. The doping elements and embedded nanoparticles in glasses were found to significantly improve the quality and the smoothness of the nanostructures and to facilitate the accumulation processes responsible for the self-organization [43, 109–111]. Additionally, Lancry et al. have reported that self-organized nanogratings consist of nanopores of few tens of nanometers, which are at the root of refractive index contrast and permanent modification [7]. The formation of nanopores is then attributed to the glass decomposition, i. e. oxygen dissociation and formation of less dense material [112]. It has been recently shown that the presence of such nanometric inhomogeneities in glass leads to quasi-periodic polarization-dependent subwavelength nanoplasma formation during irradiation by ultrashort laser pulses [82].

This way, the numerical model comprising the nonlinear electromagnetic interaction with randomly distributed scattering centers or inhomogeneities is chosen in this thesis. The following model could include automatically the processes, which were put in the basis of the proposed scenarios, such as the interference between the incident light and the scattered waves from inhomogeneities/rough interfaces, the nanoplasmonics scenario, the excitation of surface plasmon waves, the electromagnetic or the nonlinear effect-driven instabilities.

Apart from the elucidation of the formation mechanisms of periodic nanostructures, the following questions remain to be answered. First of all, the conditions for nanogratings formation and erasure

are to be elucidated and defined as a function of laser irradiation parameters, such as laser pulse energy, laser pulse duration and repetition rate. Secondly, the ability to control over the properties of nanogratings, such as their size, orientation and periodicity, is to be discussed. And finally, it is still unclear whether it is possible to inscribe the nanostructures in any transparent materials or not. For instance, it has been reported that the nanogratings can be created in fused silica [4,39], borosilicate glasses [21,23], ULE glass [23,113], soda-lime glasses [19], germanium-doped silicate glasses [23] or germanium dioxide glasses [20], lithium-niobium silicate glass [114], sodium gallophosphate glass [115], transparent crystals as 4H-SiC [24] or TeO_2 [116], sapphire [117], indirect semiconductors such as c-Si and GaP [25,26].

The experimentally revealed influence of laser parameters, such as pulse energy, pulse duration and repetition rate, on nanogratings formation is still far from being clearly explained. Various controversial values of the electron densities from $n_e = 10^{25}$ m^{-3} to $n_e = 10^{27}$ m^{-3} and electron temperatures from $T_e = 3.5 \cdot 10^5$ K to $T_e = 5 \cdot 10^7$ K of different orders of magnitude associated to this regime have been previously reported [2, 4, 7, 17, 62, 75, 118]. This fact does not allow one to easily identify the mechanism of their periodic organization. Finally, debates are still open regarding the ways of glass decomposition and how the modifications can be permanently conserved in the form of nanogratings [23,75]. On one hand, cavities of one hundred nanometer sizes are typically formed after single pulse irradiation [11,34,118]. On the other hand, the appearance of nanopores after multiple laser irradiation points out that nucleation takes place in accumulation regime [7,23]. The nucleation followed by laser-induced cavitation was reported in several experiments [119–121]. Up to now, the competition between cavitation and nucleation processes in the regimes of ultrafast laser irradiation of fused silica, has not been investigated previously. The conditions for nanopore formation, stability and growth also remain to be elucidated.

To answer these questions, a multiphysical model is required which would be able not only to describe the electronic modifications induced by ultrashort laser pulse, but also the further evolution of laser-affected zone up to permanent glass modification. Two-temperature model is of interest due to the possibility to define the spatial temperature distribution directly from the calculated electronic modification. Then, thermo-elastoplastic model could be helpful to obtain the spatio-temporal density distributions. To connect the laser irradiation parameters with the final modifications, simple criteria of glass decomposition are required. Finally, hydrodynamic approach is desirable to understand the following evolution of the heat-affected zone after the modification processes have already taken place.

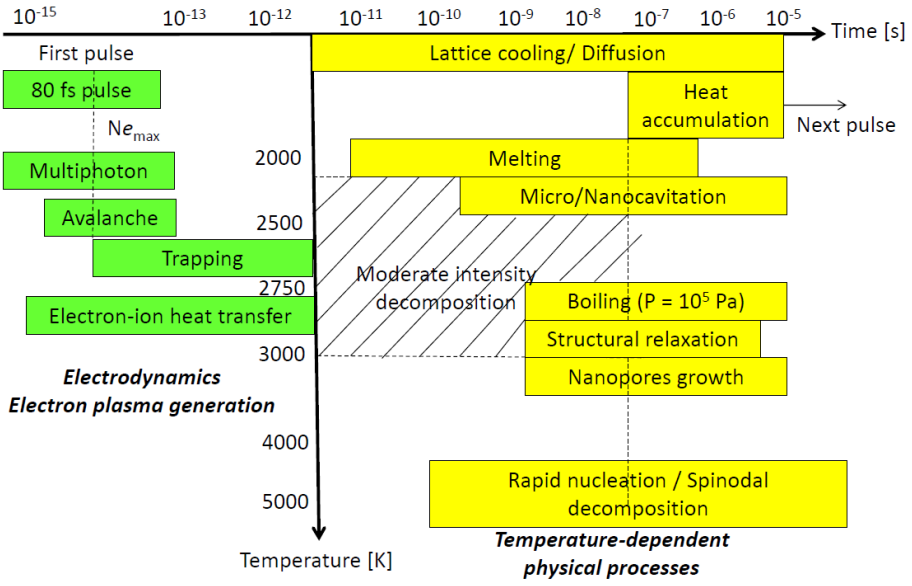

Figure 1.5: Schematics of main physical processes involved in the ultrashort laser processing of fused silica bulk.

Self-organization of periodic nanoporous structures in glass is shown to be a complex multi-physical phenomenon covering a wide range of processes occurring at different time scales as illustrated in Fig.

1.5. These processes form the basement for the multiphysical model discussed in this thesis. The first part of the processes take place at femtosecond or picosecond timescales and lead to the free carrier generation, and the formation of a heat-affected zone. The periodic nanoplasmas are likely to be formed during ultrashort laser pulse duration. The second part involves the glass decomposition and material reorganization at nanosecond and microsecond scales up to fast cooling of the lattice, resulting in the permanent modification. The laser-induced nanopores influence the ultrashort laser propagation during the next pulse irradiation.

In this thesis, the problem is also sub-divided into two parts. In the first part, the ultrashort laser interaction with inhomogeneous media is investigated based on three-dimensional Maxwell's equations coupled with rate equation. In the second part, two-dimensional multiphysical approach is applied, where two-temperature and thermo-elastoplastic models are combined with Maxwell's and multiple rate equations and supplemented by criteria for glass decomposition and hydrodynamic approach.

This thesis was prepared in Laboratoire Hubert Curien, Saint-Etienne, France in the frame of NANODIELEC project, LABEX MANUTECH SISE (ANR-10-LABEX-0075) of Université de Lyon, within the program "Investissements d'Avenir" (ANR-11-IDEX-0007) operated by the French National Research Agency (ANR).

The thesis is organized as follows.

In Chapter 1, the up-to-date experimental literature related to the phenomenon of volume nanogratings has been reviewed. The questions, concerning the mechanism of their formation, have been arisen and the scenarios, proposed previously by independent experimental and theoretical groups, have been discussed. The analysis allows us to choose adequately the physical model, which includes most of the involved processes and checks the validity of the proposed scenarios.

In Chapter 2, the multiphysical model is introduced, describing a wide range of processes such as electromagnetic nonlinear interaction, free carrier generation, electron-ion energy transfer, hydrodynamics, thermoelastic wave propagation, and mechanisms of glass decomposition. The physical processes are connected together, enabling a detailed theoretical investigation of the influence of laser parameters on the processes of glass decomposition for a deeper understanding of femtosecond laser-induced phenomena.

Chapter 3 proposes a numerical approach to solve the described system of equations. Particular attention is paid to the development of a novel method for fast solution of nonlinear optics problems. The electromagnetic finite-difference time-domain approach is expanded for dispersive nonlinear media, where the iterative procedure is used for solving the nonlinear Maxwell-Ampere's equations. The numerical methods for solving two temperature model and thermo-elastoplastic wave equations are equally discussed.

Chapter 4 and Chapter 5 include the numerical results obtained by the electromagnetic approach coupled with excitation/relaxation processes.

In Chapter 4, the ultrashort laser irradiation of a single nanoparticle is investigated. For low intensity irradiation in the absence of changes in fused silica optical properties, the numerical model is validated by comparing with the analytical Mie theory. The electron density evolution is then investigated in a nonlinear case. The growth of nanoplasma perpendicular to laser polarization from the nanometric inhomogeneity is predicted by the numerical model.

Chapter 5 provides the main results concerning three-dimensional periodic nanostructure formation inside fused silica bulk. The electronic modifications induced by ultrashort laser are investigated as a function of laser pulse energy and polarization, as well as the initial concentration of randomly distributed inhomogeneities which are shown to play the key role in the periodic nanoplasma formation. The mechanisms of the nanostructure formation on the surface and in the bulk of fused silica are shown to have similar nature. Results of multipulse simulations are included to support the scenario of void-like nanoplane growth on a shot-to-shot basis.

Chapter 6 extends the approach by combining two-temperature, thermo-elastoplastic and hydrodynamic models. The simulations provide the evolution of the heat-affected zone after ultrashort laser interaction. Criteria for glass decomposition are additionally applied to predict the nanovoid formation inside glass. The threshold conditions for nanogratings formation and erasure are finally connected with laser irradiation parameters and a laser parameter window for nanostructuring is proposed based

on the numerical calculations.

Finally, the main results and conclusions are summarized in Chapter 7. Suggestions for future research are discussed.

Chapter 2

Modeling details

In this chapter, we describe a multiphysical self-consistent model for ultrashort laser interaction with dielectrics. Firstly, the propagation dynamics of light in dispersive, nonlinear dielectric media during femtosecond laser duration is given by a set of nonlinear Maxwell's equations. Then, Maxwell's equations are coupled with time-dependent electron density equation, where the electron excitation/relaxation processes are taken into account. Specific attention is paid to the processes of nonlinear ionization such as multiphoton, tunneling and avalanche ionizations and their relative contribution to the changes in optical properties of the media. The nonlinear contributions due to the third-order Kerr nonlinearity and due to the ponderomotive force are considered in the model. Then, the electron-ion heat transfer equations are incorporated into the model to describe the temperature dynamics from femtosecond to microsecond timescales. The system of equations is closed with thermoelastic wave equations, enabling to estimate the stresses, the densities and the transient changes of the refractive index. The viscoelastic model and classical nucleation theory (CNT) serving as criteria for glass decomposition are detailed. Finally, Rayleigh-Plesset equation is introduced to investigate the hydrodynamics of nanovoids/nanopores.

2.1 Maxwell's equations for dispersive nonlinear media

The propagation of electromagnetic wave in media is described by the system of Maxwell's equations

$$\begin{cases} \dfrac{\partial \vec{D}}{\partial t} = \nabla \times \vec{H} - \vec{J} \\ \dfrac{\partial \vec{B}}{\partial t} = -\nabla \times \vec{E}, \end{cases} \tag{2.1}$$

where $\vec{E}$ is the electric field, $\vec{B}$ is the magnetic field, $\vec{D}$ is the displacement current, $\vec{H}$ is the magnetizing field, and $\vec{J}$ is the electric current density. The first equation is called Maxwell-Ampere equation, whereas the second is Maxwell-Faraday equation.

In the case of non-magnetic material, the magnetic field is proportional to the magnetizing field $\vec{B} = \mu_0 \vec{H}$, where μ_0 is the permeability of free space. The displacement field for a non-linear media is defined as $\vec{D} = \epsilon_0 \epsilon(\omega) \vec{E} = \epsilon_0 \epsilon_\infty \vec{E} + \vec{P} = \epsilon_0 \epsilon_\infty \left[1 + \chi(\omega)\right] \vec{E}$, where $\vec{P}$ is the polarization field, ϵ_0 is the free space permittivity, $\epsilon(\omega)$ and $\chi(\omega)$ are the material permittivity and susceptibility, which in general case depend on the frequency of the incident electromagnetic wave ω, and ϵ_∞ is the value of material permittivity at infinite frequency. For simplicity, the polarization current is defined as $\vec{J}_p = \frac{\partial \vec{P}}{\partial t}$. The system of Maxwell's equations is rewritten in the following way

$$\begin{cases} \dfrac{\partial \vec{E}}{\partial t} = \dfrac{\nabla \times \vec{H}}{\epsilon_0 \epsilon_\infty} - \dfrac{1}{\epsilon_0 \epsilon_\infty} (\vec{J}_p + \vec{J}) \\ \dfrac{\partial \vec{H}}{\partial t} = -\dfrac{\nabla \times \vec{E}}{\mu_0}. \end{cases} \tag{2.2}$$

2.2 Drude and Lorentz models for dispersive media

To account for the complex index of material dielectric constant, as well as its variation with the frequency of light ω, a classical model based on the equation of a motion for a harmonically bound classical electrons interacting with an electric field $\vec{E}$ was proposed by Drude and Lorentz. The equation of motion is written as

$$m_e\left(\frac{\partial^2\vec{r}}{\partial t^2}+\gamma\frac{\partial\vec{r}}{\partial t}+\omega_0^2\vec{r}\right)=-e\vec{E}(\vec{r},t), \tag{2.3}$$

where ω_0 is the natural frequency of the oscillator, γ is the damping constant, m_e and e are the electron mass and charge, respectively. For an incident electromagnetic field of frequency ω, $\vec{E}(\vec{r},t)$ is represented by a complex exponential $\vec{E}=\vec{E_0}exp(-i\omega t)$. The solution of the equation (2.3) in complex form is given by $\vec{r}=-\frac{e}{m_e}\left(\omega_0^2-\omega^2-i\gamma\omega\right)^{-1}\vec{E}_0$. The electric dipole moment of the electron is given by $\vec{p}=-e\vec{r}$. The polarization field per unit volume is defined as $\vec{P}(\omega)=\epsilon_0\epsilon_\infty\chi\vec{E}=Np(\omega)=\frac{e^2N}{m_e}\left(\omega_0^2-\omega^2-i\gamma\omega\right)^{-1}\vec{E}(\omega)$, resulting in the following differential equation by taking Fourier transform

$$\frac{\partial^2\vec{J_L}}{\partial t^2}+\gamma\frac{\partial\vec{J_L}}{\partial t}+\omega_0^2\vec{J_L}=\epsilon_0\epsilon_\infty\omega_0^2\frac{\partial\vec{E}}{\partial t}, \tag{2.4}$$

where $\vec{J_L}=\frac{\partial\vec{P}}{\partial t}$ is the Lorentz current applied directly to Maxwell-Ampere equation (2.2).

The dielectric function ϵ for the material with one resonance is given by $\epsilon=\epsilon_\infty+\frac{\omega_0^2}{\omega_0^2-\omega^2-i\gamma\omega}$. The frequency dependent dielectric constant of the material with several optical resonances can be modeled by a set of Lorentz poles

$$\epsilon(\omega)=\epsilon_\infty+\sum_j\frac{G_j\omega_0^2}{\omega_j^2-\omega^2-i\gamma_j\omega}, \tag{2.5}$$

where γ_j is the damping factor for each Lorentz pole or collision wavelength, G_j is the oscillator strength such as $\sum_j G_j=1$, ω_j is the oscillating wavelength or the resonant frequency.

For Lorentz model, the real and the imaginary parts of the dielectric permittivity $\epsilon=Re(\epsilon)+iIm(\epsilon)$ are given by

$$\begin{aligned}\epsilon_1=Re(\epsilon)&=\epsilon_\infty+\sum_j\frac{G_j\omega_0^2(\omega_j^2-\omega^2)}{(\omega_j^2-\omega^2)^2+\gamma_j^2\omega^2}\\ \epsilon_2=Im(\epsilon)&=\sum_j\frac{G_j\omega_0^2\gamma_j\omega}{(\omega_j^2-\omega^2)^2+\gamma_j^2\omega^2}.\end{aligned} \tag{2.6}$$

If we neglect bound electrons, oscillating with resonant frequency, there is no natural frequency for free electron gas. In this case, the Drude model can be derived from the Lorentz model by making the assumption that $\omega_j=0$. This way, the real and imaginary parts of the dielectric permittivity are written as

$$\begin{aligned}\epsilon_1=Re(\epsilon)&=\epsilon_\infty-\sum_j\frac{G_j\omega_0^2}{\omega^2+\gamma_j^2}\\ \epsilon_2=Im(\epsilon)&=\sum_j\frac{G_j\omega_0^2\gamma_j}{\omega^3+\gamma_j^2\omega}.\end{aligned} \tag{2.7}$$

The general expression for the dielectric permittivity of the material with several optical resonances is known as Sellmeier's formula

$$\epsilon(\omega)=1+\sum_j\frac{G_j\omega_j}{\omega_j^2-\omega^2}. \tag{2.8}$$

For fused silica, a set of parameters was introduced and tested by comparing with experimental results by Nakamura et al. [122, 123]. A set of parameters for noble metals was proposed by Johnson and Christy [124].

The Lorentz equation (2.4) under the assumption $\omega_0 = 0$ and by substituting $\vec{J_D} = \frac{\partial P}{\partial t}$ takes form of the Drude equation for dispersive media

$$\frac{\partial \vec{J}_D}{\partial t} = -\frac{\vec{J}_D}{\tau_e} + \omega_p^2 \vec{E}, \tag{2.9}$$

where e is the elementary charge; m_e is the electron mass; n_e is the time-dependent free carrier density, $\omega_p^2 = \frac{e^2 n_e}{\epsilon_0 m_e}$ is the plasma frequency and $\tau_e = \gamma^{-1}$ is the electron collision time. The equation describes the heating of the conduction band electrons. The current $\vec{J_D}$ is applied directly to Maxwell-Ampere equation (2.2).

In our case, the dielectrics with time-varying optical properties are of interest, so the most convenient model is the Drude model, where the polarization current is defined by the equation (2.9).

The real and the imaginary parts of permittivity ϵ have been derived from a simple Drude model with time-varying electron density n_e (2.7). In fact, the time-dependent changes of the permittivity are associated both with state and band filling and the free carrier response [125] as follows

$$\begin{cases} \epsilon_1(n_e) = \epsilon - (\epsilon - 1)\dfrac{n_e}{n_a} - \dfrac{e^2 n_e}{m_e(\omega_L^2 + {\nu_e}^2)} \\ \epsilon_2(n_e) = \dfrac{e^2 n_e \nu_e}{m_e \omega_L (\omega_L^2 + {\nu_e}^2)}, \end{cases} \tag{2.10}$$

where $\epsilon = n^2$ is the dielectric constant of non-excited glass at $n_e = 0$, $\omega_L = 2\pi c/\lambda$ is the frequency of the laser and $\nu_e = {\tau_e}^{-1}$ is the electron collision frequency. The contribution of the valence electrons to glass permittivity is insignificant. One can estimate, that for $\nu_e = 2 \cdot 10^{15}$ s^{-1} and $n_{cr} = 1.74 \cdot 10^{27}$ m^{-3} for laser wavelength $\lambda = 800$ nm, the contribution of the conduction electrons is $\frac{e^2 n_e}{m_e(\omega_L^2 + {\nu_e}^2)} \approx 1.15$, whereas the one of the valence electrons is $(\epsilon - 1)\frac{n_e}{n_a} \approx 0.096$. As a result, their influence on the propagation is neglected in (2.2).

The permittivity of the material is directly related to the optical properties of the medium $\epsilon = (n + ik)^2$, where n is the refractive index, which indicates the phase velocity information, and k is the extinction coefficient, which indicates the amount of absorption loss while propagating through the material. One can derive the expressions for them as $n = \sqrt{(\sqrt{\epsilon_1^2 + \epsilon_2^2} + \epsilon_1)/2}$ and $k = \sqrt{(\sqrt{\epsilon_1^2 + \epsilon_2^2} - \epsilon_1)/2}$. Finally, the absorption coefficient is related to the extinction coefficient as $\alpha_{abs} = 4\pi k/\lambda$.

2.3 Kerr effect

Besides the frequency dependent linear contribution to the polarization field $\vec{P}$, the material responds nonlinearly to the applied electric field $\vec{E}$ due to Kerr effect. The third nonlinear electric polarization field is defined as $P_i = \epsilon_0 \epsilon_\infty \sum_{j=1}^{3} \sum_{k=1}^{3} \sum_{l=1}^{3} \chi^{(3)}_{ijkl} E_j E_k E_l$, where $\chi^{(3)}_{ijkl}$ - the 4^{th} order component of the electrical susceptibility [126]. For isotropic materials, there are 21 nonzero susceptibilities, of which only 3 are independent

$$\begin{aligned} &\chi^{(3)}_{1133} = \chi^{(3)}_{1122} = \chi^{(3)}_{2233} = \chi^{(3)}_{2211} = \chi^{(3)}_{3311} = \chi^{(3)}_{3322} \\ &\chi^{(3)}_{1331} = \chi^{(3)}_{1221} = \chi^{(3)}_{3223} = \chi^{(3)}_{2112} = \chi^{(3)}_{3113} = \chi^{(3)}_{2332} \\ &\chi^{(3)}_{1313} = \chi^{(3)}_{1212} = \chi^{(3)}_{2323} = \chi^{(3)}_{2121} = \chi^{(3)}_{3131} = \chi^{(3)}_{3232} \\ &\chi^{(3)}_{1111} = \chi^{(3)}_{2222} = \chi^{(3)}_{3333} = \chi^{(3)}_{2211} + \chi^{(3)}_{2112} + \chi^{(3)}_{2121}. \end{aligned} \tag{2.11}$$

The condition of the invariance of indices to all permutations of the input signals and the resulting beam comes from the assumption of Kleinman symmetry. This approximation applied to solve the problem numerically in reasonable times holds if the frequency of the laser is far below the material resonant frequency and there is no dispersion in the nonlinear response over the entire range of frequencies involved [127]. Finally, the components of the polarization field are given by

$P_i = \epsilon_0 \epsilon_\infty \chi_3 \left|\vec{E}\right|^2 E_i$, where χ_3 is the third-order susceptibility equal for all polarization components and without any frequency dependent contributions. This way, the complete displacement current is given by $\vec{D} = (\epsilon \vec{E} + \epsilon_\infty \chi_3 E^2 \vec{E})\epsilon_0$. Substituting the expression for the polarization field to $\vec{J}_{Kerr} = \dfrac{\partial \vec{P}}{\partial t}$ results in the following Kerr polarization current

$$\vec{J}_{Kerr} = \epsilon_0 \epsilon_\infty \chi_3 \frac{\partial \left(\left|\vec{E}\right|^2 \vec{E} \right)}{\partial t}. \tag{2.12}$$

The nonlinear current (2.12) is incorporated to the system of Maxwell's equations (2.2), analogically to the polarization Drude current $\vec{J}_p$. Note, that the third-order susceptibility is related to Kerr nonlinear refractive index as $\chi_3 = \frac{8 \cdot n_{Kerr}}{3} \frac{n}{2} \sqrt{\frac{\epsilon_0}{\mu_0}}$. The Kerr nonlinear refractive index is taken to be $n_{Kerr} = 3.89 \cdot 10^{-20} \mathrm{m}^2/\mathrm{W}$ for fused silica [61] (corresponding to $\chi_3 \approx 2 \cdot 10^{-22}$ $\mathrm{m}^2/\mathrm{V}^2$) and $n_{Kerr} = 3.45 \cdot 10^{-20} \mathrm{m}^2/\mathrm{W}$ for borosilicate glass [31,35].

2.4 Electron collision time

In the femtosecond laser-excited dielectrics, the electron collision time τ is variable during the process of the energy deposition, as the electron density and the electron temperature grow rapidly and the electron energy distribution is far from equilibrium during the whole pulse duration. On the same time, it is one of the most crucial parameters of the Drude model (2.7). For fused silica, the averaged values for the electron collision parameter reported in the literature vary from 0.2 fs [62,128,129] to 23.3 fs [69], revealing that it is definitely determined by the excitation conditions. As a result, attempts to evaluate the levels of electron plasma densities may lead to an error more than an order of magnitude and influence the balance between multiphoton and collisional ionization mechanisms [130].

On one side, a certain analogy can be drawn with temperature dependence of the collision time in metals, which is the sum of the contributions from the electron-phonon and electron-ion collisions. The general trend of behavior of the total collision time with the increasing laser intensity and electron temperature is that it decreases continuously, finally reaching the lower physical limit $\tau_{min} = d/V = 0.2$ fs [129], where V is the electron velocity and d is the interatomic distance. With further increase in intensity and temperature, the collision time increases as in ideal hot plasma, for which Spitzer's formula can be applied [90, 131] as

$$\tau_{Spitzer} = \frac{3}{4} \frac{(m_e k_b T_e)^{3/2}}{(2\pi)^{1/2} Z_{av} e^4 m_e n_e ln\Lambda}, \tag{2.13}$$

where Z_{av} is the ionization degree, T_e is the electron temperature, $ln\Lambda \approx 10$ is the Coulomb logarithm or the relationship between the maximum and minimum collisional parameter. Taking the electron temperature approximately equal to the energy of electron motion $T_e \approx \frac{m_e}{2} \left(\frac{eE}{m_e \omega}\right)^2$, one can estimate the collision time $\tau = 1$ fs [71]. In contrast, in the limit of a cold solid at temperatures below the Fermi temperature, the electrons are in a degenerate state. The collision frequency is no longer dependent on the electron temperature, but governed by the scattering of electrons by phonons or lattice vibrations, giving the maximum value of the collision time for room temperature $\tau_e \approx 25$ fs [129]. Thus, the minimum value at room temperature and the maximum limited value for the effective collision rate are well defined.

On the other side, it is well-known that the collision time decreases with the free electron density increasing up to the near-critical density $n_{cr} = \epsilon_0 m_e \omega^2 / e^2$, resulting in a decrease of reflectivity [132]. Therefore, an inversely proportional relation with the free electron density can be assumed analogically to semiconductors, where the charge carriers are electrons and holes and their numbers are controlled by the concentration of impurity elements and the electron mobility is characterized by the empirical relationship

$$\mu_e = \mu_{min} + \frac{\mu_{max} - \mu_{min}}{1 + \left(\frac{n_e}{n_{cr}}\right)^\alpha}. \tag{2.14}$$

As there is also strong relationship between the electron collision time and the electron mobility, common empirical dependence can be applied for $\tau = \tau_{min} + \frac{\tau_{max}-\tau_{min}}{1+\left(\frac{n_e}{n_{cr}}\right)^{\alpha}}$, where, for example, $\tau_{min} = 0.2$ fs, $\tau_{max} = 2$ fs and $\alpha = 0.7$. The maxima and minima of the parameter are taken from the work [133], where the calculated reflectivity for different electron collision times is compared with the experimental results. Thus, with growing intensity smaller values for collision time are obtained. For critical value of density, the value for the collision time equals $\tau = 1.1$ fs [134]. The comparison between the electronic modifications obtained by taking into account different collision times as parameters is given in Chapter 4. If not mentioned, the electron collision time taken in this thesis is $\tau_e = 0.5$ fs [2].

2.5 Ponderomotive force

The electrons move under the effect of the laser electric and magnetic fields described by the equation of motion $m\frac{d\vec{v}}{dt} = -e\vec{E}(\vec{r}) - e\vec{v} \times \vec{B}(\vec{r})$. If the electromagnetic wave varies in space and $\vec{v}$ is not constant due to nonlinear propagation in media, there is a time-averaged charged force, causing the electrons to move along the propagation direction. The expression for the nonlinear ponderomotive force can be found by time-averaging the second order solution of the equation of motion for the charged particle, taking account the term $\vec{v} \times \vec{B}$ and the expression for $\vec{B}$ from Maxwell-Faraday equation. The force is inversely proportional to the squared frequency of irradiation $F_p = -\frac{e^2}{4m_e\omega^2}\nabla(E^2) = -\nabla\Phi_{PM}$ in an oscillating electromagnetic field [14,105], where Φ_{PM} is the ponderomotive potential and $\vec{E}(\vec{r})$ is the local field amplitude of the electric field. The sign indicates that the force pushes the electrons away from the regions of high intensity. The carrier density generated due to the ponderomotive potential is given by $n_p = \frac{1}{3\pi^2}(\frac{3m_e}{\hbar})^{3/2}(E_f - \Phi_{PM})^{3/2}$, where E_f is the Fermi energy and $\hbar$ is the reduced Plank constant. Therefore, the permittivity related to the ponderomotive force in the frequency domain is described by

$$\epsilon_{PM}(\left|\vec{E}\right|^2) = 1 - \frac{e^2}{3\pi^2\epsilon_0 m_e\omega^2}\left(\frac{2m_e}{\hbar^2}\right)^{3/2}\left(E_f - \frac{e^2\left|\vec{E}\right|^2}{2m_e\omega^2}\right)^{3/2}. \tag{2.15}$$

By truncating Taylor series, one can find the Kerr-like nonlinearity due to the presence of the charged force [135]

$$\epsilon_{PM}\left(\left|\vec{E}\right|^2\right) = \epsilon_\infty + \frac{3}{2}\left(\frac{\omega_p}{3\pi^2\epsilon_0 m_e e}\right)^{2/3}\frac{e^4}{\omega^4\hbar^2}\left|\vec{E}\right|^2 = \epsilon_\infty + \chi_{PM}\left|\vec{E}\right|^2. \tag{2.16}$$

It is worth noting, that the contribution of the ponderomotive force to the glass permittivity increases with the increasing wavelength in fourth order λ.

Analogically to the polarization current, the convolution marked by $*$ is introduced as $G(t) = \chi_{PM}(t) * E^2(t)$ [136] with the corresponding Fourier transform $G(\omega) = \chi_{PM}(\omega)\vartheta[E^2(t)]$, where ϑ stands for Fourier transform. Taking into account the frequency dependence of χ_{PM}, the differential equation is obtained by applying the inverse Fourier transform

$$\frac{\partial^4 G}{\partial t^4} = \frac{3}{2}\left(\frac{\omega_p}{3\pi^2\epsilon_0 m_e e}\right)^{2/3}\frac{e^4}{\hbar^2}E^2. \tag{2.17}$$

The nonlinear current corresponding to the ponderomotive force contribution, which is incorporated to Maxwell-Ampere equation (2.2), is given by

$$\vec{J}_{PM} = \epsilon_0\epsilon_\infty\chi_{PM}\frac{\partial\left(\left|\vec{G}\right|\vec{E}\right)}{\partial t}. \tag{2.18}$$

2.6 Free carrier rate equation

It is well established that three main mechanisms are responsible for the material excitation and the flow of electrons from valence to conduction band [68,69,137]: ionization produced by simultaneous absorption of multiple photons in Fig. 2.1(a), tunneling through the potential barrier in Fig. 2.1(b), and

avalanche or electron impact ionization in Fig. 2.1(c). The relative contribution of the mechanisms depends on laser wavelength, pulse duration, intensity and electron density. The time-dependent conduction-band carrier density evolution is described with a rate equation, firstly proposed by Stuart [137], taking into account photoionization, avalanche ionization, recombination and electron diffusion as

$$\frac{\partial n_e}{\partial t} = \frac{n_a - n_e}{n_a} w_{pi}(I) + W_{av}(I, n_e) + D\Delta n_e - \frac{n_e}{\tau_{rec}}, \tag{2.19}$$

where τ_{rec} is the electron recombination time, w_{pi} is the photoionization rate, W_{av} is the contribution due to avalanche ionization, n_a is the saturation particle density, and D is the diffusion coefficient. The diffusion coefficient is estimated as $D = V^2\tau$, where $V = 2 \cdot 10^8 cm/s$ is the thermal velocity for fused silica and τ is the electron collision time [107].

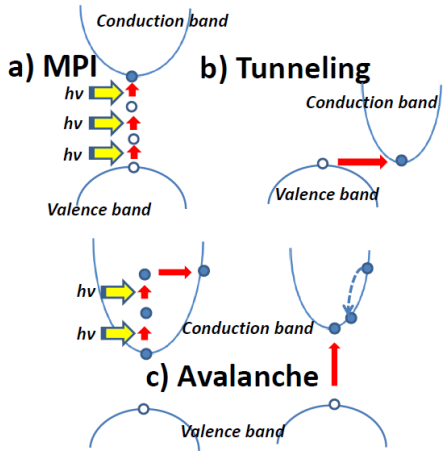

Figure 2.1: Mechanisms of nonlinear ionization in dielectrics: (a) multiphoton ionization (MPI), (b) tunneling ionization, (c) avlanche ionization.

Photoionization leads not only to the increase of the free electron density but also to the reduction in optical pulse energy required to ionize the medium. To take into account the losses, the effective current $\vec{J_{pi}}$ is incorporated to Maxwell-Ampere equation (2.2). The value of the current is found by setting the laser energy gain of electrons due to photoionization equal to the energy loss of the electric field $\vec{J_{pi}}\vec{E} = E_g w_{pi} n_a$ [71, 82, 104]. One can derive the following photoionization current

$$\vec{J}_{pi} = E_g \frac{w_{pi}(I)\vec{E}}{\left|\vec{E}\right|^2} \frac{n_a - n_e}{n_a}. \tag{2.20}$$

Here, E_g is the electron band gap in the absence of the electric field; n_a is the saturation density; $I = \frac{n}{2}\sqrt{\frac{\epsilon_0}{\mu_0}}\left|\vec{E}\right|^2$ is the intensity and n is the refractive index of unexcited material with $n_e = 0$. The energy gap E_g refers to the energy difference between the top of the valence band and the bottom of the conduction band in Fig.2.1.

The rate $w_{pi}(I)$ depends on the laser intensity. For intensities lower than $I = 10^{17} W/m^2$, tunneling ionization effect is negligible, whereas multiphoton ionization could be described by six-photon ionizaton approximation $w_{pi} = \sigma_6 I^6$ [69]. For intensities significantly higher than $I = 10^{17} W/m^2$, the tunneling effect may play a role. Both effects are included in a model proposed by Keldysh [138]. The parameter allowing to estimate which effect is essential (multiphoton ionization or tunneling effect) was introduced by Keldysh $\gamma = \frac{\omega\sqrt{m^* E_g}}{eI} = \frac{\omega\sqrt{2m^* W_{ion}}}{eE}$, where $\omega = 2\pi \cdot c/\lambda \approx 2.355 * 10^{15} s^{-1}$ is the frequency at the wavelength $\lambda = 800$ nm, $E_g = 9$ eV for fused silica, $m^* = \frac{m_e \cdot m_h}{m_e + m_h} \approx 0.5 \cdot 9.1 \cdot 10^{-31} kg$ is the reduced mass of the electron and the hole. For a fixed laser wavelength, the value of the photoionization rate can be found separately from the complete Keldysh formalism [138] and incorporated in the equation (2.19). Note that the cycle averaged expression for laser intensity or electric field should be used to apply with photoionization rate. In this work, however, we evaluate directly the

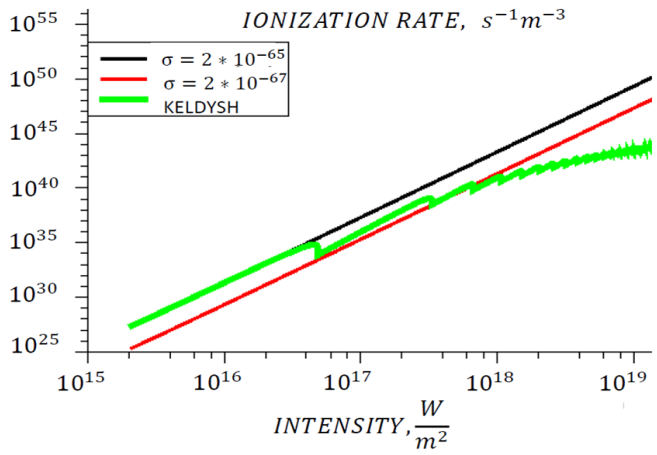

Figure 2.2: Comparison of photoionization rates given by Keldysh theory [138] for laser wavelength $\lambda = 800$ nm, six-photon approximations with $\sigma_6 = 2 \cdot 10^{-65} m^9 W^{-6} s^{-1}$ and $\sigma_6 = 2 \cdot 10^{-67} m^9 W^{-6} s^{-1}$ [69].

time-dependent intensity not averaged by period to calculate the free carrier electron density (2.19) and the photoionization current (2.20).

In the case of fused silica and $\lambda = 800$ nm laser irradiation, the six-photon ionization approximation is commonly used. Fig. 2.2 shows that applying the six-photon ionization approximation instead of the complete Keldysh ionization rate leads to an overestimation (in case of $\sigma_6 = 2 \cdot 10^{-65} m^9 W^{-6} s^{-1}$) or to an underestimation (in case of $\sigma_6 = 2 \cdot 10^{-65} m^9 W^{-6} s^{-1}$) of the ionization rate up to three orders in magnitude for intensities higher or less than $I = 10^{17} W/m^2$ [69, 132, 134, 139]. In contrast, three-photon ionization approximation $w_{pi} = \sigma_3 I^3$ is commonly applied for low electron band gap glasses, as it gives better agreement with the experimental results [31, 140–143]. The reported multiphoton ionization coefficients for fused silica and borosilicate glasses are summarized in Table 2.1.

Another mechanism, which is responsible for the electron density increase is the avalanche ionization (AI). There are several models frequently used in the literature for predicting the AI rate [144].

Stuart et al. proposed that the rate depends linearly on the laser intensity as $W_{av} = \alpha \cdot I(t)$, where the avalanche ionization coefficient $\alpha = 10^{-3} \frac{m^2}{s \cdot W}$ for fused silica was found by numerically solving a Fokker-Planck equation describing the electron dynamics [145]. Note, that the assumption that the avalanche rate scales linearly with the laser intensity is valid only for low intensities [144].

A simplified model of avalanche ionization rate assuming constant collision frequencies and energy loss was proposed by Sparks [144, 146]. This model assumes energy gain of a conduction electron from an alternating electric field, once the conduction electron has attained the energy equal to E_g, it can excite a valence electron across the band gap, and this process repeats itself as

$$W_{Sparks} = \frac{0.693 e^2 E^2 \tau_K}{m_e{}^* E_g (1 + \omega^2 {\tau_K}^2)} - \frac{0.693 h\omega_p}{E_g \tau_L}, \tag{2.21}$$

where $\tau_K = 1.36 \cdot 10^{-15} s$ is the electron-phonon relaxation time when only large-angle scattering is considered, $\tau_L = 8.77 \cdot 10^{-16} s$ is the relaxation time when both large- and small- angle scatterings are considered, ω_p is the average phonon frequency, and $h\omega_p = 0.025 eV$. The Thornber AI model is based on the excursion and acceleration of the electrons in a direct current electric field and is applicable for all electric field strengths [146].

The avalanche ionization rate can be also derived from the Drude model [74, 147, 148], where the heating of free electrons is associated with the absorption coefficient. In this case, the avalanche ionization rate is described via the Drude formalism as

$$W_{av} = \frac{e^2 \tau_e n_e \left|\vec{E}\right|^2}{nc\epsilon_0 m_e E_g (1 + \omega^2 {\tau_e}^2)(1 + m_e{}^*/m_e)} \frac{n_a - n_e}{n_a}, \tag{2.22}$$

where τ_e is the electron collision time, $m_e{}^*$ is the reduced electron mass, n is the refractive index of the non-excited material, and n_a is the saturation electron density.

All the introduced approaches fail to account for the fact that only the most energetic electrons are able to induce the avalanche ionization. A more general approach can be used to estimate accurately the contribution of the avalanche ionization $W_{av}(I,\rho)$ based on the multiple rate equation [68]. The system of P coupled equations $i=[1,..,P]$ writes as follows

$$\begin{cases} \dfrac{\partial n_1}{\partial t} = (n_a - n_e)w_{pi} - W_{1,pt}n_1 + 2\bar{\alpha}n_i - \dfrac{n_1}{\tau_{rec}} \\ \dfrac{\partial n_2}{\partial t} = W_{1,pt}n_1 - W_{1,pt}n_2 - \dfrac{n_2}{\tau_{rec}} \\ ..... \\ \dfrac{\partial n_i}{\partial t} = W_{1,pt}n_{i-1} - \bar{\alpha}n_i - \dfrac{n_i}{\tau_{rec}}, \end{cases} \tag{2.23}$$

where P is defined by the critical energy of the impact ionization and the corresponding one-photon energy; the total electron carrier density $n_e = \sum_{i=1}^{P} n_i$; $\bar{\alpha}$ is the avalanche parameter; and $W_{1,pt}$ is the mean value of the one-photon absorption probability for fused silica. Unlike the single-rate equation, the multiple rate equation takes into account the fact that only the electrons of i population, which have sufficiently high energy, contribute to the avalanche ionization [68]. The number of discrete energy states is calculated as $P = 1 + [\frac{\epsilon_{crit}}{\hbar\omega}]$, where the critical energy for impact ionization is defined as

$$\epsilon_{crit} = (1 + m^*/m_e)\left(E_g + \frac{e^2 I}{4m^*\omega^2}\right), \tag{2.24}$$

where the laser frequency is $\omega = 2\pi c/\lambda$ and the corresponding photon energy is $\hbar\omega$. One can note, that the critical energy (2.24) takes into account the changes of the electron band gap E_g. The one-photon absorption probability is defined as $W_{1,pt} = \frac{\sigma}{ln(2)\epsilon_{crit}} \frac{1}{\sqrt[P-1]{2}-1} I$, where the absorption cross section is described by the Drude formalism as $\sigma = \frac{e^2}{m^*\nu_e[1+(\omega/\nu_e)^2]}$ [149]. For the avalanche parameter, the asymptotic value $\bar{\alpha} = [\sqrt[P-1]{2} - 1]W_{1,pt}$ is proposed [68].

Recent experiments have revealed that the electron recombination time τ_{rec} is strongly dependent on the energy deposition, electron densities and laser-induced temperatures [2,28,59,60]. The precise knowledge of the characteristic time dependency is still lacking. Here, electron recombination time is taken to be $\tau_{rec} = 1$ps [150]. This value is within the reported times for similar laser irradiation conditions, i. e. moderate laser pulse energies $\Sigma < 4\mu J$ and sub-picosecond pulses [28, 60]. Note, that the electron recombination time is longer than the commonly reported decay $\tau_{tr} = 150$ fs [61,62], attributed to ultrafast self-trapping phenomena. Sub-picosecond electron plasma lifetimes are restricted to low electron densities $n_e < 10^{25}$ m^{-3} [61], low temperatures and low laser pulse energies. The electron densities are one-two order of magnitude greater in the laser irradiation regimes, discussed in this thesis.

In the case of low band gap glasses such as borosilicate and soda-lime glasses the electron trapping is measured to be somewhat two orders higher $\tau_{rec} = 100$ ps [62]. It was also shown that the recombination depends strongly on the electron density [35, 151]. As an example, for borosilicate glass, the following density-dependent electron trapping time was proposed $\tau_{rec} = \nu_{rec} n_e$, where $\nu_{rec} = 2 \cdot 10^{-15} m^3/s$ [35]. This dependence is used further in this thesis for borosilicate glass.

To define the nonlinear processes, playing the important role in ultrashort laser-induced irradiation, we investigate the final electron density distribution. The basic model takes account the photoionization given by Keldysh formalism, the avalanche ionization by Drude model, the photoionization depletion by $\vec{J}_{pi}$ current, electron collisions with $\tau = 0.5$ fs, electron recombination with $\tau_{rec} = 1$ ps, and Kerr effect (black dashed line). We consider moderate focusing conditions and the resulting electron densities, slightly overpassing the critical value $n_{cr} = 1.74 \cdot 10^{27}$ m^{-3}. If we add the ponderomotive force, the distribution as well as the maximum electron densities do not change significantly as marked by dashed line in Fig. 2.3. Analogically, the contribution of the electron diffusion defined by $D = V^2\tau$ for $\tau = 0.5$ fs is not significant (not shown here). If the coefficient $D \approx 0.04$ m^2/s proposed by Gildenburg et al. [107] is considered, the contribution is relatively weak but visible as shown by dashed-dotted line

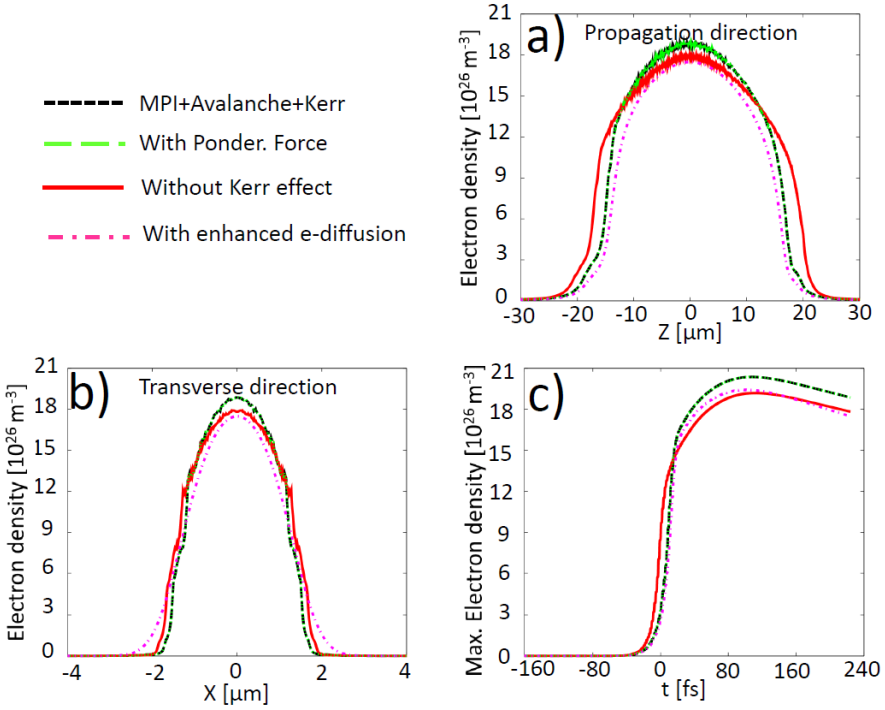

Figure 2.3: The contribution of nonlinear processes (Kerr effect, electron diffusion and ponderomotive force) to the final electron density distribution (a) in the propagation direction, (b) in the transverse direction, (c) maximum values of the electron densities. Laser irradiation conditions: laser wavelength is $\lambda = 800$ nm, the laser pulse energy is fixed to be $2\mu J$, the waist beam is $2\mu m$, the pulse duration is fixed to be 80 fs.

in Fig. 2.3. Note, that the electron collision time $\tau = 10$ fs was proposed there. Finally, if we do not consider the Kerr effect, both the maximum electron density and the spatial distributions are modified by more than 10% (solid line).

We conclude that the contribution caused by the ponderomotive force and the electron diffusion are not significant at moderate irradiation conditions, however, the Kerr effect should be taken into account.

We show that the electron collisions define mostly the spatial electron density profile in Fig. 2.4. Main nonlinear processes such as photoionization, avalanche ionization and Kerr effect are included but slightly different electron collision times are used $\tau = 0.5$ fs and $\tau = 1$ fs. As a result, different optical properties are given for the fixed laser pulse energy and focusing irradiation conditions by equations (2.7).

2.7 Electron-ion heat transfer equations

The ionization process locally transforms dielectric material into an absorbing plasma with metallic properties. The electrons in the conduction band are heated by the laser, and transfer their energy to the lattice. Heating of the dielectric and establishment of the energy equilibrium between the electrons and the lattice can be described by the two-temperature model, and the energy conservation law as follows

$$\begin{cases} C_e \dfrac{\partial T_e}{\partial t} = \nabla \cdot (k_e \nabla T_e) - \gamma_{ei}(T_e - T_i) + I\alpha_{abs} \\ C_i \dfrac{\partial T_i}{\partial t} = \nabla \cdot (k_i \nabla T_i) + \gamma_{ei}(T_e - T_i) - B\beta T_0 \dfrac{\partial}{\partial t}(\nabla \cdot \vec{u}), \end{cases} \tag{2.25}$$

where γ_{ei} is electron-lattice coupling factor, C_e and C_i are the electron and the lattice heat capacity respectively, k_e and k_i are the electron and the lattice thermal conductivities, α_{abs} is the bremsstrahlung

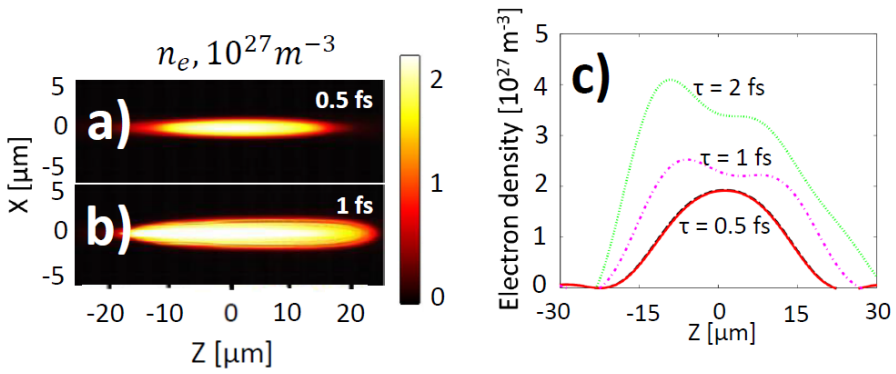

Figure 2.4: Spatial electron density distributions for electron collision time (a) 0.5 fs (b) 1 fs (c) maximum electron densities in the propagation direction. Laser irradiation conditions: laser wavelength is $\lambda = 800$ nm, the laser pulse energy is fixed to be $2\mu J$, the waist beam is $2\mu m$ and the pulse duration 80 fs.

absorption coefficient related to the extinction coefficient as $\alpha = \frac{4\pi k}{\lambda}$, $\vec{u}$ is the displacement vector, β is the coefficient of thermal expansion, and B is the bulk elastic modulus. The last term stands for the transform of mechanical energy to thermal energy and describes heat dissipation of the stress wave [152, 153].

The coupling factor is estimated from known data on the characteristic times of electron-lattice relaxation $\gamma_{ei} = \dfrac{C_e}{\tau_{ei}}$, where $\tau_{ei} = 1$ ps for transparent dielectrics [154]. The electron heat capacity is defined as $C_e = \dfrac{3}{2} k_B n_e$, where $k_B = 1.38 \cdot 10^{-23} m^2 kg s^{-2} K^{-1}$ is the Boltzman constant. The heat conductivity for electrons is $k_e = 2{k_B}^2 \mu_e n_e T_e / e$, where $\mu_e = 3 \cdot 10^{-5} \frac{m^2}{V \cdot s}$ is the electron mobility [154].

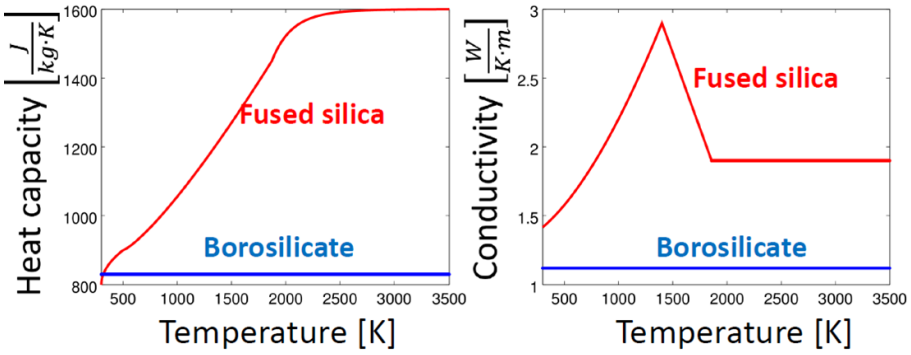

Figure 2.5: Heat capacity and thermal conductivity temperature dependencies for fused silica [59, 155, 156] and constant values for borosilicate glass [23].

The adaptive fit shown in Fig. 2.5 is used to reproduce the temperature dependence of the fused silica thermal conductivity with slope discontinuities at the annealing temperature $T_{anneal} = 1400$ K and the melting temperature $T_{melt} = 1875$ K [156] as follows

$$k_i = \begin{cases} 1.3 + 1.6 \cdot \left(\frac{T_i}{1400}\right)^{1.7} \frac{W}{Km}, & 300K \leq T_i < 1400K \\ 2.9 - \frac{T_i - 1400}{475} \frac{W}{Km}, & 1400K \leq T_i < 1875K \\ 1.9 \frac{W}{Km}, & T_i \geq 1875K. \end{cases} \tag{2.26}$$

The ion heat capacity temperature dependence for fused silica shown in Fig. 2.5 is taken from

recent experimental data [59, 155] approximated as

$$C_i = \begin{cases} 1.6 \cdot \left(1 + \sqrt{\frac{T_i - 300}{200}}/8\right) \frac{MJ}{m^3 K}, 300K \leq T_i < 500K \\ 1.8 \cdot \left[1 + \left(\frac{T_i - 500}{1375}\right)^{1.25} \frac{11}{18}\right] \frac{MJ}{m^3 K}, 500K \leq T_i < 1875K \\ [3.2 - 0.3\left(\frac{1875}{T_i}\right)^{10}] \frac{MJ}{m^3 K}, \quad T_i \geq 1875K, \end{cases} \tag{2.27}$$

The commonly reported values of thermal conductivities and ion heat capacities for fused silica and for borosilicate glasses are shown in Table 2.1.

2.8 Thermo-elastic wave equations

Thermo-elastic deformation caused by nonuniform temperature distribution in glasses is determined by thermo-elastic wave equations [157–159] as

$$\rho \frac{\partial^2 \vec{u}}{\partial t^2} = G\nabla^2 \vec{u} + \frac{G}{1-2\nu} \nabla(\nabla \cdot \vec{u}) - B\beta \nabla T_i, \tag{2.28}$$

where ν is Poisson coefficient, ρ is the material density, E is the longitudinal elastic modulus or Young's modulus, $B = \frac{E}{3(1-2\nu)}$ is the bulk elastic modulus, and $G = \frac{E}{2(1+\nu)}$ is the shear elastic modulus. The anomalous temperature dependence of elastic moduli and Poisson coefficient is taken into account as it was proposed by Parc et al. [160] for fused silica as follows

$$\begin{cases} E = (97 - \frac{1200}{T_i + 1200} \cdot 24)\text{GPa} \\ B = (60 - \frac{1200}{T_i + 1200} \cdot 23.2)\text{GPa} \\ G = (33.5 - \frac{1173}{T_i + 1173} \cdot 2.3)\text{GPa} \\ \nu = 0.2 - \frac{1200}{T_i + 1200} \cdot 0.03. \end{cases} \tag{2.29}$$

Since no temperature dependency has been found for borosilicate glass, the constant value is taken for E and ν, whereas the expressions for the bulk and the shear elastic moduli are defined by the formulas indicated above. The reported values of elastic moduli and Poisson coefficient for fused silica and borosilicate glasses are summarized in Table 2.1. Note, that the temperature dependence of thermal expansion coefficient β, bulk moduli and Poisson coefficient is known only for solid phase (up to melting temperature $T_{melt} = 1875$ K). The applicability of thermoelastic wave equations is limited by these temperatures. Furthermore, the equations do not describe glass decomposition processes and can not be used to describe the laser-induced dynamics at strong shock wave propagation ($\sigma > 1$) GPa and strong material compression ($\rho/\rho_0 > 1$) [89, 90]. In this case, hydrodynamic equations supported by the equation of state and shock data should be used to predict the material displacement behavior [90]. These regimes are out of the scope of the proposed numerical model and are not considered in this work.

Density is obtained based on the continuity equation as follows

$$\frac{\partial \rho}{\partial t} + \nabla \cdot \left(\rho \frac{\partial \vec{u}}{\partial t}\right) = 0. \tag{2.30}$$

The laser-induced stress are calculated from the displacement vector using the stress-strain relation [152, 153, 159] as follows

$$\begin{cases} \sigma_{xx} = 2G\left(\frac{\partial u_x}{\partial x} + \frac{\nu}{1-2\nu}\frac{\partial u_y}{\partial y}\right) - B\beta(T - T_0) \\ \sigma_{yy} = 2G\left(\frac{\partial u_y}{\partial y} + \frac{\nu}{1-2\nu}\frac{\partial u_x}{\partial x}\right) - B\beta(T - T_0) \\ \sigma_{xy} = G\left(\frac{\partial u_x}{\partial y} + \frac{\partial u_y}{\partial x}\right), \end{cases} \tag{2.31}$$

where $T_0 = 300$ K is the initial temperature. Von Mises criterion suggests that the material withstands loads tending to elongate till the tensile strength σ_{tens} defined as

$$\sigma_{tens} = \sqrt{\sigma_{xx}^2 - \sigma_{xx}\sigma_{yy} + \sigma_{yy}^2 + 3\sigma_{xy}^2} \tag{2.32}$$

reaches the critical value [161]. The critical value for fused silica is 48.3 MPa [153].

The transient refractive index change can be induced in two main ways as a consequence of ultrashort laser interaction with glasses. The first way is a mechanical way, where the changes are associated with the modification induced by stresses. The second way is due to structural properties of the glass, which are commonly related to the lattice temperature by thermo-optic coefficients [162, 163]. This way, the complete transient refractive index can be written as

$$\Delta n_i = -\frac{{n_0}^3}{2}\sum_{j=1}^{2} p_{ij}\frac{\partial u_j}{\partial j} + \frac{\partial n}{\partial T_i}(T_i - T_0), \tag{2.33}$$

where $i, j = 1, 2$ correspond to x, y and p_{ij} is the photo-elastic matrix with coefficients $p_{11} = p_{22} = 0.121$ and $p_{12} = p_{21} = 0.27$ for glass [83, 164, 165] and $\frac{\partial n}{\partial T_i}$ is the experimentally measured thermo-optic coefficient. For fused silica, it equals to $9.33 \cdot 10^{-6}$ K^{-1} for the temperatures up to 800 K [162, 163], whereas for borosilicate glasses the coefficient is smaller $3.41 \cdot 10^{-6}$ K^{-1} [162]. The presented expression, however, does not give the information about final permanent refractive index changes in glasses related to type-I (densification) and type-II (rarefaction). The conditions for void formation are discussed below.

2.9 Viscosity and relaxation time

While irradiated by ultrashort laser, glasses are heated up to high temperatures [29], at which the material properties significantly change during glass-liquid transition [156, 166]. One of the crucial properties is viscosity η, which is a measure of the material resistance to the gradual tensile material deformation. Glass viscosity is known to decrease exponentially with the increasing temperature [167–169]. This way, if the temperatures are higher than a certain critical value, the material will be relaxed viscoelastically faster than cooling time [109].

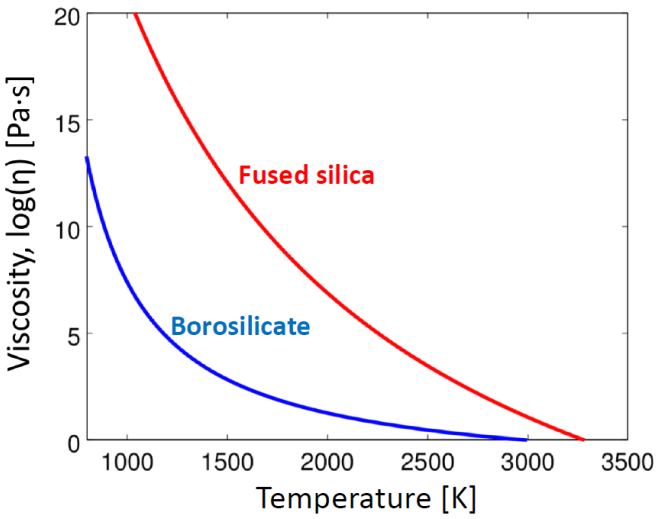

Figure 2.6: Viscosity temperature dependencies for fused silica and borosilicate glass [170].

One of the possibilities to describe the temperature dependence of viscosity is to use the Vogel-Fulcher-Tammann (VTF) model, which describes viscosity data at intermediate temperatures over many orders of magnitude with a high accuracy [169]

$$ln[\eta(T_i)] = A + B/(T_i - T_V), \tag{2.34}$$

where $A = -7.925$ and $B = 31555.9$ are constants, and $T_V = -142$ K is Vogel's temperature for fused silica; $A = -1.97$, $B = 4912.5$, $T_V = 475.4$ K for borosilicate glass. The parameters are taken from the book [170]. The resulting viscosity curves shown in Fig. 2.6 fit well the experimental measurements [167, 168, 171] and consistent with the other viscosity models [169].

The viscosity also governs viscoelastic relaxation processes. For viscoelastic materials, the stress depends not only on the strain rate but also changes due to viscous damping. Maxwell model approximates the stress evolution in the material in the case of small deformations, comprising of a spring and a Newton damper in series as follows

$$\frac{\partial \varsigma}{\partial t} = \frac{1}{E}\frac{\partial \sigma}{\partial t} + \frac{\sigma}{\eta}, \tag{2.35}$$

where $\zeta = -\frac{\Delta\rho}{\rho\Delta t}$ is the strain rate, $\Delta\rho < 0$ is the density change, corresponding to material's expansion and rarefaction, Δt is the characteristic time of the deformation, and $\rho = 2.2$ g/cm^3 is fused silica density.

For short picosecond timescales $\frac{\partial \varsigma}{\partial t} \gg \frac{\sigma}{\eta}$, therefore all the energy is stored elastically $\sigma = \varsigma E$. At nanosecond-microsecond timescales the viscous loss term can play an important role $\frac{\sigma}{\eta} \approx \frac{1}{E}\frac{\partial \sigma}{\partial t}$, which leads to the relaxation of the stress within a characteristic time $\tau_M = \eta/E$. Thus, Maxwell viscoelastic relaxation time τ_M gives the time required for material parameters stabilization. The temporal evolution of the stress due to viscous loss is not considered in calculations, as it is shown that the viscoelastic relaxation takes place before fast cooling of the lattice only for high temperatures $T_i \approx 3000$ K and low glass viscosity. For these extreme conditions, the system of thermo-elasoplastic equations can not be applied to evaluate correctly the laser-induced stress evolution.

2.10 Glass decomposition criteria

Here the criteria for void-like structure formation are detailed. Two major pathways are considered: a mechanical way or cavitation/fragmentation, represented by viscoelastic criterion based on the energy conservation law [172] and a thermal way or phase explosion, described by the classical nucleation theory.

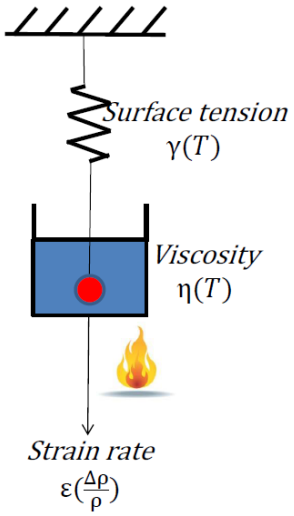

Figure 2.7: Illustration of Grady's viscoelastic model for spall in liquid.

To define the conditions for cavitation inside fused silica bulk, the viscoelastic energy conservation law is used. According to the Grady's spall criterion for liquids [172], the sum of both elastic and kinetic energies should be greater than the surface energy, required to fracture the liquid into nanocavities of size R, plus the local viscous dissipation during void growth and coalescence in the cavitation process as follows

$$\frac{P_{dyn}^2}{4B} + \frac{\rho\zeta^2 R^2}{120} \geq \frac{6\sigma}{R} + \eta\zeta, \tag{2.36}$$

where $B = \frac{\rho c_s^2(1+\nu)}{3(1-\nu)} \approx \rho c_s^2/2 \approx 40$ GPa is the elastic bulk modulus [160], $c_s \approx 5.9 \cdot 10^3$ m/s^2 is the sound speed in fused silica, $\nu \approx 0.2$ is Poisson ratio [160], P_{dyn} is the dynamic tensile strength required for cavitation, $\eta(T)$ is the viscosity, $\sigma = \sigma_0(1 - T/T_{cr})^{\alpha}$ is the surface tension, $\sigma_0 = 0.3$ N/m is the surface tension constant [173], $\alpha = 1.25$ is the critical index [174]. The first term $\frac{P_{dyn}^2}{4B}$ has the main contribution and expresses the elastic energy of deformation. The second term $\frac{\rho\zeta^2 R^2}{120}$ is the corresponding kinetic energy. The work against tension forces $\frac{6\sigma}{R}$ and dissipation forces $\eta\zeta$ are proportional to the surface tension $\sigma(T)$ and the viscosity $\eta(T)$, which both depend on the laser-induced temperatures in glass (decrease with the increasing temperature).

The viscoelastic criterion could be interpreted in terms of a mechanical model: a mass suspended by an elastic spring (surface tension) and put in a viscous liquid (viscosity) illustrated in Fig. 2.7. The laser-induced strain of the material plays the role of someone pulling the rope. Besides the deformation process, the glass is heated and then cools down fast in a microsecond timescale. Note that the required temporal temperature evolution should be calculated by solving (2.25), whereas the evolution of the strain rate by solving both the momentum (2.28) and continuity equations (2.30).

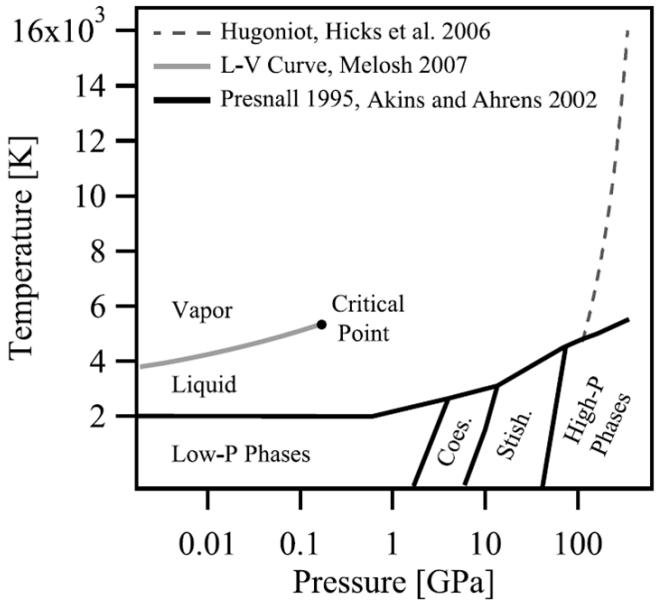

Figure 2.8: Phase diagram for fused silica taken from Ref. [174] indicating fused silica phases such as low-pressure phase, liquid and vapor phases, coesite, stishovite and high-pressure phases.

According to the classical homogeneous nucleation theory (CNT), the rate, at which nucleation occurs is given by the free energy of the critical nucleus $W = \frac{16\pi\sigma^3}{3\Delta P^2}$, where σ is the surface tension, defined previously, ΔP is the difference in free energy per unit volume between the thermodynamic phase nucleation and the phase that is nucleating, $T_{cr} \approx 5400$ K is the critical point temperature for fused silica [174]. The nucleation growth begins after a characteristic time $\tau_{nucl} = \exp(\frac{W}{k_B T})/N$, where $N = V\rho N_a/M \approx 2.1 \cdot 10^{10} s^{-1}$ is the number of sites available for nucleation in $V = 1\mu$m^3, N_a is Avogadro number, and $M \approx 60$ g/mole is the fused silica molar mass. The critical nucleus is defined by the minimum of homogeneous nucleation barrier $W = \frac{4}{3}\pi r^3 \Delta P + 4\pi r^2 \sigma$, i. e. $r_{cr} = -\frac{2\sigma}{\Delta P}$, satisfying $\partial W(r_{cr})/\partial r = 0$. The pressure at thermodynamic equilibrium is taken from the liquid-vapor curve for fused silica calculated by the equation of state (EOS) [174–176]. Pressure-temperature phase diagram is shown in Fig. 2.8. Note, that the regime of void-like structure formation (type-II) at moderate laser pulse irradiation, mostly considered in this thesis, takes place for temperatures higher than the melting point $T_{melt} > 1875$ K and pressures $P < 10$ GPa, therefore, the nucleation here is the transition from the metastable liquid phase to the vapor phase.

2.11 Rayleigh-Plesset equation

The Rayleigh-Plesset equation is then solved to analyze the nanopores dynamics [177,178], which is written as follows

$$\ddot{R} = -\frac{3}{2}\frac{(\dot{R})^2}{R} - \frac{4\eta\dot{R}}{\rho R^2} - \frac{\Delta P}{\rho R} - \frac{2\sigma}{\rho R^2}, \tag{2.37}$$

where $R(t)$ is the characteristic size of nanopores, $\dot{R}$ and $\ddot{R}$ are the first and the second derivatives of the size function, $\Delta P \approx -\frac{3}{2}n_a k_B T$ is the negative pressure within the formed nanobubble. The initial conditions are set as $R(0) = R_0$ and $\dot{R}(0) = 0$, where R_0 is the initial size of nanopores. The pressure term $-\frac{\Delta P}{\rho R}$ has a positive contribution and, therefore, stands for the growth of the nanopores. The surface tension term $-\frac{2\sigma}{\rho R^2}$ and the term $-\frac{3}{2}\frac{(\dot{R})^2}{R}$ have a negative contribution and can contribute to nanovoid collapse. Finally, the viscosity term $-\frac{4\eta\dot{R}}{\rho R^2}$ can be associated with the resistance to the material deformation, as it acts always against the direction of the nanovoid evolution $\dot{R}$.

Note that Rayleigh-Plesset model can be used only to predict the evolution of individual nanovoids. The collective thermo-mechanical effects of nanopores and their influence on the final modification is neglected in this work and requires a separated study based on solving the full system of Navier-Stokes equations and the equation of state (EOS). Furthermore, the following assumptions are made while deriving from Navier-Stokes equations:

(i) spherical symmetry of the nanobubble (the contribution of the surface tension is different in the case of non-spherical microcavities, for instance)

(ii) bubble contains a homogeneously distributed vapor/gas with uniform temperature and pressure (the assumption of the ideal gas is made in this work)

(iii) an infinite domain of liquid with constant density ρ and viscosity η outside the bubble (the influence of other nanobubbles on the considered one as well as the inhomogeneity of the liquid temperature/density distribution are neglected).

2.12 Conclusions

In this chapter, the fundamental system of equations has been introduced to describe the dynamics of ultrafast laser-induced interaction from femtoseconds to microseconds, considering the nonlinear optics of ultrashort laser propagation during the pulse duration, ionization, excitation/relaxation processes, electron-ion heat transfer and thermoelastic dynamics. Furthermore, the criteria for cavitation/fragmentation and nucleation are described. The analysis is completed by Rayleigh-Plesset equation for considering hydrodynamics of nanopores/nanovoids. It is shown that the ionization and the electron collision processes play the key role in the definition of the final electron density distributions, whereas the nonlinear effects caused by the electron diffusion and the ponderomotive force are negligible at moderate intensity irradiation conditions. The model is for a wide range of dielectrics, but in this thesis, the results will be mainly presented for fused silica glass. It should be noted, however, that the application of the model is not limited to glasses but can be used also for modeling other materials, such as water, or, expanded for semiconductors or metals. The optical, thermal and mechanical parameters of the modeling as well as the temperature dependencies of thermophysical properties are reviewed for fused silica and borosilicate glasses in the appendix. In what follows, we will discuss how the system of equations describing the multiphysical model is solved numerically.

2.13 Appendix

Heat capacity, thermal conductivity and viscosity temperature dependencies for fused silica are shown in the graphs taken from Ref. [155,156,170]. Below, the optical and thermo-mechanical properties of different glasses are summarized in the table 2.1 from independent experimental measurements or theoretical works.

Table 2.1: Optical and thermo-mechanical properties of fused silica, borofloat (B33) and BK7 glasses.

Physical properties	Fused silica	Borosilicate glass
Density $\rho[g/cm^3]$	2.2 [23,113,113,179–181]	2.2 [23,113] (B33) 2.51 [31,35,113,181] (BK7)
Refractive index n $\lambda = 800$ nm	1.45 [69,83]	1.47 (B33) 1.52 [35] (BK7)
Electron band gap E_g[eV]	9 [83], 9.3 [90] 7.2-7.8 [59,65,87]	4.2-4.28 [31,140] (BK7) 3.7 [35] (BK7)
Kerr effect, $10^{-16} n_{Kerr}[cm^2/W]$	3.54 [69,83], 3.89 [61]	3.45 [31,35] (BK7)
Electron recombin. time τ_{rec}[ps]	0.15 [61,62,69,83,90] 0.06 [141], 1-2 [2,28] 30 [59], >100 [2,28]	5-100 [35,62] (BK7)
Photoionization rate w_{pi} $\lambda = 800$ nm $\sigma_6[\frac{m^9}{W^6 s}]$ or $\sigma_3[\frac{m^3}{W^3 s}]$	Keldysh [69] 6-photon: $2 \cdot 10^{-65}$ [69,83,90] $6 \cdot 10^{-63}$ [69,140,154] $3.15 \cdot 10^{-67}$ [69,141]	Kennedy's approx. [35] 3-photon: $7 \cdot 10^{-13}$ [31,140](BBS) $3 \cdot 10^{-14}$ [141](BBS) $1.343 \cdot 10^{-12}$ [143](BK7)
Heat capacity $C_i[J/(kgK)]$	772-790 [23,113] 730-752 [83,153,179] 1450 [59] (1873K) 704-845 [87], 1100 [181] 1335-1440 [174](1600-2400K)	830 [23,113] (B33) 860 [113] 878 [31] (BK7) 820 [35,181] (BK7)
Thermal conductivity $k_i[W/(mK)]$	1.38-1.67 [23,87,179] 1.31 [113], 1.4-2.514 [153] 1.4-3.0 [156](300-2500K)	1.1-1.2 [23,113] 0.96 [35] (BK7) 1.114 [113] (BK7)
Softening temperature T_{melt}[K]	1993-2006 [153,154,180,181] 1750 [179],1873-1875 [59,113]	1093 [113] 1051 [181]
Thermal expansion $10^{-7}\beta[1/K]$	5.0 [113,182], 5.5 [83,153,181] 1.4-6.0 [183] (300-970K) 6.0-6.1 [65,162]	32.5 [113] (B33) 51 [162] 71-72 [113,181,182](BK7)
Young's modulus E[GPa]	65 [179], 72-73 [83,113,153] 76-90 [160] (200-1800K) 73-80 [184] (300-1700K)	64 [113] (B33) 82 [113] (BK7)
Bulk modulus B[GPa]	36.9 [153], 35-44 [160] (200-1800K) 38-45 [180] (300-1700K)	35 (B33) 45.6 (BK7)
Shear modulus G[GPa]	31.2 [153], 30-33.5 [160] (200-1800K) 31-33 [180] (300-1700K)	26.2 (B33) 34.2 (BK7)
Poisson ratio ν	0.17-0.2 [83,153,180](300-1700K)	0.2
Tensile strength σ_{tens}[MPa]	48.3 [153]	35-100

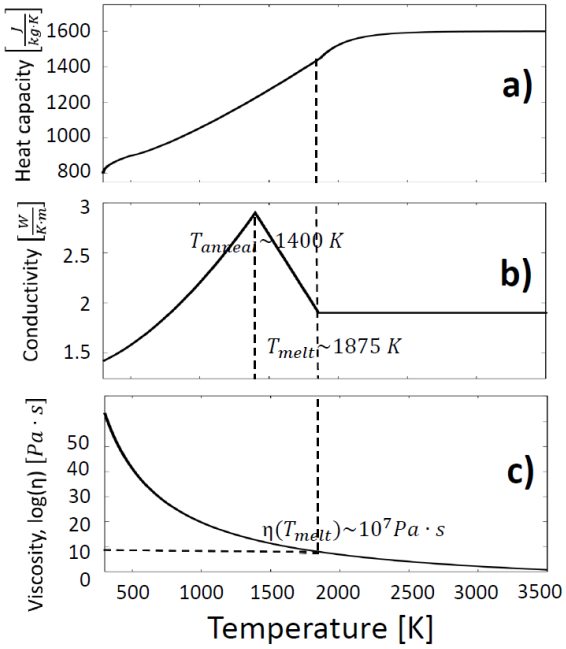

Figure 2.9: Heat capacity, thermal conductivity and viscosity temperature dependencies for fused silica glass.

Chapter 3

Numerical method

In this chapter, we describe a new numerical approach developed for fast solution of complex dynamic problems in ultrashort laser-matter interaction.

The first part of the model describing the electrodynamics is based on nonlinear Maxwell's equations coupled with time-dependent electron density equation. The approach uses the Finite-Difference Time-Domain (FDTD) and the auxiliary differential equation (ADE) methods for frequency-dependent Drude media with a time-dependent carrier density, changing due to Kerr, photoionization, avalanche and recombination effects. The system of nonlinear Maxwell-Ampere's equations is solved by an iterative fixed-point procedure. The proposed approach is shown to remain stable even for complex nonlinear media and strong gradient fields.

The second part of the model consists of solving electron-ion heat transfer equations and thermoelastic wave equations. As the concerned physical processes take place on large timescales from femtoseconds to microseconds, the procedure of changing the temporal step is discussed, the appropriate discrete schemes for solving the numerical problem are given.

Graphics-processing-units (GPU) technique is implemented by using an efficient algorithm enabling solution of massively three-dimensional problems within reasonable computation time.

3.1 Yee algorithm

Here and further we consider the non-magnetic Maxwell's equations written in the following "point" form

$$\begin{cases} \dfrac{\partial \vec{E}}{\partial t} = (\nabla \times \vec{H} - \vec{J}) \cdot \sqrt{\dfrac{\mu_0}{\epsilon_0}} \cdot c/\epsilon_\infty \\ \dfrac{\partial \vec{H}}{\partial t} = -\nabla \times \vec{E} \cdot c \cdot \sqrt{\dfrac{\epsilon_0}{\mu_0}}, \end{cases} \tag{3.1}$$

where $\vec{E}$ is the electric field, $\vec{H}$ is the magnetizing field, $c = \frac{1}{\sqrt{\epsilon_0 \mu_0}}$ is the speed velocity, ϵ_0 is the free space permittivity, μ_0 is the permeability of free space, ϵ_∞ is the material permittivity at infinite frequency, and $\vec{J}$ is the nonlinear current, which might include the contributions due to heating, Kerr effect, photoionization and ponderomotive force, as discussed in the previous chapter.

A finite-difference time-domain (FDTD) is a numerical technique used for modeling computational electrodynamics and based on solving the system of Maxwell's equations. It was proven to be one of the most powerful numerical techniques in the modeling of micro and nanoscale optical devices. The choice of a time-domain spatially discretized method in this thesis is justified by the need to investigate the spatial distributions of the intensity-dependent physical values taking into account for several nonlinear effects, having particular timescales. As coherent ultrashort laser is a source of the irradiation, a single frequency is produced, so the dispersion of the laser beam is neglected and we take account only for the dispersion of the media. The algorithm for solving numerically the time-dependent three-dimensional Maxwell's equations in differential form for linear non-dispersive media ($\vec{J} = 0$) by

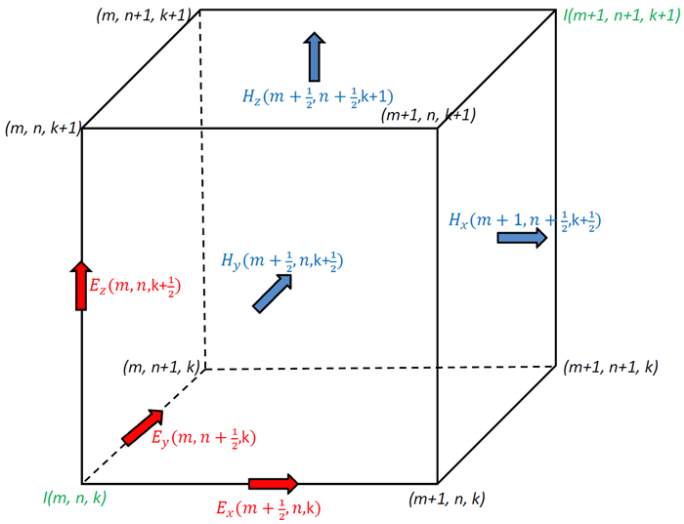

Figure 3.1: Spatial discretization of electric and magnetic fields in 3D-FDTD grid.

simple explicit scheme was firstly introduced by Yee in 1966 [185] as follows

$$
\begin{cases}
{H_x}^{(t+1)}_{(m,n+1/2,p+1/2)} = C_z\sqrt{\frac{\epsilon_0}{\mu_0}}({E_y}^{t}_{(m,n+1/2,p+1)} - {E_y}^{t}_{(m,n+1/2,p)}) \\
-C_y\sqrt{\frac{\epsilon_0}{\mu_0}}({E_z}^{t}_{(m,n+1,p+1/2)} - {E_z}^{t}_{(m,n,p+1/2)}) + {H_x}^{t}_{(m,n+1/2,p+1/2)} \\
{H_y}^{(t+1)}_{(m+1/2,n,p+1/2)} = C_x\sqrt{\frac{\epsilon_0}{\mu_0}}({E_z}^{t}_{(m+1,n,p+1/2)} - {E_z}^{t}_{(m,n,p+1/2)}) \\
-C_z\sqrt{\frac{\epsilon_0}{\mu_0}}({E_x}^{t}_{(m+1/2,n,p+1)} - {E_x}^{t}_{(m+1/2,n,p)}) + {H_y}^{t}_{(m+1/2,n,p+1/2)} \\
{H_z}^{(t+1)}_{(m+1/2,n+1/2,p)} = C_y\sqrt{\frac{\epsilon_0}{\mu_0}}({E_x}^{t}_{(m+1/2,n+1,p)} - {E_x}^{t}_{(m+1/2,n,p)}) \\
-C_x\sqrt{\frac{\epsilon_0}{\mu_0}}({E_y}^{t}_{(m+1,n+1/2,p)} - {E_y}^{t}_{(m,n+1/2,p)}) + {H_z}^{t}_{(m+1/2,n+1/2,p)} \\
{E_x}^{(t+1)}_{(m+1/2,n,p)} = \frac{C_y}{\epsilon_\infty}\sqrt{\frac{\mu_0}{\epsilon_0}}({H_z}^{t}_{(m+1/2,n+1/2,p)} - {H_z}^{t}_{(m+1/2,n-1/2,p)}) \\
-\frac{C_z}{\epsilon}\sqrt{\frac{\mu_0}{\epsilon_0}}({H_y}^{t}_{(m+1/2,n,p+1/2)} - {H_y}^{t}_{(m+1/2,n,p-1/2)}) + {E_x}^{t}_{(m+1/2,n,p)} \\
{E_y}^{(t+1)}_{(m,n+1/2,p)} = -\frac{C_x}{\epsilon_\infty}\sqrt{\frac{\mu_0}{\epsilon_0}}({H_z}^{t}_{(m+1/2,n+1/2,p)} - {H_z}^{t}_{(m-1/2,n+1/2,p)}) \\
+\frac{C_z}{\epsilon}\sqrt{\frac{\mu_0}{\epsilon_0}}({H_x}^{t}_{(m,n+1/2,p+1/2)} - {H_x}^{t}_{(m,n+1/2,p-1/2)}) + {E_y}^{t}_{(m,n+1/2,p)} \\
{E_z}^{(t+1)}_{(m,n,p+1/2)} = \frac{C_x}{\epsilon_\infty}\sqrt{\frac{\mu_0}{\epsilon_0}}({H_y}^{t}_{(m+1/2,n,p+1/2)} - {H_y}^{t}_{(m-1/2,n,p+1/2)}) \\
-\frac{C_y}{\epsilon}\sqrt{\frac{\mu_0}{\epsilon_0}}({H_x}^{t}_{(m,n+1/2,p+1/2)} - {H_x}^{t}_{(m,n-1/2,p+1/2)}) + {E_z}^{t}_{(m,n,p+1/2)},
\end{cases}
\tag{3.2}
$$

where (m, n, p) are the spatial mesh points and t is the temporal mesh point, $\sqrt{\frac{\mu_0}{\epsilon_0}} = 377$ is the electromagnetic impedance, $C_x = \frac{c\Delta t}{\Delta x} = \frac{1}{2}$, $C_y = \frac{c\Delta t}{\Delta y} = \frac{1}{2}$ and $C_z = \frac{c\Delta t}{\Delta z} = \frac{1}{2}$ are Courant numbers, connecting temporal Δt and dimensional steps Δx, Δy and Δz. The spatial discretizations of electric and magnetic fields are presented in Fig. 3.1. The time increment $1/2$ is chosen to satisfy 1D, 2D and 3D's stability criteria (Courant-Friedrichs-Lewy's condition) [186]

$$
\Delta t \leq \frac{1}{c\sqrt{\frac{1}{\Delta x^2} + \frac{1}{\Delta y^2} + \frac{1}{\Delta z^2}}} \tag{3.3}
$$

According to Courant's relationship for the spatial step $\Delta x = 1$ nm, the timestep should satisfy $\Delta t = \frac{C_x \Delta x}{c} \approx 1.66$ as. The maximum spatial step providing the sufficiently low numerical dispersion is limited by the following expression related to the wavelength in media $\Delta x_{max} \leq \lambda/(10 n_{max})$. Therefore, the method is effective to investigate the electromagnetic processes on nano/micrometer spatial scales (from several tenths of nanometers to several microns) and on femtosecond timescales.

It is important to note, that the electric and the magnetic fields are spatially displaced on a half-step and defined in following positions in the grid: $H_x(m, n+1/2, p+1/2)$, $H_y(m+1/2, n, p+1/2)$,

$H_z(m+1/2, n+1/2, p)$, $E_x(m+1/2, n, p)$, $E_y(m, n+1/2, p)$, $E_z(m, n, p+1/2)$. This asymmetry provides conditional stability of the Yee scheme in contrast to other explicit leapfrog differential schemes. As an example, for the standard symmetric explicit leapfrog scheme for one dimensional Maxwell-Ampere equation written as

$$\frac{E^{(m,t+1)} - E^{(m,t)}}{\Delta t} = c \cdot \frac{H^{(m+1,t)} - H^{(m-1,t)}}{\Delta x}, \tag{3.4}$$

one can use von Neumann stability analysis and search the solution in the form $t^z \cdot e^{i\lambda m}$ as follows

$$\frac{z-1}{\Delta t} = c \cdot \frac{e^{i\lambda} - e^{-i\lambda}}{\Delta x} = 2c \cdot \frac{i \cdot sin(\lambda)}{\Delta x}. \tag{3.5}$$

According to the stability criterium, $|z| \leq 1$, however, one can obtain

$$|z| = 1 + \left(2c \cdot sin(\lambda)\frac{\Delta t}{\Delta x}\right)^2 \geq 1. \tag{3.6}$$

It means that the explicit symmetric leapfrog differential scheme is unconditionally unstable. Applying the same procedure for numerical scheme used in Yee method yields

$$\begin{aligned} \frac{z-1}{\Delta t} &= c \cdot \frac{e^{i\lambda} - 1}{\Delta x} \\ |z| = \left|1 + \left(\frac{c \cdot \Delta t}{\Delta x}(e^{i\lambda} - 1)\right)\right| &= (1 + \frac{c \cdot \Delta t}{\Delta x}(cos(\lambda) - 1))^2 + (\frac{c \cdot \Delta t}{\Delta x} sin(\lambda))^2 = \\ &= 1 + \frac{2c \cdot \Delta t}{\Delta x}(1 - cos(\lambda))\left(\frac{c \cdot \Delta t}{\Delta x} - 1\right). \end{aligned} \tag{3.7}$$

Thus, the numerical scheme is stable under the Courant-Friedrichs-Lewy's condition $\frac{c \cdot \Delta t}{\Delta x} \leq 1$.

3.2 Initial conditions

There are two ways to introduce the source into the electromagnetic code. The simplest method is to give some values, changing in time to the electric or the magnetic fields, which is the realization of the "hard source" and is useful for testing the initial equations. The major issue with the hard sources is that they reflect [187, 188]. In most cases, the problem consists in measuring the scattered field without having it interrupted by the source [188]. To avoid this problem, a soft source should be realized, where the value is added to the field at the previous timestep, simulating a current. The physical meaning of the soft source is well understood and its analytical solution is well known, whereas there is no analytical solution for the hard source excitation.

The soft source can be introduced in sinusoidal form as

$$E_x(t+1, x, y, z) = \sin(\omega(t - z/C_z) - \varphi) + E_x(t, x, y, z), \tag{3.8}$$

in Gaussian form as

$$E_x(t+1, x, y, z) = \exp\left[-\left(\frac{t - z/C_z - \varphi}{\theta}\right)^2\right] + E_x(t, x, y, z), \tag{3.9}$$

and in general form as

$$E_x(t+1, x, y, z) = \sin(\omega(t - z/C_z) - \varphi) \cdot exp\left[-\left(\frac{t - z/C_z - \varphi}{\theta}\right)^2\right] + E_x(t, x, y, z), \tag{3.10}$$

where t and z are time and spatial coordinates, C_z is the Courant number, φ is the delay, θ is the pulse duration in timesteps, $\omega = 2\pi\frac{\Delta x}{\lambda}C_z$ is the frequency. Since the pulse $f(t) = sin(\omega t - \varphi) \cdot exp(-\left(\frac{t-\varphi}{\theta}\right)^2)$ is infinitely long in the time domain, it has to be truncated so that only values larger than γ are

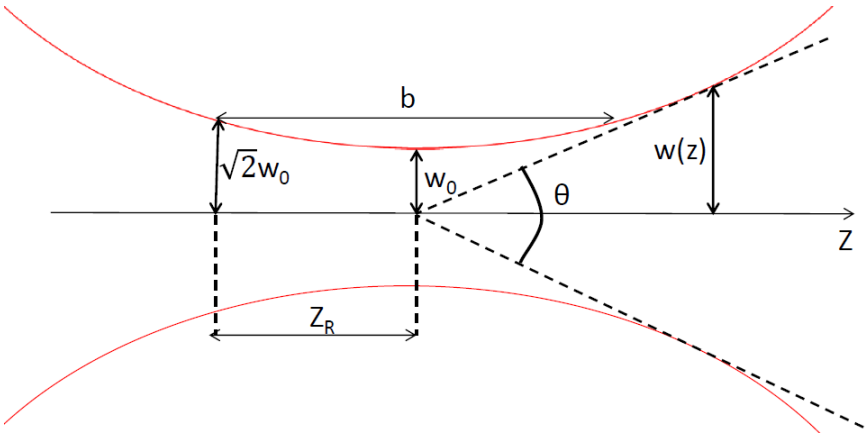

Figure 3.2: Geometrical parameters of the Gaussian beam.

included into the discrete representation. In many cases, sufficient initial choices are $\gamma = 10^{-9}$, $\varphi = [-ln(\gamma)]^{-1/2}\theta \approx 4.55\theta$ and time duration $t_{max} = 2\varphi$. For $\gamma = 10^{-4}$, $\varphi \approx 3\theta$.

In realistic physical problems, a focused Gaussian beam source is used to simulate the irradiation by laser as follows

$$E_x(t+1,x,y,z) = \frac{w_0}{w(z)}\exp\left[-\frac{r^2}{w(z)^2} - ikz - ik\frac{r^2}{2R(z)} + i\varsigma(z) - \frac{(t-t_0)^{2\,2}}{\theta}\right] + E_x(t,x,y,z), \quad (3.11)$$

where the geometry and behavior are governed by a set of beam parameters presented in Fig. 3.2: w_0 is the waist beam, $w(z) = w_0\sqrt{1+(\frac{z}{z_R})^2}$ is the variation of spot size and the radius at which the field amplitude drops to $1/e$ of their axial values, $z_R = \frac{\pi {w_0}^2 n_0}{\lambda}$ is the Rayleigh range or length, $r = x^2 + y^2$ is the radial distance from the beam's narrowest point (waist), $R(z) = z[1 + (\frac{z_R}{z})^2]$ is the radius of curvature of the wavelength comprising the beam, and $\varsigma(z) = \arctan(\frac{z}{z_R})$ is the Gouy phase shift, an extra contribution to the phase that is seen in Gaussian beams. At a distance from the waist equal to Rayleigh range z_R, the width w of the beam is $w(\pm z_R) = \sqrt{2}w_0$. The distance between these two points is called the confocal parameter or depth of focus of the beam $b = 2z_R = \frac{2\pi {w_0}^2 n_0}{\lambda}$. The parameter w_z increases linearly from z to z_R. This means that far from the waist the beam is cone-shaped. The angle between the straight line $r = w(z)$ and the central axis of the beam $r = 0$ is called the divergence of the beam and is given by $\theta \approx \frac{\lambda}{\pi w_0}$. The numerical aperture is defined to be $NA = nsin(\theta)$, the Rayleigh range is related to the numerical aperture by $z_R = \frac{w_0}{NA}$.

Since the Gaussian beam uses the paraxial approximation, it fails when wavefronts are tilted by more than about $\pi/6$ from the direction of the propagation. From the expression of the divergence, this means that the Gaussian beam model is valid only from beams with waists larger than about $\frac{2\lambda}{\pi}$. For the laser irradiation wavelength $\lambda = 800$ nm, $w_0 \geq \frac{2\lambda}{\pi} \approx 500$ nm. For large focusing angles, the Gaussian form of the beam entering the sample can result in appearance of exponentially diverging harmonics [130]. The error becomes larger with the decreasing beam waist. As it becomes comparable to the reduced wavelength λ/n, higher-order terms in the expansion should be included. For example, the interval of application of the paraxial approximation of the Gaussian beam's profile can be expanded by taking into account corrections to higher numerical apertures [189, 190].

The input laser pulse energy is defined as

$$\Sigma = \sqrt{\frac{\pi}{2}}\frac{\pi w_0^2}{2}\theta I, \quad (3.12)$$

where θ is the pulse duration (FWHM) and the laser fluence corresponds to $F_0 = \Sigma/(\frac{\pi {w_0}^2}{2})$.

3.3 Absorbing boundary conditions (ABC)

A wave, hitting an object, scatters the applied wave into potentially many directions. In general, the boundary conditions on the boundary are needed to avoid the nonphysical reflections of the scattered waves from the boundaries of the grid. Absorbing boundary conditions (ABC) provide a relatively simple way to terminate the grid, relying on the fact, that the solution of Maxwell's coupled curl equations via an FDTD algorithm is equivalent to the solution of the second-order wave equation for any one of the fields components. Although the wave equation naturally supports waves propagating in both forward and backward directions, it can be divided into two one-way equations, each of which supports waves in only one direction. The wave equation that governs the propagation of the field in 1D can be written in the following form

$$\left(\frac{\partial}{\partial x} - \sqrt{\mu\epsilon}\frac{\partial}{\partial t}\right)\left(\frac{\partial}{\partial x} + \sqrt{\mu\epsilon}\frac{\partial}{\partial t}\right) E_y = 0. \tag{3.13}$$

Approximating the derivatives, first-order Mur's condition are obtained for $m = 0$ and $m = i_{max}$ border spatial mesh points as

$$\begin{aligned} E_0^{t+1} &= E_1^t + \frac{C_x - 1}{C_x + 1}(E_1^{t+1} - E_0^t) \\ E_{i_{max}}^{t+1} &= E_{i_{max}-1}^t + \frac{C_x - 1}{C_x + 1}(E_{i_{max}-1}^{t+1} - E_{i_{max}}^t). \end{aligned} \tag{3.14}$$

In three-dimensional case, the wave equation is written as

$$\left(\frac{\partial}{\partial x} - \sqrt{\frac{1}{C^2}\frac{\partial^2}{\partial t^2} - \frac{\partial^2}{\partial y^2} - \frac{\partial^2}{\partial z^2}}\right)\left(\frac{\partial}{\partial x} + \sqrt{\frac{1}{C^2}\frac{\partial^2}{\partial t^2} - \frac{\partial^2}{\partial y^2} - \frac{\partial^2}{\partial z^2}}\right) E_y = 0. \tag{3.15}$$

Using the approximation $\sqrt{1 - s^2} \approx 1 - \frac{s^2}{2}$, where $s^2 = \frac{\partial^2}{\partial y^2} + \frac{\partial^2}{\partial z^2}$, one obtain the following equation for second-order Mur's ABC [191]

$$\left(\frac{\partial}{\partial x} - \frac{1}{C}\frac{\partial}{\partial t} + \frac{c}{2}\frac{\frac{\partial^2}{\partial y^2} + \frac{\partial^2}{\partial z^2}}{\frac{\partial}{\partial t}}\right)\left(\frac{\partial}{\partial x} - \frac{1}{C}\frac{\partial}{\partial t} + \frac{c}{2}\frac{\frac{\partial^2}{\partial y^2} + \frac{\partial^2}{\partial z^2}}{\frac{\partial}{\partial t}}\right) E_y = 0, \tag{3.16}$$

where the derivatives are approximated in the following way

$$\begin{aligned} \left[\frac{\partial^2 E}{\partial x \partial t}\right]_{3/2j}^n &= \frac{1}{2\Delta t}\left(\frac{E_{2,j}^{n+1} - E_{1,j}^{n+1}}{\Delta x} - \frac{E_{2,j}^{n-1} - E_{1,j}^{n-1}}{\Delta x}\right) \\ \left[\frac{\partial^2 E}{\partial t^2}\right]_{3/2j}^n &= \frac{1}{2}\left(\frac{E_{2,j}^{n+1} - 2E_{2,j}^n + E_{2,j}^{n-1}}{(\Delta t)^2} - \frac{E_{1,j}^{n+1} - 2E_{1,j}^n + E_{1,j}^{n-1}}{(\Delta t)^2}\right) \\ \left[\frac{\partial^2 E}{\partial y^2}\right]_{3/2j}^n &= \frac{1}{2}\left(\frac{E_{2,j+1}^n - 2E_{2,j}^n + E_{2,j-1}^n}{(\Delta y)^2} - \frac{E_{1,j+1}^n - 2E_{1,j}^n + E_{1,j-1}^n}{(\Delta y)^2}\right). \end{aligned} \tag{3.17}$$

Final approximation scheme of second-order Mur's conditions is given by

$$\begin{aligned} E_{0,j}^{n+1} &= -E_{1,j}^{n-1} - \frac{1 - C_x}{1 + C_x}\left[E_{1,j}^{n+1} + E_{0,j}^{n-1}\right] + \frac{2}{1 + C_x}\left[E_{0,j}^n + E_{1,j}^n\right] + \\ &+ \frac{C_y^2}{2(1 + C_x)}\left[E_{,j+1}^n - E_{0,j}^n + E_{0,j-1}^n + E_{1,j+1}^n - 2E_{1,j}^n + E_{1,j-1}^n\right] \\ E_{i,0}^{n+1} &= -E_{i,1}^{n-1} - \frac{1 - C_x}{1 + C_x}\left[E_{i,1}^{n+1} + E_{i,0}^{n-1}\right] + \frac{2}{1 + C_x}\left[E_{i,0}^n + E_{i,1}^n\right] + \\ &+ \frac{C_y^2}{2(1 + C_x)}\left[E_{i+1,0}^n - E_{i,0}^n + E_{i-1,0}^n + E_{i+1,1}^n - 2E_{i,1}^n + E_{i-1,1}^n\right]. \end{aligned} \tag{3.18}$$

The repeated application of the operator may still only be approximately satisfied. Nevertheless, it performs better than the first-order alone and results in better reflection coefficients.

However, a number of drawbacks of ABC are evident. Firstly, the reflection coefficient that results from the analytical ABC is a function of the incident angle, and can be very high for grazing angles. Therefore, for higher accuracy the one-way wave equation that must be applied at the boundary becomes increasingly complex, and requires the storage of the fields at previous time steps, eliminating one of the great advantages of the FDTD method, which does not require the storage of any fields more than one time step back. Secondly, ABC were initially designed to absorb homogeneous travelling waves. In fact, the global performance of the one-way wave boundary condition can not be improved significantly by increasing the order of the ABCs over order 2. Finally, the ABC can not be placed close to the sources, which are in the evanescent region, whatever may be their order. In most cases, it results in a computational domain significantly larger than the optimum domain that would be used with an ideal ABC that could absorb both traveling and evanescent waves and could be placed nearby the region of the interest [192].

3.4 Perfectly matched layers (PML)

The other family of methods are called perfect matched layers (PML), which define a thin lossy layer with evolving artificial conductivities around the boundary. The boundary layer is designed so that it absorbs enough of outgoing wave, prevents the reflections from the interface between the actual medium and the boundary medium and make the reflections from the actual boundary acceptably low. The PML are of great importance since they allow to simulate semi-infinitely extended media and to avoid nonphysical reflections at the edges of the simulation grid.

The first effective PML was introduced by Berenger in 1994 [193]. The Berenger or split-field perfectly matched layer method is based on field-splitting of Maxwell's equations and selectively choosing different values for the "conductivities" in different directions. In three-dimensional modeling, 12 subcomponents are required, thus the Maxwell's equations are replaced by 12 equivalent equations [194]. The proposed method was compared with ABC and it was shown that PML significantly reduced the reflection from the truncation of the computational grid [195, 196].

Waves, incident on the PML border, run into a "brick wall" of lossy material but as the fields are spatially displaced by half a spatial step, they encounter the PML border differently. To reduce the resulting reflection factor, Berenger proposed grading the PML conductivity smoothly from zero to some maximum value at the outer border with either a polynomial or a geometric variation [197]. For a wave, impinging the PML at angle θ, the reflection is given by $R(\theta) = exp(-2\sigma\eta dcos\theta)$, where η is the characteristic wave impedance, d is the thickness of PML layer, and σ is the PML's artificial conductivity. Berenger's grading reduces the reflection error, as the PML losses gradually rise from zero along the direction normal to the interface. For example, for polynomial grading $\sigma_x = \left(\frac{x}{D}\right)^q \cdot \sigma_{max}$, the reflection coefficient is given by $R(\theta) = exp\left(-\frac{2\nu\sigma_{max}dcos\theta}{q+1}\right)$.

In general, the lowering of $R(\theta)$ is achieved either by increasing the thickness of the layer, either by increasing the conductivity. In actual numerical experiments, it is not true because sharp variations of the conductivity in a discrete space result in spurious numerical reflections. Choosing the conductivity and the thickness of the PML is a major question in applications, because contradictory requirements hold. Firstly, the thickness of the PML must be as thin as possible to reduce the computational cost. Secondly, the variations of the conductivity must be small enough to reduce the spurious reflection. Finally, the theoretical reflection must be as small as possible.

However, the Berenger PML medium can not be considered a physical medium, because different conductivities are acting on non-physical split-fields. There is an alternative formulation of the PML absorbing boundary condition in terms of a physical anisotropic medium having tensor permittivity and permeability called uniaxial perfect matched layer (UPML) [198]. The general tensors can be presented in the following form by the product of the three s matrices $\epsilon' = \begin{bmatrix} s_x^{-1}s_y s_z & 0 & 0 \\ 0 & s_y^{-1}s_x s_z & 0 \\ 0 & 0 & s_z^{-1}s_x s_y \end{bmatrix} \epsilon$, where

$$\begin{pmatrix} s_x \\ s_y \\ s_z \end{pmatrix} = 1 + \frac{1}{i\omega\epsilon} \begin{pmatrix} \sigma_x \\ \sigma_y \\ \sigma_z \end{pmatrix}.$$

The Berenger PML is a simple example of an anisotropic medium, although it is not as flexible as the uniaxial PML method. In fact UPML's approach does not involve modification of Maxwell's equations and is easy to implement in codes with anisotropic material properties [199–201]. Furthermore, UPML has the unique feature of being Maxwellian, because it satisfies Maxwellian equations. This interpretation of stretched coordinates facilitates the extension of the PML concept to more general media and to other partial differential equations of physics.

The Maxwell's equations in the frequency form are written as follows

$$\begin{cases} i\omega \left(1 + \frac{\sigma_x}{i\omega\epsilon_0}\right)^{-1} \left(1 + \frac{\sigma_y}{i\omega\epsilon_0}\right) \left(1 + \frac{\sigma_z}{i\omega\epsilon_0}\right) H_x = -\frac{1}{\mu_0} \left(\frac{\partial E_z}{\partial y} - \frac{\partial E_y}{\partial z}\right) \\ i\omega \left(1 + \frac{\sigma_x}{i\omega\epsilon_0}\right) \left(1 + \frac{\sigma_y}{i\omega\epsilon_0}\right)^{-1} \left(1 + \frac{\sigma_z}{i\omega\epsilon_0}\right) H_y = -\frac{1}{\mu_0} \left(\frac{\partial E_x}{\partial z} - \frac{\partial E_z}{\partial x}\right) \\ i\omega \left(1 + \frac{\sigma_x}{i\omega\epsilon_0}\right) \left(1 + \frac{\sigma_y}{i\omega\epsilon_0}\right) \left(1 + \frac{\sigma_z}{i\omega\epsilon_0}\right)^{-1} H_z = -\frac{1}{\mu_0} \left(\frac{\partial E_y}{\partial x} - \frac{\partial E_x}{\partial y}\right) \\ i\omega \left(1 + \frac{\sigma_x}{i\omega\epsilon_0}\right)^{-1} \left(1 + \frac{\sigma_y}{i\omega\epsilon_0}\right) \left(1 + \frac{\sigma_z}{i\omega\epsilon_0}\right) E_x = \frac{1}{\epsilon_0} \left(\frac{\partial H_z}{\partial y} - \frac{\partial H_y}{\partial z}\right) \\ i\omega \left(1 + \frac{\sigma_x}{i\omega\epsilon_0}\right) \left(1 + \frac{\sigma_y}{i\omega\epsilon_0}\right)^{-1} \left(1 + \frac{\sigma_z}{i\omega\epsilon_0}\right) E_y = \frac{1}{\epsilon_0} \left(\frac{\partial H_x}{\partial z} - \frac{\partial H_z}{\partial x}\right) \\ i\omega \left(1 + \frac{\sigma_x}{i\omega\epsilon_0}\right) \left(1 + \frac{\sigma_y}{i\omega\epsilon_0}\right) \left(1 + \frac{\sigma_z}{i\omega\epsilon_0}\right)^{-1} E_z = \frac{1}{\epsilon_0} \left(\frac{\partial H_y}{\partial x} - \frac{\partial H_x}{\partial y}\right). \end{cases} \tag{3.19}$$

Let us consider only first equation as all the equations are equivalent

$$i\omega(1 + \frac{\sigma_y}{i\omega\epsilon_0} + \frac{\sigma_z}{i\omega\epsilon_0} - \frac{\sigma_y\sigma_z}{\omega^2\epsilon_0^2})H_x = -\frac{1}{\mu_0} \left(\frac{\partial E_z}{\partial y} - \frac{\partial E_y}{\partial z}\right) (1 + \frac{\sigma_x}{i\omega\epsilon_0}). \tag{3.20}$$

Passing to the time domain,

$$i\omega H_x \to \frac{\partial H_x}{\partial t}, \frac{\sigma_x}{i\omega\epsilon_0} \left(\frac{\partial E_z}{\partial y} - \frac{\partial E_y}{\partial z}\right) \to \frac{\sigma_x \Delta t}{\epsilon_0} \sum_{n=0}^{T} \left(\frac{\partial E_z}{\partial y} - \frac{\partial E_y}{\partial z}\right) \tag{3.21}$$

.

The procedure requires the curl of the magnetic or electric field at each time step, in this case the integral can be discretized as a summation. Furthermore, there is one more integral left $\frac{\sigma_y\sigma_z}{i\omega\epsilon_0^2} x \to \frac{\sigma_y\sigma_z\Delta t}{\epsilon_0^2} \sum_{n=0}^{T} H_x$. In the book of Sullivan [202], it is assumed that the contribution of the integral is negligible. However, the following equation can be written in general case

$$\begin{gathered} \frac{\partial H_x}{\partial t} + \frac{H_x}{\epsilon_0}(\sigma_y + \sigma_z) + \frac{\sigma_y\sigma_z\Delta t}{\epsilon_0^2} \sum_{n=0}^{T} H_x = \dots \\ -\frac{1}{\mu_0} \left[\frac{\partial E_z}{\partial y} - \frac{\partial E_y}{\partial z} + \frac{\sigma_x \Delta t}{\epsilon_0} \sum_{n=0}^{T} \left(\frac{\partial E_z}{\partial y} - \frac{\partial E_y}{\partial z}\right)\right]. \end{gathered} \tag{3.22}$$

Finally, an appropriate differential scheme for the equation is given by

$$\begin{cases} H_x^{t+1}(m,n^*,p^*) = A \cdot {H_x}^t(m,n^*,p^*) + B \cdot C_z \sqrt{\dfrac{\epsilon_0}{\mu_0}} \left[E_y^t(m,n^*,p+1) - E_y^t(m,n^*,p)\right] - \dots \\ B \cdot C_y \sqrt{\dfrac{\epsilon_0}{\mu_0}} \left[E_z^t(m,n+1,p^*) - E_z^t(m,n,p^*)\right] + \dots \\ B\dfrac{\sigma_x \Delta t}{\epsilon_0} {P_{hx}}^t(m,n^*,p^*) - B\dfrac{\sigma_y \sigma_z \Delta t^2}{\epsilon_0^2} {R_{hx}}^t(m,n^*,p^*) \\ {P_{hx}}^{t+1}(m,n^*,p^*) = C_z \sqrt{\dfrac{\epsilon_0}{\mu_0}} \left[E_y^t(m,n^*,p+1) - E_y^t(m,n^*,p)\right] - \dots \\ C_y \sqrt{\dfrac{\epsilon_0}{\mu_0}} \left[E_z^t(m,n+1,p^*) - E_z^t(m,n,p^*)\right] + {P_{hx}}^t(m,n^*,p^*) \\ {R_{hx}}^{t+1}(m,n^*,p^*) = {R_{hx}}^t(m,n^*,p^*) + {H_x}^t(m,n^*,p^*) \\ A = \dfrac{2\epsilon_0 - \Delta t(\sigma_y + \sigma_z)}{2\epsilon_0 + \Delta t(\sigma_y + \sigma_z)}, B = \dfrac{2\epsilon_0}{2\epsilon_0 + \Delta t(\sigma_y + \sigma_z)}, \end{cases} \tag{3.23}$$

where (m,n,p) and $(m^*n^*p^*) = (m+1/2, n+1/2, p+1/2)$ are the spatial mesh points, t is the temporal mesh point, P_{hx} and R_{hx} are the additional arrays required for summation.

The coefficients, proposed in the book [202], are defined as $\sigma_{max} = 0.333 \cdot \dfrac{2\epsilon_0}{\Delta t}, q = 3$. As $\dfrac{\epsilon_0}{\Delta t} = \dfrac{1}{\eta \Delta x C_x}$, one can obtain the following formula for the reflection coefficient

$$R(\theta) = exp\left(-\frac{2\eta\sigma_{max} dcos\theta}{q+1}\right) \approx exp(-\frac{dcos(\theta)}{3}) \tag{3.24}$$

.

However, the implementation of the UPML is cumbersome, involving running integrals which must be stored for each grid cell in the PML. Furthermore, while the Berenger's split-field PML and UPML described above are both very robust and efficient at terminating most FDTD simulation spaces, both suffer from the inability to absorb evanescent waves [203]. This means the PML must be placed sufficiently far from any scattering objects. This restriction can lead to simulation spaces that are larger than desired. In order to absorb evanescent waves, a strictly causal form of the PML has been derived by Kuzuoglu and Mittra [204].

The most effective implementation of this complex-frequency-shifted method (CPML) was derived by Roden and Gedney [205, 206]. In this method, a more general stretched coordinate is introduced $s_i = k_i + \dfrac{\sigma_i}{\alpha_i + i\omega\epsilon_0}$, $k_i \geq 1$, $\alpha_i \geq 0$. The CPML implementation can be applied to any kind of the material, be it dispersive, anisotropic or nonlinear. It is shown that using CPML results in significantly faster convergence speed than using UPML [207]. Such a difference in the convergence behavior is explained by the analysis of the condition number of the coefficient matrices. The implementation of the CPML can be done by simply adding components to the normal update equations [187,208]. Here,

we write the equations only for two-dimensional case

$$
\begin{cases}
P_{hx}^{t+1}(m^*,n^*) = B_x P_{hx}^t(m^*,n^*) + (B_x-1)C_x\sqrt{\dfrac{\epsilon_0}{\mu_0}}\left(E_y^t(m+1,n^*) - E_y^t(m,n^*)\right) \\
P_{hy}^{t+1}(m^*,n^*) = B_y P_{hy}^t(m^*,n^*) + (B_y-1)C_y\sqrt{\dfrac{\epsilon_0}{\mu_0}}\left(E_x^t(m^*,n+1) - E_x^t(m^*,n)\right) \\
H_z^{t+1}(m^*,n^*) = H_z^t(m^*,n^*) + \dfrac{C_y}{K_y}\sqrt{\dfrac{\epsilon_0}{\mu_0}}\left(E_x^t(m^*,n+1) - E_x^t(m^*,n)\right) - \dots \\
\dfrac{C_x}{K_x}\sqrt{\dfrac{\epsilon_0}{\mu_0}}\left(E_y^t(m+1,n^*) - E_y^t(m,n^*)\right) + P_{hy}^t(m^*,n^*) - P_{hx}^t(m^*,n^*) \\
P_{ex}^{t+1}(m,n^*) = B_x P_{ex}^t(m,n^*) + (B_x-1)\dfrac{C_x}{\epsilon}\sqrt{\dfrac{\mu_0}{\epsilon_0}}\left(H_z^t(m^*,n^*) - H_z^t(m-1/2,n^*)\right) \\
P_{ey}^{t+1}(m^*,n) = B_y P_{ey}^t(m^*,n) + (B_y-1)\dfrac{C_y}{\epsilon}\sqrt{\dfrac{\mu_0}{\epsilon_0}}\left(H_z^t(m^*,n^*) - H_z^t(m^*,n-1/2)\right) \\
E_x^{t+1}(m^*,n) = E_x^t(m^*,n) + \dfrac{C_y}{K_y\epsilon}\sqrt{\dfrac{\mu_0}{\epsilon_0}}\left(H_z^t(m^*,n^*) - H_z^t(m^*,n-1/2)\right) + P_{ey}^t(m^*,n) \\
E_y^{t+1}(m,n^*) = E_y^t(m,n^*) - \dfrac{C_x}{K_x\epsilon}\sqrt{\dfrac{\mu_0}{\epsilon_0}}\left(H_z^t(m^*,n^*) - H_z^t(m-1/2,n^*)\right) - P_{ex}^t(m,n^*) \\
\sigma_x = \left(\dfrac{m}{D}\right)^q \cdot \sigma_{max}, \qquad \sigma_y = \left(\dfrac{n}{D}\right)^q \cdot \sigma_{max} \\
\alpha_x = \left(\dfrac{D-m}{D}\right)^{q_\alpha} \cdot \alpha_{max}, \qquad \alpha_y = \left(\dfrac{D-n}{D}\right)^{q_\alpha} \cdot \alpha_{max} \\
K_x = 1 + \left(\dfrac{m}{D}\right)^q \cdot (K_{max}-1), \qquad K_y = 1 + \left(\dfrac{n}{D}\right)^q \cdot (K_{max}-1) \\
B_x = \exp\left(-\dfrac{\Delta t}{\epsilon_0}(\dfrac{\sigma_x}{k_x} + \alpha_x)\right), \qquad B_y = \exp\left(-\dfrac{\Delta t}{\epsilon_0}(\dfrac{\sigma_y}{k_y} + \alpha_y)\right),
\end{cases}
\tag{3.25}
$$

where (m,n), $(m^*,n^*) = (m+1/2, n+1/2)$ are the spatial mesh points, t is the temporal mesh point, σ and κ are scaled along their respective axes and graded in the same way as in the Berenger's split-field formulation and α is graded in the opposite manner, being non-zero at the PML interface and fading to zero at the boundary. A and B are 1D functions and there is no need to store them over the entire 3D space. Similarly, the additive fields are zero outside the PML regions, and so can be stored only within the PML, saving computational time and storage space.

Table 3.1: The computation requirements of different PML's.

	Storage	Operations	Multiplications	Additions
Regular split PML	10	56	16	40
Eight-variable split PML	8	60	18	42
Uniaxial PML	8	48	20	28
CPML	10	56	20	36

The maximum conductivity can be defined as [187,205,207,209,210]

$$
\sigma_{max} = -\frac{(q+1)ln[R(0)]}{2\eta d} \approx \frac{3(q+1)}{\eta d}, \tag{3.26}
$$

where $R(0) = \exp\left(-\frac{2\eta\sigma_{max}d}{q+1}\right) = 10^{-6}$ is the desired reflection at normal incidence, q is the polynomial parameter, D is the thickness of PML, $\eta = \sqrt{\frac{\mu_0}{\epsilon_0}}$ is zero impedance. One can derive $\dfrac{\sigma_{max}\Delta t}{\epsilon_0} \approx \dfrac{3(q+1)}{d}$, where d is the number of cells reserved for PML.

In the simplified case ($\alpha_{max} = 0$,$\kappa_{max} = 1$), it has only one parameter which usually lays in the interval $2 \le q \le 4$. Even with a regular stretch the reflection from the CPML differs from that of the split PML or UPML. From a few experiments provided by Roden and Gedney [205,206], it seems that the reflection of homogeneous waves from CPML is slightly smaller than from the other three PML implementations. However, the difference is not significant. The interest of the CPML implementation is mainly in using a CFS stretching factor with more adjustable parameters.

In the most general case there are more parameters: κ_{max}, α_{max}, q, q_α. For example, in the work [211] the following coefficients were defined as $\kappa_{max} = 5$, $\alpha_{max} = 0.05$, $q = 3$, $q_\alpha = 1$, $\sigma_{max} = \frac{0.8(q+1)}{\eta D}$. Generally, the optimal choice of parameters depends on the geometry, resolution and frequency range of the problem. Parameter α governs the absorption of the evanescent fields. Typically, it should be larger for the problems with strongly evanescent waves, and smaller for problems with only weakly evanescent fields. The optimal value does not depend on the frequency, being inversely proportional to the size of the problem.

Finally, the computational requirements of the different PMLs are compared [192] and summarized in Table 3.1. Although CPML method requires more arrays to store in the memory and slightly more operations to perform, it is beneficial in both two-dimensional and three-dimensional problems, as the method enables considering the scattering objects in the vicinity of the lossy layer. Simplified UPML method, however, gives comparable performance, while the object of interest is far from the boundary, for example, in the case of tightly focused laser beam in the center of the grid.

3.5 Temporal discretization

In this part, we show how FDTD method can be adopted to describe the propagation of light in nonlinear dispersive media during the ultrashort laser pulse irradiation. In what follows, the system of nonlinear Maxwell's equations (2.2) is discretized temporally as follows

$$\begin{cases} \dfrac{\vec{H}^{t+1/2} - \vec{H}^{t-1/2}}{\Delta t} = -\dfrac{\left(\nabla \times \vec{E}\right)^t}{\mu_0} \\ \dfrac{\vec{E}^{t+1} - \vec{E}^t}{\Delta t} = \dfrac{\left(\nabla \times \vec{H}\right)^{t+1/2}}{\epsilon_0} - \dfrac{1}{\epsilon_0}(\vec{J}_D^{t+1/2} + \vec{J}_{Kerr}^{t+1/2} + \vec{J}_{pi}^{t+1/2} + \vec{J}_{PM}^{t+1/2}), \end{cases} \tag{3.27}$$

where $\vec{J}_D$ is the current derived from the Lorentz-Drude model for the dispersive media (2.9), $\vec{J}_{Kerr}$ is Kerr polarization current (2.12), $\vec{J}_{pi}$ is the photoionization term (2.20), and $\vec{J}_{PM}$ is the contribution due to the ponderomotive force (2.18). The terms are added to the Maxwell-Ampere electric field update equation and defined on $t + \frac{1}{2}$ timestep.

3.5.1 Implementation of the Lorentz-Drude model

In this part, we describe the auxiliary differential (ADE) technique, firstly proposed by Taflove [212] to implement the Lorentz-Drude dispersive models to Yee numerical scheme. The basis of the method is to express the relationship between the electric displacement field $\vec{D}$ and the electric field $\vec{E}$ with a differential equation rather than with a convolutional integral which was proposed in recursive convolutional method [213]. The major advantage of the ADE is the simplicity in modeling complex materials. In this approach, the dispersive complex media is modeled simply by adding the current directly to the Maxwell-Ampere differential equation (3.27). ADE does not complicate the method if the other nonlinear effects are considered [214,215], whereas the recursive convolutional method can not handle nonlinear dispersive materials due to the linearity of the convolutional integral.

The Drude current, responsible for the heating of the conduction band electrons and defined from the equation (2.9), is discretized as

$$\vec{J}_D^{t+1} = \vec{J}_D^t \frac{1 - \nu_e \Delta t/2}{1 + \nu_e \Delta t/2} + \frac{e^2 \Delta t}{m_e \left(1 + \nu_e \Delta_t/2\right)} \frac{{n_e}^{t+1} \vec{E}^{t+1} + {n_e}^t \vec{E}^t}{2}. \tag{3.28}$$

Applying the approximation $\vec{J}_D^{t+1/2} = (\vec{J}_D^t + \vec{J}_D^{t+1})/2$, one can find the Drude current's discretization on times $t + 1/2$ to introduce directly in Maxwell-Ampere equation (2.2) as follows

$$\vec{J}_D^{t+1/2} = \frac{\vec{J}_D^t}{1 + \frac{\nu_e \Delta t}{2}} + \frac{e^2 \Delta t}{m_e \left(2 + \nu_e \Delta t\right)} \frac{{n_e}^{t+1} \vec{E}^{t+1} + {n_e}^t \vec{E}^t}{2}. \tag{3.29}$$

In the general case of the dispersive material with multiple poles m with the damping factors γ_m and the strengths G_m (2.8), one can rewrite

$$\vec{J}_m^{t+1/2} = \frac{\vec{J}_m^t}{1+\frac{\gamma_m \Delta t}{2}} + \frac{G_m \omega_p \Delta t}{(2+\gamma_m \Delta t)} \frac{\vec{E}^{t+1}+\vec{E}^t}{2}. \tag{3.30}$$

The electric field can be found from Maxwell-Ampere equation (3.27) and discretized as follows

$$\begin{gathered} \vec{E}^{t+1} = C_1 \vec{E}^t + C_2 \left([\nabla \times \vec{H}]^{t+1/2} - \frac{1}{2} \sum_{m=1}^{M} \left[(1+A_{1m}) \vec{J}_m^t \right] \right) \\ C_1 = \frac{2\epsilon_\infty - \frac{1}{2}\sum_{m=1}^{M} A_{2m}}{2\epsilon_\infty + \frac{1}{2}\sum_{m=1}^{M} A_{2m}}, C_2 = \frac{2\Delta t}{2\epsilon_\infty + \frac{1}{2}\sum_{m=1}^{M} A_{2m}} \\ A_{1m} = \frac{1-\gamma_m \Delta t/2}{1+\gamma_m \Delta t/2}, A_{2m} = \frac{\omega_p^2 \Delta t^2}{1+\gamma_m \Delta t/2}. \end{gathered} \tag{3.31}$$

For Lorentz multipole media (2.4) with damping factors γ_m, oscillator strengths G_m, resonant frequencies ω_m and polarization fields $\vec{P_m}$, the discretization equations are found analogically and are given by

$$\begin{gathered} \vec{E}^{t+1} = C_1 \vec{E}^t + C_2 \vec{E}^{t-1} + C_3 \left([\nabla \times \vec{H}]^{t+1/2} - \frac{1}{2} \sum_{m=1}^{M} \left[(1+A_{1m}) \vec{P}_m^t + A_{2m} \vec{P}_m^{t-1} \right] \right) \\ C_1 = \frac{2\epsilon_\infty}{2\epsilon_\infty + \frac{1}{2}\sum_{m=1}^{M} A_{3m}}, C_2 = \frac{\frac{1}{2}\sum_{m=1}^{M} A_{3m}}{2\epsilon_\infty + \frac{1}{2}\sum_{m=1}^{M} A_{3m}}, C_3 = \frac{2\Delta t}{2\epsilon_\infty + \frac{1}{2}\sum_{m=1}^{M} A_{3m}} \\ \vec{P}_m^{t+1} = A_{1m} \vec{P_m}^{\,t} + A_{2m} \vec{P_m}^{\,t-1} + A_{3m} \frac{\vec{E}_m^{t+1} - \vec{E}_m^{t-1}}{2\Delta t} \\ A_{1m} = \frac{2-\omega_m^2 \Delta t^2}{1+\gamma_m \Delta t/2}, A_{2m} = \frac{\gamma_m \Delta t - 2}{\gamma_m \Delta t + 2}, A_{3m} = \frac{G_m \omega_p^2 \Delta t^2}{1+\gamma_m \Delta t/2}. \end{gathered} \tag{3.32}$$

3.5.2 Nonlinear currents

Kerr contribution (2.12) is introduced by using the following equation

$$\vec{J}_{Kerr}^{t+1/2} = \epsilon_0 \chi_3 \frac{\left(I^{t+1} \vec{E}^{t+1} - I^t \vec{E}^t \right)}{\xi \Delta t}, \tag{3.33}$$

where $\xi = \frac{n}{2}\sqrt{\frac{\epsilon_0}{\mu_0}}$ is the normalization constant.

The finite-difference equation for the ionization current (2.20) is given by

$$\vec{J}_{pi}^{t+1/2} = \xi E_g \left(\frac{w_{pi}^{t+1} \vec{E}^{t+1} (n_a - {n_e}^{t+1})}{2 n_a I^{t+1}} + \frac{w_{pi}^t \vec{E}^t (n_a - {n_e}^t)}{2 n_a I^t} \right). \tag{3.34}$$

3.5.3 Fixed-point iteration algorithm

By substituting (3.29, 3.33, 3.34) to (3.27), a system of nonlinear Maxwell's equations is to be solved. One can note, that all nonlinear processes here (2.9, 2.12, 2.20) are intensity-dependent. Thus, the equations for each electric field could not be solved separately as it was possible for nonlinear Kerr and Raman media in 2D-TE case by recursive convolutional dispersive method with iterative and non-iterative schemes [216–218] or by finding the analytical solution for cubic equation [219].

The first algorithm for nonlinear dispersive media which could be implemented for 3D-FDTD and could handle any kind of nonlinearities was proposed by Greene and Taflove [220]. The algorithm was based on the multi-dimensional Newton's iteration for three electric field components. The method

requires the calculation of the Jacobian matrix at each iteration which is cumbersome from a view of computational speed [221] and is delicate in the case when the nonlinear process is not defined by analytical formula as Keldysh photoionization in the considering model. Furthermore, the nonlinear equation is of high order with electric field as a variable which results in high number of required iterations.

Recently, a new method for solving the system of nonlinear equations has been proposed and investigated by Ammann [221] and then implemented by Francés [222, 223]. In this method, the Newton's iteration for ${E_x}^{t+1}$, ${E_y}^{t+1}$ and ${E_z}^{t+1}$ is replaced by fixed-point iteration for I^{t+1}. The intensity has to be introduced in the equations and is calculated as $I^{t+1} = \xi({E_x}^{t+1}{E_x}^{t+1} + {E_y}^{t+1}{E_y}^{t+1} + {E_z}^{t+1}{E_z}^{t+1})$, where ${E_x}^{t+1}$, ${E_y}^{t+1}$ and ${E_z}^{t+1}$ are taken from the ADE method for nonlinear medium. In our case, the algorithm is especially advantageous as all the nonlinear processes are intensity-dependent. At the same time, computational speed is increased and the accuracy is maintained.

The schematics of the calculation procedure is shown in Fig. 3.3. Firstly, the magnetic fields are updated according to simple Yee's discretization [185]. Then, the iteration is started and the electric fields are calculated according to nonlinear ADE method as

$$\vec{E}^{t+1} = C_1(I_k^t, I_k^{t+1})\vec{E}^t + C_2(I_k^t, I_k^{t+1})\left[(\nabla \times \vec{H})^{t+1/2} - \frac{\Delta t}{\epsilon_0}\frac{\vec{J}_D^t}{1 + \frac{\nu_e \Delta_t}{2}}\right], \tag{3.35}$$

with the coefficients that include the Kerr effect and the photoionization's contributions

$$\begin{aligned} C_1(I_k^t, I_k^{t+1}) &= \frac{2\epsilon_\infty - \frac{\omega_{pl}^t}{\nu_e \Delta t + 2} + 2\chi I_k^t - \xi \frac{w_{pi}^t}{I_k^t}\frac{E_g \Delta t}{\epsilon_0}(1 - \frac{{n_e}^t}{n_a})}{2\epsilon_\infty + 2\chi I_k^{t+1} + \xi \frac{w_{pi}^{t+1}}{I_k^{t+1}}\frac{E_g \Delta t}{\epsilon_0}(1 - \frac{{n_e}^{t+1}}{n_a}) + \frac{\omega_{pl}^{t+1}}{\nu_e \Delta t + 2}} \\ C_2(I_k^t, I_k^{t+1}) &= \frac{2\Delta t}{2\epsilon_\infty + 2\chi I_k^{t+1} + \xi \frac{w_{pi}^{t+1}}{I_k^{t+1}}\frac{E_g \Delta t}{\epsilon_0}(1 - \frac{{n_e}^{t+1}}{n_a}) + \frac{\omega_{pl}^{t+1}}{\nu_e \Delta t + 2}}, \end{aligned} \tag{3.36}$$

where the plasma frequency is $\omega_{pl}^t = \frac{e^2 \Delta t^2 {n_e}^t}{m_e \epsilon_0}$, $\chi = \frac{\chi_3}{\xi}$, and ϵ_∞ is the medium permittivity. After that, one should check if the resulting intensity as the sum of the squared electric fields satisfies the Maxwell-Ampere's nonlinear equation with possible deviation not more than a tolerance ϵ (Fig. 3.3). If not, the C_1 and C_2 coefficients and electric fields are updated again taking into account the new value of the calculated intensity. If yes, the iteration procedure is finished, the electron density is given by (2.19), the polarization currents are updated according to (3.28) which are used at the next timestep for calculation of C_1 and C_2 (3.36).

3.5.4 On the convergence of the iteration procedure

In what follows, we investigate the convergence of the proposed iteration algorithm. According to Banach fixed-point theorem [224], fixed-point iteration method $f(I^{t+1}) = \xi(\vec{E}^{t+1}\vec{E}^{t+1}) = I^{t+1}$ converges if the derivation of the intensity function $\left|\frac{\partial f(I^{t+1})}{\partial I^{t+1}}\right| < 1$ is limited $\forall I^{t+1}$ from the applied intensity interval. This condition yields

$$\begin{aligned} &\xi\left[C_1(I^{t+1})\vec{E}^t + C_2(I^{t+1})\left((\nabla \times \vec{H})^{t+1/2} - \frac{\Delta t}{\epsilon_0}\frac{\vec{J}_D^t}{1 + \frac{\nu_e \Delta_t}{2}}\right)\right] \cdot \\ &\left[{C_1}'(I^{t+1})\vec{E}^t + {C_2}'(I^{t+1})\left((\nabla \times \vec{H})^{t+1/2} - \frac{\Delta t}{\epsilon_0}\frac{\vec{J}_D^t}{1 + \frac{\nu_e \Delta_t}{2}}\right)\right] < \frac{1}{2}. \end{aligned} \tag{3.37}$$

Because of the continuity of the equations, and because temporal and spatial grid have accurately high resolutions respectively, the terms containing spatial and temporal derivations as $(\nabla \times \vec{H})^{t+1/2}$ and $\vec{J}_D^t$ can be considered small compared with the terms proportional to the electric field and hence can be neglected. Therefore, the condition yields

$$C_1(I^{t+1}){C_1}'(I^{t+1})I^t < \frac{1}{2}. \tag{3.38}$$

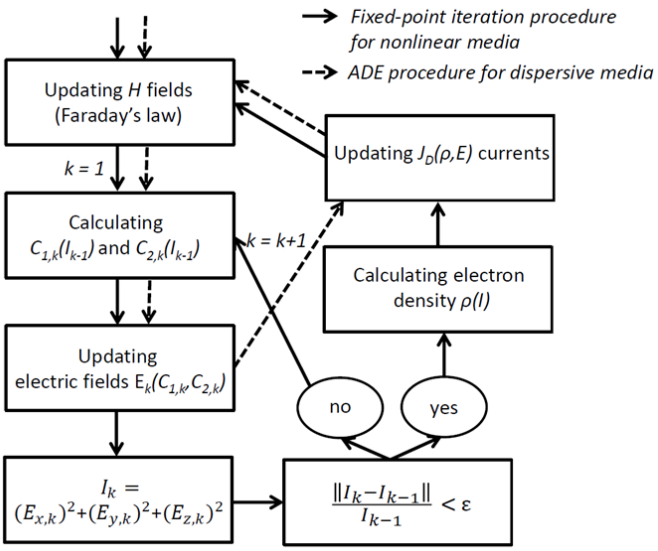

Figure 3.3: Schematics of the calculation procedure.

Substituting (3.36) and calculating the derivation, one can find the following condition

$$\frac{\left[2\epsilon_\infty - \frac{\omega_{pl}}{\nu_e\Delta t+2} + 2\chi I^t - \xi\frac{w_{pi}}{I^t}\frac{E_g\Delta t}{\epsilon_0}(1-\frac{{n_e}^t}{n_a})\right]^2\left[2\chi + \xi\left(\frac{w'_{pi}}{I^{t+1}} - \frac{w_{pi}}{(I^t)^2}\right)\frac{E_g\Delta t}{\epsilon_0}(1-\frac{{n_e}^t}{n_a})\right]I^t}{\left[2\epsilon_\infty + 2\chi I^{t+1} + \xi\frac{w_{pi}^{t+1}}{I^{t+1}}\frac{E_g\Delta t}{\epsilon_0}(1-\frac{{n_e}^{t+1}}{n_a}) + \frac{\omega_{pl}^{t+1}}{\nu_e\Delta t+2}\right]^3} < \frac{1}{2}. \quad (3.39)$$

From the above expression, the timestep Δt has to be chosen in order to respect the convergence condition. The choice depends on the particular properties of the medium, as Kerr nonlinearity χ, photoionization w_{pi}, the medium permittivity ϵ_∞, and the laser intensity I. However, for wide range of dielectric materials the condition will be met as the contribution of nonlinear parts in the expression is significantly smaller than $2\epsilon_\infty$ even for high laser intensities $I \approx 10^{18} Wm^{-2}$. Here, we show that for fused silica the algorithm is stable even for large spatial and temporal steps. In nanometric calculation, the reasonable spatial step will be $1nm \leq \Delta x \leq 20nm$. The timestep is related to the spatial step by Courant-Friedrichs-Lewy's condition [186] for three-dimensional grid with identical spatial step $\Delta t = \frac{\Delta x}{2c} < \frac{1}{c\sqrt{\frac{1}{\Delta x^2}+\frac{1}{\Delta y^2}+\frac{1}{\Delta z^2}}}$. Therefore, $1.5as < \Delta t < 35as$.

Thus, the nonlinear component due to Kerr effect with $\chi_3 = 2\cdot 10^{-22} m^2 V^{-2}$ for fused silica [61] is

$$\frac{2\chi_3 I}{\xi} \approx 0.07 < 2\epsilon_\infty \approx 4. \quad (3.40)$$

The highest value of the component responsible for heating of the conduction band electrons is

$$\frac{\omega_{pl}}{\nu_e\Delta t+2} = \frac{e^2\Delta t^2 n_e}{m_e\epsilon_0(2+\nu_e\Delta_t)} \leq \frac{e^2\Delta t^2 n_a}{2m_e\epsilon_0} < 0.035 < 2\epsilon_\infty, \quad (3.41)$$

where the saturation density is $n_a = 2\cdot 10^{28} m^{-3}$ for fused silica. Finally, we estimate roughly the highest value for photoionization to be

$$\xi\frac{w_{pi}}{I^t}\frac{E_g\Delta t}{\epsilon_0}\left(1-\frac{{n_e}^t}{n_a}\right) \leq \xi\frac{w_{pi}}{I^t}\frac{E_g\Delta t}{\epsilon_0} \leq 0.245 < 2\epsilon_\infty, \quad (3.42)$$

where $E_g = 9$ eV for fused silica [61]. Note, that $\frac{w_{pi}(I)}{I}$ increases with the increasing intensity and $w_{pi}(I = 10^{18} Wm^{-2}) \approx 10^{41} s^{-1} m^{-3}$ [138]. The last nonlinear term appears to be the most essential at high laser intensities and one order higher than the other contributions. At such intensities Keldysh photoionization rate $w_{pi} < \sigma I^6$, where $\sigma = 2\cdot 10^{-65} m^9 W^{-6} s^{-1}$. If one consider now $w_{pi} = \sigma I^6$, the

condition will be only reinforced. In what follows, $\xi\left[w'_{pi}(I)-\frac{w_{pi}}{I}\right]\frac{E_g\Delta t}{\epsilon_0}=5\frac{w_{pi}}{I}\frac{\alpha E_g\Delta t}{\epsilon_0}$ is five times higher than estimated value but still lower than ϵ_∞. In fact, one can find, that

$$\frac{\left[2\epsilon_\infty-\xi\frac{w_{pi}}{I}\frac{E_g\Delta t}{\epsilon_0}(1-\frac{\rho}{\rho_0})\right]^2\left[\left(\frac{w'_{pi}}{I}-\frac{w_{pi}}{(I)^2}\right)\frac{\xi E_g\Delta t}{\epsilon_0}(1-\frac{n_e}{n_a})\right]I}{\left[2\epsilon_\infty+\xi\frac{w_{pi}}{I}\frac{E_g\Delta t}{\epsilon_0}(1-\frac{n_e}{n_a})\right]^3}<\frac{\frac{5w_{pi}}{I}\frac{\xi E_g\Delta t}{\epsilon_0}}{2\epsilon_\infty}\leq 0.3<\frac{1}{2}. \tag{3.43}$$

Therefore, the algorithm converges for timestep $\Delta t<35as$ and $I\approx 10^{18}Wm^{-2}$. It is possible to widen the interval of the applied intensities for which it converges by reducing the spatial and temporal steps. No instability problems have been encountered in investigations. Regarding the iterative process, an experimental procedure was done in order to establish an upper limit in the number of iterations. The maximum number of the iterations was fixed to 10 steps achieving good results near the upper limit of convergence of the method $\frac{|I_k-I_{k-1}|}{I_{k-1}}<\epsilon=10^{-12}$.

In case I^{t+1} is replaced by I^t, one can obtain the simplified algorithm for which is not necessary to keep in the memory both intensities at each spatial step. The algorithm is more stable and convenient for larger interval of intensities but deviation from the exact solution is possible [221] due to the error in discretization of nonlinear currents (3.33) and (3.34).

3.5.5 Electron density equation

We use a simple implicit scheme for single rate electron density equation (2.19)

$$\begin{aligned}\frac{{n_e}^{t+1}-{n_e}^t}{\Delta t}=&\frac{(n_a-{n_e}^{t+1})w_{pi}^{t+1}+(n_a-{n_e}^t)w_{pi}^t}{2}+\dots\\&\frac{w_{av}^{t+1}{n_e}^{t+1}+w_{av}^t{n_e}^t}{2}-\frac{{n_e}^t+{n_e}^{t+1}}{\tau_{rec}},\end{aligned} \tag{3.44}$$

where $w_{av}(I)$ is considered to be dependent only on the laser intensity. The discretization of multiple rate equations propsoed by Rethfeld [68] is analogical to the discretization of the single rate equation.

The electron carrier density at the next temporal step can be calculated as

$${n_e}^{t+1}=B\left[1-\frac{(w_{pi}^t-w_{av}^t)\Delta t}{2}-\frac{\Delta t}{2\tau_{rec}}\right]{n_e}^t+B\frac{n_a(w_{pi}^{t+1}+w_{pi}^t)\Delta t}{2}, \tag{3.45}$$

where the coefficient B is defined as $B=\dfrac{1}{1+\frac{(w_{pi}^{t+1}-w_{av}^{t+1})\Delta t}{2}+\frac{\Delta t}{2\tau_{rec}}}$.

3.6 Spatial discretization

In what follows, we discuss the particularity of spatial discretization for polarization currents (3.28) and electric fields (3.35) by FDTD method coupled with the free carrier density equation. Due to initial asymmetrical behavior of the numerical scheme proposed by Yee [185], the electric and magnetic fields are spatially displaced on a half-step (Fig. 3.1). On the contrary, intensity I, electron density n_e, C_1 and C_2 should be defined at one grid position (Fig. 3.1). There are two ways to introduce the intensity of laser beam. The first way is to find the arithmetic mean of the squared neighbor electric fields

$$\begin{aligned}I(m,n,k)=&\frac{1}{2}\left[{E_x}^2(m+1/2,n,k)+{E_x}^2(m-1/2,n,k)\right]+\\&\frac{1}{2}\left[{E_y}^2(m,n+1/2,k)+{E_y}^2(m,n-1/2,k)\right]+\\&\frac{1}{2}\left[{E_z}^2(m,n,k+1/2)+{E_z}^2(m,n,k-1/2)\right],\end{aligned} \tag{3.46}$$

where (m,n,k) corresponds to spatial dimension in the direction x, y and z correspondingly. Note, that for simplicity, we omit here $\xi=\frac{n}{2}\sqrt{\frac{\epsilon_0}{\mu_0}}$. The approximation for each squared electric field component gives a second-order error by truncating Taylor series

$$\begin{aligned}\Delta E_x^2 &= \frac{1}{2}\left(E_x^{m+1/2}\right)^2 + \frac{1}{2}\left(E_x^{m-1/2}\right)^2 - (E_x^m)^2 \\ &= \frac{1}{2}\left[E_x^m + \frac{\Delta x}{2}(E_x^m)' + O(\Delta x^2)\right]^2 + \frac{1}{2}\left[E_x^m - \frac{\Delta x}{2}(E_x^m)' + O(\Delta x^2)\right]^2 - (E_x^m)^2 \\ &= O(\Delta x^2). \end{aligned} \tag{3.47}$$

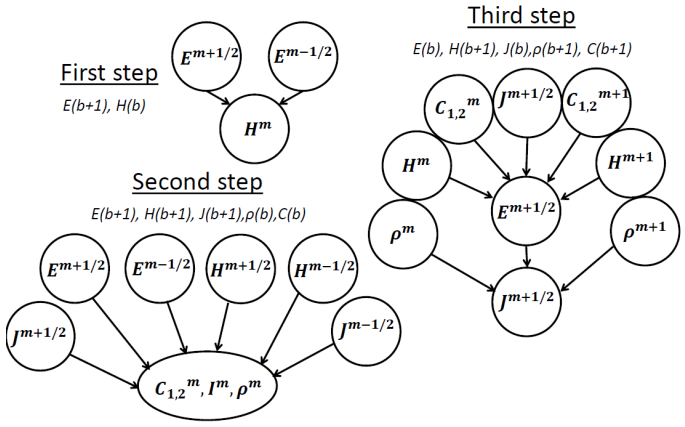

Figure 3.4: Steps of the calculation procedure and shared memory allocation of the required arrays for each step.

The alternative way is to define firstly the electric fields in (m, n, k) and then, to calculate the intensity

$$\begin{aligned} I(m,n,k) = &\frac{1}{4}\left[E_x(m+1/2,n,k) + E_x(m-1/2,n,k)\right]^2 + \\ &\frac{1}{4}\left[E_y(m,n+1/2,k) + E_y(m,n-1/2,k)\right]^2 + \\ &\frac{1}{4}\left[E_z(m,n,k+1/2) + E_z(m,n,k-1/2)\right]^2. \end{aligned} \tag{3.48}$$

In this case, it is a fourth-order approximation which results in the smaller error

$$\begin{aligned}\Delta E_x^2 &= \frac{1}{4}(E_x^{m+1/2} + E_x^{m-1/2})^2 - (E_x^m)^2 \\ &= \frac{1}{4}\left[E_x^m + \frac{\Delta x}{2}(E_x^m)' + \frac{\Delta x^2}{8}(E_x^m)'' + E_x^m - \frac{\Delta x}{2}(E_x^m)' + \frac{\Delta x^2}{8}(E_x^m)'' + O(\Delta x^4)\right]^2 - (E_x^m)^2 \\ &= O(\Delta x^4). \end{aligned} \tag{3.49}$$

In the first case, one should calculate separately the electric fields for each neighbor cells, which increases twice the calculation procedure and is especially cumbersome in the iterative procedure. As one will see, simplifications are possible in the second case, where the sum of two neighbor electric fields can be found directly.

Electron density and coefficients (3.36) have the same discretization as the intensity. One can note that they are used for calculation of Drude currents (3.28) and electric fields (3.35) having different discretizations. Ignoring this fact will lead to the asymmetry in the numerical scheme and to unphysical results, especially when an interface between two different media is considered. To avoid such problem, we propose to modify (3.36) and to achieve equal spatial discretization in both parts of the equations. For the E_x electric field, we apply

$$E_x^{m+1/2} = \frac{C_1^{m+1} + C_1^m}{2} E_x^{m+1/2} + \frac{C_2^{m+1} + C_2^m}{2}\left[(\nabla \times \vec{H})^{m+1/2} - \frac{\Delta t}{\epsilon_0}\frac{J_x{}_D^{m+1/2}}{1 + \frac{\nu_e \Delta t}{2}}\right]. \tag{3.50}$$

Note, that to find $E_x^m = (E_x^{m+1/2} + E_x^{m-1/2})/2$, we use the following finite-difference expression of (3.35) centered at x spatial position m

$$E_x^m = C_1^m \frac{E_x^{m+1/2} + E_x^{m-1/2}}{2} + C_2^m \left[(\nabla \times \vec{H})^m - \frac{\Delta t}{\epsilon_0} \frac{{J_{xD}}^{m+1/2} + {J_{xD}}^{m-1/2}}{2 + \nu_e \Delta t} \right]. \tag{3.51}$$

For the Drude current J_x, one can apply

$$\begin{aligned} {J_{xD}}^{m+1/2,t+1} &= {J_{xD}}^{m+1/2,t} \frac{1 - \nu_e \Delta t/2}{1 + \nu_e \Delta t/2} + \dots \\ &\frac{e^2 \Delta t^2}{m_e \epsilon_0} \frac{\left({n_e}^{m+1,t+1} + {n_e}^{m,t+1} \right) E_x^{m+1/2,t+1} + \left({n_e}^{m+1,t} + {n_e}^{m,t} \right) E_x^{m+1/2,t}}{2 + \nu_e \Delta t}. \end{aligned} \tag{3.52}$$

Similar procedure applies to y and z field and current components, correcting spatial discretization for n and k correspondingly.

3.7 Electron-ion heat transfer equations

The following numerical scheme based on the implicit Crank-Nicolson method [225] is proposed for solving the two-dimensional equation for electron temperature (2.25)

$$\begin{aligned} \frac{3k_B(n_e^{t+1} + n_e^t)}{4} \frac{(T_e)^{t+1} - (T_e)^t}{\Delta t} &= \frac{{k_B}^2 \mu_e}{2e} \nabla \cdot (n_e T_e \nabla T_e)^{t+1} + \dots \\ \frac{{k_B}^2 \mu_e}{2e} \nabla \cdot (n_e T_e \nabla T_e)^t - \frac{3k_B}{4\tau_{ei}} \left[T_e^{t+1} n_e^{t+1} + T_e^t n_e^t - (n_e^{t+1} + n_e^t) T_i \right] &+ I \alpha_{abs}, \end{aligned} \tag{3.53}$$

where the electron density-dependent heat capacity C_e, thermal conductivity k_e and electron-lattice relaxation time γ_{ei} are incorporated into the equation. In what follows, we define $r = \frac{n_e^t}{n_e^{t+1}}$ as the relationship between the electron densities, $Q = \frac{8\pi \Delta t I k}{3\lambda n_e k_B}$ as the source, $k_e = \frac{k_B \mu_e \Delta t}{3e\Delta x^2}$ as the effective constant thermal conductivity divided by heat capacity, $\gamma_e = \frac{\Delta t}{\tau_{ei}}$ as the effective relaxation time. One can find the solution for the electron temperature at the next temporal step as follows

$$\begin{aligned} T_e^t &= E_1 {T_e}^{t-1} + E_2(\gamma_e T_i + Q) + \dots \\ E_k &\left[T_{e_{n+1}}^2 + T_{e_{n-1}}^2 + r \left(T_{e_{n+1}}^{t-1} \right)^2 + r \left(T_{e_{n-1}}^{t-1} \right)^2 \right] + \dots \\ E_k &\left[T_{e_{m+1}}^2 + T_{e_{m-1}}^2 + r \left(T_{e_{m+1}}^{t-1} \right)^2 + r \left(T_{e_{m-1}}^{t-1} \right)^2 \right] \\ E_1 &= E_2 \left(1 - 2k_e {T_e}^{t-1} \frac{r}{1+r} - \gamma_e \frac{r}{1+r} \right), \\ E_2 &= 1/\left(1 + \frac{2k_e T_e}{1+r} + \frac{\gamma_e}{1+r} \right), \qquad E_k = \frac{k_e E_2}{2(1+r)}, \end{aligned} \tag{3.54}$$

where (m, n) are the spatial mesh points, t is the temporal mesh point. If not precised, the temperatures T_e and T_i and the electron densities n_e are defined at (m, n) spatial step and t temporal step.

Once the laser energy is transferred to the electron system and $Q \approx 0$, the discrete scheme is unconditionally stable, so the temporal step can be safely increased up to tens of femtoseconds. In fact, one can investigate the stability in the form $t^z \cdot e^{i\lambda m}$ as follows

$$\begin{aligned} z - \frac{r}{z} &= \left[-2sin^2(\frac{\lambda}{2}) \frac{k_e \Delta t}{\Delta x^2} - \frac{\gamma_e}{2} \right] (z + \frac{r}{z}) \\ z^2 &= \frac{r - 2sin^2(\frac{\lambda}{2}) \frac{k_e \Delta t}{\Delta x^2} - \frac{\gamma_e}{2}}{r + 2sin^2(\frac{\lambda}{2}) \frac{k_e \Delta t}{\Delta x^2} + \frac{\gamma_e}{2}} \leq 1. \end{aligned} \tag{3.55}$$

Nevertheless, to avoid the decaying oscillations, the condition $k_e T_e = \frac{k_B \mu_e T_e \Delta t}{3e\Delta x^2} \leq \frac{1}{2}$ is to be hold. One can estimate, that for a spatial step $\Delta x = 20$ nm and high electron temperatures of order $T_e = 10^6 - 10^7$ K, $\Delta t < 50$ fs.

The similar implicit Crank-Nicolson scheme is used for solving the equation for ion temperature (2.25)

$$\begin{gathered}\rho_i C_i \frac{{T_i}^{t+1} - {T_i}^t}{\Delta t} = \frac{k_i}{2}\left[\nabla\cdot(\nabla T_i)^{t+1} + \nabla\cdot(\nabla T_i)^t\right] + \ldots \\ \frac{3k_B\left[{n_e}^{t+1}({T_e}^{t+1} - {T_i}^{t+1}) + {n_e}^t({T_e}^t - {T_i}^t)\right]}{8\tau_{ei}} - \frac{B\beta T_0(\nabla\vec{u}^{t+1} + \nabla\vec{u}^t)}{2}.\end{gathered} \tag{3.56}$$

As in previous case, we define $\gamma_i = \frac{3k_B\Delta t}{4C_i}$. One can find the lattice temperature defined at the next temporal step as follows

$$\begin{gathered}T_i^{t+1} = I_1 T_i + I_2\gamma_i\left({T_e}^{t+1}{n_e}^{t+1} + T_e n_e\right)/2 + \ldots \\ I_3(T_{in+1} + T_{in-1} - 4T_{in} + T_{im+1} + T_{im-1} - 4T_{im}) - \ldots \\ I_4(u_{m+1}^{t+1} - u_{m-1}^{t+1} + u_{m+1} - u_{m-1} + u_{n+1}^{t+1} - u_{n-1}^{t+1} + u_{n+1} - u_{n-1}) \\ I_1 = I_2(1 - \gamma_i n_e/2), \qquad I_2 = \frac{1}{1 + \gamma_i {n_e}^{t+1}/2}, \\ I_3 = \frac{k_i I_2 \Delta t}{\rho_i C_i \Delta x^2}, \qquad I_4 = \frac{B\beta I_2}{4\rho_i C_i \Delta x}.\end{gathered} \tag{3.57}$$

If not precised, the temperatures T_e and T_i, the electron densities n_e and the displacements u are defined at (m, n) spatial step and t temporal step. As the previous scheme, it is unconditionally stable. The decaying oscillations are completely avoided as the condition $\frac{k_i\Delta t}{\rho_i C_i \Delta x^2} \leq \frac{1}{2}$ is satisfied. One can note, that the temporal step can be also increased up to few picoseconds to solve heat diffusion equation when the electron-ion transfer is finished and the system is in equilibrium. For example, for a spatial step $\Delta x = 20$ nm, $\Delta t \leq \Delta x^2/D \approx 400$ ps.

For both electron and ion temperatures, the initial and boundary conditions are expressed as

$$\begin{cases} T_e^{t=0} = T_i^{t=0} = T_0 = 300K \\ \left(\dfrac{\partial T_e}{\partial t}\right)^{t=0} = \left(\dfrac{\partial T_i}{\partial t}\right)^{t=0} = 0 \\ \left(\dfrac{\partial T_e}{\partial x}\right)_{(m=0,x_{max})} = \left(\dfrac{\partial T_i}{\partial x}\right)_{(m=0,x_{max})} = 0 \\ \left(\dfrac{\partial T_e}{\partial z}\right)_{(n=0,z_{max})} = \left(\dfrac{\partial T_i}{\partial z}\right)_{(n=0,z_{max})} = 0, \end{cases} \tag{3.58}$$

where T_0 is the initial temperature, $0, x_{max}$ and $0, z_{max}$ are boundaries of the numerical grid. The boundary conditions are discretized by the second order numerical scheme.

3.8 Thermo-elastic wave equations

The equation for displacements (2.28) is solved numerically by the following discrete scheme

$$\begin{gathered}\rho\frac{u^{t+1} - 2u^t + u^{t-1}}{\Delta t^2} = \frac{G}{2}(\nabla^2\vec{u}^{t+1} + \nabla^2\vec{u}^{t-1}) + \ldots \\ \frac{G}{2-4\nu}\left[\nabla(\nabla\cdot\vec{u}^{t+1}) + \nabla(\nabla\cdot\vec{u}^t)\right] - B\beta\nabla T_i.\end{gathered} \tag{3.59}$$

Finally, the two-dimensional displacements can be expressed at the next temporal step as

$$\begin{gathered}
u_x^{t+1} = \frac{2u_x^t - u_x^{t-1}}{1+4C_1+2C_2} + \frac{C_1(u_{xm+1} + u_{xm-1} + u_{xn+1} + u_{xn-1})}{1+4C_1+2C_2} + \dots \\
\frac{C_2(4u_{xm+1} + 4u_{xm-1} + u_{zm+1,n+1} - u_{zm+1,n-1} + u_{zm-1,n-1} - u_{zm-1,n+1}}{4(1+4C_1+2C_2)} - \dots \\
\frac{C_3T_{im+1} - C_3T_{im-1}}{2(1+4C_1+2C_2)} \\
u_z^{t+1} = \frac{2u_z^t - u_z^{t-1}}{1+4C_1+2C_2} + \frac{C_1(u_{zn+1} + u_{zn-1} + u_{zm+1} + u_{zm-1})}{1+4C_1+2C_2} + \dots \\
\frac{C_2(4u_{zn+1} + 4u_{zn-1} + u_{xm+1,n+1} - u_{xm+1,n-1} + u_{xm-1,n-1} - u_{xm-1,n+1}}{4(1+4C_1+2C_2)} - \dots \\
\frac{C_3T_{in+1} - C_3T_{in-1}}{2(1+4C_1+2C_2)} \\
C_1 = \frac{G\Delta t^2}{\rho \Delta x^2}, \qquad C_2 = C_1/(1-2\nu), \qquad C_3 = \frac{B\beta\Delta t^2}{\rho\Delta x}.
\end{gathered} \tag{3.60}$$

If not precised, the temperatures T_i, the densities ρ and the displacements u are defined at (m,n) spatial step and t temporal step. The particularity of the thermoelastic wave equation is a pressure wave solution. The changes in displacements due to pressure wave launching take place up to nanosecond timescales on a few micrometers spatial grid, as the longitudinal sound velocity of the pressure wave $C_L = \sqrt{G/\rho}$ is about 6 km/s or $6\mu m/ns$. Therefore, the stability criterium for hyperbolic system of equations yields $C_1 = \frac{G\Delta t^2}{\rho\Delta x^2} \leq 1$ and can be rewritten as $\Delta t \leq \Delta x/C_L < 3$ ps. At few nanoseconds, the laser-induced system is stabilized and then the relaxation follows. Therefore, the temporal step can be increased up to hundreds of picoseconds.

The initial and boundary conditions for displacements are written as follows

$$\begin{cases}
u_x^0 = u_z^0 = 0 \\
\left(\dfrac{\partial u_x}{\partial t}\right)^{t=0} = \left(\dfrac{\partial u_z}{\partial t}\right)^{t=0} = 0 \\
\left(\dfrac{\partial u_x}{\partial x}\right)_{(m=0,x_{max})} - \dfrac{B\beta}{B+\frac{4}{3}G}(T_{i(m=0,x_{max})} - T_0) = 0 \\
\left(\dfrac{\partial u_z}{\partial z}\right)_{(n=0,z_{max})} - \dfrac{B\beta}{B+\frac{4}{3}G}(T_{i(n=0,z_{max})} - T_0) = 0,
\end{cases} \tag{3.61}$$

where T_0 is the initial temperature, $(0, x_{max})$ and $(0, z_{max})$ are boundaries of the numerical grid. The equations for boundary conditions are approximated by the corresponding second-order differential scheme.

The implicit difference scheme for the density equations (2.30) is written as follows

$$\begin{gathered}
\rho^{t+1} = \rho^t/F - \frac{(u_x - u_x^{t-1})(\rho_{m+1} - \rho_m)}{2\Delta x F} - \frac{(u_z - u_z^{t-1})(\rho_{n+1} - \rho_n)}{2\Delta x F} - \dots \\
\frac{\rho^t(u_{xm+1} - u_{xm+1}^{t-1} - u_{xm-1} + u_{xm-1}^{t-1} + u_{zn+1} - u_{zn+1}^{t-1} - u_{zn-1} + u_{zn-1}^{t-1})}{4\Delta x F} \\
F = 1 + \frac{u_{xm+1} - u_{xm+1}^{t-1} - u_{xm-1} + u_{xm-1}^{t-1} + u_{zn+1} - u_{zn+1}^{t-1} - u_{zn-1} + u_{zn-1}^{t-1}}{4\Delta x}.
\end{gathered} \tag{3.62}$$

If not precised, the displacements u and the densities ρ are defined at (m,n) spatial step and t temporal step. The initial and boundary conditions for the density equation are written as follows

$$\begin{cases}
\rho^0 = \rho_0 \\
\left(\dfrac{\partial \rho}{\partial x}\right)_{(m=0,x_{max})} = \left(\dfrac{\partial \rho}{\partial z}\right)_{(n=0,z_{max})} = 0,
\end{cases} \tag{3.63}$$

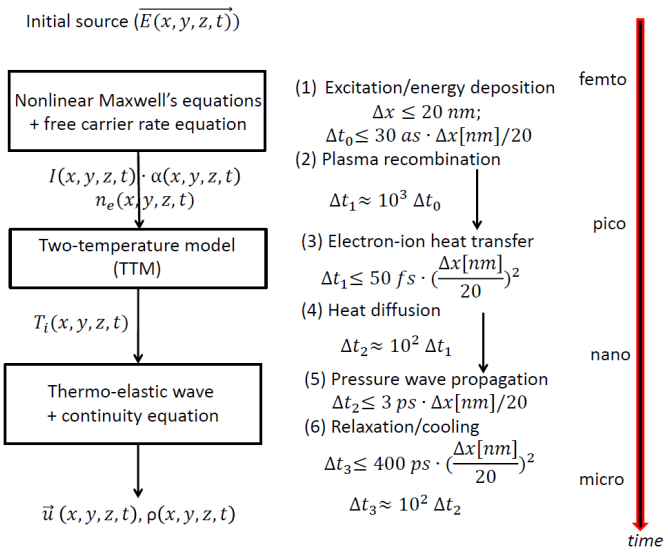

Figure 3.5: Schematics and limitations of the multiphysical calculation procedure.

where $\rho_0 = 2.2$ g/cm^3 for fused silica and borosilicate glass is the density of non-deformed material, $(0, x_{max})$ and $(0, z_{max})$ are boundaries of the numerical grid. The equations for boundary conditions are approximated by the corresponding second-order differential schemes.

Fig. 3.5 illustrates the structure of the self-consistent multiphysical model. The electromagnetic model sets the spatial limitation of the mesh. The nonlinear system of Maxwell's equations coupled with free carrier rate equation are solved with the smallest timestep in attosecond range. The calculated spatio-temporal distributions of the electron density, intensity and absorption serve as the initial conditions for solving electron-ion heat transfer equations. The temporal step can be increased up to 1000 times as soon as the laser pulse has passed (then, the electromagnetic calculations are switched off). Electron-ion heat transfer sets the spatio-temporal lattice temperature distribution, used as the initial source for the thermo-elastic wave equations coupled with the continuity equation for the lattice density. After the electron and ion temperatures find the equilibrium, the timestep can be increased 100 times more. The following limitation is because of the pressure wave launch, taking place up to several nanoseconds. After this process, the only limitation is caused by solving heat diffusion equation and enables the timestep increase up to tenths-one hundred of picoseconds.

3.9 Conclusions

We have presented in details the numerical method for solving the system of equations describing ultrashort laser interaction with dielectrics.

The fundamental part of the method is devoted to solving complex dynamic problems in nonlinear optics and is based on the Maxwell's equations coupled with time-varying electron density equation, taking into account the variety of nonlinear processes which take place under high-intensity ultrashort laser irradiation like Kerr effect, photoionization, avalanche and recombination processes. The proposed numerical approach allows reaching a sufficient stability, finding a good compromise between the model accuracy and ease of use. In particular, the method is advantageous in the case of ultrafast laser material processing [3], for modeling ultrashort laser nanoparticle interaction [134, 226], and to study the periodic nanostructure formation in dielectric materials by femtosecond laser irradiation [227, 228]. The electrodynamic approach is applied in Chapter 4 and Chapter 5. The proposed parallel GPU implementation detailed in Appendix leads to a significant decrease in the computation time.

Finally, the appropriate discrete schemes are written for solving electron-ion heat transfer equations, thermoelastic wave equation and continuity equation for density and the temporal steps required for the numerical stability are discussed. Chapter 6 describes the numerical results obtained by modeling of ultrashort laser interaction with fused silica solving full system of equations.

3.10 Appendix: GPU implementation

It should be noted that realistic 3D-calculations are extremely time-consuming and require storage and manipulation of massive data on each timestep. To implement parallel algorithm to code, the numerical grid should be divided into thread blocks. The cells situated at the borders of the blocks need to access to adjacent blocks, which makes the parallel procedure complex and disadvantageous in the case of implementation on multi-processors using the Message Passing Interface (MPI) library [229,230]. Note, that in this case, two dimensional arrays of electric and magnetic fields have to be sent to neighbor processors at each timestep. For example, using 1D-block data redistribution between the processors, for a 3D-grid with $350 \times 350 \times 350$ cells, after each timestep and for each processor, there are two square faces of neighbor cells $350 \cdot 350 \cdot 2 = 2.45 \cdot 10^5$ to interchange with 6 electromagnetic fields, 3 Drude currents and one electron density array of type "'double"' ($10 \cdot 8 = 80$ bytes), so approximately 20 Mbytes to transfer. Considering that it takes about few seconds [231] and 48000 timesteps are modeled, the time needed just to transfer the required neighbor fields exceeds one hundred hours, which is comparable to the computation time. Furthermore, the communication time between the processors rises rapidly both with the number of processors and the size of the grid, resulting in bad speedups [231,232].

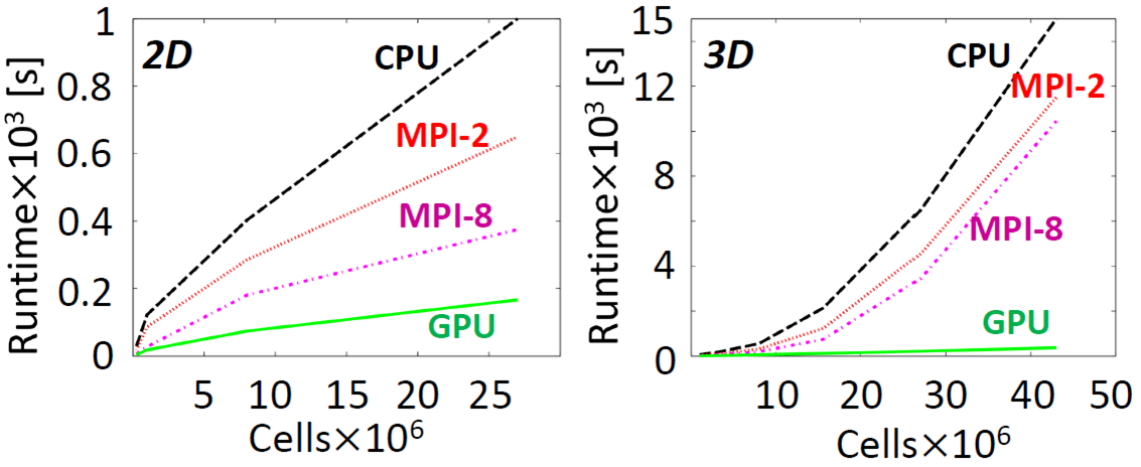

Figure 3.6: Computation time dependence on the size of the grid for CPU, MPI with 2 processors, MPI with 8 processors and GPU in the case of two-dimensional and three-dimensional problems of 400 timesteps.

On the contrary, the proposed GPU technique is extremely beneficial, accelerating the calculation by hundreds of times, because context switching between GPU threads does not require the state to be stored/restored in contrast to CPU threads [233] and the peak memory bandwidth could be as high as 288 Gb/s. Even a non-optimized parallel implementation of the FDTD on a GPU can lead to a significant decrease in computation time with respect to a CPU implementation [234]. However, the code should be optimized avoiding unnecessary use of global memory.

The implementation of the proposed method involves allocating and initializing on the GPU global memory six arrays for the E_x, E_y, E_z electric field components of the current and previous timesteps and three arrays for the H_x, H_y, H_z magnetic field components, three arrays for the polarization currents J_{xD}, J_{yD}, J_{zD}, twenty four arrays for the UPML (six faces and four arrays for each square face), the arrays for intensities I and electron densities n_e for current and previous timesteps. Once on the device, it is advantageous to use the fast but limited shared memory to handle updating equations [233–236]. To reduce the number of memory access transitions and to exploit the availability of the shared memory, we propose to expand the dimensions of the blocks loading therein all the needed components, including the ones corresponding to adjacent blocks as it was implemented for linear FDTD [234]. Instead of two common steps of updating electric and magnetic fields for simple FDTDs [234,235], the model requires three steps shown in Fig. 3.4. Between the steps, the threads are synchronized by *syncthreads*(). At each step, only shared memory is used for computation and the

expanded shared memory allocations of the required arrays using $b+1$ cells are outlined in Fig. 3.4. Thus, for example, calculation of the intensity by (3.48) as a sum of the neighbor electric fields defined by (3.51) requires the allocation of electric and magnetic fields, and polarization currents at $m+1/2$ and $m-1/2$ in shared memory at the beginning of the second step. Analogically, calculation of the polarization current by (3.52) requires the electron densities stored at m and $m+1$ at the beginning of the third step.

Table 3.2: CPU, MPI & GPU computation time.

Grid	Grid points	Timesteps	Single CPU	MPI (8 processors)	GPU
2000×2000	$4 \cdot 10^6$	32000	75 h	14 h 40	1 h 20
$350 \times 350 \times 350$	$42.875 \cdot 10^6$	48000	1200 h	750 h	7 h 35
$500 \times 500 \times 500$	$125 \cdot 10^6$	48000	3500 h	-	12 h 30

The advantage of using GPU-based algorithm over CPU or non-optimized classical MPI-based algorithm can be already seen after 400 timesteps calculation in Fig. 3.6. In particular, when the communication between the processors in 3D problems is of the same order as the calculation time, using multiple processors turns out to be inefficient, whereas GPU conserves its high performance speedups. In what follows, I give an example of approximate calculation time required to solve a massive nonlinear dynamic problem on a single CPU, by using MPI in parallel on 8 processors, and by GPU *QuadroK*6000 with 2880 CUDA cores in Table 3.2. For two-dimensional case, $\Delta x = 5$ nm is used to calculate light propagation in the grid $10 \times 10 \mu m^2$ with timestep $\Delta t = 7.5$ as and irradiation during 240 fs with intensity $I = 5 \cdot 10^{17}$ W m^{-2}. The GPU acceleration is more than 50 times, which could be achieved only by using many processors. The GPU technique is even more beneficial in three-dimensional case, where using a lot of processors is disadvantageous due to large data array manipulation (Table 3.2). The spatial step is $\Delta x = 10nm$, resulting in $3.5 \times 3.5 \times 3.5 \mu m^3$ and $5 \times 5 \times 5 \mu m^3$ grids. The corresponding timestep is $\Delta t = 15$ as and irradiation during 720 fs with similar intensities. The acceleration on GPU reaches 280 times which enables calculating realistic problems in nonlinear optics within reasonable time.

Chapter 4

Ultrashort laser interaction with nanoparticle in dielectric media

This chapter is devoted to the numerical study of ultrashort laser interaction with a single spherical nano-inhomogeneity in a dielectric medium. The aim is to describe the evolution of intensity and free carrier density distribution in the vicinity of the nanoparticle as a function of the nanoparticle's size and density in optical medium with varying optical properties due to femtosecond laser irradiation. Particular attention is paid to the differences of ultrashort laser interaction with nanovoids and metallic nanoparticles embedded in fused silica. Depending on the size and on the density, different behavior is shown in the near-field and in the far-field of the nanoparticle. Finally, the presented study explains the growth of polarization-dependent nanoplasmas from single inhomogeneities of different optical properties, which is a significant step toward understanding of ultrafast laser interaction with inhomogeneous dielectric medium.

4.1 Main parameters from Mie theory

Nonlinear electrodynamics of ultrafast laser interaction with nanoparticles (NPs) could not be described by electrostatic approach. To take into account the changes in the optical properties of the medium and ionization processes in dielectrics, nonlinear Maxwell's equation should be coupled with electron density equation, as it was discussed in the previous chapter.

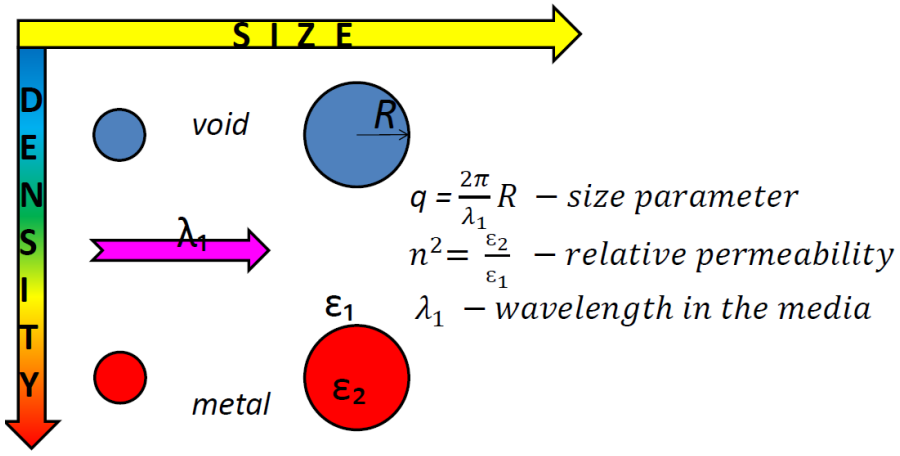

Figure 4.1: Main parameters resulting in different ultrashort laser interaction with nanoparticles.

Nevertheless, till optical changes in dielectric medium are not significant, the initial intensity distribution created by scattering from a single sphere in homogeneous medium is given by the analytical solution of the Mie scattering problem [237]. In general, the electric fields scattered by homogeneous sphere of radius R in spherical coordinates (r, θ, φ) are expressed as infinite sums of the multiplied

electric B^e and magnetic B^m moments, spherical Henkel functions of the first kind and their derivatives, and Legendre polynomials of the first kind, which are functions of kr, q and nq (see appendix), where $k = 2\pi/\lambda_1$ is the wave number in the medium, r is the radial distance from the center of the nanoparticle, $\lambda_1 = \lambda/n$ is the wavelength in the medium with relative permittivity $n^2 = \epsilon_2/\epsilon_1$, $q = 2\pi R/\lambda_1$ is the size parameter, ϵ_1 and ϵ_2 are medium's and nanoparticle's electric permittivities, respectively [237,238]. Therefore, it is reasonable to choose q and n as the main parameters of interest in further investigation [Fig. 4.1].

Simple solutions are known in the near-field $kr \ll 1$ and in the far-field $kr \gg 1$ of the sphere of a nanometric size $q \ll 1$ with relatively low $nq \ll 1$ or high density $nq \gg 1$. In this case, Henkel functions are approximated by their asymptotes, magnetic and electric moments of the second order and higher are negligible [238]. The scattering of light by spheres which are much smaller than the irradiation wavelength is called Rayleigh scattering [238]. The scattering has dipole character and does not depend on the exact shape of particles.

The described approximation of the Mie solution is helpful for analyzing qualitatively the initial static optical response of nanoparticles in dielectric medium. To follow the kinetics of electron plasma generated due to the presence of the embedded nanoparticles, the method based on the nonlinear Maxwell's equations coupled with electron density equation is used in this chapter.

4.2 Role of material optical properties and NP's size

As an example, we consider firstly femtosecond laser interaction with a small spherical gold nanoparticle in fused silica.

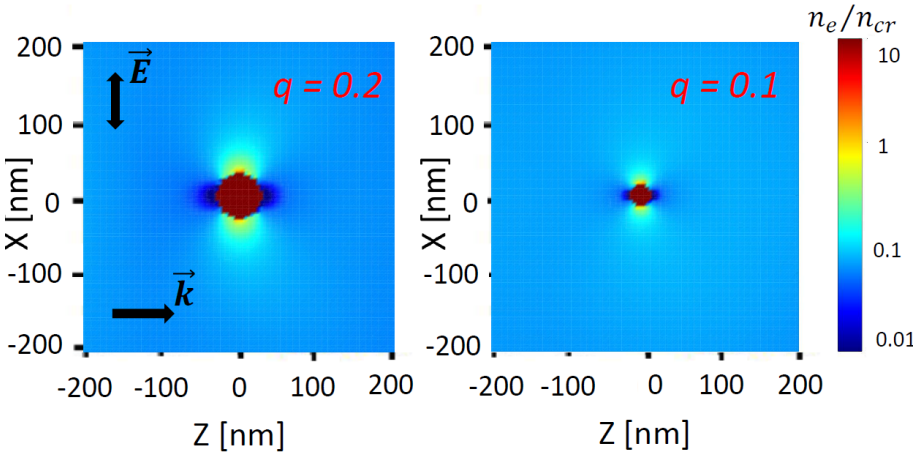

Figure 4.2: Electron density distributions of generated plasma normalized to critical value $n_{cr} = 1.74 \cdot 10^{27} m^{-3}$ after $\lambda = 800$ nm irradiation of gold nanoparticles of different size ($q = 0.2$ and $q = 0.1$) in fused silica at the end of the pulse. The input pulse has the energy of 250 nJ.

A simple analysis based on the electrostatic analytic solution of the scattering problem can already give the qualitative information about the near-field intensity distribution. The local field distribution in the vicinity of the nanoparticle strongly depends on the parameters q and n according to the Mie theory. In the present study, the conditions $q = 2\pi R/\lambda_1 \ll 1$ and $nq \ll 1$ are satisfied, so that the scattering has a dipole character. For instance, for nanoparticles with radius $R \ll 90$ nm the condition is valid at laser irradiation wavelength $\lambda_1 = \lambda/n \approx 550$ nm in fused silica. In the near-field

approximation ($kr \ll 1$), the scattered electric fields can be written in the following form [238]:

$$E_r^{(s)} = -\frac{2icos\varphi sin\theta}{(kr)^3} B_1^e$$
$$E_\theta^{(s)} = \frac{cos\varphi}{kr}\left[\frac{iB_1^e cos\theta}{(kr)^2} + \frac{B_1^m}{kr}\right] \tag{4.1}$$
$$E_\varphi^{(s)} = -\frac{sin\varphi}{kr}\left[\frac{iB_1^e}{(kr)^2} + \frac{B_1^m cos\theta}{kr}\right],$$

where B_1^e and B_1^m and the first order electric and magnetic moments. In what follows, the polarization is along x direction and the light propagation is along z direction. This way, both electric field $\vec{E}$ and wave vector $\vec{k}$ lie in $x0z$ plane (corresponding to $\varphi = 0$). By considering the near-field approximation in this plane and by neglecting the magnetic dipole moments, the intensity distribution can be estimated as

$$I^2 = E_\theta^{(s)} \bar{E}_\theta^{(s)} + E_r^{(s)} \bar{E}_r^{(s)} \approx \frac{(4sin^2\theta + cos^2\theta)(B_1^e)^2}{(kr)^6}, \tag{4.2}$$

where the $\bar{E}$ stands for the complex conjugate values.

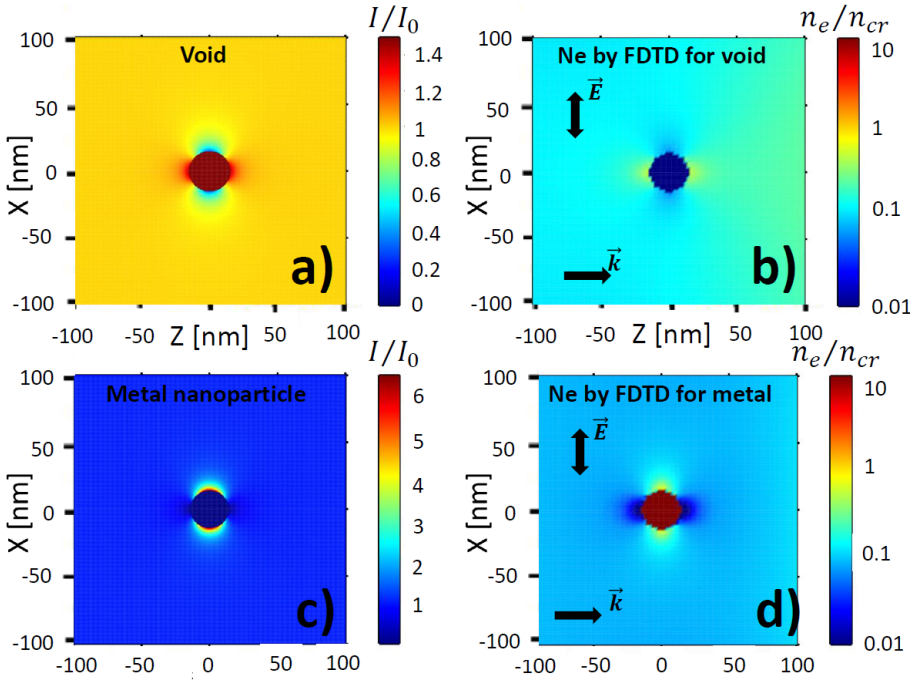

Figure 4.3: (a,c): Near-field approximation of the intensity distribution created by nanovoid (a) and small gold nanoparticle (c) with parameter size $q = 0.2$ given by the analytical Mie solution. (b,d): Electron density distribution of fused silica generated plasma normalized to critical value $n_{cr} = 1.74 \cdot 10^{27} m^{-3}$ at $\lambda = 800$ nm irradiation of void (b) and gold nanoparticle (d) at the end of the pulse (left). The input pulse has the energy of 250 nJ.

From this expression, one can see that the intensity is higher in the x direction ($\theta = \pi/2$) than in the z direction ($\theta = 0, \pi$), creating elliptical distribution of intensities in the near-field of nanoparticle.

In what follows, to find the quantitative distributions of the intensity and the electron density in the vicinity of the nanoparticle, we solve the nonlinear system of Maxwell's equations coupled with electron density equation (2.2,2.19). As the intensity increases, the ionization processes start to play essential role and lead to the generation of plasma in the enhanced intensity regions. The plasma is confined to the interface between fused silica and gold. The calculation results show that free carrier density distribution strictly follows the intensity one (Fig. 4.2). The process of the plasma generation is quite similar for an inhomogeneity of a smaller size, which gives the opportunity to understand what happens in the near-field of very small inhomogeneities considering nanoparticles larger in size but still satisfying the conditions $q \ll 1$ and $nq \ll 1$.

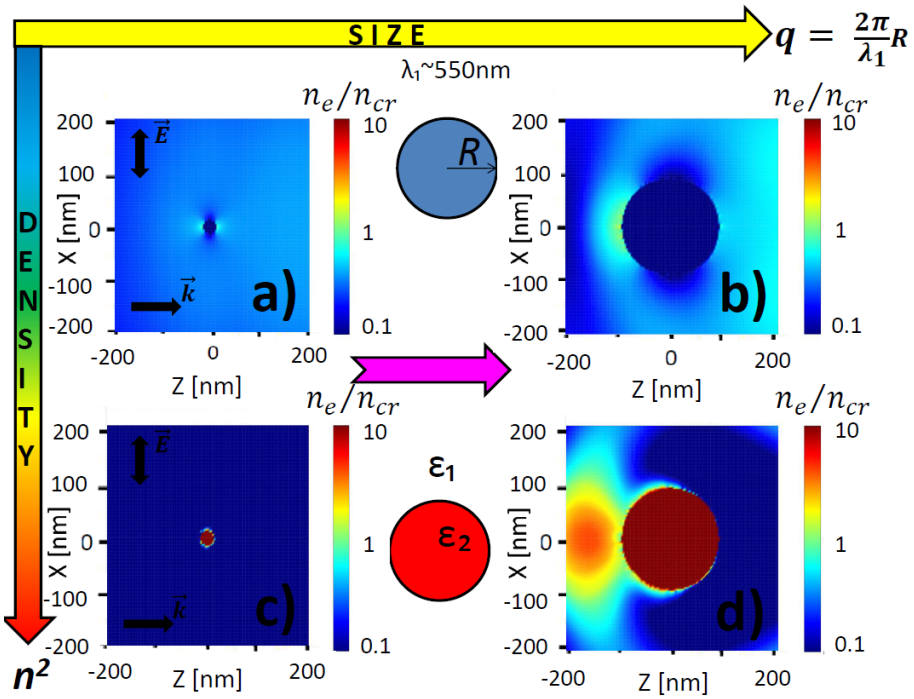

Figure 4.4: Electron density distribution of fused silica generated plasma normalized to critical value $n_{cr} = 1.74 \cdot 10^{27} m^{-3}$ at $\lambda = 800$ nm irradiation of nanovoid (a, b) and gold nanoparticle (c, d) with parameter size $q = 0.2$ (a, c) and $q = 1$ (b, d) at the end of the pulse. The input pulse has the energy of 250 nJ.

Different intensity distributions are expected for nanovoids $\epsilon_2 = 1 < \epsilon_1$ and metallic nanoparticles $\epsilon_2 > \epsilon_1$ embedded in fused silica, with enhancements in the propagation direction z for nanovoids and in the polarization direction x for metallic nanoparticles [Fig. 4.3 (a, c)]. In fact, the resulting distributions could be explained by the analytical Mie solution. The electric moment of a small nanometric spherical inhomogeneity is defined as $B_1^e \approx iq^3 \frac{n^2-1}{n^2+2}$. Therefore, different signs of the resulting scattered electric fields for voids $n^2 < 1$ and metallic nanoparticles $n^2 > 1$ (see appendix) are obtained.

Fig. 4.3 (b, d) shows that the free carrier density distribution calculated by solving (2.2,2.19) after ultrafast laser irradiation of a nanovoid or a nanoparticle has also characteristic enhancements in z or x directions, respectively. Note, that both the intensity enhancement and free carrier density caused by irradiation of a single nanovoid is significantly lower than in the case of metallic nanoparticle.

Free electron densities follow the initial Rayleigh intensity distribution if the ionization is weak and the size of the sphere is considerably small, which requires that the conditions $q \ll 1$ and $nq \ll 1$ are satisfied. In what follows, we investigate the evolution of the electron plasma in case of larger voids and nanoparticles. Fig. 4.4 compares the electron density distributions in the vicinity of small $q \ll 1$ and large $q = 1$ nanoparticles. Strong backward scattering is common for both inhomogeneities of critical size $q = 1$ independent of their nature, which means that these regions are firstly ionized during ultrashort laser irradiation. As in previous case, higher electron densities are generated in the vicinity of gold nanoparticle. We note that this enhancement is no more related to the near-field of the nanoparticle as $kr > 1$ for the critical size $q = 1$. We conclude that for particle sizes larger than a resonant value, defined as $q \approx 1$, the scattered field distribution and therefore, the electron density distributions are no more symmetrically localized close to the nanoparticle-glass interface and have a preferential extrema in the propagation direction.

4.3 Role of optical properties of dielectric media

The optical parameters of the media play a crucial role in the electromagnetic modeling. As frequency dependence of fused silica is described by Drude formalism, the complex permittivity of the media, dependent also on the electronic carrier density, can be written in the following way:

$$\epsilon(n_e) = \epsilon_\infty - \frac{e^2 n_e}{m_e(\omega^2 + \nu_e^2)} + i\frac{e^2 n_e \nu_e}{m_e \omega(\omega^2 + \nu_e^2)}, \tag{4.3}$$

where $\omega = 2\pi c/\lambda$ is the frequency of the irradiated wavelength and ν_e is the electron collision frequency. In several works, the electron collision time $\tau_e = 1/\nu_e$, which in reality depends both on the electron carrier density and on the electron temperature, is assumed to be constant. The values commonly used in the analysis of experimental measurements and in numerical simulations vary from 0.1 fs to 10 fs [129,133,239–242].

The calculations are first performed with $\tau = 0.5$ fs. In addition, two models taking into account for time-varying density-dependent electron collision time dependencies are considered. One possibility is to use the following empirical expression that was proposed in Ref. [242]

$$\tau(t) = \begin{cases} 3.5fs, & n_e(t) \le 5 \cdot 10^{25} m^{-3} \\ \dfrac{16\pi\epsilon_0^2\sqrt{m_e^*(0.1E_g)^3}}{\sqrt{2}e^4 n_e(t)}, & n_e(t) \ge 5 \cdot 10^{25} m^{-3}, \end{cases} \tag{4.4}$$

where $E_g = 9$ eV is the electron band gap and $m_e^* = 0.64 m_e$ is the reduced electron mass. The following model considers the electron collision time inversely proportional to the electron density, taking account the decrease of the time between electron's collision for large laser pulse energies [133].

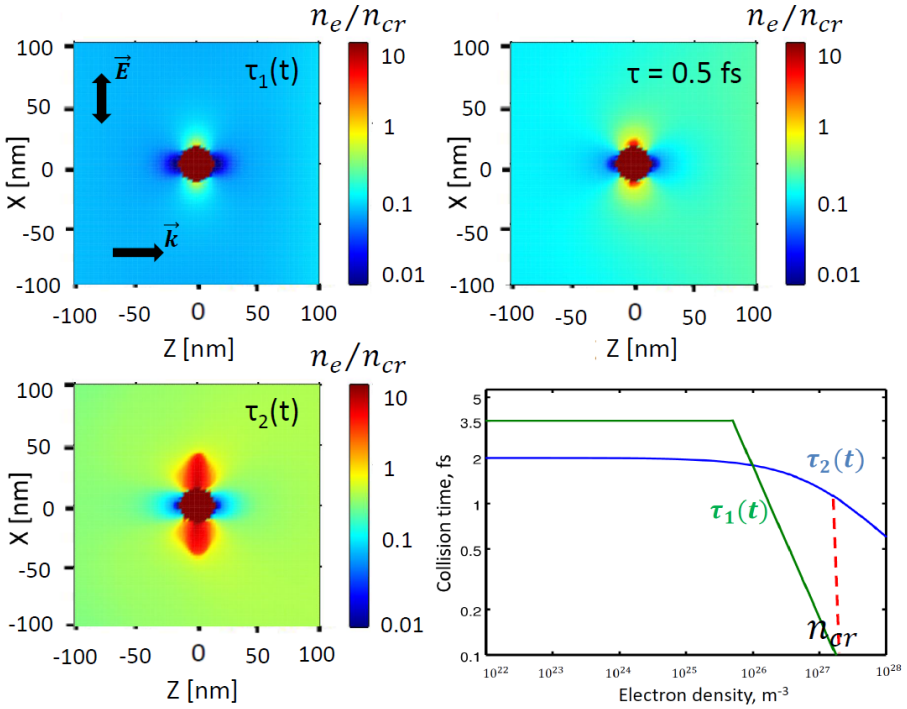

Figure 4.5: Electron density distributions normalized to fused silica critical value $n_{cr} = 1.74 \cdot 10^{27} m^{-3}$ at $\lambda = 800$ nm irradiation in the vicinity of a gold nanoparticle for three different electron collision times models: $\tau_1(t)$, according to (4.4) used in reference [242]; $\tau = 0.5$ fs; $\tau_2(t)$, according to (4.5) proposed in [134]. The input pulse has the energy of 300 nJ. The graph shows $\tau_1(t)$ and $\tau_2(t)$ as the functions of free carrier density.

In dielectric materials electron collision time also depends on electron mobility, so that the following empirical equation is to be checked out:

$$\tau_e(t) = \tau_{min} + \frac{\tau_{max} - \tau_{min}}{1 + (n_e(t)/n_{cr})^\alpha}, \tag{4.5}$$

where $\tau_{min} = 0.2$ fs; $\tau_{max} = 2$ fs; and $\alpha = 0.7$. The maxima and minima of the parameter used in simulations are taken from the work [133], where the calculated reflectivity for different electron collision times is compared with the experimental results. Thus, with growing density smaller values for collision time are obtained, fitting well the experimental independent measurements [89,240,241].

The calculation results obtained by using different parameters, as follows, constant electron collision time $\tau = 0.5$ fs, and empirical relationships (4.4) and (4.5) are shown in Fig. 4.5. One can see that the results obtained by using equation (4.4) are close to the ones obtained for $\tau = 0.5$ fs and reveal smaller effects of the particles, whereas the results calculated by using equation (4.5) demonstrate stronger changes in the field in the vicinity of the particle.

In what follows, we compare the spatial free carrier density distributions of the fused silica plasma generated in the near-field of the gold nanoparticle after the end of the pulse. The higher the collision time is, the closer the properties of the media to the metallic ones, as the real part of the dielectric constant (4.3) is getting closer to its minimum negative value $Re(\epsilon) = \epsilon_\infty - \frac{e^2 n_e}{m_e \omega^2}$. Moreover, one can note, that the electron collision time which corresponds to the near-critical density value plays a crucial role in plasma generation. Thus, in the first proposed empirical model (4.4) $\tau_1(n_{cr}) \approx 0.1$ fs and in the second (4.5) $\tau_2(n_{cr}) \approx 1.1$ fs. These facts explain the differences in the calculation results.

4.4 Far-field interaction

In what follows, we investigate how the presence of the inhomogeneity and the generated plasma in the near-field of the inhomogeneity affects the laser propagation in the far-field.

As in previous cases, we propose to start the qualitative analysis considering the static analytical Mie solution. The scattered electric fields in the far-field approximation ($kr \gg 1$) could be written as [238]

$$\begin{aligned} E_r^{(s)} &= -\frac{2cos\varphi sin\theta}{k^2 r^2} B_1^e exp(ikr) \\ E_\theta^{(s)} &= -\frac{icos\varphi}{kr} exp(ikr)\,[B_1^e cos\theta + B_1^m] \\ E_\varphi^{(s)} &= \frac{isin\varphi}{kr} exp(ikr)\,[B_1^e + B_1^m cos\theta]. \end{aligned} \tag{4.6}$$

As one can note, Mie solution for the far-field $kr \gg 1$ (4.6) differs qualitatively from the near-field solution $kr \ll 1$ (4.1) due to the different asymptotes of Henkel's functions (see appendix). In the near-field of the nanoparticle, the asymptote writes as $\varsigma_1^{(1)}(kr) = -\frac{i}{kr}$, it is non-harmonic function and the electric fields decrease fast in the radial direction, which means that the energy density is concentrated in the vicinity of the nanoparticle. In contrast, the asymptote for the far-field writes as $\varsigma_1^{(1)}(kr) = -exp(ikr)$, which means that the solution is a harmonic function. Henkel function is multiplied by $1/kr$, so anyway the solution decreases in the radial direction but not as fast, as in the case of the near-field electric field approximation.

Because of the interference of the incident wave with the scattered far-field spherical wave, the periodic maxima and minima are organized in the direction of light propagation leading to the regions of the enhanced intensity in Fig. 4.6(a) [134,226]. This phenomenon can be explained by analyzing the far-field dipole approximation of Mie solution (see appendix). We consider, as for the near-field problem, the laser interaction with the inhomogeneity in xz plane, corresponding to $\varphi = 0$. Note, that in this case $E_\varphi^{(s)} = 0$ and in the far-field $E_\theta^{(s)} >> E_r^{(s)}$. Converting the scattered electric field to Cartesian coordinates, it becomes evident that the scattered electric field $E_x^{(s)} \propto E_\theta^{(s)} \propto -iB_1 e \frac{exp(ikz)}{kz}$ interferes with the incident polarization field $E_x^{(i)} \propto exp(-ikz)$ (see appendix). Fig. 4.6(a) shows that the interference results in the organization of the standing wave with the intensity distribution $I \propto \frac{exp(2ikz)}{(kz)^2}$ having maxima and minima in the axis z backward direction separated by $\Delta z = \lambda/2n$. However, the intensity decreases very fast in the radial direction, as $1/r^2$, explaining why local maxima are getting weaker.

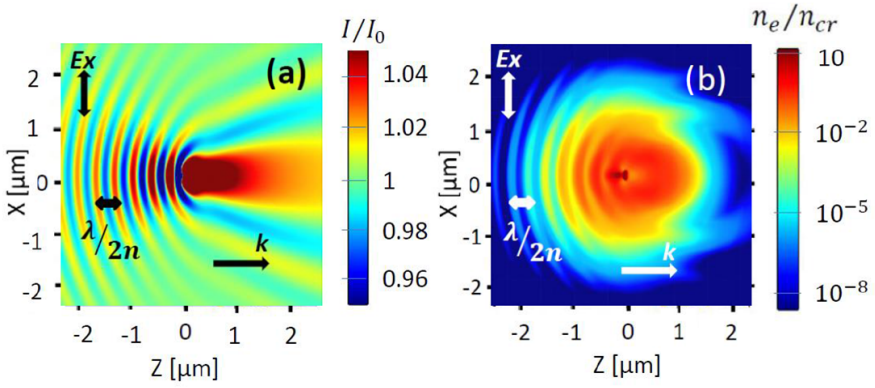

Figure 4.6: (a) Static analytical Mie theory intensity distribution for a small nanoparticle of radius $R = 5$ nm localized in (0,0) (interference between the incident plane wave and the scattered spherical wave).(b) Electron density distribution is calculated by 2D-Maxwell's equations coupled with electron density equation at the peak of 80 fs laser pulse irradiating a single nanoparticle; Here, laser irradiation conditions: pulse duration $\theta = 80$ fs (FWHM), irradiation wavelength in air $\lambda = 800$ nm, pulse energy $E = 300$ nJ. Electron density is normalized to its critical value at 800 nm $n_{cr} = 1.74 \times 10^{27} m^{-3}$ and $\vec{k}$ is the incident laser wave vector.

The free carrier density distribution calculated by solving (2.2,2.19) is shown in Fig. 4.6(b). In the far-field of the nanoparticle, one can clearly see the periodic maxima of the electron density with the interval $\lambda/2n$. Note, that the interference also leads to the organization of the second nanoplasma structure created in backward direction of laser propagation [134], which is explained by stronger backward scattering from larger inhomogeneities, as in Fig. 4.4. The dynamics of the interaction of the laser light with plasma is defined by strong enhancement in the direction backward to the laser propagation and is discussed in details in the next part of this chapter.

We investigate also the far-field scattered fields in the plane yx, perpendicular to laser propagation direction with $\theta = \pi/2$. In this case, $E_\theta^{(s)} = 0$ and in the far-field $E_\varphi^{(s)} >> E_r^{(s)}$. The component of the scattered field can be written in the following way in Cartesian coordinates $E_x^{(s)} \propto E_\varphi^{(s)} \propto -iB_1 \frac{e^{\exp(iky)}}{ky}$ (see appendix). The interference of the incident field with the scattered field results in the spherical periodic intensity distribution with $\Delta = \lambda/n$, enhanced in y direction. Therefore, the enhanced patterns are quasi-parallel to the electric field polarization in yx plane. Note, that the solution is real if $\vec{k}$ is real (non-excited dielectric). In contrast, for a nanoparticle in a metallic media, which is complex, the imaginary solution will result in the intensity decrease in y direction $E_x^{(s)} \propto \exp(-ky)$, and, therefore, the preferential radiation remnants along the polarization. This enhancement contributes to the formation of quasi-perpendicular patterns. The following approach can be used as an approximation to explain the preferential periodic intensity enhancement due to the interference of the incident field with the scattered field from the nano-inhomogeneity on/near the dielectric/metallic surface if the light propagates on the surface. The ultrashort laser interaction with fused silica rough surface will be discussed in the next chapter.

4.5 Evolution from a single inhomogeneity to a nanoplane

Here, we consider the nonlinear dynamics of further interaction of ultrashort laser pulses with the generated plasma. Interestingly, electron density profiles calculated around single inhomogeneities of different nature (nanovoid $\epsilon_2 = 1$ or metallic nanoparticle) already reveal a remarkable plasma elongation backwards in the direction perpendicular to laser polarization in Fig. 4.7. Note, that the process is very rapid and nonlinear. In addition, local field enhancement leads to sufficiently high intensities, so that the multiphoton ionization starts playing a crucial role changing the refractive index of the medium. Therefore, changes both in scattering and in absorption characteristics of the medium also take place.

In the near field of the nanoparticle, where $r \ll \lambda/2\pi n$, the intensity is strongly enhanced. One

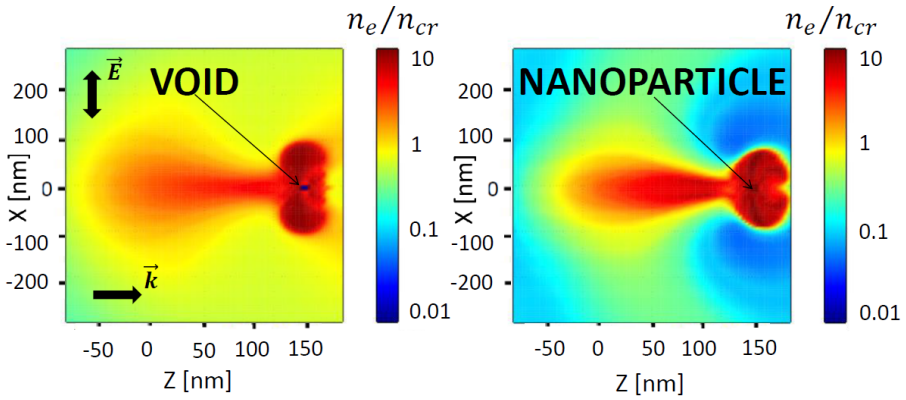

Figure 4.7: Electron density distributions are calculated by coupled 2D-FDTD demonstrating the electron plasma growth due to the presence of a single nanovoid and a single metallic nanoparticle of radius $R = 5$ nm in fused silica localized in $(0.15,0)\mu m$ at the pulse peak. Laser irradiation conditions: pulse duration $\theta = 120$ fs (FWHM), irradiation wavelength $\lambda = 800$ nm, pulse energy $E = 2\mu J$ and $\tau = 10$ fs for a nanovoid and $E = 500$ nJ and $\tau = 0.5$ fs for metallic nanoparticle. Here and further, electron density is normalized to its critical value at 800 nm $n_{cr} = 1.74 \times 10^{27} m^{-3}$ and $\vec{k}$ is the incident laser wave vector.

can thus expect that multiphoton ionization is also higher in these areas. The enhancement as well as the initial intensity distribution are different for inhomogeneities of different nature (see Fig. 4.3). For voids, or for inhomogeneities with an enhanced ionization cross section [82], the scattering is weaker than for metallic nanoparticles or high-density plasma nanospheres with reduced ionization cross section. In the case of the nanospheres with the reduced bandgap, high-density plasma is confined inside the nanospheres making them quasi-metallic scattering centers responsible for further elongation and formation of the nanoplane perpendicular to laser polarization. In the case of voids/inhomogeneities with higher bandgap, which are more difficult to ionize, the nanoplane elongation is possible if the quasi-metallic plasma is generated in the vicinity of the inhomogeneities due to the intensity enhancement in the near-field of the scattering centers. For instance, the growth of the nanoplane from a void could be drastic if the optical properties of the medium are very sensible to the intensity of the irradiation, which is the case of fused silica (six-photon ionization cross section). The results of numerical calculations in Fig. 4.7 with a single void and with a high-density inhomogeneity demonstrate, that in spite of different nature of the inhomogeneities, initial intensity distribution and different parameters, the physics of the nanoplasma formation is qualitatively the same in both cases. It is related to the fact that after a thin plasma layer with metallic properties $Re(\epsilon) < 0$ is generated in the near-field of the initial nanosphere, further plasma generation is guided only by scattering from already organized plasma independent of the initial inhomogeneity nature. This means that the physics discussed in this chapter is applicable to any kind of initial inhomogeneities of the size rather smaller than the irradiation wavelength.

If the condition $r \ll \lambda/2\pi n$ is satisfied, the intensity distribution near nanometric laser-induced inhomogeneity is enhanced only in the direction of the electric field polarization. Fig. 4.8(a) shows that plasma generated due to this enhancement has roughly an ellipsoid form. Interestingly, the size of the resulting ellipsoid depends only on the irradiation wavelength and optical parameters of the media, but not on the initial NP's size. As the plasma dimension overcomes the laser wavelength range, the growth slows down and the backward scattering starts playing an essential role [Fig. 4.8(b)]. Such change in the scattering behavior, related to the resonance is the size of the inhomogeneity ($kr \approx 1$ in terms of Mie scattering) [243] enables nanoplane elongation in the backward propagation direction [Fig. 4.8(c)].

In the far-field $r \gg \lambda/2\pi n$, the interference between the incident and the scattered wave leads to the organization of periodic standing spherical waves, with intensity proportional to $1/r^2$ and with a period $\lambda/(2n)$ in the backward propagation direction [Fig. 4.8(a)]. This effect can be also observed for larger inhomogeneities consisting of quasi-metallic plasma as in Fig. 4.8(b) and even for long nanoplanes acting as nanoantennas with reflectivity maxima at half-integer wavelength in the me-

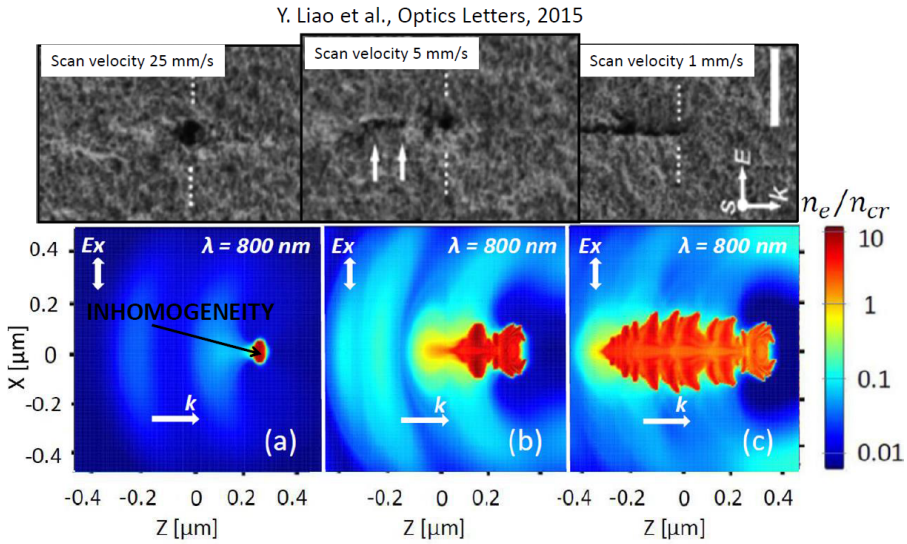

Figure 4.8: Electron density snapshots are calculated by coupled 2D-FDTD demonstrating the evolution from a single inhomogeneity of radius $R = 5$ nm localized in $(0.3,0)\mu m$ to nanoplane taken at (a) 40 fs before the pulse peak, (b) at the pulse peak, (c) 40 fs after the pulse peak. Laser irradiation conditions: pulse duration $\theta = 120$ fs (FWHM), irradiation wavelength $\lambda = 800$ nm, pulse energy $E = 300$ nJ. Here and further, electron density is normalized to its critical value at 800 nm $n_{cr} = 1.74 \times 10^{27} m^{-3}$ and $\vec{k}$ is the incident laser wave vector. SEM images are taken from Ref. [18] at different scan velocities. Experimental details: pulse energy 50 nJ, pulse duration 100 fs at central wavelength 800 nm, repetition rate 250 KHz and focusing conditions $NA = 1.1$. Scale bar $1\mu m$.

dia [82]. Although the enhancement in the far-field backward propagation direction is rather weaker than in the near-field and quickly decreases with r, Fig. 4.8(b) shows that it is possible to ionize the nearest enhanced regions by multiphoton absorption mechanism. As a result, the second nanoplasma structure is formed in the backward propagation direction. It affects the light propagation in a similar way. Fig. 4.8(c) clearly demonstrates that such incubation process results in the formation of a nanoplane elongated in the backward propagation direction perpendicular to the laser polarization. As the nanoplane is already formed, the process is now guided mostly by the near-field intensity enhancement at the tip of the nanoplasma [44], leading to further elongation in the direction perpendicular to laser polarization. The length of the resulting nanoplasmas depends on the pulse duration and on the laser pulse energy, however, the final width in the polarization direction is independent of these parameters. High-fidelity visualization in fused silica confirms experimentally the evolution mechanism from a single inhomogeneity to nanocrack [18]. Only qualitative comparison is possible in Fig. 4.8 as the calculations indicate the temporal electron density evolution during one pulse duration, whereas the SEM images show the nanocrack growth on the shot-to-shot basis.

4.6 Conclusions

In this chapter, we have investigated numerically nanoplasma formation near inhomogeneities of different size and density due to local field enhancement during femtosecond laser irradiation by solving the system of nonlinear Maxwell's equations coupled with electron density equation. As an example, fused silica is taken as a dielectric medium, spherical nanovoid with the dielectric constant $\epsilon = 1$ and spherical gold metallic nanoparticle are considered as inhomogeneities.

At the initial stage of ionization, the spatial electron density distribution follows the intensity distribution, which could be qualitatively predicted by electrostatic analytical Mie solution. Different configurations of intensity and electron density distributions are shown in the near-field of a small metallic nanoparticle and a small nanovoid ($q \ll 1$). For inhomogeneities of bigger size ($q = 1$) and different density, the backward scattering results in the regions of high intensity enhancements. In the far-field of inhomogeneities, the interference between the plane incident wave and the spherical

scattered wave leads to the organization of periodical spatial minima/maxima of the intensity and of the electron density.

At later stages of ionization, the dynamics of femtosecond laser irradiation could not be described any more by electrostatic approach. It is shown that the transient properties of the material surrounding the inhomogeneity strongly impact the distribution and the size of the generated plasma. Therefore, collisional frequency and irradiation conditions are the parameters which are crucial for electromagnetic modeling. Two different models taking into account the electron density dependence of the collision frequency are investigated giving different resulting spatial electron density configurations.

Finally, it is shown that further ultrashort laser irradiation of inhomogeneities results in the nanoplasma growth backwards to the laser propagation and perpendicular to laser polarization. The dynamics of the laser-matter interaction is defined by the optical properties of the medium but has similarities in the case of the inhomogeneities of different densities.

4.7 Appendix: Elements of Mie scattering by homogeneous sphere

The electric fields scattered by homogeneous sphere in spherical coordinates (r, θ, ϕ) can be written as follows [237, 238]

$$\begin{cases} E_r^{(s)} = \dfrac{cos\phi}{k^2 r^2} \displaystyle\sum_{l=1}^{\infty} l(l+1) B_l^e \varsigma_l^{(1)}(kr) P_l^{(1)}(cos\theta) \\ E_\theta^{(s)} = -\dfrac{cos\phi}{kr} \displaystyle\sum_{l=1}^{\infty} \left(B_l^e \varsigma_l^{(1)\prime}(kr) P_l^{(1)\prime}(cos\theta) sin\theta - i B_l^m \varsigma_l^{(1)}(kr) P_l^{(1)}(cos\theta) \dfrac{1}{sin\theta} \right) \\ E_\phi^{(s)} = -\dfrac{sin\phi}{kr} \displaystyle\sum_{l=1}^{\infty} \left(B_l^e \varsigma_l^{(1)\prime}(kr) P_l^{(1)}(cos\theta) \dfrac{1}{sin\theta} - i B_l^m \varsigma_l^{(1)}(kr) P_l^{(1)\prime}(cos\theta) sin\theta \right), \end{cases} \tag{4.7}$$

where B_l^e and B_l^m are electric and magnetic dipole moments, k is the wave vector in the medium, $\varsigma_l^{(1)}(kr)$ are the spherical Henkel functions of the first kind, and $P_l^{(1)}(cos\theta)$ are Legendre polynomials of the first kind. Additionally, the fields have a time dependence factor $exp(-i\omega t)$ that has been suppressed in the above equations.

The asymptotes for Henkel functions are as follows

i) Near-field ($kr \ll 1$): $\varsigma_1^{(1)}(kr) = -\frac{i}{kr}$ and $\varsigma_1^{(1)\prime}(kr) = \frac{i}{(kr)^2}$.

ii) Far-field ($kr \gg 1$): $\varsigma_1^{(1)}(kr) = -exp(ikr)$ and $\varsigma_1^{(1)\prime}(kr) = -i \cdot exp(ikr)$.

Small size approximations ($q \ll 1, nq \ll 1, l = 1$): $B_1^e = iq^3 \frac{n^2-1}{n^2+2}$, $B_1^m = iq^5 \frac{n^2-1}{30}$, $B_l^e \to 0$, $B_l^m \to 0$, $l > 1$.

For small metallic nanoparticle ($q \ll 1, nq \gg 1, l = 1$): $B_1^e = iq^3$, $B_1^m = i\frac{q^3}{2}$, $B_l^e \to 0$, $B_l^m \to 0$, $l > 1$.

Legendre polynomials for $l = 1$: $P_1^{(1)}(cos\theta) = sin\theta$ and $P_l^{(1)\prime}(cos\theta) = -\frac{cos\theta}{sin\theta}$.

The scattered electric fields in Cartesian coordinate system:

$$\begin{cases} E_x^{(s)} = E_r^{(s)} sin\theta cos\phi + E_\theta^{(s)} cos\theta cos\phi - E_\phi^{(s)} sin\phi \\ E_y^{(s)} = E_r^{(s)} sin\theta sin\phi + E_\theta^{(s)} cos\theta sin\phi + E_\phi^{(s)} cos\phi \\ E_z^{(s)} = E_r^{(s)} cos\theta - E_\theta^{(s)} sin\theta. \end{cases} \tag{4.8}$$

Chapter 5

Investigation of periodic nanostructure formation in glass

In this chapter, we present numerical insights in ultrashort laser-induced nanostructuring modeling. Particularly, the mechanism of self-organized nanograting formation is investigated by a numerical approach based on Maxwell's equations coupled with free carrier density equation and previously described in Chapter 2 and Chapter 3. It is shown that randomly distributed nanoscale inhomogeneities significantly affect the light propagation, resulting in the formation of periodically arranged nanoplasmas. The influence of laser parameters such as laser pulse energy, laser wavelength, laser polarization, as well as the influence of the inhomogeneity concentration and concentration profiles on the resulting characteristics of the nanoplasmas are numerically investigated. For a first time, a correlation of the concentration of inhomogeneities with the number of laser pulses is demonstrated, and an explanation of the pulse number effect on the nanograting periodicity is proposed. The physical origin of the self-organization is discussed in details, and a multipulse feedback mechanism is proposed to explain the growth of nanoplasmas consisting of nanovoids during multipulse laser irradiation. The similarity between surface nanostructuring and bulk nanostructuring is discussed. Finally, the obtained calculation results are compared with numerous independent experimental findings.

5.1 Transient nanoplasmonics of laser-induced inhomogeneities

In this part, the particularities and the assumptions of the considered model are discussed in details.

In the previous chapter, the evolution from a single inhomogeneity to a nanoplane has been discussed. Taylor et al. proposed that the origin of self-organized nanogratings could be explained by a so-called transient nanoplasmonics model [39], in which the nanoplasmas grew periodically pulse by pulse from the hot-spots organized inhomogeneously around defects or color centers as shown in Fig. 5.1(a-d). Later, electron density kinetics in glass containing tiny voids was firstly considered and a certain periodicity of electron density profiles was revealed [82]. We propose also that the physical origin of nanograting self-organization is the result of the electrodynamic processes and electron plasma evolution which take place during the laser pulse in the dielectric medium containing nanoscale inhomogeneities. Therefore, we investigate the mechanism of formation by numerical approach based on Maxwell's equations coupled with time-dependent carrier density equation detailed in Chapter 2 and Chapter 3 to describe the electron dynamics on nanoscale. In the equation, the complete Keldysh ionization rate takes into account multiphoton and tunneling effects and multiple rate equation is considered to estimate accurately the contribution of the avalanche ionization. The model is used to investigate the evolution of the electron density distribution during the pulse irradiation by Gaussian ultrashort laser beam, where initially a smooth distribution of nanoscale inhomogeneities simulating the bulk nanoroughness is introduced. The randomly distributed inhomogeneities with different initial concentrations correspond to the state of the laser-induced fused silica after different number of pulses. During femtosecond laser pulse irradiation, the electron density distribution evolves because of the ionization processes driven by inhomogeneous intensity distribution, resulted from local field enhancements around the inhomogeneities and strong interference effects from the inhomogeneity scattered waves.

An example of maximum three-dimensional electron density distribution as a result of the numerical calculation based on nonlinear Maxwell's equations coupled with the free carrier rate equation is shown in Fig. 5.1(e). Remarkably, the spatial distribution is quasi-periodical and polarization-dependent.

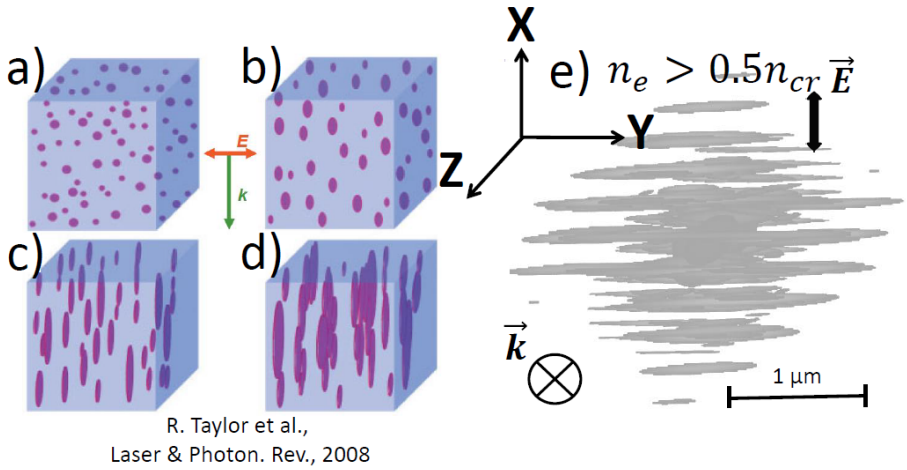

Figure 5.1: (a-d) Transient nanoplasmonics model is demonstrated schematically [39]. (e) Maximum electron density distribution ($n_e > 0.5n_{cr}$) calculated by coupled 3D-FDTD with initial randomly distributed inhomogeneities. Laser irradiation wavelength $\lambda = 800$ nm. The average initial distance between the inhomogeneities is $d = 70$ nm.

For simplicity, firstly we consider nano-regions with a reduced ionization potential to be inhomogeneities formed as a result of multiple laser interactions. Then, a multipulse feedback mechanism with a threshold for nanovoids formation is proposed, generalizing the previously obtained results. The inhomogeneities are initially set to be spheres of $5-10$ nm radius of the dielectric material. The electromagnetic field in these regions is modeled by resolving the same system of equations (2.2,2.23) with a narrower electron band gap $E_g = 5.2$ eV [61, 130, 244, 245]. As long as the size of the inhomogeneity is considerably smaller than the irradiation wavelength, the initial plasma generation follows the Rayleigh scattering distribution [134]. The dynamics of the femtosecond laser interaction with such inhomogeneities is qualitatively the same giving the opportunity to simulate up to $a = 10$ nm nanospheres for $\lambda = 800$ nm [82, 134]. The laser-induced inhomogeneity concentration increases with the number of pulses due to nonlinear ionization memory [246] or glass decomposition processes, which take place on longer timescales and are discussed in Chapter 6. Therefore, we investigate the resulting electron density distribution by laser irradiation of randomly distributed inhomogeneities with different initial concentration corresponding to the state of laser-induced fused silica after several pulses. In fact, such an approach allows me not only studying the pulse number effect on the nanograting characteristics but also modeling of initially slightly doped fused silica with corresponding concentrations of inhomogeneities [23, 109, 110].

In this part, the terms "nanogratings", "nanoplanes" or "nanostructures" designate only free carrier density profile. The experimental evidence of the electron density influence on the formation of the final structure can be found in [246–249].

In what follows, the initial Gaussian electric field profile is considered as a focused beam source with the beam waist from $w_0 = 1\mu m$ up to $w_0 = 3\mu m$ and the numerical aperture $NA = \sin(\frac{\lambda}{\pi w_0})$ for irradiation wavelength from $\lambda = 400$ nm up to $\lambda = 1200$ nm relatively not high, for which the paraxial approximation of the Gaussian beam's profile is still valid [74, 130]. Pulse width at half maximum (FWHM) is varied from $\theta = 80$ fs up to $\theta = 240$ fs. For such ultrashort pulses, ionization takes place before thermal effects such as heat diffusion occur [250], thus, the numerical model, neglecting the electron-lattice exchange, is able to describe the modification in dielectric during the pulse duration. Recent thermo-elastoplastic modeling of laser-matter interaction has shown that the final modification structure is imprinted into bulk glass already at sub-nanosecond timescale [75], which is less than common interval between two femtosecond pulses in experiments. These results can be supported by time-resolved diffraction measurements [251].

First, we report the results of 2D-FDTD modeling of the TM-polarized mode. Thus, all the resulting snapshots of the electric fields, intensity and electron density are in the plane xOz, where the focused beam is polarized along x direction and z is the propagation direction. Then, numerical results of 3D-FDTD modeling are presented and discussed.

5.2 Nanograting organization from random inhomogeneities

By using previously proposed idea of the pulse to pulse memory [246], we consider several distributions of the laser-generated inhomogeneities, as shown in Fig. 5.2. First, there are regions modified and unmodified by the previous laser pulse with an evident interface between them as it was experimentally reported in [18,97]. Second, the inhomogeneities can be uniformly distributed. And finally and more realistically, there is a smooth gradient concentration profile.

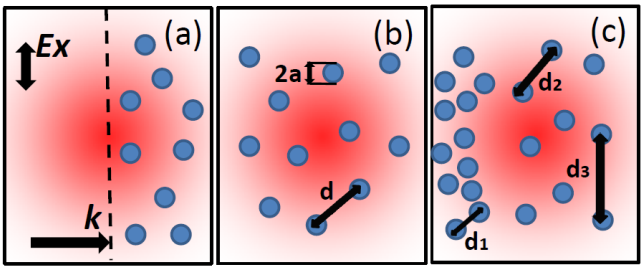

Figure 5.2: Schematic representation of three possibilities of localization of laser-induced inhomogeneities before irradiation by femtosecond laser focused beam: (a) with interface between modified and unmodified regions, (b) with homogeneous concentration, (c) with variable concentration ($d_1 < d_2 < d_3$). d is the average distance between the centers of the nanospheres and a is the nanosphere radius.

5.2.1 Sharp interface

Let us consider the first case. To analyze how the nanoplanes evolve in the presence of a sharp interface between concentration profiles, we divide the calculation volume in two regions: unmodified, without any initial inhomogeneities, and modified, with randomly distributed inhomogeneities. Electron density snapshots taken during the pulse duration reveal the temporal evolution of nanoplanes (Fig. 3). Similar behavior was reported in experiments [18,97]. The interference between the incident and scattered waves and incubation process induced by multiphoton ionization lead to the organization of first nanoplanes from the laser-induced interface. If there are few laser-induced inhomogeneities, each nanoplane grows strictly from its seed. Fig. 5.3(a) shows, however, that several periodic intensity patterns are obtained in the region free of inhomogeneities near the interface if the concentration of inhomogeneities is increased. Nanoplasmas start following these intensity enhancements, elongating perpendicular to the laser polarization with a common period of λ/n in Fig. 5.3(b,c). Further, we refer to this kind of nanogratings as low-frequency nanogratings (LFNGs). Moreover, in the region with initially localized inhomogeneities, corresponding to the second configuration in our numerical investigation, the structures with the periodicity twice smaller are organized, high-frequency nanogratings (HFNGs). Only qualitative comparison is possible with the experimental SEM images shown in Fig. 5.3, because the calculation results indicate the temporal electron density evolution during one pulse duration, whereas the SEM images show the periodic nanostructure formation and growth on the shot-to-shot basis.

To demonstrate the effect of the irradiation wavelength on the periodicity of LFNGs and HFNGs, Fig. 5.4 shows electron density profiles calculated for three laser wavelengths frequently used in the experiments with femtosecond lasers [14,16,18,39,95,97,252]. One can see that the periodicity of the self-organized nanoplanes is proportional to λ, in agreement with several experimental observations [16, 44]. Interestingly, the nanoplanes become thicker with the increasing irradiation wavelength. Firstly,

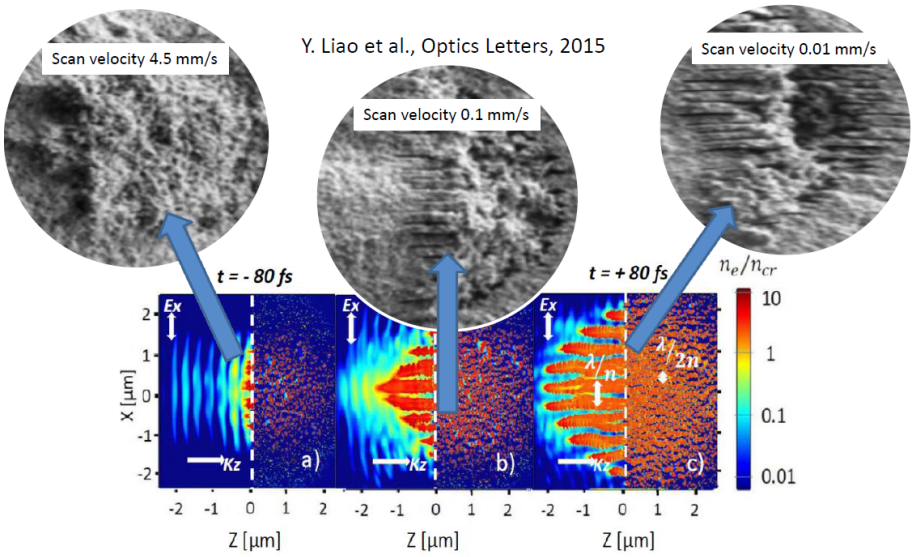

Figure 5.3: Electron density snapshots are calculated by coupled 2D-FDTD (2.2, 2.23) revealing the evolution of nanogratings (a) 80 fs before the pulse peak, (b) at the pulse peak, (c) 80 fs after the pulse peak. Laser irradiation conditions: pulse duration $\theta = 240$ fs (FWHM), irradiation wavelength $\lambda = 800$ nm, pulse energy $E = 500$ nJ. The line separates the region with initially localized nanospheres (modified) and the region, initially free from any inhomogeneities (unmodified). The schematic representation of the initial distribution of inhomogeneities is shown in Fig. 5.2(a). The concentration of the initial inhomogeneities of $r = 5$ nm in the right part of the volume is $C_i = 1\%$. SEM images are taken from Ref. [18] at different scan velocities. Exp. details: laser pulse energy is $1.2\mu J$, pulse duration 100 fs at central wavelength 800 nm and repetition rate 250 kHz, focusing conditions $NA = 1.1$.

we explain the physical origin of LFNGs. Secondly, we will focus on HFNGs, the structures with smaller periodicity.

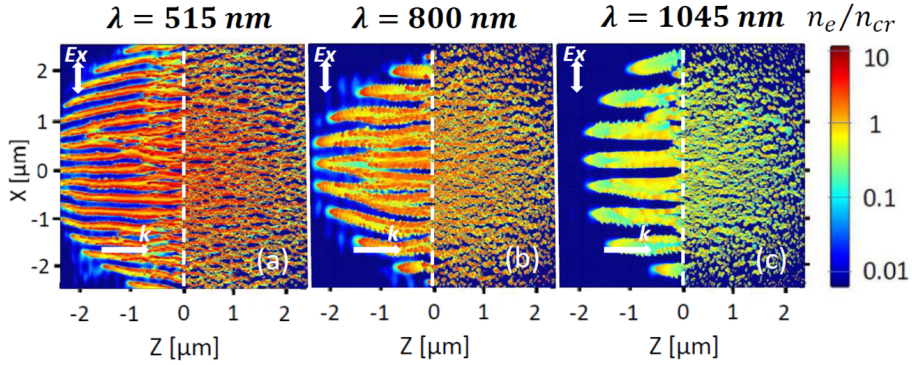

Figure 5.4: Electron density snapshots are calculated by coupled 2D-FDTD (2.2, 2.23) suggesting that nanograting period is proportional to the irradiation wavelength: (a) $\lambda = 515$ nm, (b) $\lambda = 800$ nm, (c) $\lambda = 1045$ nm. Here, electron density is normalized to its critical value at 800 nm $n_{cr} = 1.7 \times 10^{27} m^{-3}$. Laser irradiation conditions: pulse duration $\theta = 240$ fs (FWHM) and corresponding pulse energies (a) $E = 400$ nJ, (b) $E = 500$ nJ, (c) $E = 600$ nJ. Snapshots are taken 80 fs after the pulse peak. The line separates the region with initially localized nanospheres (modified) and the region, initially free from any inhomogeneities (unmodified). The schematic representation of the initial distribution of inhomogeneities is shown in Fig. 5.2(a). The concentration of the initial inhomogeneities of $r = 5$ nm in the right part of the volume is fixed to $C_i = 0.5\%$ for all wavelengths (a-c). Note, that for each wavelength, different corresponding parameters are used for multiple rate equation (2.23) and Keldysh photoionization rate w_{pi}.

Periodic structures formed at rough interface between two media is usually associated with an

interference between the incident wave and the scattered waves [80]. This interference causes periodic energy deposition [76, 79]. In addition, an interference of the incident wave with the excited surface plasmon polaritons also leads to an enhancement of surface periodic structure formation under the conditions required for the surface plasmons [253–256]. Moreover, both scenarios were used to explain VNG formation [91,97,98]. Here, to elucidate the mechanism of the periodic organization of LFNGs, we study the role of each nonlinear current from the system of equations (3.27). The performed calculations demonstrate, that the nanoplanes are formed even for $J_{Kerr} = 0$, $J_{pi} = 0$ and $J_{Dz} = 0$. The last condition means that the electron oscillation along the axis z is neglected. In this case, the fields E_x and E_z can be directly separated if the intensity is given as $I = \frac{n}{2}\sqrt{\frac{\epsilon_0}{\mu_0}}{E_x}^2$. Hence, electron density changes only due to the field component E_x. The periodicity of these nanoplanes is independent of the collision frequency of excited fused silica ν_e and periodic intensity patterns appear even for the case of non-excited surface plasmons $Re(\epsilon) > -n^2$ [255,256], where ϵ is dielectric permittivity defined by the Drude formalism. This fact suggests, that the organization of LFNGs here is due to interface roughness. Furthermore, several phenomena contribute to the periodic nanoplane evolution: excitation of surface plasmon wave, scattering from the already organized elongated nanoplasmas, interference between the scattered waves from several laser-induced inhomogeneities and backward scattering from a system of randomly distributed inhomogeneities.

5.2.2 Smooth concentration profile

Now, let us turn to a more general case of a smooth concentration profile, distributing randomly inhomogeneities in the entire numerical volume. Fig. 5.5 reveals that nanograting formation process depends on the inhomogeneity concentration in this case. To describe the influence of the inhomogeneities on the nanoplane periodicity, we propose to define the average distance between two initial nanospheres as $d = 1/\sqrt{C_i}$, where $C_i = N/S$ is the concentration of inhomogeneities, N is the number of the inhomogeneities in the laser-induced area S. The interference between multiple scattered waves from randomly distributed inhomogeneities strongly depends on this parameter. For widely separated nanospheres, the interference between the incident and the scattered fields dominates over all other plasmonic modes. If particle dimensions are much smaller than the wavelength, the interference effect is negligible but inter-particle coupling becomes significant, enabling high local concentration of electromagnetic energy in the vicinity of the interfaces of nearly touching nanoplasmas.

If there are very few nanospheres, so that $d > \lambda/n$ ($C_i < 0.05\%$), each inhomogeneity acts as a seed for one nanoplasma and they are elongated randomly in the grid as shown in Fig. 5.1(c). For higher concentration and if $\lambda/2n < d < \lambda/n$ ($0.05\% < C_i < 0.5\%$) as in the case of pure dielectric with the seeds at its interface, the nanoplasmas elongate perpendicular to the laser polarization direction from the laser-modified inhomogeneities and the dominant period is close to λ/n due to the described interference mechanism leading to the organization of LFNGs [Fig. 5.5(a,d)]. However, the mechanism of the organization changes dramatically for larger concentration of inhomogeneities. This effect is due to the mutual enhancement induced by multiple scattering from nanoplasmas that becomes dominant over the interference between the incident and the scattered fields.

Electron density snapshots demonstrate the temporal evolution of HFNGs from randomly distributed initial inhomogeneities in Fig. 5.2. The organization of HFNGs is completely different from LFNG formation. Even at the pulse peak no periodicity can be revealed yet. Nanoplasmas develop from random inhomogeneities into well-ordered patterns consequently, controlled by strong local field enhancement. From the Fourier transform of the electron density snapshot taken at the end of the pulse [Fig. 5.5(e)], one can see that the dominant period is close to $\lambda/(2n)$. The periodicity does not depend on the laser energy density, which is the highest in the center and decreases towards the edge of the focal region as a Gaussian distribution. Note, that several phenomena contribute to the observed period reduction such as intensity enhancement due to multiple scattering from the nanospheres, intensity enhancement between two organized nanoplasmas [54,98,257] and half-wavelength cavity feedback [91]. If the inhomogeneity concentration is increased, nanoplasmas tend to merge together. Fig. 5.5(c,f) shows that self-organized nanogratings are separated by $\lambda/(3n)$. At larger concentration, there is no more dominant characteristic period. This fact is due to a very short average distance between the initial nanospheres, as $d \approx 50 - 100$ nm ($C_i \approx 5\%$). The plasma is organized by femtosecond laser

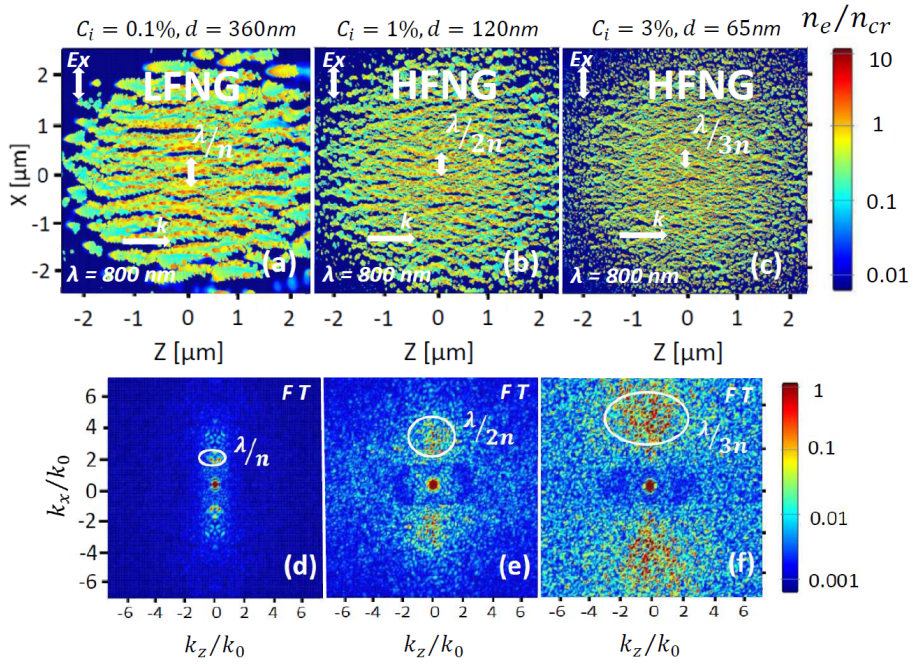

Figure 5.5: (a-c) Electron density snapshots are calculated by coupled 2D-FDTD (2.2, 2.23) at the end of the pulse duration $\theta = 240$ fs (FWHM) for different initial concentration of randomly distributed inhomogeneities of $r = 5$ nm and (d-f) Fourier Transform (FT) of the images: (a) and (d) $C_i = 0.1\%$, (b) and (e) $C_i = 1\%$, (c) and (f) $C_i = 3\%$. The wave numbers k_z and k_x are normalized to the norm of the incident wave number $k_0 = 2\pi/\lambda$. The pulse energy is fixed to $E = 500$ nJ. The irradiation wavelength is 800 nm. The schematic representation of the initial distribution of inhomogeneities is shown in Fig. 5.2(b).

irradiation of such inhomogeneities and occupies all the gaps between inhomogeneities. Thus, VNGs spaced by less than $\lambda/4n$ are out of the scope of the present modeling.

To identify the physical phenomenon responsible for the organization of HFNGs, as in the previous case, we study the contributions of nonlinear currents in nanograting formation from the system of equations (3.27). Firstly, we check that J_{Kerr} and J_{pi} do not influence the physical process. Secondly, we perform calculations with $J_{Dz} = 0$ to check whether the role of electron oscillations along the axis z is negligible. In this case we observe no periodic organization. The electron density snapshots in Fig. 5.6 reveal that even for high concentration, the inhomogeneities do not interact creating nanoplanes elongated perpendicular to the laser polarization. We underline that the same procedure of switching off the J_{Dz} component in the case of LFNGs does not destroy the self-organization process. It means that different physical processes are responsible for creating LFNGs and HFNGs. This numerical result can be explained by the different local field response of the inhomogeneities, when $J_{Dz} = 0$ is assumed. In fact, in this case, the material responds in the propagation direction z with $\epsilon_z = n^2$ (non-excited dielectric), which excludes the quasi-metallic properties of the inhomogeneity and does not result in the formation of the final elongated nanoplasma. This observation supports the role of local field effects in the formation of HFNGs.

5.2.3 Smooth gradient profile

Finally, to demonstrate the influence of concentration on the nanograting period, we consider the third case with a smooth gradient profile. The results shown in Fig. 5.7 are obtained by varying the average distance between initial nanospheres from 50 nm to 500 nm in space along the axis z. Electron density reveals changes in the nanograting periodicity and thickness corresponding to initial local concentration of inhomogeneities. LFNGs with period of λ/n do not have initially the interface with modified region and grow in the backward propagation direction. Therefore, the resulting structure formation is not related to the surface wave excitation as it was suggested in [97,98]. Instead, it is an

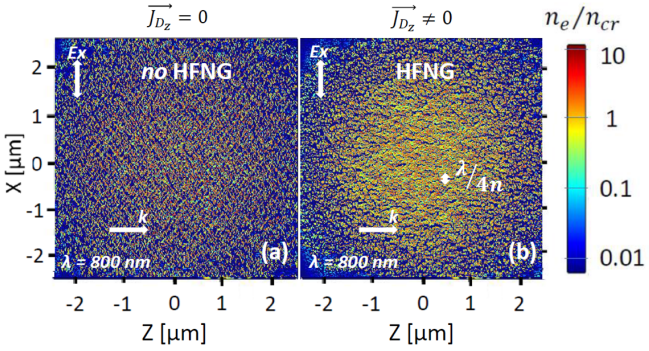

Figure 5.6: Electron density snapshots are obtained by coupled 2D-FDTD (2.2, 2.23) assuming a) $J_{Dz} = 0$ and b) $J_{Dz} \neq 0$ at the end of the pulse duration $\theta = 240$ fs (FWHM), laser irradiation of 800 nm and pulse energy of 500 nJ with initial concentration of inhomogeneities $C_i = 9\%$. The schematic representation of the initial distribution of inhomogeneities of $r = 5$ nm is shown in Fig. 5.2(b).

entirely volume effect as it was previously underlined by Buschlinger et al. [82]. If the gradient of the concentration is reversed, the nanostructures correspond again to the initial concentrations. Thus, the physical origin of sub-wavelength self-organized structures is connected to the stationary wave induced either by the interference of the incident and inhomogeneity-scattered waves in the case of LFNGs, or by an interference of several scattered waves from multiple inhomogeneities in the case of HFNGs. By increasing the concentration, the scattering behavior is changed. As a result, nanoplanes with different periodicity are obtained depending on the local inhomogeneity concentration.

5.3 Comparison with experimental data

In the previous section, we have examined ultrashort laser irradiation of fused silica with initial randomly distributed inhomogeneities of different profiles. This section presents a more detailed comparison with the available experimental results.

Fig. 5.8 shows the calculated electron density distributions for various pulse energies. For laser pulse with energies smaller than $0.1\mu J$, the modification is smooth and the electron densities do not exceed the critical value [i, Fig. 5.8(a)]. Thus, the scattering from the laser-induced inhomogeneities is rather weak to initiate the growth of planar nanoplasmas. Experimentally, smooth modification characterized by a uniform positive change in the material refractive index and absence of nanogratings is attributed to small laser pulse energies [39]. By increasing the pulse energy, the conditions for nanoplanes elongation perpendicular to the laser polarization are met [ii, Fig. 5.8(b)]. In addition, by varying energy from $0.2\mu J$ to $1\mu J$, no changes in nanogratings period are observed, as experimentally reported in [13,20,44,252]. However, beyond the energy of $1\mu J$, high densities above the critical value are created in the center of tightly focused region. At these laser pulse energy conditions, a complex disrupted region is interconnected with nanoplanes in the top portion of the laser-induced region [iii, Fig. 5.8(c)], as experimentally reported in numerous independent experimental works [13, 39, 250]. Typically, these conditions will lead to the nanogratings erasure in the center of the laser-induced area, however, this process does not have an electromagnetic origin and will be considered in the next chapter by multiphysical model.

To examine the role of temporal pulse width, we vary pulse duration from $\theta = 80$ fs up to $\theta = 240$ fs. We observe that the nanogratings are self-organized with the same characteristic period for each of the pulse durations. These results also agree with the following experiments [4, 13, 39, 44, 53]. Note, that the nanogratings with a characteristic period of $\lambda/(2n)$ have been recently revealed even for pulse duration as long as 8 ps [250]. One can conclude, for instance, that the differences of the final laser-induced modification by applying different pulse durations do not have an electromagnetic origin and will be discussed in the next chapter.

Only qualitative electrodynamic approach is considered here to investigate the influence of laser

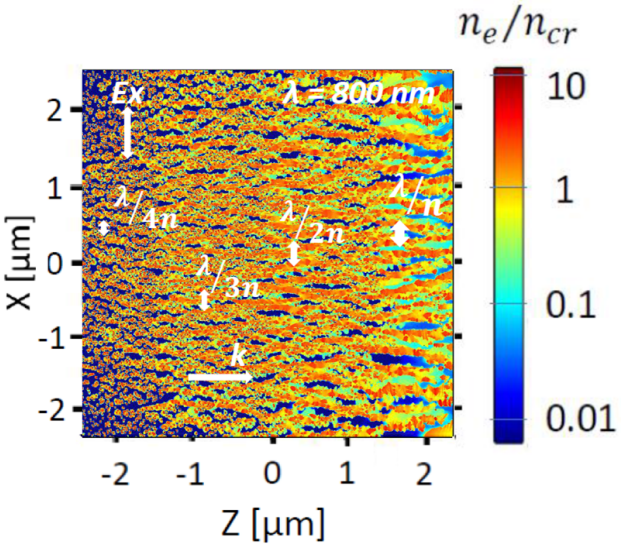

Figure 5.7: Electron density snapshot is obtained by coupled 2D-FDTD taken 80 fs after the peak of the pulse duration $\theta = 240$ fs (FWHM), laser irradiation of 800 nm and pulse energy of 500 nJ with initial variable concentration of inhomogeneities of $r = 5$ nm decreasing linearly in the z direction from $C_i = 5\%$ to $C_i = 0.05\%$. The schematic representation of the initial distribution of inhomogeneities is shown in Fig. 5.2(c).

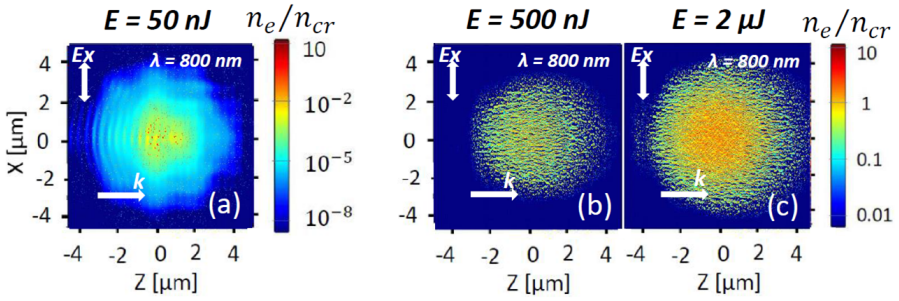

Figure 5.8: Electron density snapshots are obtained by coupled 2D-FDTD (2.2, 2.23) taken at the end of the pulse duration $\theta = 240$ fs (FWHM) and laser irradiation of 800 nm with laser beam energy: (a) $E = 50$ nJ (smooth modification), (b) $E = 500$ nJ (birefringent modification), (c) $E = 2\mu J$ (disrupted modification). Electron density is normalized to its critical value at 800 nm $n_{cr} = 1.7 \times 10^{27} m^{-3}$. Note, that in Fig. 5.8(a) the scale is different than in Fig. 5.8(b) and in Fig. 5.8(c). The schematic representation of the initial distribution of inhomogeneities is shown in Fig. 5.2(b). The concentration of the initial inhomogeneities of $r = 5$ nm is $C_i = 1\%$. Note, that different number of rate equations (5) are solved for different amplitudes of the electric field: (a) $i_m = 9$, (b) $i_m = 10$, (c) $i_m = 21$.

pulse energy and pulse duration on nanogratings formation mechanism. In Chapter 6, the method is coupled with two-temperature model equations to estimate quantitatively the attained electron densities and temperatures as well as the conditions for nanogratings formation and erasure.

Nevertheless, one can already see that the electron density distributions calculated by coupled FDTD (2.2,2.23) have strong similarities with the nanogratings observed in most experiments. For instance, Fig. 5.9 shows that the calculated free carrier density profile qualitatively reproduces the experimentally measured profile of the refractive index change at similar focusing conditions. A good agreement between the periods obtained numerically and experimentally [14, 39, 44, 258] is achieved. It is worth noting that the proposed mechanism of nanograting self-organization also explains possible coexistence of several characteristic periods [20, 259] as well as the nanostructures separated by sub-wavelength periods shorter (around $\lambda/(3n)$) [4, 16, 52, 102, 110] at higher number of pulses and larger

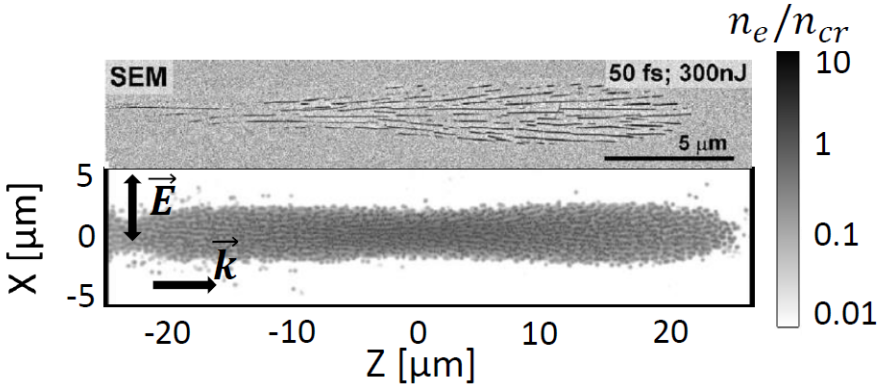

Figure 5.9: Electron density profile in the propagation plane calculated by 2D-FDTD coupled with electron density equation at the pulse peak. Pulse duration is 50 fs (FWHM), the waist beam is fixed to be $1\mu m$, laser pulse energy is 500 nJ. Initial concentration of randomly distributed inhomogeneities $C_i = 0.25\%$. Initial size of inhomogeneities $r = 20$ nm. The experimental SEM image is taken from Ref. [13]. Exp. details: laser pulse energy 300 nJ, pulse duration 50 fs, central wavelength 800 nm, repetition rate 100 kHz, focusing conditions $NA = 0.65$.

(around λ/n) [5,34,53,97] than $\lambda/(2n)$. According to numerical calculations, a uniform concentration profile of inhomogeneities is the most probable in the experiments, because of the strong arrangement due to high number of pulses. Moreover, we underline the crucial role of laser-induced inhomogeneities in nanograting self-organization and the possibility of regulating the period of the nanostructures changing the inhomogeneity concentration as it has been recently evidenced experimentally either by doping fused silica [23,110] or by varying the applied number of pulses [19,34,53,54].

Similar experimental results of nanograting period dependence on laser pulse number were obtained for $\lambda = 515$ nm [16] and for $\lambda = 1550$ nm [53]. The graphs are presented in Fig. 5.10(c, d). In fact, these experimental findings correlate fairly well with the concentration of inhomogeneities in numerical modeling, as Fig. 5.10(a) shows. Based on the mechanism of nonlinear ionization memory from pulse to pulse [246], new inhomogeneities are organized pulse by pulse. Hence, the concentration of inhomogeneities is proportional to the number of pulses. Such assumption allows me to explain the phenomenon of the decreasing nanograting period in terms of the decreasing average distance between the laser-induced inhomogeneities. The period depends strongly on the concentration and continuously decreases depending on different ways of scattering from the multiple nanoplasmas. We note that the exact values of the number of pulses are correlated with the corresponding inhomogeneity concentrations without any straightforward equivalence. Thus, if the applied number of pulses remains low, the periodicity sharply decreases. At high number of pulses, a smoother transition emerges. The same tendency has been obtained for low and high inhomogeneity concentrations.

Fig. 5.10(b) shows also that in the calculations, each nanoplane consists of numerous high density laser-induced plasmas initiated from randomly distributed initial inhomogeneities and "frozen" at different steps of their evolution. Thus, there are two types of nanoplasmas: (i) those that are significantly elongated up to several hundreds of nanometers perpendicular to the laser polarization; and (ii) the other ones with a diameter of ten-twenty nanometers. Similar structures were observed in [53,248,258].

The presented model does not describe all sets of complex thermo-mechanical and chemical processes taking place between two pulses in fused silica during VNG formation. Nevertheless, these simplified calculation results help to shed new light at the role of laser-induced inhomogeneities, interference between the incident and inhomogeneity-scattered waves, multiple scattering, local field enhancement resulting in plasma elongation and nanograting self-organization in direction perpendicular to the laser irradiation. In particular, the model is able to explain previously observed period to be close to $\lambda/2n$.

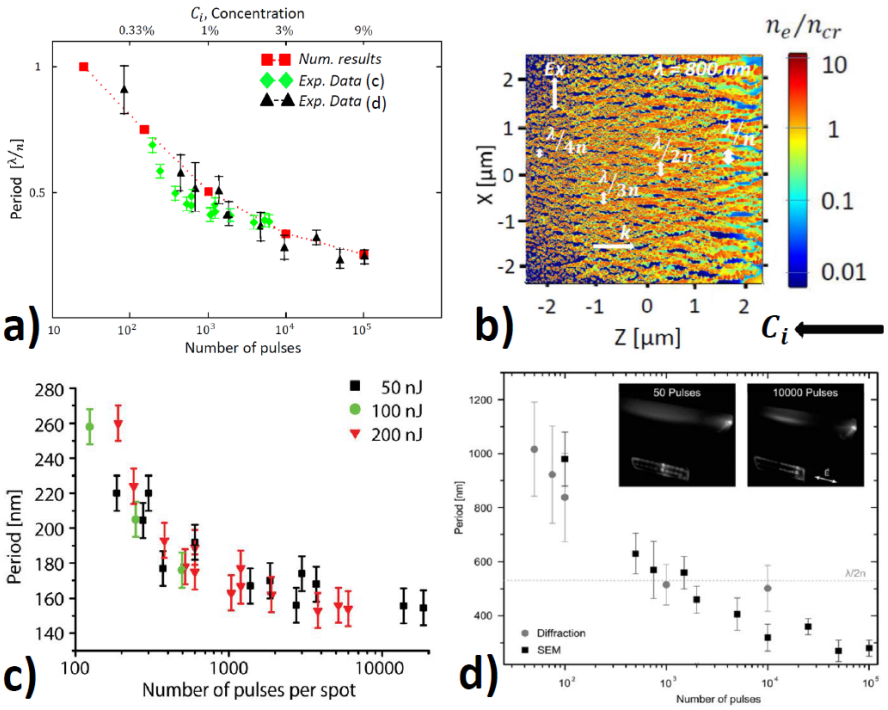

Figure 5.10: Period dependence on the number of pulses from experimental data [16,53] (c, d) comparing with the dependence on the concentration of inhomogeneities from numerical modeling (a). (b) Gradient free carrier density profile with varying initial concentration of inhomogeneities and different resulting periods.

5.4 Influence of polarization state on ultrafast laser-induced bulk nanostructuring

In this part, the results of complete 3D-FDTD simulations coupled with electron density equation are discussed and the influence of different polarizations, including linear, radial, azimuthal, circular and mixed, is investigated. The resulting electronic modifications are compared with available experimental literature data. Some of the numerical results are published in Ref. [260].

Previously, the advantage of using complex cylindrical polarizations was discussed. Firstly, both radial and azimuthal polarization beams are rotationally symmetric and isotropic. Secondly, they are expected to increase processing efficiency, quality and speed of the femtosecond laser processing [261–264]. Thus, radial polarized fields are better than linear scalar fields for excitation of surface plasmon polaritons [265–267], detection, manipulating, optical trapping and reshaping of nanoparticles [268–270], quantum information processing [271], and sub-wavelength nanostructuring [46,49–51,272].

Recent experimental approaches offer a possibility not only to create vector fields with azimuthally-dependent polarization [46,49,50,273,274], but also to apply arbitrarily patterned vector optical fields varying spatial arrangement and distributions of states of polarization by using spatial light modulators [275–278]. Here, we propose that such a technique could be useful not only for high-speed fabrication of periodic nanostructures with femtosecond laser processing, but also for improving and controlling the characteristics of the nanostructures. Particularly, using the vector optical fields with combined azimuthal- and radial-variant polarization [278–283] might serve to tune the period and the thickness of the nanostructures.

Ripple formation and distortions might be on the contrary undesirable for accurate femtosecond material processing, laser drilling and laser lithography [182, 284]. Circularly polarized beams were shown to produce no gratings but random nanodot deposits [5,285–289] and much less likely to undergo multiple filamentation than linearly polarized beams [290,291] because the input circular polarization state does not induce a preferred direction in the transverse plane. Therefore, they are advantageous to prevent the nanostructure organization on the surface [292,293] and in bulk of dielectrics [5,44,48,

284,294]. To determine more precisely the mechanisms taking place during ultrashort laser irradiation, we investigate numerically laser-matter interaction with circularly polarized beams.

5.4.1 Linear polarization state

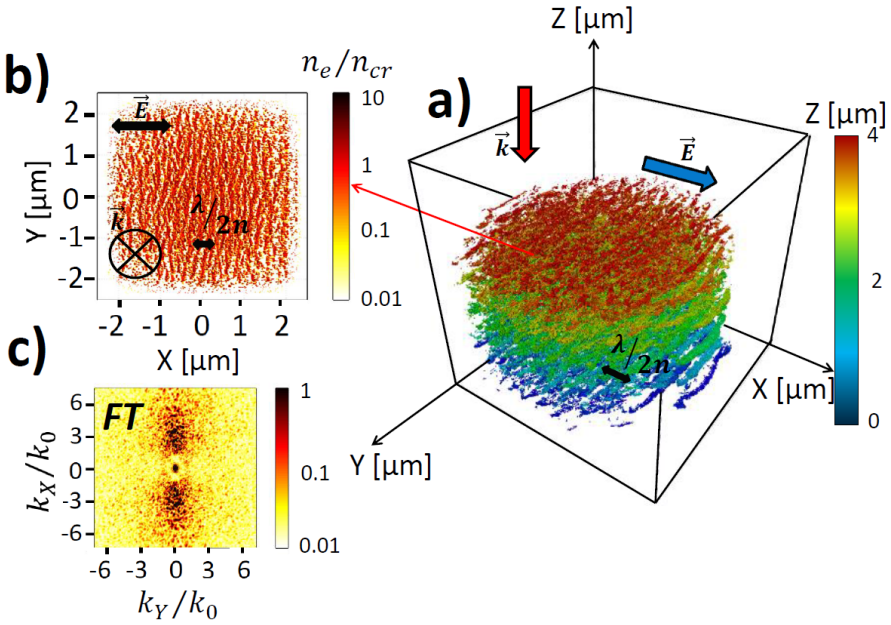

Figure 5.11: Calculation results obtained by linear polarization irradiation. (a) Electron density distribution $n_e > 0.1n_{cr}$ calculated by 3D-FDTD coupled with electron density equation 80 fs after the pulse peak. Pulse duration is 120 fs (FWHM). (b) Cross-section of the electron density, corresponding to $z = 4\mu m$. (c) Corresponding Fourier Transform (FT). The pulse energy is fixed to 500 nJ. Laser wavelength λ is 800 nm in air. The wave numbers kx and ky are normalized to the incident wave number $k_0 = 2\pi/\lambda$. Initial con-centration of randomly distributed inhomogeneities $Ci = 1\%$. Initial size of inhomogeneities $r = 5$ nm.

Fig. 5.11 shows the electron density profiles calculated by 3D-FDTD coupled with electron density evolution equation (2.2, 2.23) for linearly polarized beam (5.2). The light propagates in z direction inside a glass sample with initial bulk nanoroughness. Nanoplasmas elongate from randomly distributed inhomogeneities perpendicular to the light polarization moving by strong near-field enhancement and multiphoton ionization of intensity enhanced regions during ultrashort laser irradiation. Fields interference due to multiple scattering from inhomogeneities leads to sub-wavelength periodicity of the electron density $n_e(x, y, z)$ both in xOz and xOy planes [228]. Fourier Transform (FT) is performed to analyze the results in the frequency domain in Fig. 5.11(c). In fact, the maximum corresponds to $k_x \approx 3k_0$, which identifies the periodicity of $\lambda/2n$ in fused silica reported in independent experiments [23,39,44,97,295].

In fact, the periodicity of the nanostructures depends on the local concentration of inhomogeneities [228], which could be controlled by the number of applied pulses. For example, an increase of the concentration from $C_i = 1\%$ to $C_i = 3\%$ significantly influences the periodicity and the thickness of the self-organized nanogratings in Fig. 5.12(a). While performing FT, the maximum is displaced closer to $k_x \approx 4.5k_0$, which corresponds to the periodicity of $\lambda/3n$ in fused silica. Therefore, different sub-wavelength periodicities obtained in experiments [4,16,54,57] are explained by variable concentration of inhomogeneities.

The displacement of the maximum, as well as the dispersion of the Fourier Transform subplot, can be presented by plotting the results of the frequency domain in one dimension for k_x wavevector (5.13). In fact, the dispersion increases in the case of higher concentration of inhomogeneities. The error is $k_x = 3 \pm 0.5$ for (5.11) and $k_x = 4.5 \pm 2$ for (5.12). However, the maximum in the second case is also displaced, which allows me to say that the periodicity of the nanostructures is different. While

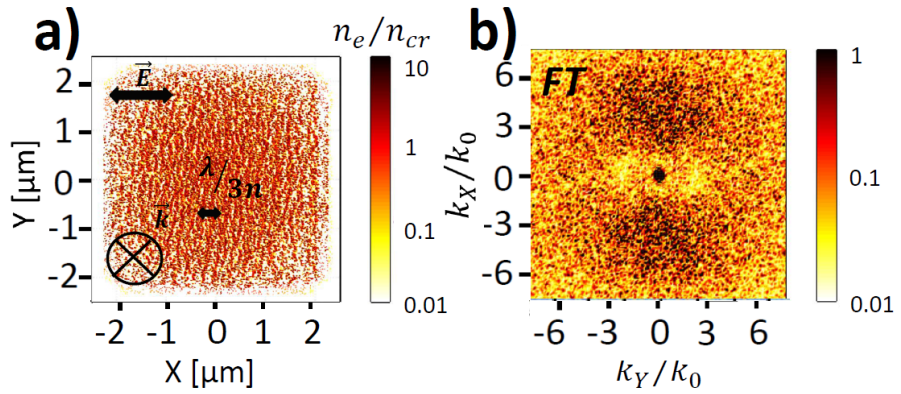

Figure 5.12: (a) Electron density profile calculated by 3D-FDTD coupled with electron density equation 80 fs after the pulse peak. Pulse duration is 120 fs (FWHM). (b) Corresponding Fourier Transform (FT). The pulse energy is fixed to 500 nJ. Laser wavelength λ is 800 nm in air. The wave numbers kx and ky are normalized to the incident wave number $k_0 = 2\pi/\lambda$. Initial concentration of randomly distributed inhomogeneities $C_i = 3\%$. Initial size of inhomogeneities $r = 5$ nm.

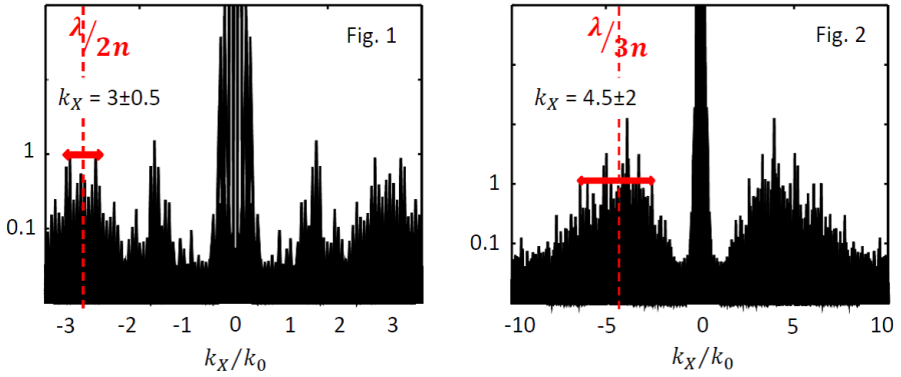

Figure 5.13: The electron density distribution in the frequency domain (using Fourier Transforms) from 5.11 and 5.12 plotted in one dimension for k_x vector.

increasing the inhomogeneity concentration, the frequency profile is getting more dispersed. However, the characteristic peak of the frequency maximum could be still identified for inhomogeneity concentrations ($C_i < 3\%$) [228]. At higher concentration ($C_i > 10\%$) the periodic formation is completely faded away.

The results of a series of complete 3D-FDTD simulations for different polarization angles are shown in Fig. 5.14. Electron density snapshot taken in the plane xOy perpendicular to the laser wave propagation presented in Fig. 5.14(b) reveals the orientation of the self-organized nanogratings strictly perpendicular to the laser polarization. Fig. 5.14(d) demonstrates that by changing the polarization of the electric field, the nanoplanes are rotated in space. Again, the nanograting orientation is perpendicular to the laser polarization in agreement with the experimental observations [20, 44, 45]. The results in xOz plane by 2D-FDTD are shown to be consistent with the results obtained by 3D-FDTD. By switching off the currents J_{Dz} or J_{Dy}, we find that the self-organization process does not occur anymore in both cases. This fact proves that the structures are formed by an interference of the multiple scattered waves of the orthogonal fields E_z and E_y. This implies that the role of the electron oscillations along z and y axes is not negligible. Therefore, the structures correspond to the HFNG type. The periodicity of the structures is close to the half of the laser wavelength in glass. We note that the same periodicity is revealed by 2D-FDTD calculations with the same initial inhomogeneity concentration of smooth distribution profile. We underline that the orientation of the HFNG structures is always perpendicular to the laser polarization. The influence of different polarization states on the resulting electronic modification is investigated in details in the next part of this chapter.

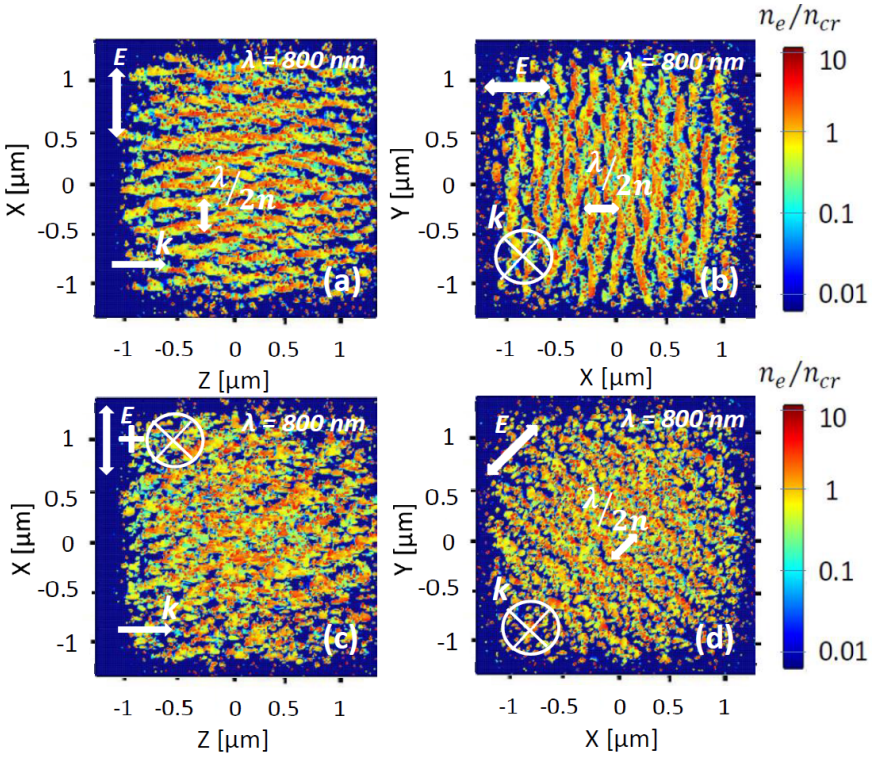

Figure 5.14: Electron density snapshots are obtained by coupled 3D-FDTD (2.2, 2.23) taken at the end of the pulse duration $\theta = 120$ fs (FWHM) with laser beam energy $E = 300$ nJ and irradiation wavelength of 800 nm for different electric field polarizations: (a) and (b) electric field is along Ox, (c) and (d) electric field lies in xOy and has $\pi/4$ angle with the axe Ox. Electron density is normalized to its critical value at 800 nm $n_{cr} = 1.7 \times 10^{27} m^{-3}$. The schematic representation of the initial distribution of inhomogeneities is shown in Fig. 5.2(b). The concentration of the initial inhomogeneities is $C_i = 1\%$.

5.4.2 Azimuthal-variant polarization states

Herein, we present the calculation results for three azimuthal variant polarization sources (5.4): radial ($Arg = 0$), azimuthal ($Arg = \pi/2$), and spiral ($Arg = \pi/4$) (see appendix). Fig. 5.15 shows that the optical material response is local and the nanostructures orientation is defined by the local electric field polarization. As in the case of linear polarization, nanoplasmas elongate strictly perpendicularly to the laser polarization. Because of azimuthal-variant behavior of the polarization state, the desirable nanostructures orientation could be achieved. Radial polarization beam induces ring-like self-organization in Fig. 5.15(a, d), whereas the azimuthal polarization beam creates radially oriented nanoplasmas in Fig. 5.15(b, e). The polarization-dependent azimuthal-variant nanostructuring was reported in numerous experimental works on surface nanostructuring [49–51,261,272,273,296,297] and in fused silica bulk [33,46,47,274].

The superposition of radial and azimuthal polarizations leads to self-organization of Archimedian nanospiral structures [49–51]. The particularity of the nanoscale spiral structures is their unique inversion symmetry with an enhanced spectrally complex optical response, making them a strong candidate for nonlinear optical applications [298–303]. The electron density profile of the corresponding windmill-like modification is shown in Fig. 5.15(c, f).

In what follows, we analyze the electron density profiles induced by different intensity irradiation with azimuthal-variant and linear polarization states in Fig. 5.16. On one hand, larger area is covered with high-density plasma and new more pronounced nanostructures are organized at high fluences. This property is referred to as self-replicating formation mechanism. On the other hand, the nanogratings period remains unchanged independently of the pulse energy in agreement with Bhardwaj et al. [44]. In fact, similar behavior was revealed experimentally by applying azimuthal and radial polarizations [33]. The period of the self-organized nanostructures was estimated to lie between $\lambda/(4n) \approx 125$ nm and $\lambda/(2n) \approx 260$ nm [101].

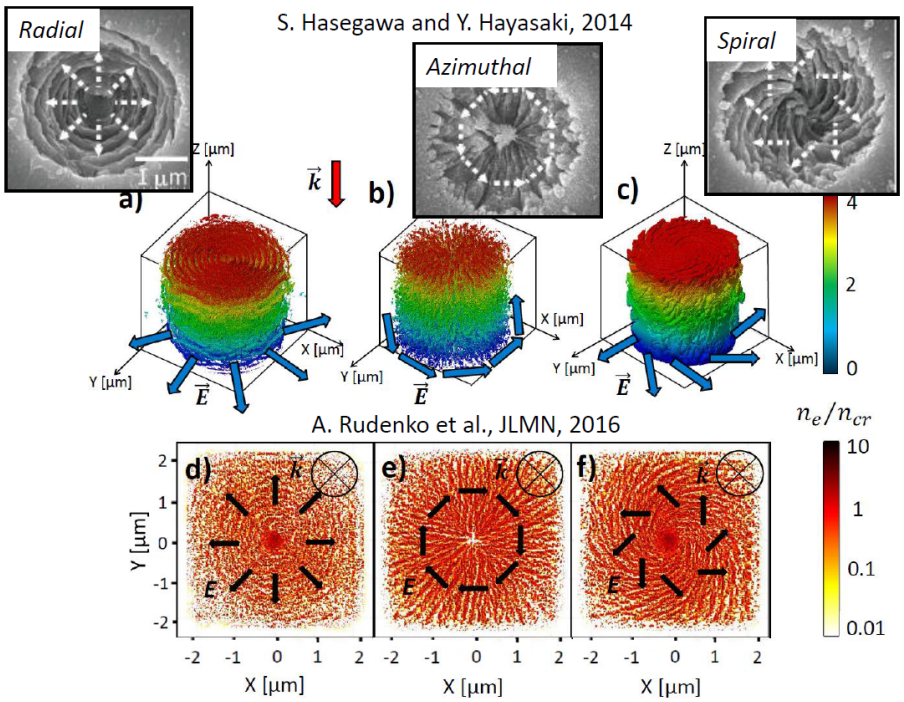

Figure 5.15: Calculated shape of the electronic modification induced by radial (a, d), azimuthal (b, e) and spiral (c, f) polarization irradiation. (a, b, c) - Electron density distribution $n_e > 0.1n_{cr}$ calculated by 3D-FDTD coupled with electron density equation 80 fs after the pulse peak. Pulse duration is 120 fs (FWHM). (d, e, f) - Cross-section of the electron density, corresponding to $z = 4\mu m$. The pulse energy is fixed to $1\mu J$. Laser wavelength λ is 800 nm in air. Initial concentration of randomly distributed inhomogeneities $C_i = 1\%$. Initial size of inhomogeneities $r = 5$ nm. The experimental results are taken from Ref. [51].

Note, that no pronounced modification is induced in the center by applying azimuthally polarized beam in Fig. 5.16(a, b), whereas the electronic densification occurs by using spiral [Fig. 5.15f, 5.16(c, d)] and radial polarizations [Fig. 5.15d, 5.18a] for the same laser irradiation conditions. Such behavior could be explained by sharp longitudinal electric field component at the focus and, consequently, larger energy deposition in the center in the case of radial polarization [264, 304]. In contrast, the electric field is purely transverse and zero in the center for azimuthal polarization, therefore, there is no electronic densification in Fig. 5.17(c, d). These numerical results are in agreement with the experimentally revealed modifications induced by single pulse irradiation by radially and azimuthally polarized beams [33] shown in Fig. 5.17(a, b).

5.4.3 Radial-variant polarization states

Experiments reveal that at certain laser conditions the laser-induced nanostructures tend to self-organize forming nanoplanes perpendicular to the local laser irradiation in fused silica [4,33,45,47,284]. Despite the ability to control the nanostructures characteristics by changing the laser parameters [2,33, 39,45,47,284], both the spatial configuration and the uniformity of the nanostructures strongly depend on the pristine glass material and bulk nanoroughness, thus, the process is not always predictable. From the other point of view, the control over the precise configuration could open new opportunities in the laser nanostructuring [51,276–278].

Previously, it was shown that radially polarized beams and, especially, beams having radial-variant states, were beneficial in nanoscale precise processing such as optical trapping of nanoparticles and plasmon excitation comparing to linearly polarized beams [265–267,276–278,280–283]. In our case, the manipulation over the nanoscale inhomogeneities is based on Mie scattering and multiphoton ionization processes which take place under femtosecond laser irradiation. Therefore, it could be advantageous to have spatial control over the nanoplasmas evolution as well by applying radial-variant polarization

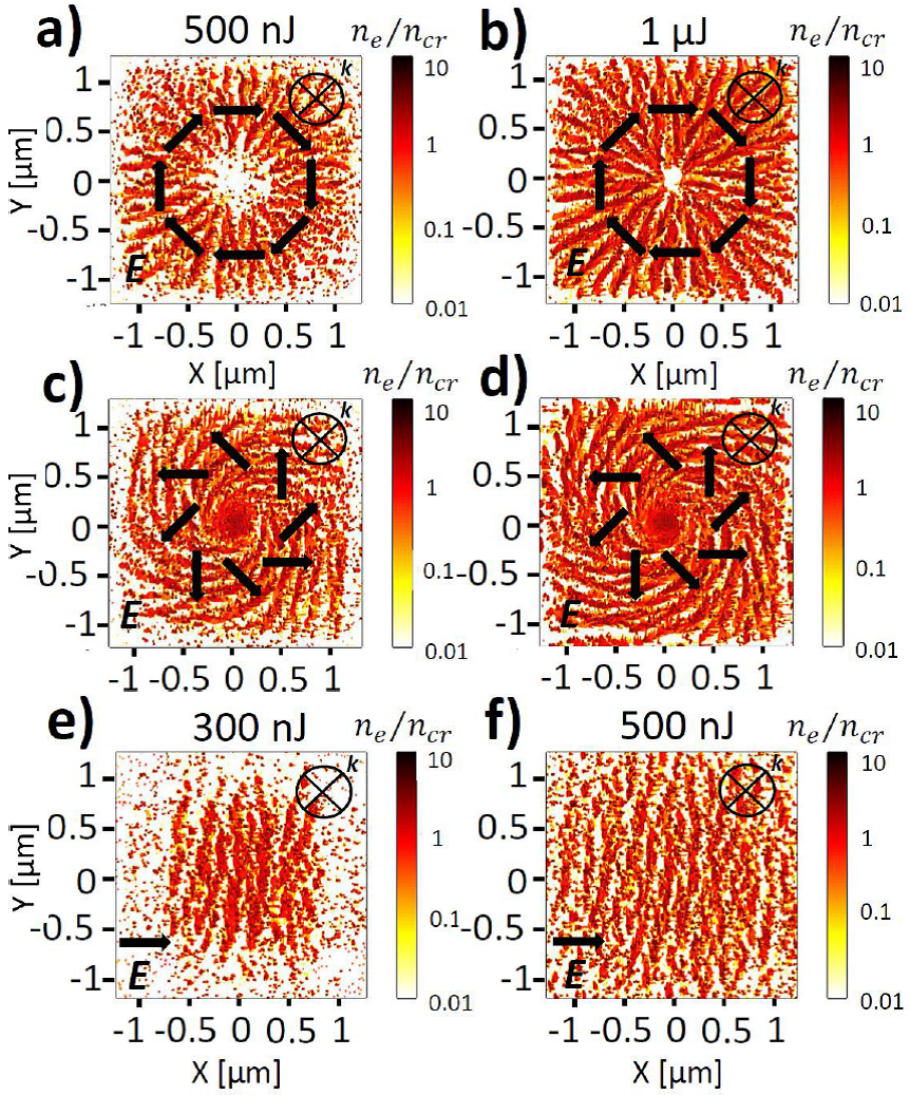

Figure 5.16: Calculated electron density profiles imprinted by azimuthal (a, b), spiral (c, d) and linear (e, f) polarization irradiation 80 fs after the pulse peak. Pulse duration is 120 fs (FWHM). The pulse energies are 300 nJ (e), 500 nJ (a, c, f) and $1\mu J$ (b, d). Laser wavelength λ is 800 nm in air. Initial concentration of randomly distributed inhomogeneities $C_i = 0.5\%$. Initial size of inhomogeneities $r = 5$ nm.

beams.

Nanoplasmas, which evolve into self-organized patterns from randomly distributed inhomogeneities, elongate during ultrashort laser irradiation in one underlined direction perpendicular to the local laser irradiation. In the case of radial-variant polarization, the local laser polarization changes from radial to azimuthal periodically along the radial direction. Local radial polarization provides strong longitudinal electric field force contributing to the formation of periodical rings, whereas local azimuthal polarization results in the local intensity enhancement along the radial direction, which defines the thickness of the ring-shape modification. Therefore, the mechanism of the electron densification in the case of the radial-variant polarization is the same as by using radial polarization. However, if in the case of radial polarization the process of self-organization and the final periodicity of the nanostructures were attributed to multiple scattering from inhomogenities, whereas it is the consequence of the initial periodic intensity distribution in the case of radial-variant polarization.

An interesting point concerning radial-azimuthal-variant polarization is that the spatial distribution is dependent on the radial vector only while it remains independent of the azimuthal angle [305]. Fig. 5.18 shows electronic modifications induced by radial polarization with $Arg = 0$ and radial-azimuthal-variant polarization with (5.4) in glass with the same bulk nanoroughness. In the first case,

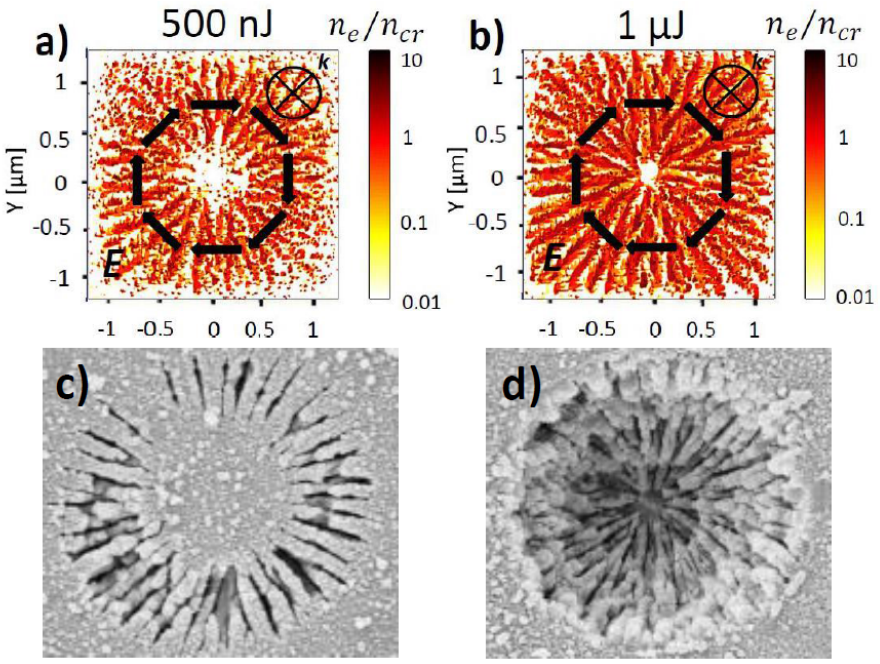

Figure 5.17: Calculated electron density profiles imprinted by azimuthal polarization irradiation 80 fs after the pulse peak. Pulse duration is 120 fs (FWHM). The pulse energies are 500 nJ (a) and $1\mu J$ (b). Laser wavelength λ is 800 nm in air. Initial concentration of randomly distributed inhomogeneities $C_i = 0.5\%$. Initial size of inhomogeneities $r = 5$ nm. The results are qualitatively compared with experiments taken from Ref. [33] (c, d). Exp. details: laser pulse energy (c) 300 nJ and (d) 500 nJ, pulse duration 200 fs (FWHM) with central wavelength 775 nm, focusing conditions $NA = 0.3$.

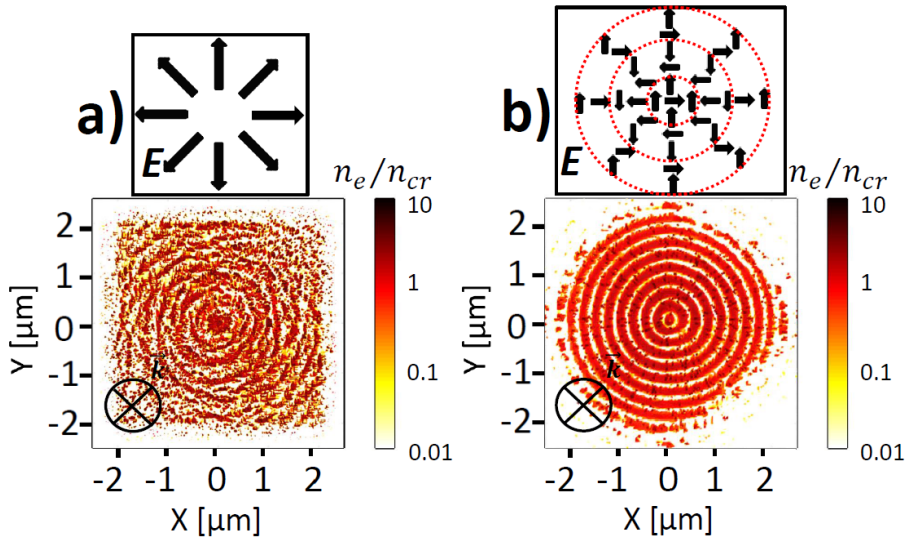

Figure 5.18: Electron density profiles imprinted by radial- (a) and radial-azimuthal-variant (b) polarization irradiation 80 fs after the pulse peak. Pulse duration is 120 fs (FWHM). The pulse energies are 500 nJ (a) and $2\mu J$ (b). Laser wavelength λ is 800 nm in air. Initial concentration of randomly distributed inhomogeneities $C_i = 0.5\%$. In the case of radial-variant state (b), the beam radius is fixed to be $R_0 = 1\mu m$ and $N = 2$, resulting in $\Delta R = 250$ nm periodicity. Initial size of inhomogeneities $r = 5$ nm.

shown in Fig. 5.18(a), the self-organization is uncontrollable, only defined by near-field interaction of laser-induced inhomogeneities and preferred direction of their elongation perpendicular to the local laser polarization. In the second case, as shown in Fig. 5.18(b), the growth of the nanoplasmas is, however, limited by the regions of the periodic enhanced intensity. The interplay between the

self-organization phenomena and the polarization geometry of the beam leads to the structures with well-defined positions and controllable thickness.

5.4.4 Circular polarization state

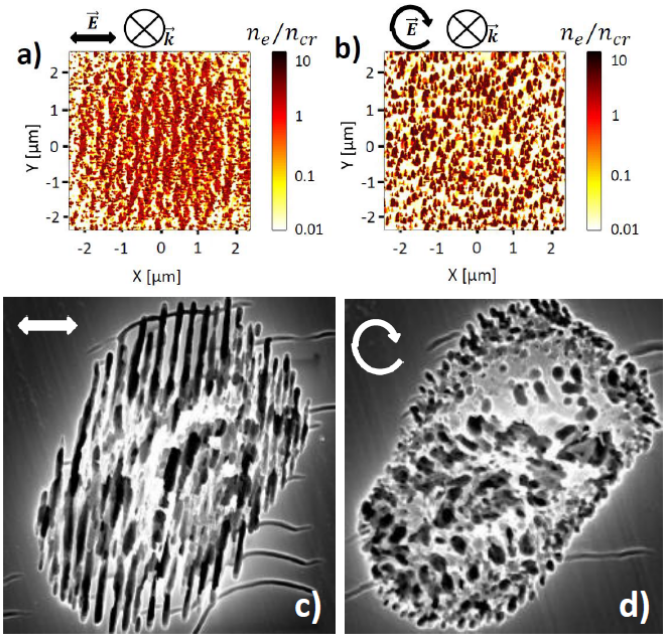

Figure 5.19: Electron density profiles imprinted by linear (a) and circular (b) polarization irradiation 20 fs after the pulse peak. Pulse duration is 120 fs (FWHM). The pulse energy is fixed to 500 nJ. Laser wavelength λ is 800 nm in air. Initial concentration of randomly distributed inhomogeneities $C_i = 0.5\%$. Initial size of inhomogeneities $r = 5$ nm. The SEM images are taken from Ref. [5] (c, d). Exp. details: laser wavelength 800 nm, pulse duration 130 fs, focusing conditions $NA = 0.45$, repetition rate 100 kHz.

In what follows, we analyze the electronic modification induced by circularly polarized beam irradiation. The particularity of the circular polarization is that there is no preferred direction in the plane $x0y$ because the electric fields E_x and E_y have equivalent contributions (5.3). In this case, the nanoplasmas from laser-induced inhomogeneities transform into random voxel nanoscale modifications [5]. Fig. 5.19 compares laser-induced electronic modification by linearly and circularly polarized beams. In the first case, nanoplasmas are stretched perpendicularly to the laser polarization direction, whereas in the second case there is no periodic organization and the laser-modified area is covered by randomly distributed nanodots resulting from the laser-induced inhomogeneities evolution. Random voxel nanoscale modifications formed after circularly polarized beam irradiation were reported in several experimental works [5, 285–289] shown in Fig. 5.19.

Finally, we perform calculations for increased laser beam energy and compare the resulting electronic modifications induced by linear and circular beam irradiation. Fig. 5.20 shows the electron density distribution after ultrashort laser irradiation by high-intensity linear and circular beams. At the center of the beam focus, high electron densities above the critical value lead to smooth electron density profile. However, laser-induced inhomogeneities contribute to the inhomogeneous energy deposition at the edges of the electronic modification. In the case of linear polarization, the modification is asymmetrical. The nanogratings elongate from the center oriented perpendicular to the laser polarization. In contrast, the electron density distribution induced by circularly polarized beam is quasi-symmetrical, even in the presence of bulk nanoroughness which results in a propeller-like density profile on the interface of the electronic modification. Therefore, laser processing with circular beam is advantageous in the case one desire to avoid distortions.

To sum up, we provide new insights into the phenomena by calculating and visualizing the three-dimensional electron density profiles, and by considering the role of different laser polarizations in

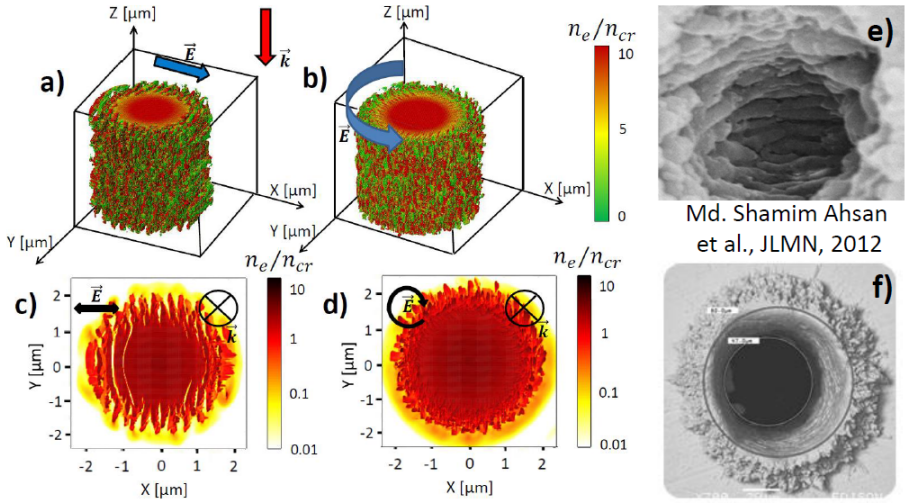

Figure 5.20: Calculated shape of the electronic modification induced by linear and circular polarization irradiation. (a, b) Electron density distribution calculated by 3D-FDTD coupled with electron density equation 80 fs after the pulse peak. Pulse duration is 120 fs (FWHM). (c, d) Cross-section of the electron density, corresponding to $z = 4\mu m$. (a, c) correspond to linear polarization, (b, d) to circular polarization. The pulse energy is fixed to $2\mu J$. Laser wavelength λ is 800 nm in air. Initial concentration of randomly distributed inhomogeneities $C_i = 1\%$. Initial size of inhomogeneities $r = 5$ nm. The experimental results are taken from Ref. [19] (e) for linear polarization.

the formation of volume nanogratings. In particular, the nanostructuring by radial, azimuthal and mixed polarizations is numerically investigated and the results of the calculations are compared with available experimental data. We suggest that radial-variant polarization discussed in a few recent articles [279–283] might be advantageous in femtosecond laser nanostructuring and confirm it by calculating electron density profiles inscribed by the radial-variant polarization and comparing with the ones of the azimuthal-variant polarization. Results of numerical calculations reveal, however, that no nanogratings are formed by applying a circular polarization. We show that random nanodots observed in experiments with circular polarization [5, 39, 285–289] are attributed to non-organized energy distribution in our calculation results. In addition, electron density profile induced by ultrashort laser irradiation with circular polarization is shown to be quasi-symmetrical even in the presence of laser-induced inhomogeneities in contrast to the electron density profile induced by linear polarization irradiation.

5.5 Nanostructuring by Bessel beams

The main advantage of non-diffractive Bessel beams over ordinary Gaussian beams lies in their ability to exhibit a near constant intensity profile along the propagation [306]. Therefore, the higher electron densities can be generated in the Bessel zone resulting in a thin plasma channel, which should be beneficial in ultrashort laser processing and, particularly, bulk nanostructuring of transparent dielectrics [2]. Previously, writing volume Bragg gratings, single-shot fabrication of voidlike sub-micron channels in fused silica as well as multipulse nanostructuring on the silicon surface by Bessel beams were reported [293, 307, 308]. The transitions between the positive index smooth modification and void-like rarefaction modifications, firstly demonstrated for Gaussian ultrashort laser processing by varying the pulse energy, pulse duration or the focusing conditions, were revealed also for Bessel beam processing [2, 308]. Recently, it has been demonstrated experimentally that self-organized nanogratings can be induced also by applying non-diffractive Bessel beam at moderate focusing conditions as shown in Fig. 5.21(c). Here, we investigate numerically the dynamics of laser-matter interaction with nanoscale laser-induced inhomogeneities using Bessel-Gaussian beam as a source.

To simulate a focused Bessel-Gaussian beam profile, the initial electric field source is introduced as

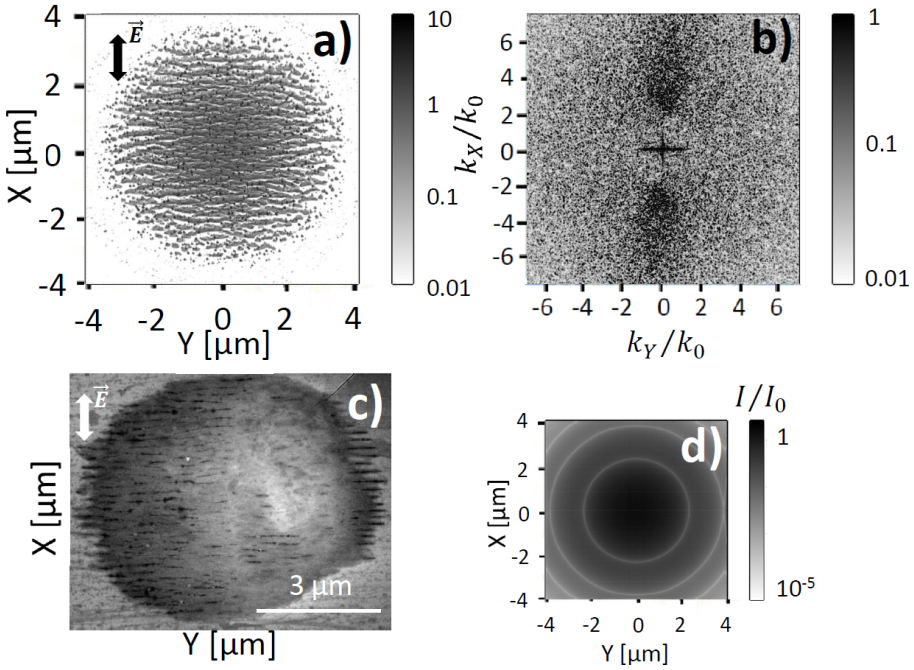

Figure 5.21: (a) Electronic modification induced by Bessel-Gaussian beam and calculated by 3D-FDTD coupled with electron density equation. Snapshot is taken at the pulse peak. Pulse duration is 150 fs (FWHM), laser pulse energy is $1\mu J$, waist beam is $1.2\mu m$ and the conical angle is 9^o C. (b) Fourier Transform (FT) of the electron density profile. (c) Experimentally revealed cross-section by scanning electron microscopy (SEM). Pulse duration is fixed to be 150 fs at the central wavelength 800 nm at a pulse repetition rate 100 kHz, and $1\mu J$ per pulse at a scan velocity $10\mu m/s$. The conical angle inside the sample $\theta = 9^o$ C and a FWHM diameter $w_0 = 1.2\mu m$. (d) Initial intensity distribution, normalized to $I_0 = 10^{17}$ W/m^2. Laser wavelength λ is 800 nm in air. Initial concentration of randomly distributed inhomogeneities is $C_i = 0.5\%$. Initial size of inhomogeneities is $r = 5$ nm.

follows

$$E_x(t,r,z) = \frac{w_0}{w(z)}\exp\left[(r^2+\frac{\beta^2 z^2}{k^2})(-w(z)^2+\frac{ik}{2R(z)}) - i(k-\frac{\beta^2}{2k})z + i\varsigma(z)\right]\cdot \\ J_0\left(\frac{\beta r}{1+iz/R(z)}\right)\exp\left[-\frac{(t-t_0)^2}{\theta^2}\right], \tag{5.1}$$

where $r = x^2+y^2$, $w(z)$ is the beam width, $\varsigma(z)$ is the phase-shift, $R(z)$ is the radius of curvature, defined analogically to ordinary Gaussian beam (3.11), $\beta = k\sin(\theta)$, θ is the inclination angle with respect to the propagation axis z or conical half-angle, and $J_0(r) = \frac{1}{2\pi}\int_0^{2\pi}[\exp(ir\cos\alpha)d\alpha]$ is a cylindrical zeroth-order Bessel function [309]. For $\beta = 0$, the expression reduces to a Gaussian beam (3.11). The initial amplitude at $z = 0$ is given by $E(r,0) = J_0(\beta r)\exp(-(r/w_0)^2)$. In our simulations, we use the conical angle 9^o C, which corresponds to the moderate focusing conditions and the beam waist diameter of $1.2\mu m$.

Fig. 5.21(a,b) shows the resulting electron density profile and the corresponding Fourier Transform for similar laser irradiation conditions. The initial intensity distribution in the plane, perpendicular to the propagation, is shown in Fig. 5.21(d). As in the case of Gaussian beam irradiation, similar periodic structures are formed inside the bulk in the transverse plane. The numerical and the experimental results concerning bulk nanostructuring by Bessel beam are described in details in Ref. [310].

5.6 Surface and bulk nanostructuring

In this part, we investigate the ultrashort laser interaction with fused silica-air surface by an electromagnetic approach coupled with electron density rate equation. We discuss the electromagnetic

formation mechanisms of different kinds of ripples and find that the similarities between the mechanisms of subwavelength nanoripples on the surface and volume nanograting formation. The ripples morphologies and the transitions between different types of ripples at different applied laser fluences are investigated. The numerical results concerning surface nanostructuring are also detailed in Ref. [311].

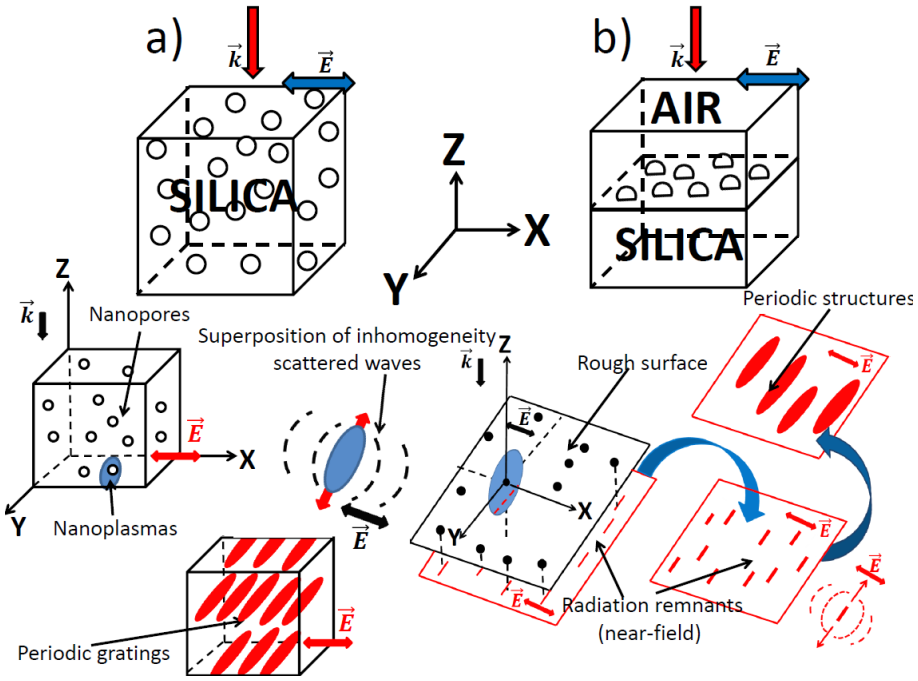

Figure 5.22: Schematic representation of the electromagnetic formation mechanisms of periodic nanostructures in (a) bulk and (b) surface ultrashort laser nanoprocessing.

5.6.1 Formation mechanisms

The electromagnetic scenarios of subwavelength nanostructure formation on the surface and in the bulk of glasses are illustrated in Fig. 5.22.

In the case of bulk nanostructuring (Fig. 5.22a), the laser-induced nanopores/nanovoids with a radius $r = 10$ nm, reported in several experimental articles [23, 24], are considered as the scattering centers. During ultrashort laser pulse irradiation, ionization processes reinforced by local field enhancement in the vicinity of the scattering centers lead to the generation of localized hot spots of higher electron densities or nanoplasmas. These nanoplasmas can then turn into void-like structures before the next pulse interacts with glass. Local field enhancement contributes to their growth into nanoplanes in the direction perpendicular to the laser polarization on a shot-to-shot basis [24,39,258]. Besides the near-field enhancement, each nanoplasma or inhomogeneity center scatters spherical waves, which are enhanced parallel to the nanoplane. The intensity enhancement is getting stronger as the nanoplasmas elongate deeper below the irradiated surface [257, 312]. Fig. 5.23(a) shows the intensity distribution from a single elongated void nanoplane. The interference of the incident field with the scattered field results in the laser wavelength in media periodic modulation perpendicular to the laser polarization. If several scattering centers are involved, the coherent superposition of the multiple scattered waves results in the subwavelength periodicity as shown in Fig. 5.23(b). In general case, the final periodicity of the nanostructures is related to the inhomogeneity concentration C or the average distance between the nanoplasmas ΔR [228]. The concentration of the inhomogeneities on the surface fused silica/air here is defined as $C = N\pi r^2/(\pi w_0^2)$, where N is the number of inhomogeneities of the characteristic radius r in the laser-induced area $S = \pi w_0^2$. The corresponding average distance is $\Delta R = \sqrt{\pi r^2/C}$.

In the case of surface nanostructuring, the rough surface between air ($\epsilon = 1$) and fused silica with half-sphere inhomogeneities of the same radius $r = 10$ nm is considered in Fig. 5.22(b). No scattering centers are introduced inside fused silica. Below the surface, random perpendicular oriented patterns

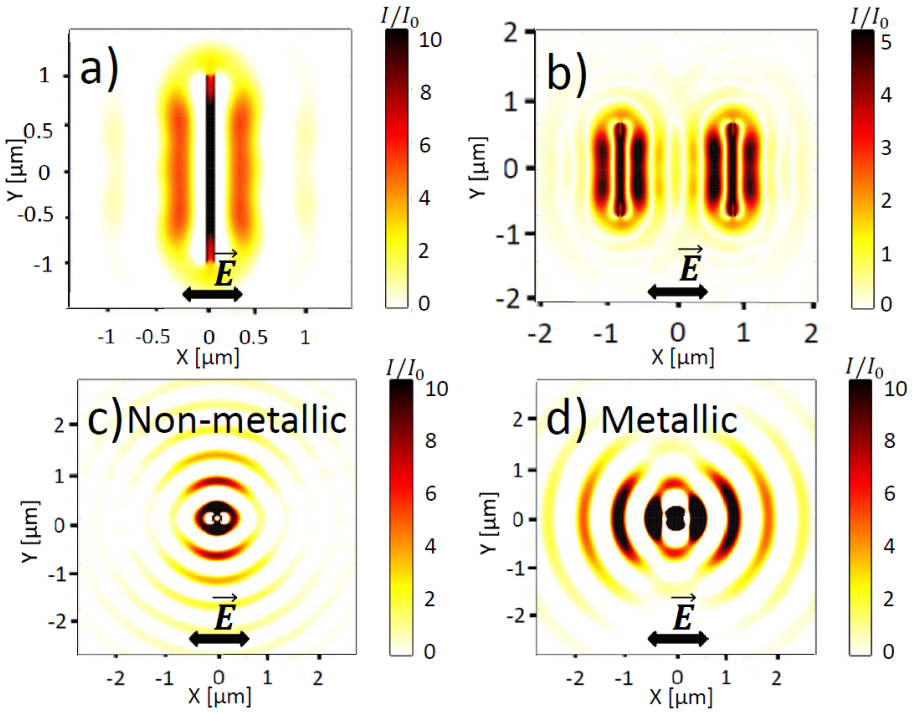

Figure 5.23: (a) Intensity distribution around a single void nanoplane $L_x = 80$ nm, $L_y = 2\mu m$, $L_z = 500$ nm. (b) Intensity distribution as a result of the superposition of the scattered waves from two void nanoplanes $L_x = 80$ nm, $L_y = 1.5\mu m$, $L_z = 50$ nm. Intensity pattern from a single inhomogeneity (hemisphere with $R = 50$ nm) (c) on the non-excited fused silica surface ($n^2 = 2.105$), (d) on the excited metallic fused silica surface ($\epsilon = -1 + 0.5 \cdot i$).

are generated by the interference of the incident field with near-field scattered waves by single inhomogeneities, so-called roughness-dependent radiation remnants [76, 79]. These patterns are the seeds for the periodic hsfl formation. Note, that small visible perpendicular oriented to the laser polarization and randomly-distributed cracks are often reported in the experimental literature for low number of applied pulses [56, 102, 287, 313]. The following scenario is similar to volume nanograting formation, as the nanoplasmas grow from the seeds due to the local field enhancement and the superposition of inhomogeneity scattered waves results in periodic modulation perpendicular to laser polarization. We emphasize that the presence of the interface air-fused silica is not necessary for the hsfl structures or volume nanograting formation [228]. We note also that neither the local field enhancement nor the interference of the scattered waves require the metallic optical properties of glass, however, the growth of the nanoplasmas can be significantly accelerated by the ionization processes in dielectrics if the pre-distributed inhomogeneous seeds for the nanostructure formation acquire the metallic properties [228].

Apart from the enhanced near-field interaction with the incident light, the rough surface is at the origin of the far-field periodic modulation, enhanced in parallel direction to the laser polarization for non-metallic surface $Re(\epsilon) > 0$ and in perpendicular direction for metallic surface $Re(\epsilon) < 0$. The typical intensity distributions from one single dielectric hemisphere on the non-excited and the metallic fused silica surfaces are shown in Figs. 5.23(c,d). The intensity patterns dominant enhancement in the directions perpendicular (Fig. 5.23c) and parallel (Fig. 5.23d) to the laser polarization is clearly seen and was firstly explained by Sipe theory [80] and then applied to explain the orientation and the laser wavelength in media periodicity of the classical laser-induced ripples [76]. We note here, that the presence of the interface (surface) is essential for generation of the far-field periodic intensity patterns. Furthermore, we underline, that the condition $Re(\epsilon) < 0$ is sufficient to generate the perpendicular oriented patterns, even if the condition for the surface plasmon wave excitation $Re(\epsilon) < -1$ is not satisfied.

In what follows, we investigate the mechanisms of ripples formation on fused silica surface by recently developed self-consistent approach [314], where Maxwell's equations are coupled to free carrier rate equation to take into account the transient changes of ultrashort laser-induced fused silica.

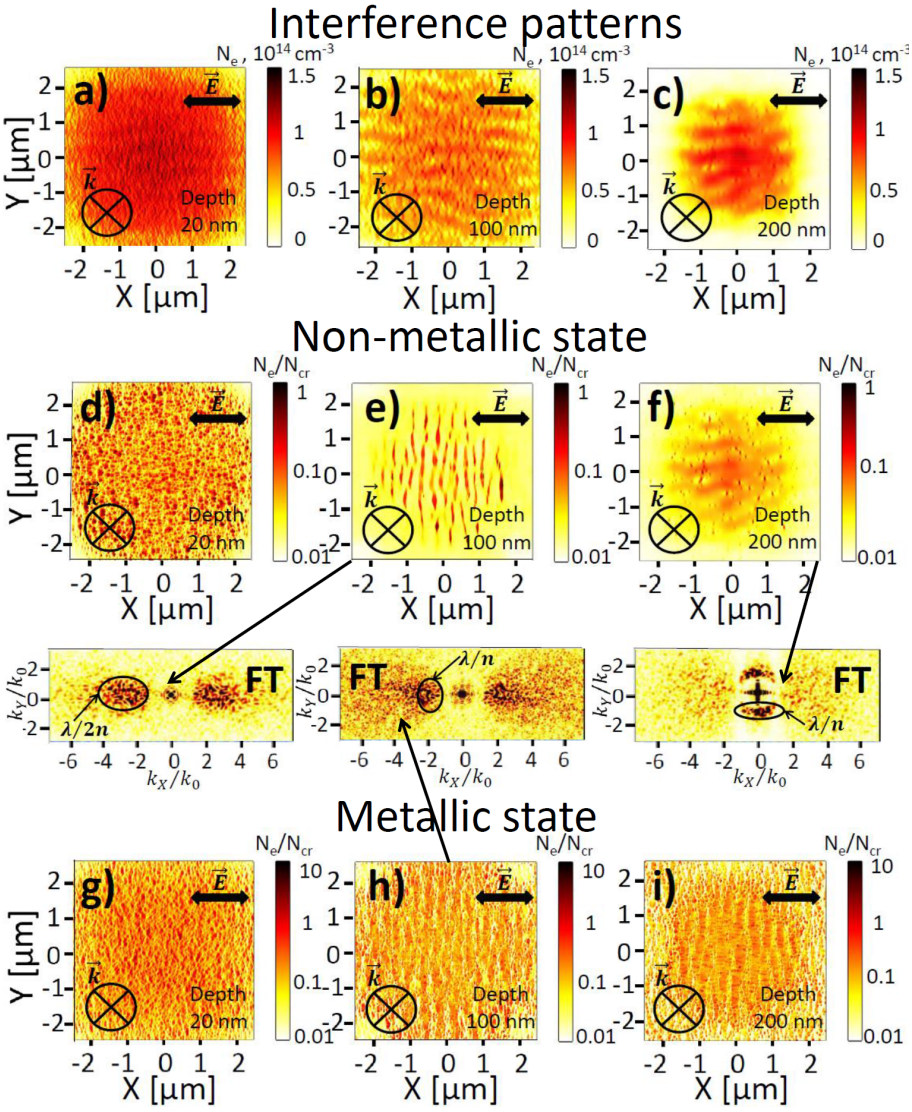

Figure 5.24: Electron density distribution calculated by 3D-FDTD coupled with electron density equation 40 fs before the pulse peak, corresponding to the interference patterns (a-c) and at the pulse peak with pulse energies $2\mu J$ (d-f) and $3\mu J$ (g-i). Pulse duration is 120 fs (FWHM). Transverse cross-sections of the electron density are taken at $z = 20$ nm (a, d), $z = 100$ nm (b, e)and $z = 200$ nm depths from the silica-air interface. The pulse energy $2\mu J$corresponds to a fluence of 8 J/cm^2 with a beam waist $w_0 = 5\mu m$. Laser wavelength λ is 800 nm in air. Concentration of inhomogeneities on the surface $C_i = 0.1\%$. Initial size of inhomogeneities on the surface $r = 10$ nm. The electron density is normalized to the critical value $N_{cr} = 1.74 \cdot 10^{21}$ cm^{-3}.

5.6.2 LIPSS morphologies

Fig. 5.24 underlines the main types of electron density patterns formed by ultrashort pulse irradiation of fused silica on different depths below the surface. At low fluence laser irradiation, the electronic modification corresponds to the exact intensity maxima, resulted from the interference of the incident wave with the scattered wave from the rough interface. At higher fluence, the local transient changes of the optical properties start playing a decisive role and could act as seeds for different type nanostructure formation.

Strongly dispersed subwavelength periodicity patterns, oriented perpendicular to the laser polarization, dominate close to the surface at the depth of 20 nm shown in Fig. 5.24(a). These electron density patterns are the consequences of the interference radiation remnants previously investigated by electromagnetic approach [76] and referred to as roughness-dependent patterns (or type-r). It was shown also that the inhomogeneous absorption triggering the formation of these patterns is due to

the interference of the incident light with the scattered near-fields of single inhomogeneities [79]. The roughness-dependent features decay rapidly with the depth below the surface [76], which could be explained by the evanescent nature of the scattered near-fields $E_{sca} \propto 1/a^2$, where a is the distance from the single inhomogeneity [226]. We emphasize that the interference of the evanescent scattered near-fields alone cannot result in the spatial periodic modulation, however, it can contribute to a significant local field enhancement [315].

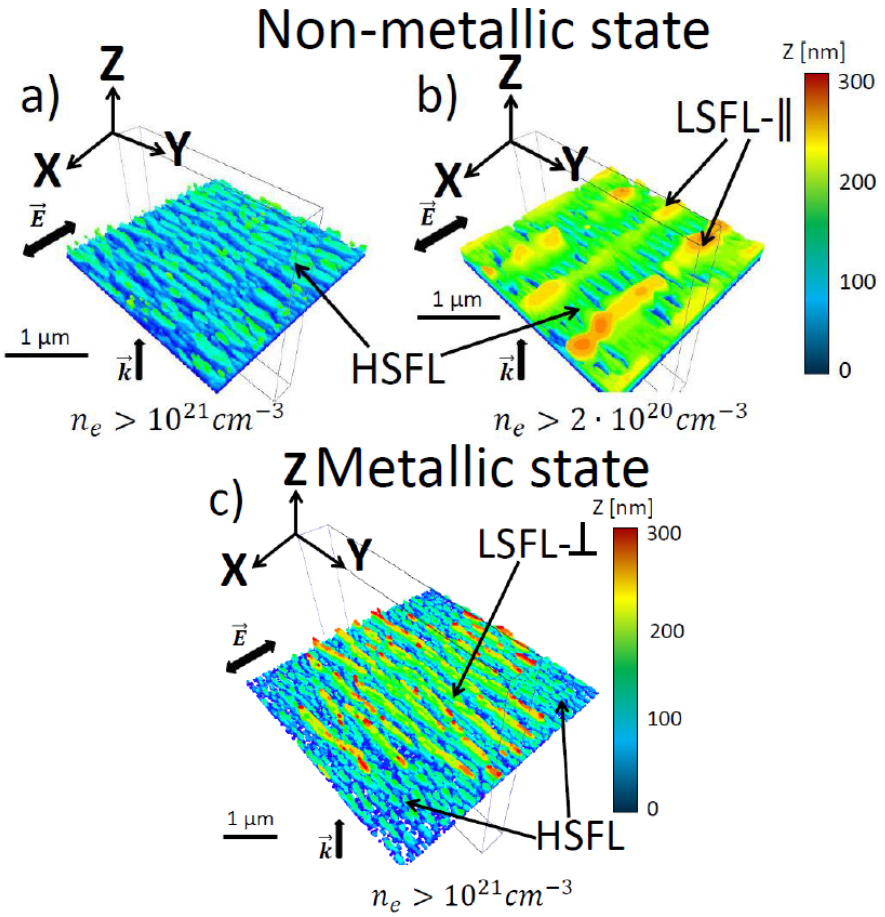

Figure 5.25: Three-dimensional electron density profiles of laser-induced surface modification (a, c) $n_e > 10^{21}$ cm^{-3} (b) $n_e > 2 \cdot 10^{20}$ cm^{-3} taken at the pulse peak. Pulse duration is 120 fs (FWHM). The pulse energy is fixed to (a, b) $2\mu J$ and to (c) $3\mu J$. Laser wavelength λ is 800 nm in air. Concentration of inhomogeneities on the surface $C_i = 0.1\%$. Initial size of inhomogeneities on the surface $r = 10$ nm.

Figs. 5.24(b,c) demonstrate that more pronounced electron density patterns with a characteristic period of the laser wavelength in medium and oriented parallel to the laser polarization, dominate at the depths of $z = 100$ nm and $z = 200$ nm. These patterns were referred to the dissident interference patterns (or type-d) [76] and were shown to be triggered by the interference of the incident light with the far-field of inhomogeneities [79]. In fact, their origin, the orientation and the periodicity can be explained as the result of the interference of the incident plane wave with the spherical scattered wave from a single nanosphere in a dielectric medium with the refractive index n given by analytical Mie theory [237]. This wave decays with the distance a below the surface as $E_{sca} \propto 1/a$ [226]. We note also that as the electron density of fused silica increases, the real part of the refractive index n decreases down to the metallic state $Re(\epsilon) = {n_0}^2 \frac{1-\omega^2\tau^2}{1+\omega^2\tau^2} < 0$, where $n_0 = 1.45$ is the refractive index of the non-excited silica, ω is the laser frequency and τ is the electron collision time. This leads to the larger periodicity of the interference patterns. In contrast, the imaginary part k, playing the role of absorption, increases, therefore, the scattered wave and the interference patterns of type-d decay faster. The parallel oriented structures on the fused silica surface or the lsfl features are commonly observed in experiments for larger pulse energies in the ablated crater [93, 316, 317]. The calculation results show that the periodic formation of these patterns does not require high electron densities, therefore,

non-plasmonic electromagnetic scenario is appropriate to explain the orientation and the periodicity of this kind of ripples [103].

Interestingly, the competition between the far-field and the near-field radiation remnants at fixed depth below the surface depends on the exact roughness. For example, low concentration of larger inhomogeneities ($C_i = 0.05\%$, $r = 20$ nm) on the surface results in stronger far-field interaction at the depth 40 nm and low frequency periodic patterns, whereas higher concentration of smaller inhomogeneities ($C_i = 0.1\%$, $r = 10$ nm) provide beneficial conditions for the high frequency patterns establishment attributed to stronger near-field interaction (not shown here). This result can be explained by an analytical electromagnetic solution for a single inhomogeneity, where the transition from the near-field to the far-field is given by $ka \approx 1$, where $k = 2\pi n/\lambda$ is the wave number and a is the distance from a single inhomogeneity. Therefore, the classical ripples are stronger (their dominance is closer to the surface) for inhomogeneities of larger size. Small-size roughness is likely to be present initially on the non-excited surface of air-fused silica, where the role of the defects in laser-induced ripples formation was previously discussed and investigated [318]. In contrast, the larger inhomogeneities can be attributed to laser-induced nanoparticles or nanovoids, formed at higher intensity irradiation due to heterogeneous nucleation or phase explosion on the silica/air interface [319].

Stronger excitation leads to higher electron densities, resulting in a significant change of the optical properties of fused silica. High electron density gradients between the inhomogeneous random hot spots, resulted from the roughness-dependent patterns, and laser-induced area are reached due to multiphoton excitation processes as shown in Fig. 5.24(d). Although these hot-spots have local metallic properties, we emphasize that the electron densities in the laser-induced area remain subcritical. The random inhomogeneities play the role of the seeds for nanoplasma growth and are the reason for the appearance of new periodic perpendicular patterns with subwavelength periodicity at greater depth $z = 100$ nm in Fig. 5.24(e). These nanoplanes continue to grow for greater depths driven by local field enhancement and multiphoton ionization processes. The Fourier transform of the electron density snapshot shown in Fig. 5.24(e) reveals the periodicity close to $\lambda/2n$. We note, that the periodicity of the final structures decreases with the increasing inhomogeneity concentration on the rough surface, therefore, even smaller subwavelength periodicities are predicted by the numerical model in the case of higher roughness (not shown here), similar to the case of bulk nanostructuring [228,260]. A similar transition from the random pre-distributed cracks to periodic nanostructures was revealed experimentally on a shot-to-shot basis during ultrashort laser irradiation of fused silica surface [56]. Deep subwavelength or the hsfl structures oriented perpendicular to laser polarization are commonly observed in dielectrics [317].

At the greater depth of $z = 200$ nm, the lsfl-$\parallel$ structures are clearly seen in Fig. 5.24(f). These electron-density patterns are likely to be reinforced by the presence of the formed deep hsfl structures [320]. To emphasize the depth-dependent transition from hsfl to lsfl-$\parallel$ structures, Figs. 5.25(a,b) shows the corresponding three-dimensional electron density modifications. The competition between the structures of two types leads to the formation of a grating-like structure, reported by several independent experimental groups [93, 316]. The deposited energy in this case is enough to melt the intensity-enhanced regions of fused silica and to generate the final morphology of the lsfl-$\parallel$ structures.

At even stronger excitation, the central laser-induced area turns metallic $Re(\epsilon) < 0$ and perpendicular oriented electron density patterns with a larger periodicity approaching to the laser wavelength are formed at the depths of $z = 100$ nm and $z = 200$ nm in Figs. 5.24(h,i). Their formation is the consequence of the interference of the incident field with the scattered far-field from the metallic rough surface (see Fig. 5.23d). Apart from these patterns, the hsfl structures are formed around the quasi-metallic area in Fig. 5.24(i). To emphasize the same orientation but different periodicity of the electron density patterns, we demonstrate also the corresponding three-dimensional electronic modification in Fig. 5.25(c). Interestingly, very similar ripples morphologies with the lsfl-$\perp$ structures in the ablation crater and subwavelength hsfl structures around were observed on the surface of several dielectrics and semiconductors [321–324].

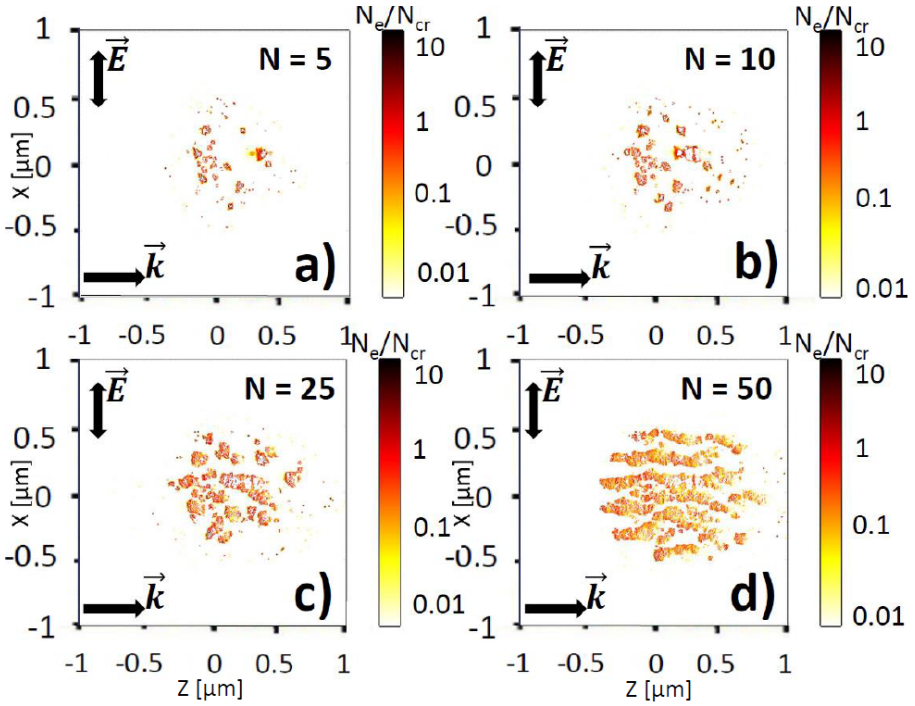

Figure 5.26: Electron density distribution calculated by Maxwell's equations coupled with rate equation at the pulse peak for different effective number of pulses evolution (a) $N = 5$, (b) $N = 10$, (c) $N = 25$, (d) $N = 50$. Pulse duration is 80 fs (FWHM). The pulse energy is fixed to be 200 nJ. Laser wavelength λ is 800 nm in air. Initial concentration of randomly distributed inhomogeneities $C_i = 0.1\%$. Initial size of inhomogeneities $r = 10$ nm.

5.7 Multipulse feedback mechanism

We have shown numerically that a single ultrashort pulse irradiation with initially presented randomly distributed inhomogeneities on the surface or in the bulk of fused silica [228] leads to the formation of three-dimensional periodic nanoplasmas oriented perpendicular to the laser polarization. However, several pulses are required to form volume nanogratings or surface nanoripples [39,56]. Furthermore, the nanoplanes were shown to consist of nanopores or less dense matter [7,24], which means that a certain threshold for nanovoid formation is overcome during ultrashort multipulse laser irradiation and the next pulse interacts with already generated nanovoids.

In order to take into account multipulse feedback during ultrashort laser irradiation, the regions where the electron density overcomes the critical value n_{cr} are considered to transform into voids with the corresponding permittivity $\epsilon = 1$ and electron density $n_e = 0$. The proposed conditions are close to the void formation thresholds [2] and n_{cr} serves as a good approximation and simplification of the real conditions. As in a single pulse irradiation, randomly distributed laser-induced inhomogeneities $r = 10$ nm with a reduced bandgap are localized in fused silica. They evolve into the hot spots with the highest electron density during the pulse duration and, therefore, turn into nanovoids up to the beginning of the next pulse. The effective number of pulses N is introduced.

Fig. 5.26 shows the electron density snapshots taken at different number of pulses and the evolution of nanoplasmas consisting of nanovoids. At first pulses, there is no periodic organization, the electron density profile is presented by randomly distributed nanovoxels surrounded by high density electron plasma as shown in Figs. 5.26(a,b). Similar non-organized laser-induced modifications were reported in several independent works [7, 11, 118, 248, 258]. At higher number of pulses, strong local enhancement around both plasma and void-like inhomogeneities contributes to the nanoplasmas elongation in one underlined direction perpendicular to the laser polarization as evidenced in Fig. 5.26(c). The distribution of the nanoplanes after $N = 50$ effective pulses is quasi-periodical with subwavelength periodicity close to $\lambda/(2n)$ in Fig. 5.26(d) because of the interference of the incident light with the

waves scattered from the growing nanovoids.

5.8 Conclusions

We have numerically investigated the mechanisms of VNGs formation under femtosecond laser irradiation of fused silica with randomly distributed nanometric inhomogeneities by solving nonlinear Maxwell's equations coupled with multiple rate electron density equation taking into account both avalanche and complex Keldysh photo-ionization. The numerical model is capable to reproduce the transition between the quasi-homogeneous electronic modification with randomly distributed scattering centers to periodic nanoplasma modification at higher laser pulse energies.

By analyzing the calculated electron density distribution, we have revealed and explained the evolution from small spherical nanometric inhomogeneities to periodical nanoplanes. Three cases have been considered: (i) with a sharp interface between modified and unmodified regions; (ii) with a constant concentration; and (iii) with a smooth concentration profile. In all these cases, periodic nanostructure formation has been observed. The obtained results have shown that the period of nanoplanes growing perpendicularly to the laser polarization depends strongly on the irradiation wavelength. These facts agree fairly well with previous experimental observations. Furthermore, 3D-FDTD modeling has shown that the nanostructures can be rotated in space by changing the electric field polarization.

The particularities of 3D electron density profiles imprinted by ultrafast laser irradiation of glass with developed bulk nanoroughness have been discussed in detail. By applying different polarization states, we have demonstrated numerically that the nanostructure orientation is perpendicular to the local laser polarization. The larger bulk nanoroughness leads to a decrease of the nanostructure periodicity, however, to more dispersed and less pronounced structures, while the laser fluence defines the area covered with the nanostructures.

Radially polarized beam is shown to induce ring-like electronic modification with a densification in the center, whereas azimuthally polarized beam creates radially oriented nanoplasmas elongated from the center, where no electronic modification occurs. In the case of windmill polarization, numerical results demonstrate the self-organization of Archimedian spiral nanostructures. Between the combinations of radial and azimuthal polarization states, arbitrary polarized laser beams might be advantageous to allow better control over the nanostructure characteristics. Circular polarization is, however, shown to be beneficial to prevent the nanostructures self-organization, inducing random nanodots at moderate intensities and quasi-symmetrical circular-shaped modification in the case of high-intensity irradiation.

It is shown that the formation of periodic subwavelength nanostructures (HFNGs) does not require the presence of a sharp interface between affected zones by laser and unaffected zones. In the presence of the rough interface, the nanoplanes of different nature and periodicity close to laser wavelength in medium (LFNGs) are formed. Their formation is due to the interference between the incident wave and the inhomogeneity-scattered waves which can be reinforced by surface plasmon wave excitation.

The mechanisms of periodic nanostructure formation are elucidated during fused silica/air surface and fused silica bulk irradiation. Volume nanogratings and subwavelength surface nanoripples (hsfl) are shown to have similar formation mechanisms, and the presence of initial inhomogeneities or scattering centers is required to start the nanoplasma growth. The orientation of the nanoplasmas is defined by the local field enhancement perpendicular to the laser polarization, whereas the subwavelength periodicity is the consequence of the coherent superposition of scattered waves by nanoplasmas. The process of the nanostructure formation does not require that fused silica glass turns metallic, because the significant local field enhancement is achieved at the tips even of a void nanoplane providing the growth on a shot-to-shot basis.

The hsfl nanoripples with the orientation perpendicular to the laser polarization develop from the intensity radiation remnants formed by the interference between the incident field and the near-field below the surface. In contrast, the lsfl classical ripples with the orientation parallel or perpendicular to the laser polarization are the results of the interference of the incident light with the far-field of rough non-metallic or metallic surfaces. Therefore, they are formed dominantly on greater depths and at higher laser fluences or irradiation dose. The numerical results indicate non-metallic nature of the transition between hsfl and lsfl-$\parallel$ and the metallic nature of the lsfl-$\perp$ structures. Therefore,

the polarization-dependent ripples morphologies, typically observed on the surface of dielectrics and semiconductors, are elucidated.

An explanation of the pulse number effect on the nanograting periodicity is furthermore proposed based on the mechanism of the nonlinear ionization memory and correlation between the concentration of inhomogeneities and the number of pulses. As the concentration is related to the separation distance between laser-induced nanospheres, the periodicity decreases with the increasing number of pulses due to different regimes of multiple scattering on nanoscale inhomogeneities.

Then, electromagnetic calculations taking into account multipulse feedback mechanism and nanovoid formation in the laser-induced regions where the electron density exceeds n_{cr} are provided. It is shown that the proposed scenario explains also the periodic nanoplasma formation on a shot-to-shot basis.

Finally, the performed numerical modeling put in evidence that laser-induced inhomogeneities play a crucial role in VNG formation. The nanometric inhomogeneities are not only the seeds and the initial reason for periodic nanograting self-organization [82] but also the attributes guiding the whole process. Without these seeds, it is impossible to explain subwavelength periodicity of the nanoplanes.

5.8.1 Appendix: Electric field sources for different polarization states

Initial electric field source for linear polarization state is introduced as follows

$$E_x^{lin}(t,r,z) = \frac{w_0}{w(z)}\exp\left(i\omega t - \frac{r^2}{w(z)^2} - ikz - ik\frac{r^2}{2R(z)} + i\varsigma(z) - \frac{(t-t_0)^2}{\theta^2}\right), \tag{5.2}$$

where θ is the pulse width at half maximum (FWHM), t_0 is the time delay, w_0 is the waist beam, $w(z) = w_0\sqrt{1+(\frac{z}{z_R})^2}$ is the Gaussian's beam spot size, $\omega = 2\pi\frac{c}{\lambda}$ is the angular frequency, λ is the laser wavelength, $z_R = \frac{\pi {w_0}^2 n_0}{\lambda}$ is the Rayleigh length, $r = \sqrt{x^2+y^2}$ is the radial distance from the beam's waist, $R(z) = z\left(1+(\frac{z_R}{z})^2\right)$ is the radius of curvature of the wavefront comprising the beam, and $\varsigma(z) = \arctan(\frac{z}{z_R})$ is the Gouy phase shift. $z = 0$ corresponds to the position of the beam waist.

For circular polarization, the initial electric field source is introduced as the superposition of two linear polarizations with a phase difference of $\pi/2$

$$\begin{cases} E_x(t,r,z) = \dfrac{w_0}{w(z)}\exp\left(-\dfrac{r^2}{w(z)^2} - \dfrac{(t-t_0)^2}{\theta^2}\right)\cos\left(\omega t - kz - k\dfrac{r^2}{2R(z)} + \varsigma(z)\right) \\ E_y(t,r,z) = \dfrac{w_0}{w(z)}\exp\left(-\dfrac{r^2}{w(z)^2} - \dfrac{(t-t_0)^2}{\theta^2}\right)\sin\left(\omega t - kz - k\dfrac{r^2}{2R(z)} + \varsigma(z)\right). \end{cases} \tag{5.3}$$

For more complex polarization states, the following parametrization is used

$$\begin{cases} E_x(t,r,z) = E_x^{lin}\left[\cos(Arg)e_x - \sin(Arg)e_y\right] \\ E_y(t,r,z) = E_x^{lin}\left[\cos(Arg)e_y + \sin(Arg)e_x\right], \end{cases} \tag{5.4}$$

where $e_x = x/\sqrt{(x^2+y^2)}$ and $e_y = y/\sqrt{(x^2+y^2)}$ are the components of the unit vector due to the conversion from cylindrical to Cartesian system of coordinates. Therefore, if $Arg = 0$, the polarization is radial; if $Arg = \pi/2$, it is azimuthal. On the whole, it could be written as

$$Arg = 2\pi Nr/R_0 - \arcsin(e_y) + \alpha_0, \tag{5.5}$$

where the first part stands for radially-varied polarization, the second gives the azimuthally-varied polarization, and α_0 is a constant. N is referred to the radial index, which defines the number of maxima/minima, and R_0 is the beam radius of radially-varied vector field. The intensity patterns exhibit the extinction rings, implying that the polarization is radial-variant. The number of the extinction rings is $2N$, the radius of the i^{th} extinction ring is given by $R_i = (2i-1)R_0/4N$ and the spatial interval between two separate rings is $\Delta R = R_0/2N$.

Chapter 6

Thermo-mechanical evolution of ultrashort laser-induced modification

This chapter is focused on multiphysical modeling of ultrashort laser-induced modifications in glasses. In particular, two-temperature model is used to investigate the thermal effects and to estimate the glass temperatures directly from the electronic modifications calculated in previous chapters. Thermo-elastoplastic wave equations are then solved to obtain the associated stresses, density and transient refractive index changes. Viscoelastic conservation law and classical nucleation theory are used to define the criteria for nanopores formation inside fused silica bulk. A simplified hydrodynamic approach based on Rayleigh-Plesset equation is then applied to investigate further evolution of the nanopores. The numerical modeling allows us to define the threshold conditions for nanograting formation and erasure. These conditions are connected with the initial laser irradiation parameters, such as laser pulse energy, pulse duration and repetition rate, via self-consistent multiphysical modeling. Finally, laser parameter window for nanogratings survival is defined.

6.1 Multiphysical model

The schematics of the multiphysical model is shown in Fig. 6.1. The main laser parameters that influence the laser-affected distribution are laser intensity, pulse duration, numerical aperture or focusing conditions, and laser wavelength. Only linear polarization is considered in this chapter. Depending on these parameters, different electron density profiles given by multiple rate equation are generated during ultrashort laser pulse propagation. As soon as the energy of the electrons is transferred to the lattice, the temperature profiles are established in the heat-affected zone, which are investigated by two-temperature model. The temperature gradients lead to the stress and density redistribution inside glass. Their profiles are defined by thermo-elastoplastic model. Glass decomposition criteria are then applied taking account temperatures and pressures within silica bulk. The hydrodynamic model based on Rayleigh-Plesset equation gives additional information about the evolution of the modification for the given temperatures and pressures. Finally, if several pulses are applied and the lattice does not have time to cool down to the room temperature, the temperature and the stress distributions are used further as the initial conditions at the beginning of the next pulse.

6.2 Laser-induced thermal effects

Fig. 6.2(a) shows the electron density and temperature distribution of the laser-induced modification, while taking into account for smooth profile of randomly distributed nanometric inhomogeneities or nanopores in glass [228]. $T_{erasure}$ indicates the minimum temperature, for which the nanogratings are locally erased in the center of heat-affected zone and is related to the threshold, reported in the experiments [10,13,16,23,39]. The area where this threshold is homogeneously overcome is attributed to the presence of uniform voids in Ref. [11,34]. The regions of high inhomogeneous electron density mark the profiles of nanoporous periodic nanostructures [7,258]. The typical two-dimensional electron

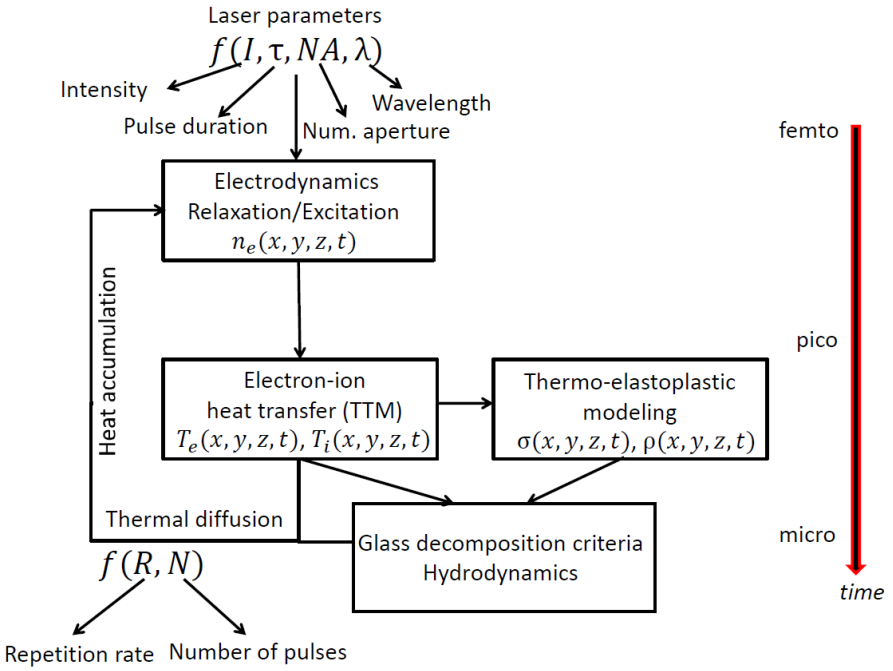

Figure 6.1: Schematic representation of multiphysical model.

density and the corresponding lattice temperature distributions calculated for the same laser parameters without any inhomogeneities are demonstrated in Fig. 6.2(b). In Fig. 6.2(a), the subwavelength periodicity electron density/temperature patterns are formed, which further turn into void-like permanent modification structures attributed to volume nanogratings. In Fig. 6.2(b), there are no periodic patterns in the spatial distribution. Note that even in the absence of inhomogeneities, two different laser-induced zones, where the nanostructures are conserved and erased, can be identified.

In what follows, we investigate the homogeneous electron density and temperature distributions, discuss the temperature thresholds for nanograting formation and erasure, find the dependence of the thresholds on the laser parameters, such as pulse energy, pulse duration and repetition rate, and summarize the main results in Figs. 6.15 and 6.16.

Laser energy strongly influences laser-induced modifications [10, 28, 29]. The results of a series of calculations for laser pulse temporal width $\theta = 80$ fs and a wide energies interval from 100 nJ to $2\mu J$ are demonstrated in Fig. 6.3. The presented electron densities, electron and lattice temperatures are calculated in the center of the photoexcited region. The maximum free carrier densities from $n_e = 2.5 \cdot 10^{26}$ m^{-3} to $n_e = 6.5 \cdot 10^{26}$ m^{-3}, created during the femtosecond pulse propagation, decay rapidly during 10 ps after excitation in Fig. 6.3(a), which is typical time of relaxation for sub-picosecond laser-induced carriers at moderate pulse energies $\Sigma \leq 4\mu J$ [28, 59, 60]. The presented electron temperatures of order $T_e = (5 - 7) \cdot 10^5$ K reach their maxima also during pulse duration. It takes about 10 ps for them to decrease and to become equal with lattice temperature in Fig. 6.3(b). The calculated lattice temperatures reach their maxima in picosecond scale, but decay slowly within several microseconds in Fig. 6.3(c). Independent of the pulse energy, the lattice temperatures decrease down to the initial temperature at $10\mu s$. Therefore, for repetition rates lower than 100 kHz, the heat accumulation effects can be safely neglected for fused silica [23, 325].

For laser pulse energies below $\Sigma = 1\mu J$, the average temperatures stay below the softening point in agreement with experimental results [29](the spatial distribution is not shown here). For energies close to $\Sigma = 1\mu J$, the electron densities of order $n_e = 5 \cdot 10^{26}$ m^{-3} are generated inside photoexcited region consistent with the reported values [15, 69–72, 75]. Under these conditions, a series of voids are generated in a single pulse irradiation regime [29, 64, 118]. Such a regime can be realized in self-organized nanogratings, while the softening point is not reached in all the heat-affected zone and the region is not completely melted [29, 39, 44, 64]. For laser pulse energies on the order of $\Sigma = 2\mu J$, fused silica temperatures are significantly higher than the melting temperature.

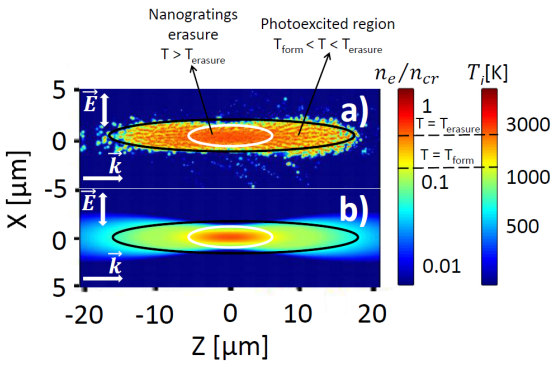

Figure 6.2: Electron density and lattice temperature distributions of laser-induced modification (a) with inhomogeneities, (b) without inhomogeneities. Two regions are underlined: $T_i > T_{erasure}$ condition defines the zone, where the nanogratings are erased, the larger zone indicates the photo-excited region, where the nanogratings are formed. Laser irradiation conditions: pulse energy $\Sigma = 1\mu J$, pulse duration $\theta = 160$ fs (FWHM), irradiation wavelength $\lambda = 800$ nm, beam waist $w_0 = 1\mu m$. Electron density is normalized to the critical electron density $n_{cr} = 1.74 \cdot 10^{27}$ m^{-3}.

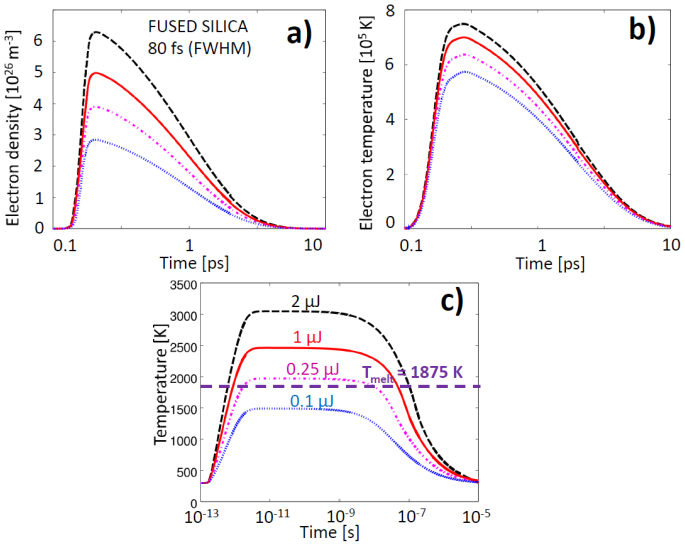

Figure 6.3: Energy-dependent temporal dynamics of single-short femtosecond laser irradiation (a, b, c). The values of maximum electron densities (a), electron and lattice temperatures (b, c) are taken at the center of focus. The energies are varied from $\Sigma = 100$ nJ to $\Sigma = 2\mu J$. Laser irradiation conditions: pulse duration $\theta = 80$ fs (FWHM), irradiation wavelength $\lambda = 800$ nm, beam waist $w_0 = 1\mu m$.

Laser pulse duration is another crucial parameter strongly influencing the nonlinear energy deposition during ultrashort laser irradiation. We consider a wide range of femtosecond pulses, for which bulk nanostructuring has been reported in the literature [4, 13–18, 39, 44]. Together with pulse energy, the pulse duration defines the contributions of photoionization and avalanche ionization. Fig. 6.4 reveals the maximum electron densities and temperatures as a function of pulse duration for different pulse energies calculated according to the numerical model.

For low pulse energies of $\Sigma = 100$ nJ and corresponding intensities $I = (2-5) \cdot 10^{17}$ W/m^2 for $w_0 = 1\mu m$ focusing (3.12), the contribution of photoionization is more significant than the contribution of the avalanche ionization [326], resulting in higher electron densities at lower pulse durations. This trend explains the experimentally measured higher breakdown threshold for longer pulses and is consistent with numerous calculations [83, 139].

In contrast, for energies of $\Sigma = 1\mu J$ and higher and for $w_0 = 1\mu m$ focusing (3.12), high intensities on the order of $I = (2-5) \cdot 10^{18}$ W/m^2 are induced in the bulk [4, 14], providing sufficiently energetic electrons for avalanche ionization. As a result, avalanche dominates over photoionization, even for

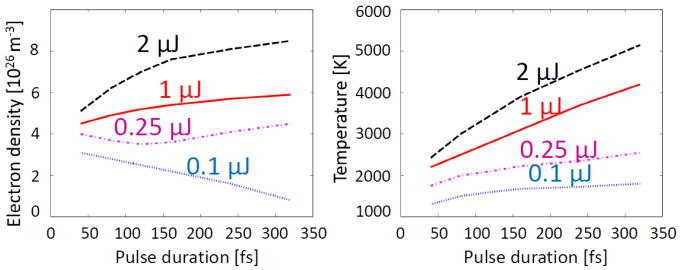

Figure 6.4: Maximum electron densities and lattice temperatures as a function of pulse duration and laser pulse energy in a single-shot femtosecond laser irradiation. The pulse durations are varied from $\theta = 40$ fs to $\theta = 320$ fs (FWHM). Irradiation wavelength is $\lambda = 800$ nm, and beam waist is $w_0 = 1\mu m$.

laser pulses as short as 40 fs [326]. In this case, the maximum electron densities and the maximum lattice temperatures rise with the increasing pulse duration. This result is consistent with lower breakdown threshold for increasing subpicosecond pulse durations in the experimental measurements [146,327–330]. The numerical calculations based on the system of Boltzmann equations [67] at relatively high intensities also agree with this dependency. Higher electron densities for longer pulse durations result in higher lattice temperatures in Fig. 6.4 and, consequently, lower temperature threshold.

Note, that the refractive index changes corresponding to both modified and unmodified material were investigated experimentally as a function of pulse duration in fused silica [10,13,15,38]. The larger values, attained for longer pulse durations, are supposed to be related to the greater local electron densities and temperatures. On the other hand, for $\theta = 160$ fs pulse duration, the temperature maximum is above the temperature $T_{relax} \approx 3000$ K for modification relaxation defined above. As a result, the nanostructures are expected to be erased. The threshold temperature is attained for subcritical electron densities of order $n_e = (5-7) \cdot 10^{26}$ m^{-3}, slightly increasing for longer pulses.

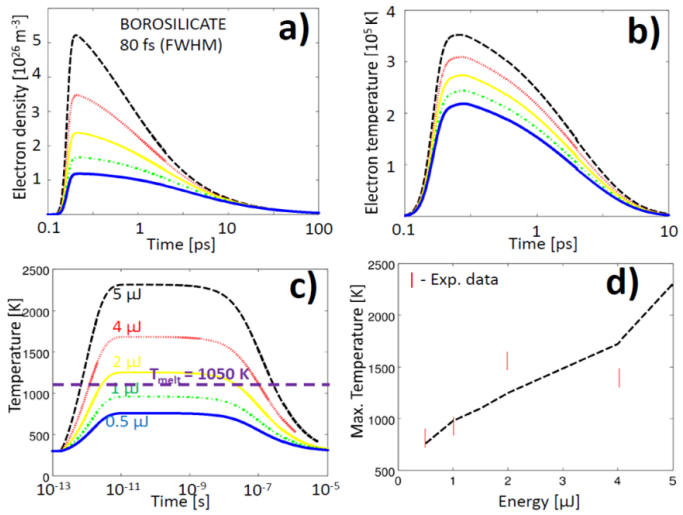

Figure 6.5: Energy-dependent temporal dynamics of single-shot femtosecond laser irradiation of borosilicate glass. The values of maximum electron densities (a), electron and lattice temperatures (b, c) are shown. The energies are varied from 500 nJ to $5\mu J$. Laser irradiation conditions: pulse duration $\theta = 80$ fs (FWHM), irradiation wavelength $\lambda = 800$ nm, beam waist $w_0 = 1\mu m$. The maximum temperatures are plotted against the pulse energies and compared with the experimental measurements [29] (d).

Fig. 6.5 shows the results of a series of calculations for borofloat glass, irradiated by the ultrashort pulse of $\theta = 80$ fs. The energies are varied within the interval $[0.5; 5]\mu J$. As in previous case, the electron densities, electron and lattice temperatures are calculated in the center of the photoexcited region. In contrast to fused silica, the electron plasma has a longer lifetime up to $\tau = 100$ ps in borosilicate glasses. Interestingly, the photoexcitation calculated by six-photon multiphoton ionization results in

lower electron densities, lower electron temperatures, and, consequently, lower lattice temperatures at fixed pulse energy and pulse duration. The temperatures lower than 1000 K for low energies of $0.5\mu J$ are consistent with the experimental findings [31], whereas the electron densities of order $1 \cdot 10^{26} m^{-3}$ were measured experimentally under tight focusing and low energies [331], in a good agreement with the numerical results in Fig. 6.5(a,c). Furthermore, even for very high pulse energies of $5\mu J$, the electron densities are at least two times less than the critical value $n_{cr} = 1.74 \cdot 10^{27} m^{-3}$ for $\lambda = 800$ nm. We propose that lower electron densities/temperatures could result in lower birefringence of ultrashort laser-induced modification [22, 332]. In the same time, the melting temperature is significantly lower $T_i = 1050$ K, therefore, the energy of $2\mu J$ is enough to melt the photoexcited region. We compare the calculated maximum temperatures in the focus of the photoexcited region with energy-dependent Raman measurements [29] and find an excellent agreement up to energies $2\mu J$.

6.3 Thermo-elastoplastic modeling for fused silica

In this section, thermo-elastoplastic wave equations (2.28, 2.30, 2.32, 2.33) are solved to estimate the stresses, density and refractive index changes for sigle-shot energy-dependent ultrashort laser irradiation regimes.

The results of a series of calculations for fused silica for ultrashort laser pulse duration $\theta = 80$ fs and wide energies interval from 500 nJ to $4\mu J$ are presented in Fig. 6.6 and in Fig. 6.7. Maximum electron densities, electron/lattice temperatures, densities, stresses and positive/negative refractive index changes are calculated. In contrast to Fig. 6.3, less tight focusing conditions are considered. Therefore, lower electron densities, electron and lattice temperatures are attained for the same laser pulse energies.

For energies below $2\mu J$, the stresses do not exceed 45 MPa, which is less than tensile strength for fused silica [153]. The typical transient negative refractive changes of order 10^{-4} due to thermal gradient are shown in Fig. 6.7(a). In contrast, the transient positive index changes are due to temperature dependence of the refractive index (see 2.33) and are estimated based on thermo-optic coefficients [162, 163] in Fig. 6.7(b). The negative density changes of order 10^{-3} calculated by Euler's equation are summarized in Fig. 6.7(c). The positive index changes of smaller order are related to the generation of the pressure wave due to thermal gradient. One can see, that the characteristic time of density change is about 100 ps.

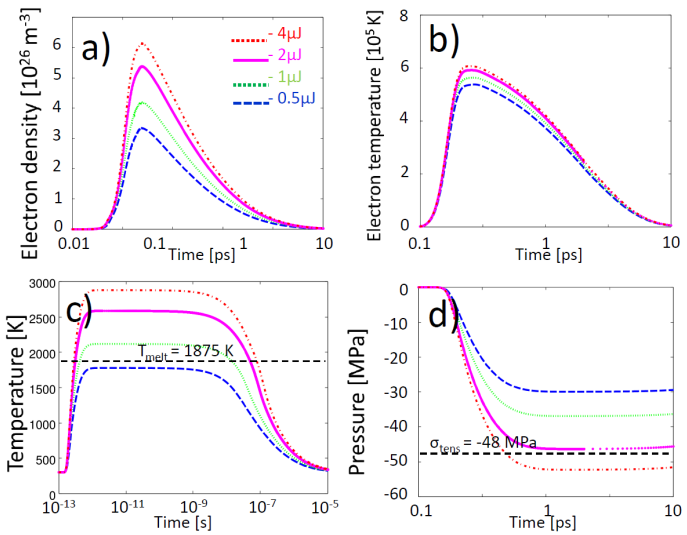

Figure 6.6: Energy-dependent temporal dynamics of single-shot femtosecond laser irradiation of fused silica. The values are taken at the center of focus. (a) Maximum electron densities, (b) Maximum electron temperatures, (c) Maximum lattice temperatures, (d) Maximum negative stresses. The energies are varied from 500 nJ to $4\mu J$. Laser irradiation conditions: pulse duration $\theta = 80$ fs (FWHM), irradiation wavelength $\lambda = 800$ nm, beam waist $w_0 = 1.5\mu m$. Thresholds for melting temperature and tensile strength are indicated.

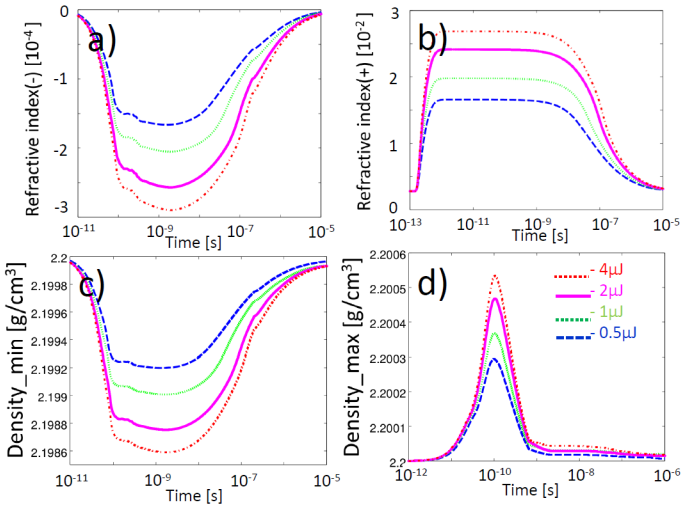

Figure 6.7: Energy-dependent temporal dynamics of single-shot femtosecond laser irradiation of fused silica. The values are taken at the center of focus. (a) Negative transient refractive index changes, (b) Positive transient refractive index changes (structural), (c) Negative density changes, (d) Positive density changes (generation of the pressure wave). The energies are varied from 500 nJ to $4\mu J$. Laser irradiation conditions: pulse duration $\theta = 80$ fs (FWHM), irradiation wavelength $\lambda = 800$ nm, beam waist $w_0 = 1.5\mu m$. Thresholds for critical electron density, softening temperature and tensile strength are indicated.

Fig. 6.8 shows the spatial temperature dynamics during fast cooling of fused silica glass. The temperatures start to decrease already at 100 ns in Fig. 6.8(b) due to strong thermal diffusion. The heat-affected zone transforms from the stretched quasi-Gaussian profile in Fig. 6.8(a) to radial in Fig. 6.8(d). The temperature significantly decreases on microsecond scale. Due to significant laser pulse energy and high laser-induced temperatures, weak temperature increase is still present even after $10\mu s$. The spatial temporal dynamics is qualitatively consistent with temporally resolved experimental temperature measurements [29].

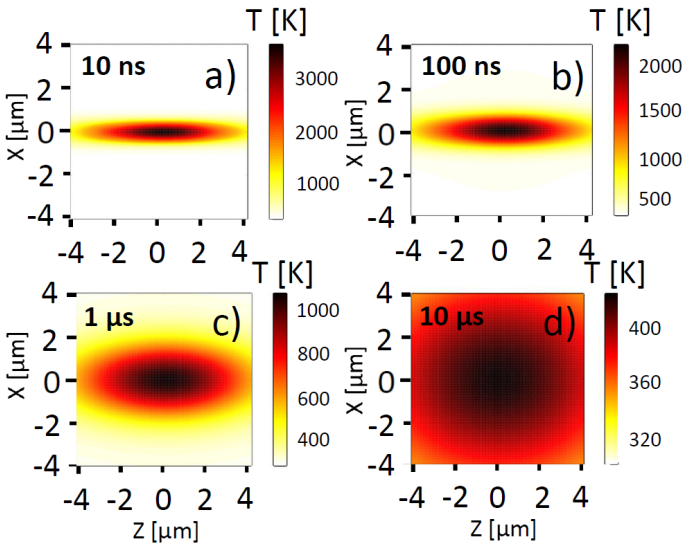

Figure 6.8: Spatial temperature dynamics during fast cooling of fused silica. Temperature snapshots are taken (a) 10 ns, (b) 100 ns, (c) $1\mu s$ and $10\mu s$ after laser irradiation. The laser pulse nergy is $4\mu J$. Laser irradiation conditions: pulse duration $\theta = 80$ fs (FWHM), irradiation wavelength $\lambda = 800$ nm, beam waist $w_0 = 1\mu m$.

6.4 Pressure wave generation

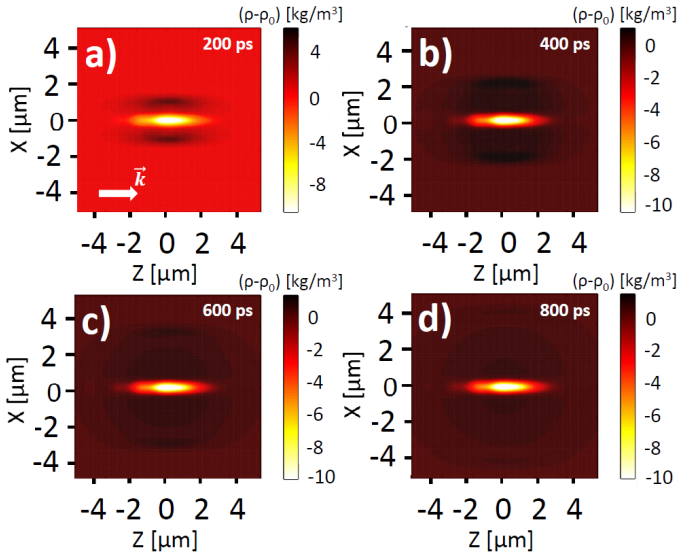

Figure 6.9: Propagation of longitudinal pressure wave in fused silica. Density snapshots are taken (a) 200 ps, (b) 400 ps, (c) 600 ps and (d) 800 ps after the pulse. Laser irradiation conditions: pulse duration $\theta = 80$ fs (FWHM), irradiation wavelength $\lambda = 800$ nm, pulse energy $E = 1.5\mu J$, beam waist $w_0 = 1\mu m$.

At timescales of several hundreds picoseconds to several nanoseconds glasses overcome the transient regime, in which the forces caused by the thermal stress lead to displacements, that propagate as longitudinal acoustic waves [159]. A generation of pressure wave was observed experimentally for fused silica and other glasses [2, 17, 63, 64, 333]. Timescales of pressure wave propagation could be expressed as $t \approx \frac{a}{C_L}$, where a is the dimension and the longitudinal sound velocity in fused silica is defined as $C_L = \sqrt{\frac{E(1-\nu)}{\rho(1+\nu)(1-2\nu)}} \approx 5968 m/s$. The dynamic evolution of the density in fused silica during the pressure wave propagation is presented in Fig.6.9. The propagation distances of the pressure wave are found to be approximately $1.2, 2.4, 3.6, 4.8\mu m$ at delays of $200, 400, 600, 800$ ps. This result is due to propagation with the longitudinal sound velocity. Fig.6.7(d) shows the maximum densities generated in the pressure wave for different pulse energies. The extremum corresponds to the initiation of the pressure wave, which corresponds to a hundred picoseconds. Then, the density decreases and the pressure wave dissipates. At nanoscale the positive stress is generated near the photoexcited region. However, the values of the stress and the density enhancements due to pressure wave are one order smaller than the ones in laser-induced thermal modification in agreement with the measurements of Sakakura et al. [65]. The glasses with larger thermal expansion coefficient like borosilicate glasses or soda-lime glasses lead to intense stress within the material [334] and, therefore, stronger pressure waves [65].

6.5 Accumulation effects

Previously, different models were proposed to take into account temperature increase during multipulse laser irradiation [35–37, 335–338]. While most of them are based on the scaling factors and the fitting parameters, which could be defined only experimentally, the application of these models to different laser conditions is questionable. Furthermore, temperature dependencies of thermal diffusivity and heat conductivity were neglected, as well as the evolution of initial heat distribution. Here, I solve the system of equations describing the temperature dynamics of glasses during multipulse ultrashort laser irradiation and repetition rates from 100 kHz to 10 MHz. From Fig. 6.8(d), it could be seen that very weak accumulation is expected for 100 kHz [23, 325], whereas the temperatures remain still high

100 ns after the pulse in Fig. 6.8(b). The results of multipulse laser irradiation of fused silica for laser wavelength $\lambda = 515$ nm and pulse duration $\theta = 450$ fs are presented in Fig. 6.10(a-d). In the case of 200 MHz, the temperature increase stays beyond 150 K, whereas for 10 MHz accumulation rate it rises up to 1300 K.

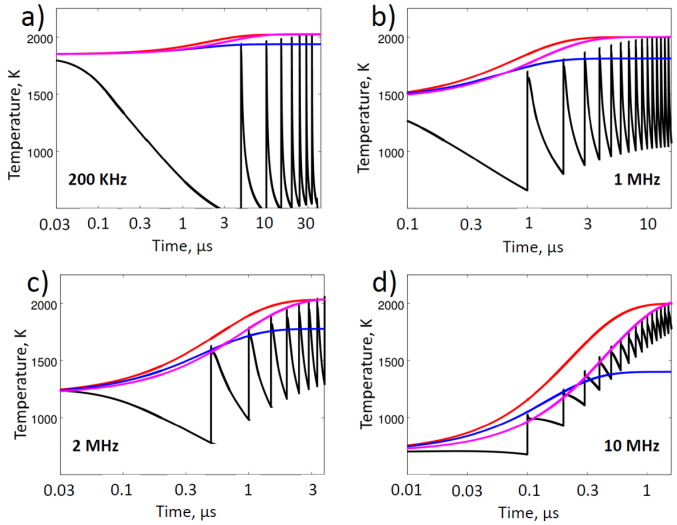

Figure 6.10: (a-d) Temperature evolution during several pulse irradiation with (a) 200 KHz, (b) 1 MHZ, (c) 2 MHz, and (d) 10 MHz repetition rates and laser pulse energies (a) 400 nJ, (b) 250 nJ, (c) 200 nJ, and (d) 50 nJ in fused silica. Red and blue lines define the temperature predictions according to (6.1) taken with α_{max} to fit the final temperature after several pulses and α_{min} to fit the temperature increase after the second pulse. Violet line refers to the temperature prediction according to (6.2) with different ξ. Laser irradiation conditions: pulse duration $\theta = 450$ fs (FWHM), irradiation wavelength $\lambda = 515$ nm, beam waist $w_0 = 1\mu m$.

Previously, a simple method was proposed to calculate the resulting temperature after several pulses irradiation [335]. There, the temperature rise of N^{th} pulse heating could be estimated as follows

$$T_N = T_1 \cdot \frac{1-\alpha^N}{1-\alpha}, \tag{6.1}$$

where $\alpha = \sqrt{\frac{t_{th}}{t_{th}+1/R_{rep}}}$, $t_{th} = \frac{l_{abs}^2}{D}$ is the characteristic cooling time, l_{abs} is the average absorption depth, R_{rep} is the repetition rate, and $D = \frac{k_i}{\rho C_i}$ is the thermal diffusivity. However, both the average absorption depth and the thermal diffusivity are functions of temperature, which does not allow the straightforward use of the formula 6.1. In what follows, we calculate the dynamics of the temperatures during multipulse ultrashort laser irradiation for different repetition rates. Note, that laser irradiation wavelength $\lambda = 515$ nm is taken to allow the comparison with experimental results [16] provided below. Numerical results could be better fitted with $t_{th} = \frac{\alpha^2}{R_{rep}(1-\alpha^2)} \approx (3-9)\cdot 10^{-8}$ s. Taking into account that $D \approx 10^{-6} m^2/s$ for fused silica, we estimate the average absorption depth $l_{abs} \approx (2-3)\cdot 10^{-7}$ m.

The method proposed in Ref. [335] could be improved in the following way. The maximum temperature just after the first pulse could be approximated as $T_1 = T_0 + Q/C_i$, where $Q = I\alpha_{abs}$ is the energy converted into the heat. The temperature after R_{rep} time is $\vartheta_1 = T_1\xi$. Therefore, the maximum temperature just after the second pulse is expressed as $T_2 = T_1(\xi+1) - T_0$. A recursive procedure to define the maximum temperature after N_{th} pulse results in

$$T_N = T_1 \cdot \frac{1-\xi^N}{1-\xi} - T_0 \cdot \frac{1-\xi^{N-1}}{1-\xi}. \tag{6.2}$$

This approximation coincides with the previously proposed expression in the case the initial temperature $T_0 = 0$, however, provides a significant correction in the case $T_0 = 300$ K for high repetition rates.

Table 6.1: Heat accumulation effects in glass.

R_{rep} [MHz]	Energy [nJ]	α_{min}	α_{max}	ξ	T_1 [K]
0.1	500	0.015	0.025	0.158	1950
0.2	400	0.045	0.085	0.235	1850
1.0	250	0.2	0.275	0.425	1450
2.0	200	0.325	0.41	0.56	1250
10.0	50	0.5	0.65	0.825	700

The results of numerical calculations for different repetition rates and comparison with analytical predictions based on (6.1) and (6.2) are shown in Fig. 6.10. For each repetition rate, we find a pulse energy required to reach $T = 2000$ K for fused silica (further referred as the cavitation threshold) during multi-pulse ultrashort laser irradiation. The results are summarized in Table 6.1. Different number of pulses is required to reach the saturation for each repetition rate. We use also the prediction proposed by Gamaly et al. [335] to find the corresponding α to fit the results in a better way. The maximum value (red line in Fig. 6.10) corresponds to α_{max}, which predicts the temperature saturation at 2000 K. This value, however, does not predict the temperature rise after the second pulse. The minimum value α_{min} is found to satisfy this condition (blue line in Fig. 6.10). In contrast, this value underestimates the temperature of saturation. We propose that the temperature rise is better described by (6.2) and we find the correspond ξ values. In fact, this analytical prediction gives the values very close to the ones of numerical simulation both for the saturation temperature and the temperature rise after first pulses for high repetition rates (Fig. 6.10). Moreover, the values of ξ correlate fairly well with the repetition rates which allows us to define the cooling time $t_{th} = (2.5 \pm 0.2) \cdot 10^{-7}$ s and the average absorption depth $l_{abs} \approx 5 \cdot 10^{-7}$ m in Fig. 6.11. This close correlation is because of smoother characteristics of the proposed function (6.2) as two parameter temperatures of the laser-induced modification T_0 and T_1 are taken into account.

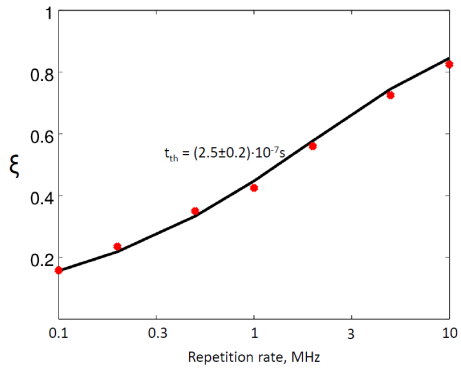

Figure 6.11: ξ is correlated with the corresponding repetition rates.

6.6 Nanovoids formation and survival

In this section, we turn to the nanograting formation and survival mechanisms. The self-organized nanogratings consist of nanopores that were connected to the strong refractive index contrast [7]. The formation of nanopores was attributed to glass decomposition, rather than structural modification, i. e. bond-breaking mechanisms [112]. It is widely accepted that the decomposition can be achieved by three main ways: nucleation, cavitation/fragmentation and spinodal decomposition [174,339], and the dominant mechanism is defined by the relative timescales of each process, where the fastest mechanism wins [12]. On the other hand, the glass decomposition is limited by fast cooling of lattice, which takes place after $\tau_{cool} = {w_0}^2/D \approx 1.68\mu s$ in ultrashort laser processing of fused silica [29], where

$D = k_i/\rho C_i$ is the diffusion coefficient. Here, we discuss the feasibility of each decomposition process for the initiation of nanopores.

The mechanism of nuclei formation was proposed to explain the formation of self-organized bubbles [75,340] as well as nanogratings in fused silica [339]. The characteristic time for nucleation depends strongly on the processing temperature and pressure values. For example, for temperatures of $T = 3000$ K, $\tau_{nucl} \approx 1.3$ s is needed for nucleation under $P = 200$ MPa pressure, $\tau_{nucl} \approx 2\mu s$ under $P = 300$ MPa, and only $\tau_{nucl} \approx 200$ ps under $P = 400$ MPa. Additionally, the characteristic time decreases by approaching to critical point temperature, which is typical to metal laser ablation [12,341]. As the exact pressure values for liquid fused silica $T_i > T_{melt}$ irradiated by ultrashort laser are not well-known, we calculate the nucleation time for a wide range of pressures up to the highest value limited by the critical pressure for fused silica. This critical value is set to be $P_{cr} = 189$ MPa, according to Melosh [175]. Importantly, even larger values were reported in literature, such as $P_{cr} = 551$ MPa in Ref. [342,343], so that the range for the nucleation can be wider.

The other scenario, widely discussed in the literature, is nanovoid formation due to cavitation [2,118]. The dynamic tensile strength required for cavitation inside fused silica bulk P_{dyn} is derived from Grady's criterion for spall in liquid [172] described by the inequality condition (2.36). Strain rate $\zeta(T)$, viscosity $\eta(T)$ and surface tension $\sigma(T)$ depend on the glass temperature evolution, which is taken into account by the numerical method. The tensile stress is evaluated as $P \approx -\beta BT$ for solid, where $\beta = 5.5 \cdot 10^{-7}$ K^{-1} is the thermal expansion coefficient of fused silica [183] and B is the elastic bulk modulus, defined previously, giving values of order 100 MPa. The corresponding strain rate is estimated from the thermoelastic wave equations modeling, where $\frac{\Delta\rho}{\rho} \approx -\beta T \approx -10^{-3}T/T_{melt}$ is reached at less than 100 ps, therefore, $\zeta \approx 10^7 T/T_{melt}$ s^{-1}. Taking into account the time dependency of the dynamic tensile strength in the expanding glass given by $P_{dyn} = 2B\zeta t$ [172], one can estimate, that the elastic energy is greater than the kinetic energy $\frac{E_e}{E_k} \geq 15$, applying the condition for the nominal cavitation size $R \leq 2c_s t$. Therefore, the following expression is valid

$$\frac{16B\zeta^2 t^2}{15} \geq \frac{6\sigma}{R} + \eta\zeta \geq \eta\zeta. \tag{6.3}$$

For temperatures slightly above the softening point $T_{melt} = 1875$ K, the viscosities are as high as $\eta \approx 10^8 Pa \cdot s$ [173], therefore, the contribution of viscous dissipation is several orders greater than of the surface tension. In fact, fused silica still resists even at high temperatures, where metals and semiconductors are fragmented [12,172,344]. By taking into account the temperature profile evolution and fast lattice cooling, we estimate the maximum viscosity and, therefore, the minimum temperature of fused silica for overcoming the dissipation forces $\eta_{max} = B\zeta\tau_{cool}^2 \approx 1.5 \cdot 10^6$ Pa·s, which corresponds to $T_{min} \approx 2000$ K [168,169]. For such temperatures, $\eta\zeta \gg 6\sigma/R$ is still satisfied even for nanometric sizes $R \ll 10$ nm, therefore, the conditions for nanocavitation are met for temperatures greater than $T_{min} = 2000$ K. The minimum characteristic time of cavitation is limited mostly by surface tension, as the viscosity sharply decreases for $T > 2800$ K [59] but the surface tension still remains significant [173]. For nanopores of $R \approx 10$ nm, the minimum required time is estimated as $t_{min} = \sqrt{6\sigma/BR\zeta^2} \approx 4.1$ ns, where $\Delta t = 100$ ps is taken to evaluate the strain rate ζ, according to the results of thermo-elastoplastic modeling [75]. In this way, at higher local temperatures and greater local strain rates induced by density fluctuations or the presence of bulk inhomogeneities in glass, the nanopores of smaller sizes are likely to be formed at nanosecond timescales. Interestingly, nanopores of smaller size were experimentally revealed by Lancry et al. in different glasses, while using higher repetition rates [23]. For larger voids of $R \approx 1\mu m$, lower tensile stresses are required to overcome the tension forces and the minimum corresponding time lies in one hundred picosecond scales as indicated in Fig. 1.5. Formation of nanocavities of sizes smaller than $1\mu m$ in the center of heat-affected zone is typical for single pulse irradiation of fused silica bulk [2,17,29,34,118,344].

The laser conditions corresponding to cavitation are somewhat different from the ones theoretically investigated by Gamaly et al. in the case of tight focusing inside sapphire [9,89]. In our case, the electron densities are less than the critical value $n_{cr} = 1.74 \cdot 10^{27}$ m^{-3}, the lattice density change and the strain rates, related to the fused silica compression, are as small as $\Delta\rho/\rho \approx 10^{-3} > 0$ and $\zeta \approx 10^7$ s^{-1} correspondingly, supported by experimental direct measurements of the modification [2,28,259] and also of the density change at the center of the pressure wave [17,65]. Therefore, the cavitation takes

place on nanosecond-microsecond timescales, passing by fused silica liquid state. In the experiments of Juodkazis et al., the shock wave compresses the material up to $\rho_{max} = 2\rho$ and the pressures are several orders greater such as $P > 100$ GPa, indicating the phase transition to high-pressure states of matter [89, 174, 175].

Finally, spinodal decomposition or critical point phase separation describes the material decomposition in the unstable liquid-vapour region of the phase diagram following an expansion passing in the neighborhood of the critical point [345] and, therefore, requires the temperatures close to the critical temperature $T_i > 0.9T_{cr} \approx 4860$ K [12, 174, 346]. The estimations indicate that nanovoids are likely to be formed by cavitation or homogenenous nucleation at temperatures $T_i < 0.9T_{cr}$, therefore the spinodal decomposition is not significant.

The competition between cavitation and nucleation scenarios as a function of temperature and pressure is illustrated by Fig. 6.12(b). The negative pressure is used to evaluate the mechanical tensile stress for the cavitation process, whereas the positive thermodynamic pressure is considered for the initiation of the nucleation process. The cavitation process takes place faster than nucleation one at lower pressures and temperatures, therefore, the nanovoid is likely to be generated at moderate intensity irradiation, where the temperatures in the center of heat-affected zone overpass the melting point and $T_{cav} \approx 2000$ K.

The nucleation process is limited by the critical pressure and temperature. According to the pressure values defined by Kraus et al. [174] and Melosh [175] and the characteristic times for the nucleation calculated by CNT, the nucleation process is faster than the cavitation process only for temperatures $T > 4000$ K. However, these temperatures do not lie within the reported values for nanograting formation $T = 2000-3000$ K [7] and are higher than the temperatures reached in moderate intensity regimes of ultrashort laser irradiation, detailed in Table 6.2, according to our calculations in Fig. 6.3. Additionally, we show that below that value the nanopores can then significantly grow. This process is driven by the hydrodynamic expansion before the fast cooling of the lattice for the temperatures $T > 3000$ K. The nanopore growth is expected to cancel the effects of the electromagnetic scattering and contribute to the nanogratings erasure. Therefore, only the cavitation process satisfies the timescales of the phenomenon, limited by a fast cooling as well as commonly used repetition rates less than 10 MHz.

6.7 Nanogratings erasure

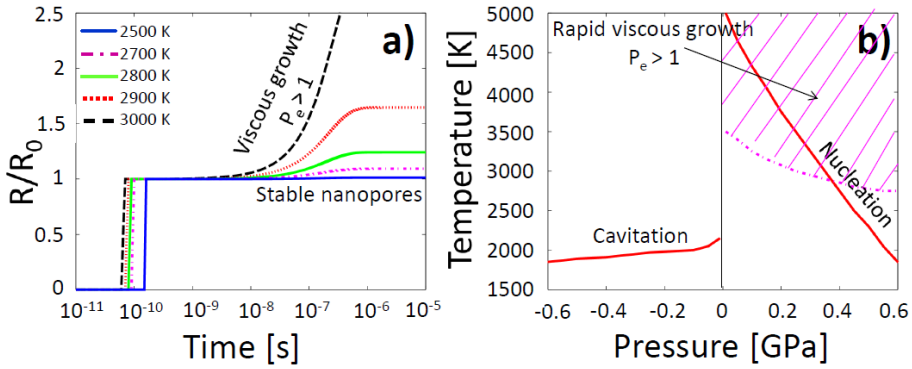

Figure 6.12: (a) Evolution of nanopore sizes in time for temperatures from $T = 2500$ K to $T = 3000$ K and pressures defined by $P = \frac{3}{2}n_a k_B T$. (b) Pressure-temperature window for cavitation, nucleation and viscous growth of nanopores.

Now, it remains to identify the nanograting erasure mechanisms. The estimated temperature threshold provides the local conditions for nanopores or nanovoid formation, but does not give the information about hydrodynamic evolution of the modification. In what follows, to analyze the dynamics of nanoscale voids, we solve the Rayleigh-Plesset equation (2.37). For temperatures slightly above the derived nanocavitation threshold $T \approx 2000$ K and relatively high viscosity, one can derive a law of viscous growth $R \approx R_0 \exp(P_e/4)$, where $P_e = \tau_{cool}/\tau_{visc} = \Delta P \tau_{cool}/\eta \ll 1$ is Peclet number,

showing the ratio between the timescales for diffusion τ_{cool} and for viscous deformation τ_{visc} [347,348]. For such conditions, the size of nanopores remains almost unchanged from one pulse to another, which is common for experiments at the regimes of self-organized nanogratings [23, 34]. In contrast, for higher temperatures $T > 3000$ K, the viscosity term rapidly decreases, giving $P_e > 1$ and providing significant growth rate of nanovoids. The condition $P_e = 1$ is used to define the threshold for rapid nanopore growth. This condition and the conclusions drawn below are independent of the initial size of nanopores R_0 till it is in the nanometric scale. The nanopores of $R_0 = 5 - 20$ nm are typically observed in the moderate intensity regimes of self-organized nanogratings [7,23,34].

Fig. 6.12(a) shows the temperature-dependent evolutions for nanopores. For temperatures lower than $T \approx 2000$ K, the conditions for cavitation and nucleation are not satisfied. As soon as the threshold is overcome, the nanovoids and nanopores are stable and are conserved up to the glass solidification. Temperatures greater than $T \approx 2750$ K lead to hydrodynamic growth of nanopores ($P_e > 1$). Fig. 6.12(b) shows the conditions for nanopore growth in terms of temperatures and pressures. The parameter window, which enables the formation of stable nanopores corresponds to temperatures $T \approx 2000 - 3000$ K. We claim that only in this case the nanostructures are formed pulse by pulse by electromagnetic scenario.

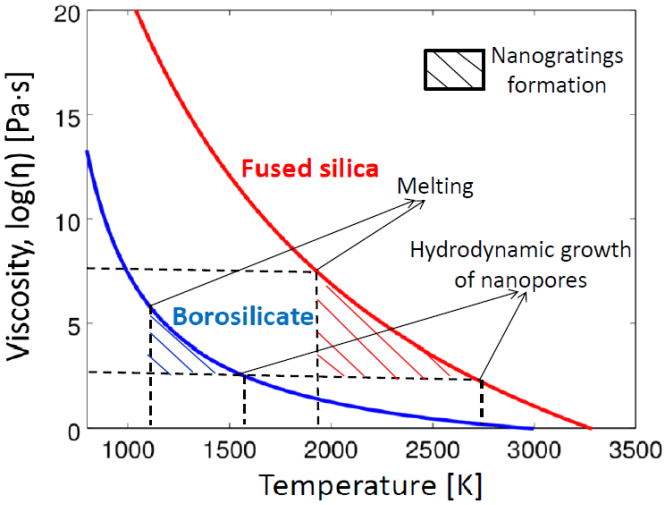

Figure 6.13: Temperature and viscosity dependent laser parameter window for nanograting formation in fused silica and borosilicate glasses.

Fig. 6.13 shows the temperature dependencies of viscosities for fused silica and borosilicate glasses taken from Ref. [170]. The melting temperature and the temperature, satisfying the condition for viscous growth of the nanopores $P_e = 1$ serve as the local indicators for nanograting formation and erasure. In fact, the condition for cavitation $\eta(T,t) = B\zeta(T,t)t^2$ gives the temperature values close to the melting temperature $T_{melt} \approx 1100$ K for borosilicate glass. One can note, that the laser parameter window for borosilicate glass is significantly narrower than for fused silica. This is logical since borosilicate glass has lower viscosity at the same temperatures and greater thermal expansion coefficient and laser-induced stresses, that result in greater Peclet number. Therefore, it is more difficult to find a convenient laser regimes for inscribing periodic structures inside borosilicate glasses [21,23].

Several previous experiments show that nanogratings were not formed in certain temperature ranges [16,23]. This observation can be explained by the phenomena taking place when the temperatures $T = 2500 - 3000$ K are established in all the heat-affected zone, see Fig. 1.5. Firstly, nanopores start growing because of low viscosities corresponding to these temperatures, which is observed experimentally [23]. The hydrodynamic growth can be the reason of disrupted regions [23,58], where the multipulse evolution of nanoporous structures is defined not only by local field enhancement and electrodynamic scenario shown in Fig. 6.2. Secondly, the Grady's criterion is satisfied for larger areas, therefore, glass can be decomposed into voids of hundreds of nanometers, which result in rather complex disruptions [58]. Finally, Lancry et al. proposed that the decomposition level was limited by heating-cooling profile allowing the glass relaxation via back-migration of oxygen and its recombination after pulse excitation

[23].

To examine the glass relaxation, we note that strongly temperature-dependent viscosity $\eta(T)$ governs the structural relaxation processes. Thus, Maxwell's viscoelastic relaxation time τ_M gives the time required for material parameters stabilization and is directly proportional to viscosity coefficient $\tau_M = \eta/E$, where E is the elastic bulk modulus. Glass viscosity is known to decrease exponentially with the increasing temperature [167–169]. Thus, if temperatures are higher than a well-defined value, the material will structurally relax faster than it will cool [109]. One can expect that the self-organized nanogratings written by multipulse irradiation of fused silica are partly erased due to viscoelastic relaxation [21]. The role of viscosity in the regime of self-organized nanogratings was also underlined, while comparing the laser-induced nanostructuring in fused silica with higher viscosity and in borosilicate glasses [21], attaining lower viscosities at the same temperatures [166].

The relaxation time changes with temperature and with time. The maximum lattice temperature defines the minimum relaxation time for laser-induced modification. During first few nanoseconds after photoexcitation, the temperature decreases insignificantly, providing the glass enough time to relax if the temperature is sufficiently high. We define the minimum structural relaxation time τ_{relax} and the corresponding minimum temperature $T_{relax} = f(\tau_{relax}E)$ as the critical parameters, for which the laser-induced modification relaxes.

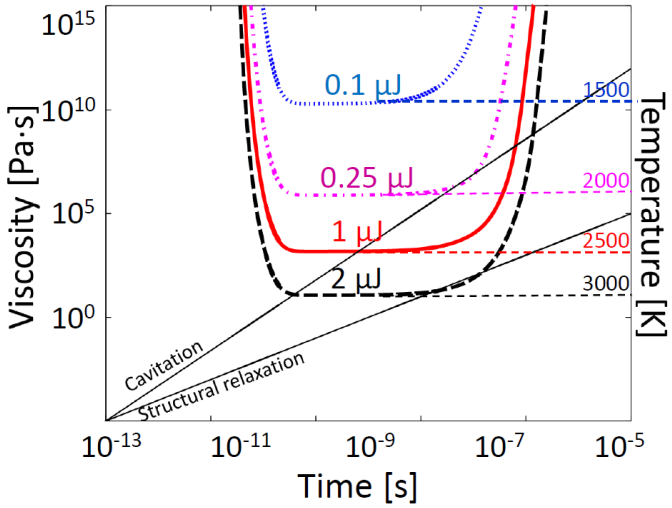

Figure 6.14: Energy-dependent temporal dependence of viscosities and temperatures during single pulse ultrashort laser irradiation. Laser irradiation conditions: pulse duration $\theta = 80$ fs (FWHM), irradiation wavelength $\lambda = 800$ nm, beam waist $w_0 = 1\mu m$, laser pulse energies from $\Sigma = 100$ nJ to $\Sigma = 2\mu J$. Straight lines indicate the cavitation threshold defined by $\eta(T,t) = B\zeta(T,t)t^2$ and the structural threshold defined by $t = \eta(T,t)/E$.

Taking into account temperature dependencies of the viscosity for fused silica and the numerical results of energy-dependent temperature dynamics for fixed pulse duration $\theta = 80$ fs in Fig. 6.3, we plot the time evolution of the relaxation time $\tau_M = \eta/E$. The point, where the curve crosses the straight line $\tau_M = t$, indicates that the relaxation takes place at time t. We estimate the critical energy $\Sigma \approx 2\mu J$ and the corresponding lattice temperature $T_{relax} \approx 2900$ K, for which structural relaxation is attained from Fig. 6.14. This value is larger than the softening temperature (see Table 2.1), but is smaller than the boiling temperature $T_b = 3220$ K at normal conditions [7,174,339,349] and is close to the experimentally defined value for viscoelastic relaxation $T_i = 2763$ K [109]. The relaxation temperature is related to the viscosity $\eta_{relax} \approx 100Pa \cdot s$ or to the relaxation time $\tau_{relax} \approx 3$ ns and is independent of the laser irradiation regime. The time τ_M is significantly shorter than the common time delay between two pulses in multipulse ultrashort laser irradiation with repetition rates 100 kHz - 10 MHz [16]. Therefore, the temperature threshold is independent of the particular repetition rate as well. Fig. 6.14 also indicates the nanocavitation threshold, defined previously by condition $\eta(T,t) = B\zeta(T,t)t^2$. The point, where two lines $\tau_{cav} = B\zeta t^2/E$ and $\tau_M = \eta/E$ cross, corresponds to the minimum threshold temperature for nanocavitation $T_{cav} \approx 2000$ K.

Table 6.2: Reported experimental regimes of self-organized nanogratings in fused silica.

Experimental group	Wavelength $[nm]$	Pulse duration $[fs]$	Energy $[\mu J]$	Numerical aperture	Repetition rate $[MHz]$
1. Shimotsuma et al. [4]	800	150	1.0	0.95	0.2
2. Hnatovsky et al. [13]	800	40-500	0.1-2.5	0.65	0.1
3. Bhardwaj et al. [44]	800	50	0.3	0.45/0.65	0.1
4. Bricchi et al. [259]	850	200	0.24-0.61	0.55	0.25
5. Yang et al. [55]	800	150	0.5	0.55	0.25
6. Liao et al. [18]	800	100	0.05-1.2	1.1	0.25
7. Mauclair et al. [15]	800	150-2000	0.1/0.3	0.42	0.1
8. Papazoglou et al. [17]	800	35	1.0	0.4	0.1
9. Horstmann et al. [97]	1045	500	0.36/0.6	0.7	0.1-5.0
10. Richter et al. [16]	515	450	0.05-0.2	0.55	0.05-9.4
11. Mishchik et al. [11]	800	150	0.2-1.0	0.45	0.1
12. Lancry et al. [7]	1030	250	0.1-2.2	0.6	0.001-0.5
13. Bellouard et al. [350]	1030	150	0.19-0.4	0.4	0.1
14. Kazansky et al. [14]	800	150	0.9	0.55	0.25
15. Stankevič et al. [351]	1040	320	0.4-0.6	0.4-0.6	0.5

From the above discussion it follows that the self-organized nanogratings are formed in the locations, where the cavitation takes place in a single pulse irradiation and the temperatures higher than $T_{cav} \approx$ 2000 K are reached. Multipulse accumulation effects lead to higher local temperatures [23] and stresses [350,352] in the photo-excited zone, which provide the conditions for nanocavitation of nanopores on the timescales shorter than the micrometer cavity is formed. The higher the temperature is, the greater the viscous growth rate of nanopores is provided. We propose that only stable nanopores result in the organization of periodic nanostructures on ultrashort timescales. In contrast, the hydrodynamic growth of nanopores leading to micrometer disruptions [23,58] should be avoided, therefore, the local temperatures should not exceed $T_{erasure} \approx 3000$ K as shown in Fig. 6.12. In fact, nanogratings can be erased by hydrodynamic or structural relaxation processes, occurring when all the heat-affected zone temperatures overcome this value. These physical processes require low viscosities, attained at high temperatures, and, therefore, we refer to the defined temperature values as to the viscoelastic nanograting erasure limit, or relaxation temperature threshold.

6.8 Comparison with experimental data

Fig. 6.15 demonstrates the parameter window for self-organized nanogratings survival as a function of pulse energies and pulse durations. This regime lies between cavitation and viscoelastic relaxation thresholds corresponding to temperatures $T_{cav} \approx 2000$ K and $T_{erasure} \approx 3000$ K. The behavior of the critical curves is mostly defined by the contribution of the avalanche ionization and, therefore, by the value of applied pulse energy [326]. For laser pulse energies higher than $\Sigma = 400$ nJ, higher electron densities are reached for longer pulse durations. They result in a temperature threshold $T_{erasure} = 3000$ K at shorter laser pulses. In contrast, for pulse energies lower than $\Sigma = 400$ nJ, the temperatures do not attain the threshold value even for long pulse durations, as the contribution of the photoionization is considerable or even more important than of the avalanche ionization. We propose that the relaxation curve, marked by the dotted line in Fig. 6.15, qualitatively describes the transition from the regime of the stable nanogratings to the disrupted regime [13,39] shown schematically in Fig. 6.2. The experimental data regimes for nanogratings taken from Table 6.2 appear well between the cavitation and relaxation curves. Furthermore, the numerical results are consistent with the experimental

measurements of the void-nanogratings threshold [10, 11, 13, 39, 350]. For example, one can see that the nanogratings are conserved for $\Sigma = 2\mu J$ pulse energy and $\theta = 40$ fs pulse duration, as well as for $\Sigma = 300$ nJ and $\theta = 150$ fs pulse duration [39], because the viscoelastic threshold is not reached in both cases in Fig. 6.15, although the intensities differ by one order of magnitude at the same focusing conditions $NA = 0.65$ and at the same irradiation wavelength $\lambda = 800$ nm. The pulse duration dependency of the threshold is also consistent with the experimental observations within the same laser pulse energy, where nanogratings are more likely to form disrupted regions for longer pulses [13, 39, 250].

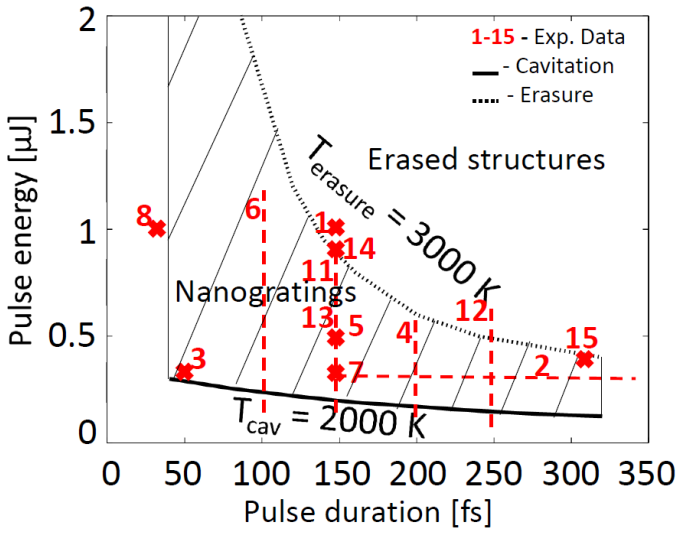

Figure 6.15: Pulse energy/pulse duration parameter window for nanogratings survival $T_{cav} < T < T_{erasure}$. The solid and the dotted curves indicate the numerically calculated cavitation threshold T_{cav} and viscoelastic erasure limit $T_{erasure}$. The crosses and the dashed lines mark the experimentally defined regimes summarized in Table 6.2, in which the self-organized nanogratings have been observed. Laser irradiation conditions: irradiation wavelength $\lambda = 800$ nm, beam waist $w_0 = 1\mu m$.

Because of non-homogeneous distribution of the electron densities in Fig. 6.2, the lattice temperatures are also distributed inhomogeneously. Therefore, the nanogratings can be erased in the center of the photoexcited region, but still remain in the regions of lower temperatures, where the viscoelastic threshold is not attained, i. e. in the head and in the tail of heat-affected zone [7, 17, 55]. In contrast, the disrupted partly melted regions are formed in the regions of higher temperatures [10, 11, 39].

During multipulse laser irradiation, the resulting laser-induced modification is also affected by heat accumulation effects [16, 23, 35, 37]. Even at moderate repetition rates temperature rises significantly [23, 36, 37]. To compare the numerical results with the experiments in Table 6.2, where different repetition rates were applied, we take into account heat accumulation effects by solving electron-ion heat transfer equations and calculating the lattice temperatures rise up to the saturation. From a series of calculations, we define the laser pulse energy threshold required to attain the temperatures $T_{cav} = 2000$ K and $T_{erasure} = 3000$ K for different repetition rates.

The number of laser pulses required for the saturation depends on the repetition rates. Generally, insignificant increase of the temperature of $\Delta T < 5$ K is calculated after the next pulse irradiation at $100 - 150$ μs. This time corresponds to $100 - 150$ pulses for 1 MHz repetition rate. Fig. 6.16(a) shows the temperature evolution up to saturation at value $T_{cav} \approx 2000$ K for fixed pulse duration $\theta = 320$ fs and different repetition rates 250 kHz, 500 kHz, and 1 MHz. For repetition rates higher than 500 kHz, the temperature is increased by more than twice compared to a single pulse irradiation. This increase is evident at first 20 pulses for all repetition rates indicated in Fig. 6.16(a). Then, the accumulated temperatures ΔT exponentially decrease. The temperature evolution is nonlinear between the annealing $T_{anneal} = 1400$ K and the melting $T_{melt} = 1875$ K temperatures. This result can be explained by the discontinuity of the thermal conductivity $k_i(T)$, as shown in Fig. 2.9(b). To justify the saturated temperature, we verify that the accumulation rate $\alpha = \Delta T/T << 1$ and $T_{cav} \approx 2000$ K coincide with the attained saturation value after the infinite number of pulses $T_\infty =$

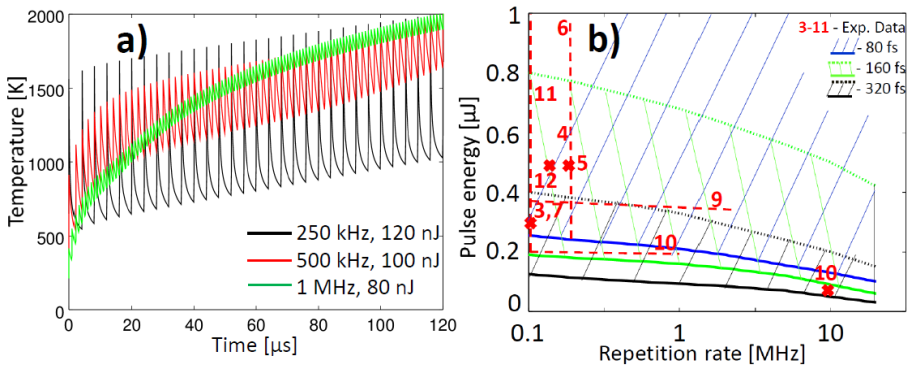

Figure 6.16: (a) Temperature evolution up to $T = 2000$ K saturation by multipulse irradiation with (1) 250 kHz, 120 nJ, (2) 500 kHz, 100 nJ and (3) 1 MHz, 80 nJ pulses with pulse duration of 320 fs. (b) Pulse energy/repetition rate parameter window for nanogratings survival for fixed pulse durations of 80 fs, 160 fs and 320 fs. The solid and dotted curves indicate the numerically calculated cavitation and viscoelastic relaxation thresholds. The crosses and the dashed vertical and horizontal lines specify the experimentally defined regimes, in which the nanogratings have been observed. Laser irradiation conditions: irradiation wavelength $\lambda = 800$ nm, beam waist $w_0 = 1\mu m$. Nanogratings are erased above the highlighted regions for corresponding pulse durations.

$T_N \lim_{n\to\infty} \frac{1-\alpha^N}{1-\alpha} = \frac{T_N}{1-\alpha}$ [335].

The calculated parameter window for nanograting survival is shown in Fig. 6.16(a). As in previous case, the reported laser regimes, where the nanogratings were observed, are mostly below the viscoelastic threshold. The required laser pulse energy for cavitation and for nanograting erasure decreases with the increasing repetition rate, as higher temperatures are reached after multipulse laser irradiation. This result is consistent with the fact that nanogratings formation in glasses is limited by heat accumulation effects [7, 16, 23]. In fact, the repetition rate dependency of the threshold for nanograting formation, experimentally observed by Richter et al. [16,22], is qualitatively reproduced.

One can expect, that short pulses $\theta = 40 - 80$ fs give still a large interval of pulse energies up to $\Sigma = 1\mu J$ commonly used in experiments [15, 44, 97], where the structure relaxation is not attained for high repetition rates. In contrast, the ultrashort pulses longer than $\theta = 150$ fs for the same pulse energies unavoidably overcome the threshold, while increasing the repetition rate.

6.9 Conclusions

We have numerically investigated the regimes of ultrashort laser irradiation of fused silica, providing a full scenario of laser-affected zone evolution from femtoseconds to microseconds and elucidating the role of laser parameters in resulting glass modifications and mechanisms of nanogratings formation and erasure. For this, a self-consistent multiphysical model has been developed including Maxwell, electron density evolution, electron-ion heat transfer and thermo-elastoplastic wave equations.

Based on the detailed analysis of the possible scenarios of glass decomposition, we have demonstrated that voids of one hundred nanometer sizes are firstly formed satisfying Grady's viscoelastic criterion of decomposition in liquid [172] if temperatures as high as $T \approx 2000$ K are reached in the center of the heat-affected zone. On one hand, higher processing temperatures/pressures allow for rapid nanocavitation responsible for nanopores formation. On the other hand, we elucidate that the temperatures higher than $T \approx 3000$ K lead to a hydrodynamic growth of nanopores by solving Rayleigh-Plesset equation. A similar temperature threshold is expected for structural relaxation of laser-induced modification, limiting the amount of decomposition. The competition processes are investigated as a function of local temperatures/pressures, and the parameter window for nanopore formation and stability, required for nanogratings formation, is defined.

By taking into account the temperature evolution up to the fast cooling of the lattice and estimated thresholds for glass modification, we have derived the critical laser regimes for different pulse energies,

pulse durations and repetition rates. An interplay between photoionization and avalanche ionization, described by multiple rate equation model [68], is shown to be responsible for the decay of the threshold with the increasing pulse duration. Furthermore, the heat accumulation effect significantly affects the threshold in the case of multipulse ultrashort laser irradiation.

The obtained dependencies explain, both qualitatively and quantitatively, the conditions for nanogratings formation and erasure consistent with the numerous independent experimental findings [10, 13, 23, 39]. Particularly, it is shown that viscoelastic relaxation is responsible for disrupted laser-induced modifications for energies higher than 500 nJ and pulse durations longer than 200 fs. A similar trend is expected for repetition rates, higher than 100 kHz, when the local temperatures overcome $T = 3000$ K. Based on the numerical results, we propose that shorter pulses are beneficial to apply for nanostructuring at high repetition rates, as they provide a larger interval of pulse energies and higher electron densities without surpassing the relaxation threshold. In fact, the described threshold dependency can be applied for any high-temperature threshold of glass decomposition, for example, for laser-induced microvoid formation [9,10]. Although the experiments are still required to elucidate and to confirm the laser parameter dependencies of void formation and dynamics on the nanoscales and microscales, the pulse duration dependencies of the modification threshold similar to the one discussed in this article have been reported [2, 10, 11, 31].

The presented results are crucial for understanding the fundamental mechanisms of ultrashort laser-induced modification. The deduced dependencies are helpful for defining the optimal laser parameters for nanostructuring or avoiding the nanostructure organization and for developing techniques for nanogratings rewriting [39, 41].

Chapter 7

General conclusions and outlook

7.1 Conclusions

This thesis provides new insights into the numerical modeling of ultrashort laser interaction with fused silica. Particularly, the mechanism of volume nanogratings formation in glasses is investigated.

A self-consistent model is developed for numerical study of femtosecond laser interaction with dielectrics. The model takes into account ultrashort laser propagation in media with transient optical properties changing nonlinearly due to excitation/relaxation processes by coupling the nonlinear Maxwell's equations with the free carrier rate equation. A numerical GPU-based method is proposed for fast computational realization.

Firstly, electromagnetic propagation model has been verified by comparing with Mie analytical solution for a small subwavelength sphere. Then, the model is coupled with nonlinear ionization to elucidate the mechanisms of volume nanograting formation in glass. The goal was also to define the influence of laser irradiation parameters on the electronic modifications. As a result of these first series of simulations, the following results have been obtained

(i) It is shown that ultrashort laser interaction with randomly distributed inhomogeneities in fused silica results in three-dimensional periodic arrangement of plasma nanoplanes perpendicular to local laser polarization without any presence of the sharp interface between laser-affected and unaffected zones.

(ii) The orientation of the nanoplanes is explained by the unidirectional local near-field enhancement resulting in the nanoplasmas growth perpendicular to the local laser polarization. This effect takes place as a result of photoionization processes, which change the local optical properties of the glass.

(iii) The subwavelength periodicity is related to the coherent superposition of the multiple far-field scattered waves from the formed nanoplanes and is shown to depend on the initial local concentration of inhomogeneities.

(iv) The locality, the self-replication mechanism of their formation and the strong local orientation dependence on the laser polarization are the other properties, investigated in this thesis, which make the laser-induced nanoplasmas a perfect candidate for explaining the volume nanogratings formation. The formation of ring-like electronic modification, radially oriented nanoplasmas and Archimedian spiral nanostructures by applying radial, azimuthal and spiral laser polarizations is investigated numerically. Circular polarized beams are shown to be beneficial to prevent the nanostructure self-organization.

(v) Importantly, it is shown that the laser-induced nanopores inside fused silica bulk can play the role of random scattering centers. The results of multipulse feedback electromagnetic simulations are provided to support the idea that the nanoplanes can grow consequently on a shot-to-shot basis, forming the nanoporous layers.

Nanopore formation processes are then investigated by a more complete multiphysical model that we have developed. This model, apart from the electromagnetic approach coupled with free carrier rate equation, includes electron-ion temperature model and thermo-elastoplastic wave equations for fused silica. The aim of this development was to connect the laser irradiation conditions with final laser-induced modifications. The spatial distributions of laser-induced temperatures, stresses, densities and transient refractive indices are calculated within this approach. Viscoelastic model for spall in

liquid and classical nucleation theory are applied to define the conditions for glass decomposition. Additionally, the further nanopores evolution is elucidated by solving hydrodynamic Rayleigh-Plesset equation for fused silica and borosilicate glasses. As a result of these simulations, we have obtained the following main results

(i) The thermomechanical conditions for cavitation and nucleation are defined. The numerical results indicate the required laser-induced pressures/temperatures for the dominance of cavitation or nucleation.

(ii) The conditions for nanogratings survival are related to the presence of the nanopores, evolving from one pulse to another by electromagnetic field enhancement but not by the hydrodynamic expansion. The results indicate a narrower laser parameter window for nanogratings inscription in borosilicate glass.

Furthermore, the influence of laser parameters on the threshold conditions for nanogratings formation and erasure is investigated. The performed calculations have shown that the laser pulse energy and pulse duration dependencies of the nanogratings formation/erasure and void formation can be qualitatively reproduced by combining electromagnetic approach, multiple rate model for fused silica excitation, two-temperature model and simple temperature criteria for cavitation, nucleation and hydrodynamic growth of nanopores. More precisely, the competition between the photoionization and the avalanche ionization given by multiple rate equation results in the decreasing laser pulse energy threshold for nanovoid formation with the increasing ultrashort pulse duration. We show that the laser pulse energy threshold can be also decreased by increasing the repetition rate in multipulse irradiation regimes.

In addition, femtosecond laser interactions with rough fused silica surface have been numerically investigated. These calculations have clearly demonstrated that

(i) The mechanism of deep-subwavelength (high spatial frequency) nanoripples formation is shown to be similar to the one for volume nanogratings, i. e. it is based on the nanoplasmas growth due to local near-field enhancement and photoionization in the intensity-enhanced areas and the periodicity is related to the standing wave formed by the coherent superposition of multiple scattered waves. The nanoplasmas grow below the surface from the pre-distributed radiation remnants formed by the interference of the incident light with near-fields of inhomogeneities on the surface.

(ii) The transitions between different ripples morphologies are investigated within one numerical approach. The transition from high spatial frequency to parallel-oriented low spatial frequency ripples is shown to have a non-metallic nature, whereas the origin of perpendicular-oriented low spatial frequency ripples is the transition to metallic optical properties of laser-irradiated dielectric.

The performed numerical analysis can be used for a better understanding of the mechanisms of periodic nanostructure formation in glasses and the laser parameter dependencies of the laser-induced modifications during and after ultrashort laser propagation. The developed model provides important insights into the definition of the optimal parameters for nanostructuring or avoiding the nanostructure organization.

7.2 Perspectives

Among the perspectives of this study, we can mention, for instance, the followings. From the numerical point of view, the next step may include

(i) Development of an analytic theoretical model to get a better understanding of the nature of subwavelength non-propagating standing waves inside the material as well as the influence of the nonlinear effects on the propagation. The extensions of Mie theory to define the scattered fields for a system of multiple spheres and a sphere near the interface with dispersive media are of particular interest.

(ii) Using alternative more precise electromagnetic methods (finite element methods, Galerkin's method, unconditionally stable and frequency-dependent methods, discrete dipole approximation etc.) and different roughness discretizations (e. g. introduced analytically or by surface integral equations).

(iii) Elucidating the role of the nonlinear effects such as ponderomotive force and electron density diffusion for high intensity irradiation as well as laser frequency chirp and spherical aberration

effects based on separate and combined numerical approaches and taking into account ultrashort laser propagation in nonlinear dispersive media.

(iv) Further investigations of periodic nanostructure formation in the bulk and on the surface of different semiconductors and dielectrics with different optical properties. For example, the formation of volume nanogratings parallel to the laser polarization has been recently reported in few indirect semiconductors (Si, 4H-SiC, GaP). Additionally, ultrashort laser-induced ripples high spatial frequency oriented parallel to the laser polarization are typically observed on the surface of metals and semiconductors.

(v) Investigation of the validity of the two-temperature model in the laser-matter interaction with dielectrics, paying a special attention on the electron-phonon transfer temporal scales, glass transition/melting processes which can influence the final results.

(vi) Development of hydrodynamic codes based on the solution of Navier-Stokes equations in order to describe the dynamics/formation mechanisms of voids/nanopores and the material movement on nanosecond and microsecond timescales due to single and collective thermo-mechanical effects and also to define better the role of high temperatures and pressures on the viscoelastic parameters and the equation of state of laser-irradiated glasses.

(vii) Molecular dynamics can be an alternative promising approach to gain better knowledge on the properties of glasses in solid and liquid state. Additionally, molecular dynamics can be coupled with the method developed in this thesis, taking into account the inhomogeneous distribution of the electrons due to nonlinear propagation and the temperature evolution after ultrafast laser material excitation.

From the applicative point of view, it will be interesting to use the developed model for:

(i) Elucidating the influence of laser parameters such as laser pulse energy, pulse duration, numerical aperture, laser wavelength, polarization and repetition rate (if several pulses are applied) on the final modification, e. g. transient refractive changes, void/nanopores formation. The laser parameter dependency on the threshold for single void nanochannel formation is essential for the applications in nanofluidics. Additionally, the numerical calculations for temperature accumulation effects and their influence on the thresholds for cavitation or erasure of the nanostructures can be used to interpret the experimental results for different repetition rates and number of applied pulses.

(ii) Investigating and optimizing the diffraction signal from the three-dimensional birefringent laser-induced structures for the development of polarization-sensitive devices and optical data storage.

(iii) Verification of simple criteria for cavitation and nucleation used in this thesis by applying to a wider range of dielectrics and semiconductors and comparing with the final laser-induced modifications revealed experimentally.

(iv) Connecting the temporal refractive index change evolution, time-resolved experimentally, with the temperature/density profiles evolution calculated by numerical approaches.

As a result, the field of the possible applications can be extended to a wide range of glasses, as well as semiconductors, crystals and other dielectric materials.

Bibliography

[1] K. Sugioka and Y. Cheng. Ultrafast lasers - reliable tools for advanced materials processing. *Light: Science & Applications*, 3:1–12, 2014.

[2] P. K. Velpula, M. K. Bhuyan, F. Courvoisier, H. Zhang, J.-P. Colombier, and R. Stoian. Spatio-temporal dynamics in nondiffractive bessel ultrafast laser nanoscale volume structuring. *Laser & Photonics Reviews*, 10(2):230–244, 2016.

[3] D. Tan, K. N. Sharafudeen, Y. Yue, and J. Qiu. Femtosecond laser induced phenomena in transparent solid materials: Fundamentals and applications. *Progress in Materials Science*, 76:154–228, 2016.

[4] Y. Shimotsuma, P. G. Kazansky, J. Qiu, and K. Hirao. Self-organized nanogratings in glass irradiated by ultrashort light pulses. *Phys. Rev. Lett.*, 91:247405, Dec 2003.

[5] K. Mishchik, G. Cheng, G. Huo, I. M. Burakov, C. Mauclair, A. Mermillod-Blondin, A. Rosenfeld, Y. Ouerdane, A. Boukenter, O. Parriaux, and R. Stoian. Nanosize structural modifications with polarization functions in ultrafast laserirradiated bulk fused silica. *Opt. Express*, 18(24):24809–24824, Nov 2010.

[6] A. Royon. Nonlinear femtosecond near infrared laser structuring in oxide glasses. *Ph.D. thesis*, 2009.

[7] M. Lancry, B. Poumellec, J. Canning, K. Cook, J.-C. Poulin, and F. Brisset. Ultrafast nanoporous silica formation driven by femtosecond laser irradiation. *Laser & Photonics Reviews*, 7(6):953–962, 2013.

[8] M. Malinauskas, A. Žukauskas, S. Hasegawa, Y. Hayasaki, V. Mizeikis, R. Buividas, and S. Juodkazis. Ultrafast laser processing of materials: from science to industry. *Light: Science & Applications*, 5(8):e16133, 2016.

[9] S. Juodkazis, K. Nishimura, S. Tanaka, H. Misawa, E. G. Gamaly, B. Luther-Davies, L. Hallo, P. Nicolai, and V. T. Tikhonchuk. Laser-induced microexplosion confined in the bulk of a sapphire crystal: Evidence of multimegabar pressures. *Phys. Rev. Lett.*, 96:166101, Apr 2006.

[10] B. Poumellec, M. Lancry, A. Chahid-Erraji, and P. G. Kazansky. Modification thresholds in femtosecond laser processing of pure silica: review of dependencies on laser parameters. *Opt. Mater. Express*, 1(4):766–782, Aug 2011.

[11] K. Mishchik, C. D'Amico, P. K. Velpula, C. Mauclair, A. Boukenter, Y. Ouerdane, and R. Stoian. Ultrafast laser induced electronic and structural modifications in bulk fused silica. *Journal of Applied Physics*, 114(13), 2013.

[12] M. E Povarnitsyn, T. E Itina, M. Sentis, K. V. Khishchenko, and P. R. Levashov. Material decomposition mechanisms in femtosecond laser interactions with metals. *Physical Review B*, 75(23):235414, 2007.

[13] C. Hnatovsky, R. S. Taylor, P. P. Rajeev, E. Simova, V. R. Bhardwaj, D. M. Rayner, and P. B. Corkum. Pulse duration dependence of femtosecond-laser-fabricated nanogratings in fused silica. *Applied Physics Letters*, 87(1):–, 2005.

[14] P. G. Kazansky, W. Yang, E. Bricchi, J. Bovatsek, A. Arai, Y. Shimotsuma, K. Miura, and K. Hirao. Quill writing with ultrashort light pulses in transparent materials. *Applied Physics Letters*, 90(15):–, 2007.

[15] C. Mauclair, M. Zamfirescu, J. P. Colombier, G. Cheng, K. Mishchik, E. Audouard, and R. Stoian. Control of ultrafast laser-induced bulk nanogratings in fused silica via pulse time envelopes. *Opt. Express*, 20(12):12997–13005, Jun 2012.

[16] S. Richter, M. Heinrich, S. Döring, A. Tünnermann, S. Nolte, and U. Peschel. Nanogratings in fused silica: Formation, control, and applications. *Journal of Laser Applications*, 24(4):–, 2012.

[17] D. G. Papazoglou, D. Abdollahpour, and S. Tzortzakis. Ultrafast electron and material dynamics following femtosecond filamentation induced excitation of transparent solids. *Applied Physics A*, 114(1):161–168, 2014.

[18] Y. Liao, J. Ni, L. Qiao, M. Huang, Y. Bellouard, K. Sugioka, and Y. Cheng. High-fidelity visualization of formation of volume nanogratings in porous glass by femtosecond laser irradiation. *Optica*, 2(4):329–334, Apr 2015.

[19] M. S. Ahsan, Y. G. Kim, and M. S. Lee. Formation mechanism of nanostructures in sodaâĂŞlime glass using femtosecond laser. *Journal of Non-Crystalline Solids*, 357(3):851 – 857, 2011.

[20] F. Zhang, H. Zhang, G. Dong, and J. Qiu. Embedded nanogratings in germanium dioxide glass induced by femtosecond laser direct writing. *J. Opt. Soc. Am. B*, 31(4):860–864, Apr 2014.

[21] F. Zimmermann, A. Plech, S. Richter, A. Tünnermann, and S. Nolte. Ultrashort laser pulse induced nanogratings in borosilicate glass. *Applied Physics Letters*, 104(21), 2014.

[22] S. Richter, D. Möncke, F. Zimmermann, E. I. Kamitsos, L. Wondraczek, A. Tünnermann, and S. Nolte. Ultrashort pulse induced modifications in ule - from nanograting formation to laser darkening. *Opt. Mater. Express*, 5(8):1834–1850, Aug 2015.

[23] M. Lancry, J. Canning, K. Cook, M. Heili, D. R. Neuville, and B. Poumellec. Nanoscale femtosecond laser milling and control of nanoporosity in the normal and anomalous regimes of geo2-sio2 glasses. *Opt. Mater. Express*, 6(2):321–330, Feb 2016.

[24] T. Okada, T. Tomita, S. Matsuo, S. Hashimoto, Y. Ishida, S. Kiyama, and T. Takahashi. Formation of periodic strained layers associated with nanovoids inside a silicon carbide single crystal induced by femtosecond laser irradiation. *Journal of Applied Physics*, 106(5), 2009.

[25] M. Mori, Y. Shimotsuma, T. Sei, M. Sakakura, K. Miura, and H. Udono. Tailoring thermoelectric properties of nanostructured crystal silicon fabricated by infrared femtosecond laser direct writing. *Physica Status Solidi A*, 212(4):n/a–n/a, 2015.

[26] Y. Shimotsuma, T. Sei, M. Mori, M. Sakakura, and K. Miura. Self-organization of polarization-dependent periodic nanostructures embedded in iii–v semiconductor materials. *Applied Physics A*, 122(3):1–7, 2016.

[27] M. Sakakura, M. Terazima, Y. Shimotsuma, K. Miura, and K. Hirao. Thermal and shock induced modification inside a silica glass by focused femtosecond laser pulse. *Journal of Applied Physics*, 109(2), 2011.

[28] C. Mauclair, K. Mishchik, A. Mermillod-Blondin, A. Rosenfeld, I.-V. Hertel, E. Audouard, and R. Stoian. Optimization of the energy deposition in glasses with temporally-shaped femtosecond laser pulses. *Physics Procedia*, 12:76–81, 2011.

[29] T. Yoshino, Y. Ozeki, M. Matsumoto, and K. Itoh. In situ micro-raman investigation of spatio-temporal evolution of heat in ultrafast laser microprocessing of glass. *Japanese Journal of Applied Physics*, 51(10R):102403, 2012.

[30] I. Miyamoto, K. Cvecek, and M. Schmidt. Crack-free conditions in welding of glass by ultrashort laser pulse. *Opt. Express*, 21(12):14291–14302, Jun 2013.

[31] A. Mermillod-Blondin, I. M. Burakov, Yu. P. Meshcheryakov, N. M. Bulgakova, E. Audouard, A. Rosenfeld, A. Husakou, I. V. Hertel, and R. Stoian. Flipping the sign of refractive index changes in ultrafast and temporally shaped laser-irradiated borosilicate crown optical glass at high repetition rates. *Phys. Rev. B*, 77:104205, Mar 2008.

[32] Y. Liao, B. Zeng, L. Qiao, L. Liu, K. Sugioka, and Y. Cheng. Threshold effect in femtosecond laser induced nanograting formation in glass: influence of the pulse duration. *Applied Physics A*, 114(1):223–230, 2014.

[33] C. Hnatovsky, V. Shvedov, W. Krolikowski, and A. Rode. Revealing local field structure of focused ultrashort pulses. *Phys. Rev. Lett.*, 106:123901, Mar 2011.

[34] F. Zimmermann, A. Plech, S. Richter, A. Tünnermann, and S. Nolte. The onset of ultrashort pulse-induced nanogratings. *Laser & Photonics Reviews*, 10(2):327–334, 2016.

[35] M. Sun, U. Eppelt, W. Schulz, and J. Zhu. Role of thermal ionization in internal modification of bulk borosilicate glass with picosecond laser pulses at high repetition rates. *Opt. Mater. Express*, 3(10):1716–1726, Oct 2013.

[36] O. Dematteo Caulier, K. Mishchik, B. Chimier, S. Skupin, A. Bourgeade, C. Javaux Léger, R. Kling, C. Hönninger, J. Lopez, V. Tikhonchuk, and G. Duchateau. Femtosecond laser pulse train interaction with dielectric materials. *Applied Physics Letters*, 107(18), 2015.

[37] S. Richter, F. Hashimoto, F. Zimmermann, Y. Ozeki, K. Itoh, A. Tünnermann, and S. Nolte. Spatial and temporal temperature distribution of ultrashort pulse induced heat accumulation in glass. *Proc. SPIE*, 9355:935515–935515–8, 2015.

[38] S. Richter, C. Miese, S. Döring, F. Zimmermann, M. J. Withford, A. Tünnermann, and S. Nolte. Laser induced nanogratings beyond fused silica - periodic nanostructures in borosilicate glasses and ule^{TM}. *Opt. Mater. Express*, 3(8):1161–1166, Aug 2013.

[39] R. Taylor, C. Hnatovsky, and E. Simova. Applications of femtosecond laser induced self-organized planar nanocracks inside fused silica glass. *Laser & Photonics Reviews*, 2(1-2):26–46, 2008.

[40] J. Zhang, M. Gecevičius, M. Beresna, and P. G. Kazansky. Seemingly unlimited lifetime data storage in nanostructured glass. *Physical review letters*, 112(3):033901, 2014.

[41] F. Zimmermann, A. Plech, S. Richter, A. Tünnermann, and S. Nolte. On the rewriting of ultrashort pulse-induced nanogratings. *Opt. Lett.*, 40(9):2049–2052, May 2015.

[42] M. Beresna, M. Gecevičius, and P. G. Kazansky. Polarization sensitive elements fabricated by femtosecond laser nanostructuring of glass. *Opt. Mater. Express*, 1(4):783–795, Aug 2011.

[43] Y. Liao and Y. Cheng. Femtosecond laser 3d fabrication in porous glass for micro- and nanofluidic applications. *Micromachines*, 5(4):1106, 2014.

[44] V. R. Bhardwaj, E. Simova, P. P. Rajeev, C. Hnatovsky, R. S. Taylor, D. M. Rayner, and P. B. Corkum. Optically produced arrays of planar nanostructures inside fused silica. *Phys. Rev. Lett.*, 96:057404, Feb 2006.

[45] Y. Dai, G. Wu, X. Lin, G. Ma, and J. Qiu. Femtosecond laser induced rotated 3d self-organized nanograting in fused silica. *Opt. Express*, 20(16):18072–18078, Jul 2012.

[46] C. Hnatovsky, V. G. Shvedov, and W. Krolikowski. The role of light-induced nanostructures in femtosecond laser micromachining with vector and scalar pulses. *Opt. Express*, 21(10):12651–12656, May 2013.

[47] R. Stoian, K. Mishchik, G. Cheng, C. Mauclair, C. D'Amico, J. P. Colombier, and M. Zamfirescu. Investigation and control of ultrafast laser-induced isotropic and anisotropic nanoscale-modulated index patterns in bulk fused silica. *Opt. Mater. Express*, 3(10):1755–1768, Oct 2013.

[48] R. S. Taylor, E. Simova, and C. Hnatovsky. Creation of chiral structures inside fused silica glass. *Opt. Lett.*, 33(12):1312–1314, Jun 2008.

[49] J. Ouyang, W. Perrie, O. J. Allegre, T. Heil, Y. Jin, E. Fearon, D. Eckford, S. P. Edwardson, and G. Dearden. Tailored optical vector fields for ultrashort-pulse laser induced complex surface plasmon structuring. *Opt. Express*, 23(10):12562–12572, May 2015.

[50] J. Nivas, S. He, A. Rubano, A. Vecchione, D. Paparo, L. Marucci, R. Bruzzese, and S. Amoruso. Direct femtosecond laser surface structuring with optical vortex beams generated by a q-plate. *Scientific Reports*, 5(17929), 2015.

[51] S. Hasegawa and Y. Hayasaki. Holographic vector wave femtosecond laser processing. *International Journal of Optomechatronics*, 8(2):73–88, 2014.

[52] S. Richter, M. Heinrich, S. Döring, A. Tünnermann, and S. Nolte. Formation of femtosecond laser-induced nanogratings at high repetition rates. *Applied Physics A*, 104(2):503–507, 2011.

[53] F. Zimmermann, S. Richter, R. Buschlinger, S. Shukla, R. Heintzmann, U. Peschel, and S. Nolte. *Ultrashort pulse-induced periodic nanostructures in bulk glass: from fundamentals to applications in high-resolution microscopy.* Walter de Gruyter GmbH & Co KG, 2015.

[54] Y. Liao, W. Pan, Y. Cui, L. Qiao, Y. Bellouard, K. Sugioka, and Y. Cheng. Formation of in-volume nanogratings with sub-100-nm periods in glass by femtosecond laser irradiation. *Opt. Lett.*, 40(15):3623–3626, Aug 2015.

[55] W. Yang, E. Bricchi, P. G. Kazansky, J. Bovatsek, and A. Y. Arai. Self-assembled periodic sub-wavelength structures by femtosecond laser direct writing. *Opt. Express*, 14(21):10117–10124, Oct 2006.

[56] F. Liang, R. Vallée, and S. L. Chin. Mechanism of nanograting formation on the surface of fused silica. *Opt. Express*, 20(4):4389–4396, Feb 2012.

[57] Md. S. Ahsan, M. S. Lee, M. K. Hasan, Y.-C. Noh, I.-B. Sohn, F. Ahmed, and Jun M. B. G. Formation mechanism of self-organized nano-ripples on quartzsurface using femtosecond laser pulses. *Optik*, 126(24):5979, 2015.

[58] S. Richter, S. Döring, F. Burmeister, F. Zimmermann, A. Tünnermann, and S. Nolte. Formation of periodic disruptions induced by heat accumulation of femtosecond laser pulses. *Opt. Express*, 21(13):15452–15463, Jul 2013.

[59] D. Puerto, J. Siegel, W. Gawelda, M. Galvan-Sosa, L. Ehrentraut, J. Bonse, and J. Solis. Dynamics of plasma formation, relaxation, and topography modification induced by femtosecond laser pulses in crystalline and amorphous dielectrics. *JOSA B*, 27(5):1065–1076, 2010.

[60] C. Mauclair, A. Mermillod-Blondin, K. Mishchik, Jörn Bonse, A. Rosenfeld, J.-P. Colombier, and R. Stoian. Excitation and relaxation dynamics in ultrafast laser irradiated optical glasses. *High Power Laser Science and Engineering*, 4(e46), 2016.

[61] P. Martin, S. Guizard, P. Daguzan, G. Petite, P. D'Oliveira, P. Meynadier, and M. Perdrix. Subpicosecond study of carrier trapping dynamics in wide-band-gap crystals. *Phys. Rev. B*, 55:5799–5810, Mar 1997.

[62] Q. Sun, H.-B. Jiang, Y. Liu, Z.-X. Wu, H. Yang, and Q.-H. Gong. Diagnose parameters of plasma induced by femtosecond laser pulse in quartz and glasses. *Frontiers of Physics in China*, 1(1):67–71, 2006.

[63] M. Sakakura, M. Terazima, Y. Shimotsuma, K. Miura, and K. Hirao. Observation of pressure wave generated by focusing a femtosecond laser pulse inside a glass. *Opt. Express*, 15(9):5674–5686, Apr 2007.

[64] A. Mermillod-Blondin, J. Bonse, A. Rosenfeld, I. V. Hertel, Yu. P. Meshcheryakov, N. M. Bulgakova, E. Audouard, and R. Stoian. Dynamics of femtosecond laser induced voidlike structures in fused silica. *Applied Physics Letters*, 94(4), 2009.

[65] M. Sakakura, M. Terazima, Y. Shimotsuma, K. Miura, and K. Hirao. Elastic and thermal dynamics in femtosecond laser-induced structural change inside glasses studied by the transient lens method. *Las. Chem.*, 2010:1–15, 2010.

[66] A. Mermillod-Blondin, H. Mentzel, and A. Rosenfeld. Time-resolved microscopy with random lasers. *Opt. Lett.*, 38(20):4112–4115, Oct 2013.

[67] A. Kaiser, B. Rethfeld, M. Vicanek, and G. Simon. Microscopic processes in dielectrics under irradiation by subpicosecond laser pulses. *Phys. Rev. B*, 61:11437–11450, May 2000.

[68] B. Rethfeld. Unified model for the free-electron avalanche in laser-irradiated dielectrics. *Phys. Rev. Lett.*, 92:187401, May 2004.

[69] A. Couairon, L. Sudrie, M. Franco, B. Prade, and A. Mysyrowicz. Filamentation and damage in fused silica induced by tightly focused femtosecond laser pulses. *Phys. Rev. B*, 71:125435, Mar 2005.

[70] I. M. Burakov, N. M. Bulgakova, R. Stoian, A. Mermillod-Blondin, E. Audouard, A. Rosenfeld, A. Husakou, and I. V. Hertel. Spatial distribution of refractive index variations induced in bulk fused silica by single ultrashort and short laser pulses. *Journal of Applied Physics*, 101(4):043506, 2007.

[71] K. I. Popov, C. McElcheran, K. Briggs, S. Mack, and Lora Ramunno. Morphology of femtosecond laser modification of bulk dielectrics. *Opt. Express*, 19(1):271–282, Jan 2011.

[72] H. Schmitz and V. Mezentsev. Full-vectorial modeling of femtosecond pulses for laser inscription of photonic structures. *J. Opt. Soc. Am. B*, 29(6):1208–1217, Jun 2012.

[73] N. S. Shcheblanov, E. P. Silaeva, and T. E. Itina. Electronic excitation and relaxation processes in wide band gap dielectric materials in the transition region of the keldysh parameter. *Applied Surface Science*, 258(23):9417 – 9420, 2012. {EMRS} 2011 Spring Symp J: Laser Materials Processing for Micro and Nano Applications.

[74] N. M. Bulgakova, V. P. Zhukov, and Y. P. Meshcheryakov. Theoretical treatments of ultrashort pulse laser processing of transparent materials: toward understanding the volume nanograting formation and "quill" writing effect. *Applied Physics B*, 113:437–449, 2013.

[75] N. M. Bulgakova, V. P. Zhukov, S. V. Sonina, and Y. P. Meshcheryakov. Modification of transparent materials with ultrashort laser pulses: What is energetically and mechanically meaningful? *Journal of Applied Physics*, 118(23), 2015.

[76] J. Z. P. Skolski, G. R. B. E. Römer, J. V. Obona, V. Ocelik, A. J. Huis in 't Veld, and J. Th. M. De Hosson. Laser-induced periodic surface structures: Fingerprints of light localization. *Phys. Rev. B*, 85:075320, Feb 2012.

[77] J. Z. P. Skolski, G. R. B. E. Römer, J. Vincenc Obona, and A. J. Huis in 't Veld. Modeling laser-induced periodic surface structures: Finite-difference time-domain feedback simulations. *Journal of Applied Physics*, 115(10):–, 2014.

[78] J.-L. Déziel, J. Dumont, D. Gagnon, L. J. Doubé, S. Messaddeq, and Messaddeq Y. Toward the formation of crossed laser-induced periodic surface structures. *Journal of Optics*, 17(075405), 2015.

[79] H. Zhang, J.-P. Colombier, C. Li, N. Faure, G. Cheng, and R. Stoian. Coherence in ultrafast laser-induced periodic surface structures. *Phys. Rev. B*, 92:174109, Nov 2015.

[80] J. E. Sipe, J. F. Young, J. S. Preston, and H. M. van Driel. Laser-induced periodic surface structure. i. theory. *Phys. Rev. B*, 27:1141–1154, Jan 1983.

[81] J.-L. Déziel, J. Dumont, D. Gagnon, and Dubé L. J. Constructive feedback for the growth of laser-induced periodic surface structures. *Phys. Status Solidi (c)*, 13:121, 2016.

[82] R. Buschlinger, S. Nolte, and U. Peschel. Self-organized pattern formation in laser-induced multiphoton ionization. *Phys. Rev. B*, 89:184306, May 2014.

[83] S. Najafi, A. S. Arabanian, and R. Massudi. Comprehensive modeling of structural modification induced by a femtosecond laser pulse inside fused silica glass. *Journal of Physics D: Applied Physics*, 49(25):255101, 2016.

[84] S. Elhadj, M. J. Matthews, and S. T. Yang. Combined infrared thermal imaging and laser heating for the study of materials thermophysical and processing properties at high temperatures. *Critical Reviews in Solid State and Materials Sciences*, 39(3):175–196, 2014.

[85] T. Doualle, L. Gallais, P. Cormont, D. Hébert, P. Combis, and J.-L. Rullier. Thermo-mechanical simulations of co2 laser–fused silica interactions. *Journal of Applied Physics*, 119(11):113106, 2016.

[86] R. M. Vignes, T. F. Soules, J. S. Stolken, R. R. Settgast, S. Elhadj, and M. J. Matthews. Thermomechanical modeling of laser-induced structural relaxation and deformation of glass: volume changes in fused silica at high temperatures. *Journal of the American Ceramic Society*, 96(1):137–145, 2013.

[87] E. A. Romanova and A. I. Konyukhov. Study of irradiation conditions and thermodynamics of optical glass in the problem of modification of materials by femtosecond laser pulses. *Optics and Spectroscopy*, 104(5):784–790, 2008.

[88] I. Mirza, N. M. Bulgakova, J. Tomáštík, V. Michálek, O. Haderka, L. Fekete, and T. Mocek. Ultrashort pulse laser ablation of dielectrics: Thresholds, mechanisms, role of breakdown. *Scientific Reports*, 6, 2016.

[89] E. G. Gamaly, S. Juodkazis, K. Nishimura, H. Misawa, B. Luther-Davies, L. Hallo, P. Nicolai, and V. T. Tikhonchuk. Laser-matter interaction in the bulk of a transparent solid: Confined microexplosion and void formation. *Phys. Rev. B*, 73:214101, Jun 2006.

[90] L. Hallo, A. Bourgeade, V. T. Tikhonchuk, C. Mezel, and J. Breil. Model and numerical simulations of the propagation and absorption of a short laser pulse in a transparent dielectric material: Blast-wave launch and cavity formation. *Physical Review B*, 76:024101, 2007.

[91] R. Buividas, L. Rosa, R. Šliupas, T. Kudrius, G. Šlekys, V. Datsyuk, and S. Juodkazis. Mechanism of fine ripple formation on surfaces of (semi)transparent materials via a half-wavelength cavity feedback. *Nanotechnology*, 22(5):055304, 2011.

[92] L. P. R. Ramirez, M. Heinrich, S. Richter, F. Dreisow, R. Keil, A. V. Korovin, U. Peschel, S. Nolte, and A. Tünnermann. Tuning the structural properties of femtosecond-laser-induced nanogratings. *Applied Physics A*, 100(1):1–6, 2010.

[93] S. Höhm, A. Rosenfeld, Jörg Krüger, and Jörn Bonse. Femtosecond laser-induced periodic surface structures on silica. *Journal of Applied Physics*, 112(1):014901, 2012.

[94] S. Richter, F. Jia, M. Heinrich, S. Döring, U. Peschel, A. Tünnermann, and S. Nolte. The role of self-trapped excitons and defects in the formation of nanogratings in fused silica. *Opt. Lett.*, 37(4):482–484, Feb 2012.

[95] M. Beresna, M. Gecevičius, P. G. Kazansky, T. Taylor, and A. V. Kavokin. Exciton mediated self-organization in glass driven by ultrashort light pulses. *Applied Physics Letters*, 101(5):–, 2012.

[96] N. M. Bulgakova and V. P. Zhukov. *Continuum Models of Ultrashort LaserMatter Interaction in Application to WideBandgap Dielectrics*, volume 191 of *Springer Series in Materials Science*. Springer International Publishing, 2014.

[97] M. Hörstmann-Jungemann, J. Gottmann, and D. Wortmann. Nano-and microstructuring of sio2 and sapphire with fs-laser induced selective etching. *J. Laser Micro/Nanoeng*, 4(2):135–140, 2009.

[98] Y. Liao, J. Ni, L. Qiao, M. Huang, Y. Bellouard, K. Sugioka, and Y. Cheng. Formation of nanogratings in a porous glass immersed in water by femtosecond laser irradiation. In *Proc. SPIE*, volume 9350, page 93500. Optical Society of America, 2015.

[99] J. Reif, O. Varlamova, S. Uhlig, S. Varlamov, and M. Bestehorn. On the physics of self-organized nanostructure formation upon femtosecond laser ablation. *Applied Physics A*, 117(1):179–184, 2014.

[100] R. Le Harzic, D. Dörr, D. Sauer, M. Neumeier, M. Epple, H. Zimmermann, and F. Stracke. Large-area, uniform, high-spatial-frequency ripples generated on silicon using a nanojoule-femtosecond laser at high repetition rate. *Opt. Lett.*, 36(2):229–231, Jan 2011.

[101] V. S. Makin and R. S. Makin. Interaction of laser radiation with an axially symmetric polarization with condensed media. *Optics and Spectroscopy*, 115(4):591–595, 2013.

[102] F. Liang, J. Bouchard, S. Leang Chin, and R. Vallée. Defect-assisted local field rearrangement during nanograting formation with femtosecond pulses. *Applied Physics Letters*, 107(6):–, 2015.

[103] S. H́ohm, M. Herzlieb, A. Rosenfeld, J. Kŕuger, and J. Bonse. Dynamics of the formation of laser-induced periodic surface structures (LIPSS) upon femtosecond two-color double-pulse irradiation of metals, semiconductors, and dielectrics. *Applied Surface Science*, 374:331 – 338, 2016.

[104] E. S. Efimenko, A. V. Kim, and M. Quiroga-Teixeiro. Ionization-induced dynamics of laser-matter interaction in a focused laser pulse: A comparative analysis. *Physics of Plasmas*, 18(3):–, 2011.

[105] B. Poumellec, M. Lancry, R. Desmarchelier, E. Hervé, F. Brisset, and J.C. Poulin. Asymmetric orientational writing in glass with femtosecond laser irradiation. *Opt. Mater. Express*, 3(10):1586–1599, Oct 2013.

[106] A. M. Gouda, H. Sakagami, T. Ogata, M. Hashida, and S. Sakabe. The formation mechanism of the periodic nanograting structure by the weibel instability. *Applied Physics A*, 122(4):1–6, 2016.

[107] V. B. Gildenburg and I. A. Pavlichenko. Volume nanograting formation in laser-silica interaction as a result of the 1D plasma-resonance ionization instability. *Physics of Plasmas*, 23(8), 2016.

[108] F. Liang, Q. Sun, D. Gingras, R. Vallée, and S. L. Chin. The transition from smooth modification to nanograting in fused silica. *Applied Physics Letters*, 96(10):–, 2010.

[109] M. Lancry, B. Poumellec, A. Chahid-Erraji, M. Beresna, and P. G. Kazansky. Dependence of the femtosecond laser refractive index change thresholds on the chemical composition of doped-silica glasses. *Opt. Mater. Express*, 1(4):711–723, Aug 2011.

[110] F. A. Umran, Y. Liao, M. M. Elias, K. Sugioka, R. Stoian, G. Cheng, and Y. Cheng. Formation of nanogratings in a transparent material with tunable ionization property by femtosecond laser irradiation. *Opt. Express*, 21(13):15259–15267, Jul 2013.

[111] M. Vangheluwe, Y. Petit, F. Liang, P. Hee, Y. Ledemi, S. Thomas, E. Fargin, T. Cardinal, Y. Messaddeq, L. Canioni, and R. Vallee. Femtosecond laser-induced nanogratings formation assisted by silver ions in a gallophosphate glass and correlated optical properties. In *Photonics North, 2015*, pages 1–6, June 2015.

[112] M. Lancry, F. Brisset, and B. Poumellec. In the heart of nanogratings made up during femtosecond laser irradiation. In *Advanced Photonics & Renewable Energy*, page BWC3. Optical Society of America, 2010.

[113] S. Richter, F. Zimmermann, S. Döring, A. Tünnermann, and S. Nolte. Ultrashort high repetition rate exposure of dielectric materials: laser bonding of glasses analyzed by micro-raman spectroscopy. *Applied Physics A*, 110(1):9–15, 2013.

[114] J. Cao, L. Mazerolles, M. Lancry, F. Brisset, and B. Poumellec. Modifications in lithium niobium silicate glass by femtosecond laser direct writing: morphology, crystallization, and nanostructure. *J. Opt. Soc. Am. B*, 34(1):160–168, Jan 2017.

[115] M. Vangheluwe, F. Liang, Y. Petit, P. Hée, Y. Ledemi, S. Thomas, E. Fargin, T. Cardinal, Y. Messaddeq, L. Canioni, and R. Vallée. Enhancement of nanograting formation assisted by silver ions in a sodium gallophosphate glass. *Opt. Lett.*, 39(19):5491–5494, Oct 2014.

[116] Y. Shimotsuma, K. Hirao, J. Qiu, and P. G. Kazansky. Nano-modification inside transparent materials by femtosecond laser single beam. *Modern Physics Letters B*, 19(05):225–238, 2005.

[117] J. Gottmann, D. Wortmann, and M. Hörstmann-Jungemann. Fabrication of sub-wavelength surface ripples and in-volume nanostructures by fs-laser induced selective etching. *Applied surface science*, 255(10):5641–5646, 2009.

[118] Y. Dai, A. Patel, J. Song, M. Beresna, and P. G. Kazansky. Void-nanograting transition by ultrashort laser pulse irradiation in silica glass. *Opt. Express*, 24(17):19344–19353, Aug 2016.

[119] K. Nakamura, Y. Hosokawa, and H. Masuhara. Anthracene crystallization induced by single-shot femtosecond laser irradiation: Experimental evidence for the important role of bubbles. *Crystal growth & design*, 7(5):885–889, 2007.

[120] A. Soare, R. Dijkink, M. R. Pascual, C. Sun, P. W. Cains, D. Lohse, A. I. Stankiewicz, and H. J. M. Kramer. Crystal nucleation by laser-induced cavitation. *Crystal Growth & Design*, 11(6):2311–2316, 2011.

[121] R. Oguri and K. Ando. Cloud cavitation induced by shock-bubble interaction in a viscoelastic solid. In *Journal of Physics: Conference Series*, volume 656, page 012032. IOP Publishing, 2015.

[122] S. Nakamura, Y. Koyamada, N. Yoshida, N. Karasawa, Sone H., M. Ohtani, Y. Mizuta, R. Morita, H. Shigekawa, and M. Yamashita. Finite-difference time-domain calculation with all parameters of sellmeier's fitting equation for 12-fs laser pulse propagation in a silica fiber. *IEEE Photonics Technology Letters*, 14(4):480–482, April 2002.

[123] S. Nakamura, N. Takasawa, and Y. Koyamada. Comparison between finite-difference time-domain calculation with all parameters of sellmeier's fitting equation and experimental results for slightly chirped 12-fs laser pulse propagation in a silica fiber. *Journal of Lightwave Technology*, 23(2):855–863, Feb 2005.

[124] P. B. Johnson and R. W. Christy. Optical constants of the noble metals. *Phys. Rev. B*, 6:4370–4379, Dec 1972.

[125] K. Sokolowski-Tinten and D. von der Linde. Generation of dense electron-hole plasmas in silicon. *Phys. Rev. B*, 61:2643–2650, Jan 2000.

[126] R. Boyd. *Nonlinear optical susceptibility*. University of Rochester, New York, 2008.

[127] Christopher A. Dailey, Brian J. Burke, and Garth J. Simpson. The general failure of kleinman symmetry in practical nonlinear optical applications. *Chemical Physics Letters*, 390(1):8–13, 2004.

[128] Xianglei Mao, Samuel S. Mao, and R. E. Russo. Imaging femtosecond laser-induced electronic excitation in glass. *Applied Physics Letters*, 82(5):697–699, 2003.

[129] E. G. Gamaly and A. V. Rode. Transient optical properties of dielectrics and semiconductors excited by an ultrashort laser pulse. *J. Opt. Soc. Am. B*, 31(11):C36–C43, Nov 2014.

[130] N. M. Bulgakova, V. P. Zhukov, Y. P. Meshcheryakov, L. Gemini, J. Brajer, D. Rostohar, and T. Mocek. Pulsed laser modification of transparent dielectrics: what can be foreseen and predicted by numerical simulations? *J. Opt. Soc. Am. B*, 31(11):C8–C14, Nov 2014.

[131] K. Eidmann, J. Meyer-ter Vehn, T. Schlegel, and S. Hüller. Hydrodynamic simulation of subpicosecond laser interaction with solid-density matter. *Phys. Rev. E*, 62:1202–1214, Jul 2000.

[132] A. Q. Wu, I. H. Chowdhury, and X. Xu. Femtosecond laser absorption in fused silica: Numerical and experimental investigation. *Phys. Rev. B*, 72:085128, Aug 2005.

[133] N. Varkentina, O. Uteza, N. Sanner, B. Chimier, M. Sentis, and T. Itina. Absorption of femtosecond laser pulse in fused silica: experiments and modelling. In *Proc. SPIE*, volume 7920, page 792003. Optical Society of America, 2011.

[134] A. Rudenko, J.-P. Colombier, and T. Itina. Femtosecond laser irradiation of fused silica with a nanometric inhomogeneity. In *Proc. of the 36th Progress in Electromagnetics Research Conference (PIERS), Prague, 2015*, pages 1870–1876. The Electromagnetics Academy, July 2015.

[135] P. Ginzburg, A. Hayat, N. Berkovitch, and M. Orenstein. Nonlocal ponderomotive nonlinearity in plasmonics. *Opt. Lett.*, 35(10):1551–1553, May 2010.

[136] N. Nozhat and N. Granpayeh. Spm and xpm nonlinear effects in plasmonic directional couplers, considering the ponderomotive metal nonlinearity. *Appl. Opt.*, 53(15):3328–3332, May 2014.

[137] B. C. Stuart, M. D. Feit, S. Herman, A. M. Rubenchik, B. W. Shore, and M. D. Perry. Nanosecond-to-femtosecond laser-induced breakdown in dielectrics. *Phys. Rev. B*, 53:1749–1761, Jan 1996.

[138] L. V. Keldysh. Ionization in the field of a strong electromagnetic wave. *Soviet Physics JETP*, 20:1307–1314, May 1965.

[139] B. Chimier, O. Utéza, N. Sanner, M. Sentis, T. Itina, P. Lassonde, F. Légaré, F. Vidal, and J. C. Kieffer. Damage and ablation thresholds of fused-silica in femtosecond regime. *Phys. Rev. B*, 84:094104, Sep 2011.

[140] M. Lenzner, J. Krüger, S. Sartania, Z. Cheng, Ch. Spielmann, G. Mourou, W. Kautek, and F. Krausz. Femtosecond optical breakdown in dielectrics. *Phys. Rev. Lett.*, 80:4076–4079, May 1998.

[141] M. Li, S. Menon, J. P. Nibarger, and G. N. Gibson. Ultrafast electron dynamics in femtosecond optical breakdown of dielectrics. *Phys. Rev. Lett.*, 82:2394–2397, Mar 1999.

[142] K. Jamshidi-Ghaleh, N. Mansour, and A. Namdar. Nonlinear optical properties of soda-lime glass at 800-nm femtosecond irradiation. *Laser physics*, 15(12):1714–1717, 2005.

[143] K. Jamshidi-Ghaleh and H. Masalehdan. Modeling of nonlinear responses in bk7 glass under irradiation of femtosecond laser pulses. *Optical and Quantum Electronics*, 41(1):47–53, 2009.

[144] X. Jing, J. Shao, J. Zhang, Y. Jin, H. He, and Z. Fan. Calculation of femtosecond pulse laser induced damage threshold for broadband antireflective microstructure arrays. *Opt. Express*, 17(26):24137–24152, Dec 2009.

[145] B. C. Stuart, M. D. Feit, A. M. Rubenchik, B. W. Shore, and M. D. Perry. Laser-induced damage in dielectrics with nanosecond to subpicosecond pulses. *Phys. Rev. Lett.*, 74:2248–2251, Mar 1995.

[146] A.-C. Tien, S. Backus, H. Kapteyn, M. Murnane, and G. Mourou. Short-pulse laser damage in transparent materials as a function of pulse duration. *Phys. Rev. Lett.*, 82:3883–3886, May 1999.

[147] P. P. Rajeev, M. Gertsvolf, P. B. Corkum, and D. M. Rayner. Field dependent avalanche ionization rates in dielectrics. *Phys. Rev. Lett.*, 102:083001, Feb 2009.

[148] M. Jupé, L. Jensen, A. Melninkaitis, V. Sirutkaitis, and D. Ristau. Calculations and experimental demonstration of multi-photon absorption governing fs laser-induced damage in titania. *Opt. Express*, 17(15):12269–12278, Jul 2009.

[149] L. Gallais, D.-B. Douti, M. Commandré, G. BataviÇÂĐiute, E. Pupka, M. SčÂĐiuka, L. Smalakys, V. Sirutkaitis, and A. Melninkaitis. Wavelength dependence of femtosecond laser-induced damage threshold of optical materials. *Journal of Applied Physics*, 117(22), 2015.

[150] T. E. Itina, O. Uteza, N. Sanner, and M. Sentis. Interaction of femtosecond laser pulses with dielectric materials: insights from numerical modelling. *Journal of Optoelectronics and Advanced Materials*, 12(3):470, 2010.

[151] U. Eppelt, S. Russ, C. Hartmann, M. Sun, C. Siebert, and W. Schulz. Diagnostic and simulation of ps-laser glass cutting. In *International Congress on Applications of Lasers & Electro Optics (ICALEO)*, volume 31, 2012.

[152] X. Wang and X. Xu. Thermoelastic wave induced by pulsed laser heating. *Applied Physics A*, 73(1):107–114, 2001.

[153] Y. P. Meshcheryakov, M. V. Shugaev, T. Mattle, T. Lippert, and N. M. Bulgakova. Role of thermal stresses on pulsed laser irradiation of thin films under conditions of microbump formation and nonvaporization forward transfer. *Applied Physics A*, 113(2):521–529, 2013.

[154] N. M. Bulgakova, R. Stoian, and A. Rosenfeld. Laser-induced modification of transparent crystals and glasses. *Quantum Electronics*, 40(11):966, 2010.

[155] J. Zhao, J. Sullivan, J. Zayac, and T. D. Bennett. Structural modification of silica glass by laser scanning. *Journal of Applied Physics*, 95(10):5475–5482, 2004.

[156] P. Combis, Ph. Cormont, L. Gallais, D. Hebert, L. Robin, and J.-L. Rullier. Evaluation of the fused silica thermal conductivity by comparing infrared thermometry measurements with two-dimensional simulations. *Applied Physics Letters*, 101(21), 2012.

[157] D. Albagli, M. Dark, L. T. Perelman, C. von Rosenberg, I. Itzkan, and M. S. Feld. Photomechanical basis of laser ablation of biological tissue. *Opt. Lett.*, 19(21):1684–1686, Nov 1994.

[158] I. Itzkan, D. Albagli, M. L. Dark, L. T. Perelman, C. von Rosenberg, and M. S. Feld. The thermoelastic basis of short pulsed laser ablation of biological tissue. *Proceedings of the National Academy of Sciences*, 92(6):1960–1964, 1995.

[159] G. Paltauf and P. E. Dyer. Photomechanical processes and effects in ablation. *Chemical Reviews*, 103(2):487–518, 2003. PMID: 12580640.

[160] R. Le Parc, C. Levelut, J. Pelous, V. Martinez, and B. Champagnon. Influence of fictive temperature and composition of silica glass on anomalous elastic behaviour. *Journal of Physics: Condensed Matter*, 18(32):7507, 2006.

[161] R. V. Mises. Mechanik der festen kÃűrper im plastisch- deformablen zustand. *Nachrichten von der Gesellschaft der Wissenschaften zu GÃűttingen, Mathematisch-Physikalische Klasse*, 1913:582–592, 1913.

[162] G. Ghosh. Model for the thermo-optic coefficients of some standard optical glasses. *Journal of Non-Crystalline Solids*, 189(1):191 – 196, 1995.

[163] C. Z. Tan and J. Arndt. Temperature dependence of refractive index of glassy sio2 in the infrared wavelength range. *Journal of Physics and Chemistry of Solids*, 61(8):1315 – 1320, 2000.

[164] R. W. Dixon. Photoelastic properties of selected materials and their relevance for applications to acoustic light modulators and scanners. *Journal of Applied Physics*, 38(13):5149–5153, 1967.

[165] A. DÁmico, C. Natale, F. Castro, S. Iarossi, A. Catini, and E. Martinelli. *Volatile Compounds Detection by IR Acousto-Optic Detectors*. Springer Netherlands, Dordrecht, 2009.

[166] M. I. Ojovan. Viscosity and glass transition in amorphous oxides. *Advances in Condensed Matter Physics*, 2008, 2008.

[167] G. Urbain, Y. Bottinga, and P. Richet. Viscosity of liquid silica, silicates and alumino-silicates. *Geochimica et Cosmochimica Acta*, 46(6):1061–1072, 1982.

[168] R. H. Doremus. Viscosity of silica. *Journal of Applied Physics*, 92(12):7619–7629, 2002.

[169] M. I. Ojovan. Viscous flow and the viscosity of melts and glasses. *Physics and Chemistry of Glasses-European Journal of Glass Science and Technology Part B*, 53(4):143–150, 2012.

[170] W. Martienssen and H. Warlimont. *Springer handbook of condensed matter and materials data*. Springer Science & Business Media, 2006.

[171] J. A. Billo, J. Jones, W. Asghar, R. L. Carter, and S. M. Iqbal. Viscosity and surface-free energy effects in thermal shrinking of solid-state nanopores. *Applied Physics Letters*, 100(23), 2012.

[172] D. E. Grady. The spall strength of condensed matter. *Journal of the Mechanics and Physics of Solids*, 36(3):353 – 384, 1988.

[173] K. Boyd, H. Ebendorff-Heidepriem, T. M. Monro, and J. Munch. Surface tension and viscosity measurement of optical glasses using a scanning co 2 laser. *Optical Materials Express*, 2(8):1101–1110, 2012.

[174] R. G. Kraus, S. T. Stewart, D. C. Swift, C. A. Bolme, R. F. Smith, S. Hamel, B. D. Hammel, D. K. Spaulding, D. G. Hicks, J. H. Eggert, et al. Shock vaporization of silica and the thermodynamics of planetary impact events. *Journal of Geophysical Research: Planets*, 117(E9), 2012.

[175] H. J. Melosh. A hydrocode equation of state for sio2. *Meteoritics and Planetary Science*, 42(12):2079–2098, 2007.

[176] A. B. Medvedev. Equation of state of silicon dioxide with allowance for evaporation, dissociation, and ionization. *Combustion, Explosion, and Shock Waves*, 52(4):463–475, 2016.

[177] M. S. Plesset. The dynamics of cavitation bubbles. *Journal of applied mechanics*, 16:277–282, 1949.

[178] A. Y. Kuksin, G. E. Norman, V. V. Pisarev, V. V. Stegailov, and A. V. Yanilkin. Theory and molecular dynamics modeling of spall fracture in liquids. *Physical Review B*, 82(17):174101, 2010.

[179] J.-X. Cai, X. Qu, H. Li, and G.-Y. Jin. Thermal effects of single-pulse laser irradiation on fused silica. In *Proc. SPIE*, volume 9671, pages 96711C–96711C–6, 2015.

[180] M. Fukuhara and A. Sanpei. High temperature-elastic moduli and internal dilational and shear frictions of fused quartz. *Japanese Journal of Applied Physics*, 33(5S):2890, 1994.

[181] Y. Okamoto, I. Miyamoto, K. Cvecek, A. Okada, K. Takahashi, and M. Schmidt. Evaluation of molten zone in micro-welding of glass by picosecond pulsed laser. *Journal of Laser Micro Nanoengineering*, 8(1):65, 2013.

[182] M. Schmidt, F. Vollertsen, M. Geiger, K. Cvecek, I. Alexeev, I. Miyamoto, and M. Schmidt. Laser assisted net shape engineering 6, proceedings of the lane 2010, part 1 defect formation in glass welding by means of ultra short laser pulses. *Physics Procedia*, 5:495 – 502, 2010.

[183] Y. Kikuchi, H. Sudo, and N. Kuzuu. Thermal expansion of vitreous silica: Correspondence between dilatation curve and phase transitions in crystalline silica. *Journal of Applied Physics*, 82(8):4121–4123, 1997.

[184] M. Sakakura, K. Yoshimura, T. Kurita, M. Shimizu, Y. Shimotsuma, N. Fukuda, K. Hirao, and K. Miura. Condensation of si-rich region inside soda-lime glass by parallel femtosecond laser irradiation. *Opt. Express*, 22(13):16493–16503, Jun 2014.

[185] K. S. Yee. Numerical solution of initial boundary value problems involving maxwell's equations in isotropic media. *IEEE Trans. Antennas and Propagation*, pages 302–307, 1966.

[186] R. Courant, K. Friedrichs, and H. Lewy. Über die partiellen differenzengleichungen der mathematischen physik. *Mathematische Annalen*, 100(1):32–74, 1928.

[187] U. S. Inan and R. A. Marshall. *Numerical electromagnetics: the FDTD method*. Cambridge University Press, 2011.

[188] Brown A.K. Costen F., Berenger J.-P. Comparison of fdtd hard source with fdtd soft source and accuracy assessment in debye media. *IEEE Transactions on Antennas and Propagation*, 57(7):2014 – 2022, 2009.

[189] C. J. R. Sheppard and S. Saghafi. Electromagnetic gaussian beams beyond the paraxial approximation. *J. Opt. Soc. Am. A*, 16(6):1381–1386, Jun 1999.

[190] Y. I. Salamin. Fields of a gaussian beam beyond the paraxial approximation. *Applied Physics B*, 86(2):319–326, 2006.

[191] G. Mur. Absorbing boundary conditions for the finite-difference approximation of the time-domain electromagnetic-field equations. *IEEE Transactions on Electromagnetic Compatibility*, EMC-23(4):377–382, Nov 1981.

[192] J.-P. Berenger. *Perfectly Matched Layer (PML) for Computational Electromagnetics*. Morgan & Claypool, 2007.

[193] J.-P. Berenger. A perfectly matched layer for the absorption of electromagnetic waves. *Journal of Computational Physics*, 114(2):185 – 200, 1994.

[194] J.-P. Bérenger. Three-dimensional perfectly matched layer for the absorption of electromagnetic waves. *Journal of Computational Physics*, 127(2):363 – 379, 1996.

[195] W. V. Andrew, C. A. Balanis, and P. A. Tirkas. A comparison of the berenger perfectly matched layer and the lindman higher-order abc's for the fdtd method. *IEEE Microwave and Guided Wave Letters*, 5(6):192–194, Jun 1995.

[196] F. D. Hastings, J. B. Schneider, and S. L. Broschat. Application of the perfectly matched layer (pml) absorbing boundary condition to elastic wave propagation. *The Journal of the Acoustical Society of America*, 100(5):3061–3069, 1996.

[197] J.-P. Bérenger. Perfectly matched layer for the fdtd solution of wave-structure interaction problems. *IEEE Transactions on Antennas and Propagation*, 44(1):110–117, Jan 1996.

[198] W. C. Chew and W. H. Weedon. A 3d perfectly matched medium from modified maxwell's equations with stretched coordinates. *Microwave and Optical Technology Letters*, 7(13):599–604, 1994.

[199] Z. S. Sacks, D. M. Kingsland, R. Lee, and J.-F. Lee. A perfectly matched anisotropic absorber for use as an absorbing boundary condition. *IEEE Transactions on Antennas and Propagation*, 43(12):1460–1463, Dec 1995.

[200] D. H. Werner and R. Mittra. A new field scaling interpretation of berenger's pml and its comparison to other pml formulations. *Microwave and Optical Technology Letters*, 16(2):103–106, 1997.

[201] S. González García, J. Juntunen, R. Gómez Martín, A. P. Zhao, B. García Olmedo, and A. Räisänen. A unified look at berenger's pml for general anisotropic media. *Microwave and Optical Technology Letters*, 28(6):414–416, 2001.

[202] D. M. Sullivan. *Electromagnetic simulation using the FDTD method.* IEEE Press Series on RF and Microwave Technology, 2000.

[203] J.-P. Bérenger. Numerical reflection of evanescent waves by pmls: origin and interpretation in the fdtd case. expected consequences to other finite methods. *International Journal of Numerical Modelling: Electronic Networks, Devices and Fields*, 13(2-3):103–114, 2000.

[204] M. Kuzuoglu and R. Mittra. Frequency dependence of the constitutive parameters of causal perfectly matched anisotropic absorbers. *IEEE Microwave and Guided Wave Letters*, 6(12):447–449, Dec 1996.

[205] J. Alan Roden and Stephen D. Gedney. Convolution pml (cpml): An efficient fdtd implementation of the cfsâĂŞpml for arbitrary media. *Microwave and Optical Technology Letters*, 27(5):334–339, 2000.

[206] S. D. Gedney, G. Liu, J. A. Roden, and A. Zhu. Perfectly matched layer media with cfs for an unconditionally stable adi-fdtd method. *IEEE Transactions on Antennas and Propagation*, 49(11):1554–1559, Nov 2001.

[207] L. Cirio, A. Richardson, and O. Picon. Accurate development of the upml absorbing boundary conditions in a 3d-fdtd algorithm for cpw and microstrip line on silicon substrate. *Microwave and Optical Technology Letters*, 44(4):334–338, 2005.

[208] Y. Yu and Z. Chen. The cpml absorbing boundary conditions for the unconditionally stable meshless modeling. *IEEE Antennas and Wireless Propagation Letters*, 11:468–472, 2012.

[209] I. Laakso, S. Ilvonen, and T. Uusitupa. Performance of convolutional pml absorbing boundary conditions in finite-difference time-domain sar calculations. *Physics in Medicine and Biology*, 52(23):7183, 2007.

[210] Feng D.-S. and Dai Q.-W. {GPR} numerical simulation of full wave field based on {UPML} boundary condition of adi-fdtd. *NDT & E International*, 44(6):495 – 504, 2011.

[211] K. Duru. Perfectly matched layers for second order wave equations. *Ph. D. thesis*, 2010.

[212] A. Taflove. *Computational electrodynamics. The Finite-Difference Time-Domain Method.* Artech House, 1995.

[213] R. J. Luebbers, F. Hunsberger, and Kunz K. S. A frequency-dependent finite-difference time-domain formulation for transient propagation in plasma. *IEEE Trans. Antennas and Propagation*, 39(1):29–34, 1991.

[214] A. S. Nagra and R. A. York. Fdtd analysis of wave propagation in nonlinear absorbing and gain media. *IEEE Trans. Antennas and Propagation*, 46(3):334–340, 1998.

[215] M. Fujii, M. Tahara, I. Sakagami, W. Freude, and P. Russer. High-order fdtd and auxiliary differential equation formulation of optical pulse propagation in 2-d kerr and raman nonlinear dispersive media. *IEEE Journal of Quantum Electronics*, 40(2):175–182, 2004.

[216] P. M. Goorjian and A. Taflove. Direct time integration of maxwell's equations in nonlinear dispersive media for propagation and scattering of femtosecond electromagnetic solitons. *Opt. Lett.*, 17(3):180–182, Feb 1992.

[217] R. M. Joseph and A. Taflove. Fdtd maxwell's equations models for nonlinear electrodynamics and optics. *Antennas and Propagation, IEEE Transactions on*, 45(3):364–374, Mar 1997.

[218] I. S. Maksymov, A. A. Sukhorukov, A. V. Lavrinenko, and Y. S. Kivshar. Comparative study of fdtd-adopted numerical algorithms for kerr nonlinearities. *Antennas and Wireless Propagation Letters, IEEE*, 10:143–146, 2011.

[219] P. Tran. Photonic-band-structure calculation of material possessing kerr nonlinearity. *Phys. Rev. B*, 52:10673–10676, Oct 1995.

[220] J. H. Greene and A. Taflove. General vector auxiliary differential equation finite-difference time-domain method for nonlinear optics. *Optics Express*, 14, 2006.

[221] M. Ammann. Non-trivial materials in em-fdtd. *Ph.D. thesis*, March 2007.

[222] J. Francés, J. Tervo, and C. Neipp. Split-field finite-difference time-domain scheme for kerr-type nonlinear periodic media. *Progress in Electromagnetic Research*, 134:559–579, 2013.

[223] J. Francés, J. Tervo, S. Gallego, S. Bleda, C. Neipp, and Márquez A. Split-field finite-difference time-domain method for second-harmonic generation in two-dimensionally periodic structures. *J. Opt. Soc. Am. B*, 32(4), 2015.

[224] S. Banach. Sur les opérations dans les ensembles abstraits et leur application aux équations intégrales. *Fund. Math.*, 3(1):133–181, 1922.

[225] J. Crank and P. Nicolson. A practical method for numerical evaluation of solutions of partial differential equations of the heat-conduction type. *Advances in Computational Mathematics*, 6(1):207–226, 1996.

[226] A. Rudenko, J.-P. Colombier, and T. E. Itina. Femtosecond laser irradiation of dielectric materials containing randomly-arranged nanoparticles. In *Proc. SPIE*, page 9737, 2016.

[227] R. Buividas, M. Mikutis, and S. Juodkazis. Surface and bulk structuring of materials by ripples with long and short laser pulses: Recent advances. *Progress in Quantum Electronics*, 38(3):119–156, 2014.

[228] A. Rudenko, J.-P. Colombier, and T. E. Itina. From random inhomogeneities to periodic nanostructures induced in bulk silica by ultrashort laser. *Phys. Rev. B*, 93:075427, Feb 2016.

[229] C. Guiffaut and K. Mahdjoubi. Introduction to gpu computing and cuda programming: A case study on fdtd. *IEEE Antennas and Propag. Magazine*, 43(2):94–103, 2001.

[230] Y. Liu, Z. Liang, and Z. Q. Yang. A novel fdtd approach featuring two-level parallelization on pc cluster. *Progress in Electromagnetics Research*, 80:393–408, 2008.

[231] D. Bhardwaj, S. Phadke, S. Yerneni, et al. On improving performance of migration algorithms using mpi and mpi-io. In *Expanded Abstracts, Society of Exploration Geophysicists*, 2000.

[232] A. S. Salh. Efficient parallel finite difference time domain algorithm for modeling electromagnetic wave interactions with dispersive objects. *Ph.D. thesis*, 2013.

[233] P. Micikevicius. 3d finite difference computation on gpus using cuda. In *Proc. 2nd workshop on General Purpose Processing on Graphics Processing Units*, pages 79–84, 2009.

[234] D. De Donno, A. Esposito, L. Tarricone, and L. Catarinucci. Introduction to gpu computing and cuda programming: A case study on fdtd. *IEEE Antennas and Propag. Magazine*, 52(3):116–122, 2010.

[235] M. R. Zinoubi and Payne J. Analysis of 3-dimensional electromagnetic fields in dispersive media using cuda. *Progress in Electromagnetics Research*, 16:185–196, 2011.

[236] D. Michéa and D. Komatitsch. Accelerating a 3d finite-difference wave propagation code using gpu graphics cards. *Geophys. J. Int.*, 182(1):389–402, 2010.

[237] M. Gustav. Beiträge zur optik trüber medien, speziell kolloidaler metallösungen. *Annalen der Physik*, 330(3):377–445, 1908.

[238] M Born and E Wolf. *Principles of Optics*. Cambridge University Press, 7 edition, 1999.

[239] L. Sudrie, A. Couairon, M. Franco, B. Lamouroux, B. Prade, S. Tzortzakis, and A. Mysyrowicz. Femtosecond laser-induced damage and filamentary propagation in fused silica. *Phys. Rev. Lett.*, 89:186601, Oct 2002.

[240] K. Starke, Detlev Ristau, Herbert Welling, Tatiana V. Amotchkina, Michael Trubetskov, Andrei A. Tikhonravov, and Anatoly S. Chirkin. Investigations in the nonlinear behavior of dielectrics by using ultrashort pulses. In *Proc. SPIE*, volume 5273, pages 501–514, 2004.

[241] Q. Sun, H. Jiang, Y. Liu, Z. Wu, H. Yang, and Q. Gong. Measurement of the collision time of dense electronic plasma induced by a femtosecond laser in fused silica. *Opt. Lett.*, 30(3):320–322, Feb 2005.

[242] X. Jing, Y. Tian, J. Zhang, S. Chen, Y. Jin, J. Shao, and Z. Fan. Modeling validity of femtosecond laser breakdown in wide bandgap dielectrics. *Applied Surface Science*, 258(10):4741 – 4749, 2012.

[243] X. Fan, W. T. Zheng, and D. J Singh. Light scattering and surface plasmons on small spherical particles. *Light: Science & Applications*, 3(June), Jan 2014.

[244] S. Itoh, K. Tanimura, and N. Itoh. Optical studies of self-trapped excitons in sio 2. *Journal of Physics C: Solid State Physics*, 21(26):4693, 1988.

[245] K. Tanimura, C. Itoh, and Itoh N. Transient optical absorption and luminescence induced by band-to-band excitation in amorphous sio 2. *Journal of Physics C: Solid State Physics*, 21(9):1869, 1988.

[246] P. P. Rajeev, M. Gertsvolf, E. Simova, C. Hnatovsky, R. S. Taylor, V. R. Bhardwaj, D. M. Rayner, and P. B. Corkum. Memory in nonlinear ionization of transparent solids. *Phys. Rev. Lett.*, 97:253001, Dec 2006.

[247] Y. Bellouard, E. Barthel, A. A. Said, M. Dugan, and P. Bado. Scanning thermal microscopy and ramananalysis of bulk fused silica exposed to lowenergyfemtosecond laser pulses. *Opt. Express*, 16(24):19520–19534, Nov 2008.

[248] S. P. Sharma, V. Oliveira, P. Herrero, and R. Vilar. Internal structure of the nanogratings generated inside bulk fused silica by ultrafast laser direct writing. *Journal of Applied Physics*, 116(5):–, 2014.

[249] M. Lancry, R. Desmarchelier, F. Zimmermann, N. Guth, F. Brisset, S. Nolte, and B. Poumellec. Porous nanogratings and related form birefringence in silicate and germanate glasses. In *Advanced Photonics*, page BW2D.2. Optical Society of America, 2014.

[250] C. Corbari, A. Champion, M. Gecevičius, M. Beresna, Y. Bellouard, and P. G. Kazansky. Femtosecond versus picosecond laser machining of nano-gratings and micro-channels in silica glass. *Opt. Express*, 21(4):3946–3958, Feb 2013.

[251] S. Höhm, A. Rosenfeld, J. Krüger, and J. Bonse. Femtosecond diffraction dynamics of laser-induced periodic surface structures on fused silica. *Applied Physics Letters*, 102(5):054102, 2013.

[252] D. Wortmann, J. Gottmann, N. Brandt, and H. Horn-Solle. Micro- and nanostructures inside sapphire by fs-laser irradiation and selective etching. *Opt. Express*, 16(3):1517–1522, Feb 2008.

[253] J. Bonse, A. Rosenfeld, and J. Krüger. On the role of surface plasmon polaritons in the formation of laser-induced periodic surface structures upon irradiation of silicon by femtosecond-laser pulses. *Journal of Applied Physics*, 106(10):–, 2009.

[254] G. D. Tsibidis, M. Barberoglou, P. A. Loukakos, E. Stratakis, and C. Fotakis. Dynamics of ripple formation on silicon surfaces by ultrashort laser pulses in subablation conditions. *Phys. Rev. B*, 86:115316, Sep 2012.

[255] S. K. Das, H. Messaoudi, A. Debroy, E. McGlynn, and R. Grunwald. Multiphoton excitation of surface plasmon-polaritons and scaling of nanoripple formation in large bandgap materials. *Opt. Mater. Express*, 3(10):1705–1715, Oct 2013.

[256] T. J.-Y. Derrien, T. E. Itina, R. Torres, T. Sarnet, and M. Sentis. Possible surface plasmon polariton excitation under femtosecond laser irradiation of silicon. *Journal of Applied Physics*, 114(8):–, 2013.

[257] J.-W. Yao, C.-Y. Zhang, H.-Y. Liu, Q.-F. Dai, L.-J. Wu, S. Lan, A. V. Gopal, V. A. Trofimov, and T. M. Lysak. High spatial frequency periodic structures induced on metal surface by femtosecond laser pulses. *Opt. Express*, 20(2):905–911, Jan 2012.

[258] S. Richter, A. Plech, M. Steinert, M. Heinrich, S. Döring, F. Zimmermann, U. Peschel, E. B. Kley, A. Tünnermann, and S. Nolte. On the fundamental structure of femtosecond laser-induced nanogratings. *Laser & Photonics Reviews*, 6(6):787–792, 2012.

[259] E. Bricchi. Femtosecond laser micro-machining and consequent self-assembled nano-structures in transparent materials. *Ph.D. thesis, University of Southampton*, September 2005.

[260] A. Rudenko, J.-P. Colombier, and T. E. Itina. Influence of polarization state on ultrafast laser-induced bulk nanostructuring. *Journal of Laser Micro/Nanoengineering*, 11:304–311, Dec 2016.

[261] O. J. Allegre, W. Perrie, S. P. Edwardson, G. Dearden, and K. G. Watkins. Laser microprocessing of steel with radially and azimuthally polarized femtosecond vortex pulses. *Journal of Optics*, 14(8):085601, 2012.

[262] J.-T. Chen, W.-C. Lai, Y.-J. Kao, Y.-Y. Yang, and J.-K. Sheu. Laser-induced periodic structures for light extraction efficiency enhancement of gan-based light emitting diodes. *Opt. Express*, 20(5):5689–5695, Feb 2012.

[263] O. J. Allegre, Y. Jin, W. Perrie, J. Ouyang, E. Fearon, S. P. Edwardson, and G. Dearden. Complete wavefront and polarization control for ultrashort-pulse laser microprocessing. *Opt. Express*, 21(18):21198–21207, Sep 2013.

[264] R. Dorn, S. Quabis, and G. Leuchs. Sharper focus for a radially polarized light beam. *Phys. Rev. Lett.*, 91:233901, Dec 2003.

[265] P. S. Tan, X.-C. Yuan, J. Lin, Q. Wang, and R. E. Burge. Analysis of surface plasmon interference pattern formed by optical vortex beams. *Opt. Express*, 16(22):18451–18456, Oct 2008.

[266] Z. J. Hu, P. S. Tan, S.W. Zhu, and X.-C. Yuan. Structured light for focusing surface plasmon polaritons. *Opt. Express*, 18(10):10864–10870, May 2010.

[267] G. H. Yuan, X.-C. Yuan, J. Bu, P. S. Tan, and Q. Wang. Manipulation of surface plasmon polaritons by phase modulation of incident light. *Opt. Express*, 19(1):224–229, Jan 2011.

[268] M. Dienerowitz, M. Mazilu, P. J. Reece, T. F. Krauss, and K. Dholakia. Optical vortex trap for resonant confinement of metal nanoparticles. *Opt. Express*, 16(7):4991–4999, Mar 2008.

[269] M. A. Tyrk, S. A. Zolotovskaya, W. A. Gillespie, and A. Abdolvand. Radially and azimuthally polarized laser induced shape transformation of embedded metallic nanoparticles in glass. *Opt. Express*, 23(18):23394–23400, Sep 2015.

[270] S. Roy, K. Ushakova, Q. van den Berg, S. F. Pereira, and H. P. Urbach. Radially polarized light for detection and nanolocalization of dielectric particles on a planar substrate. *Phys. Rev. Lett.*, 114:103903, Mar 2015.

[271] V. Parigi, V. D'Ambrosio, C. Arnold, L. Marrucci, F. Sciarrino, and J. Laurat. Storage and retrieval of vector beams of light in a multiple-degree-of-freedom quantum memory. *Nature communications*, 6, 2015.

[272] G. D. Tsibidis, E. Skoulas, and E. Stratakis. Ripple formation on nickel irradiated with radially polarized femtosecond beams. *Opt. Lett.*, 40(22):5172–5175, Nov 2015.

[273] K. Lou, S.-X. Qian, X.-L. Wang, Y. Li, B. Gu, C. Tu, and H.-T. Wang. Two-dimensional microstructures induced by femtosecond vector light fields on silicon. *Opt. Express*, 20(1):120–127, Jan 2012.

[274] B. McMillen and Y. Bellouard. On the anisotropy of stress-distribution induced in glasses and crystals by non-ablative femtosecond laser exposure. *Opt. Express*, 23(1):86–100, Jan 2015.

[275] Y. Jin, O. J. Allegre, W. Perrie, K. Abrams, J. Ouyang, E. Fearon, S. P. Edwardson, and G. Dearden. Dynamic modulation of spatially structured polarization fields for real-time control of ultrafast laser-material interactions. *Opt. Express*, 21(21):25333–25343, Oct 2013.

[276] K. Lou, S.-X. Qian, Z.-C. Ren, C. Tu, Y. Li, and H.-T. Wang. Femtosecond laser processing by using patterned vector optical fields. *Scientific reports*, 3, 2013.

[277] S. Hasegawa and Y. Hayasaki. Polarization distribution control of parallel femtosecond pulses with spatial light modulators. *Opt. Express*, 21(11):12987–12995, Jun 2013.

[278] M.-Q. Cai, P.-P. Li, D. Feng, Y. Pan, S.-X. Qian, Y. Li, C. Tu, and H.-T. Wang. Microstructures fabricated by dynamically controlled femtosecond patterned vector optical fields. *Opt. Lett.*, 41(7):1474–1477, Apr 2016.

[279] M. Suzuki, K. Yamane, K. Oka, Y. Toda, and R. Morita. Full quantitative analysis of arbitrary cylindrically polarized pulses by using extended stokes parameters. *Scientific reports*, 5, 2015.

[280] X.-L. Wang, J. Ding, W.-J. Ni, C.-S. Guo, and H.-T. Wang. Generation of arbitrary vector beams with a spatial light modulator and a common path interferometric arrangement. *Opt. Lett.*, 32(24):3549–3551, Dec 2007.

[281] X.-L. Wang, Y. Li, J. Chen, C.-S. Guo, J. Ding, and H.-T. Wang. A new type of vector fields with hybrid states of polarization. *Opt. Express*, 18(10):10786–10795, May 2010.

[282] Z.-Y. Rong, Y.-J. Han, S.-Z. Wang, and C.-S. Guo. Generation of arbitrary vector beams with cascaded liquid crystal spatial light modulators. *Opt. Express*, 22(2):1636–1644, Jan 2014.

[283] R.-P. Chen, Z. Chen, K.-H. Chew, P.-G. Li, Z. Yu, J. Ding, and S. He. Structured caustic vector vortex optical field: manipulating optical angular momentum flux and polarization rotation. *Scientific Reports*, 5:1–8, 2015.

[284] C. Hnatovsky, R. S. Taylor, E. Simova, P. P. Rajeev, D.M. Rayner, V. R. Bhardwaj, and P. B. Corkum. Fabrication of microchannels in glass using focused femtosecond laser radiation and selective chemical etching. *Applied Physics A*, 84(1-2):47–61, 2006.

[285] N. Yasumaru, K. Miyazaki, and J. Kiuchi. Femtosecond-laser-induced nanostructure formed on hard thin films of tin and dlc. *Applied Physics A*, 76(6):983–985, 2003.

[286] O. Varlamova, J. Reif, S. Varlamov, and Bestehorn M. The laser polarization as control parameter in the formation of laser-induced periodic surface structures: Comparison of numerical and experimental results. *Applied Surface Science*, 257:5465–5469, 2011.

[287] G. Miyaji and K. Miyazaki. Origin of periodicity in nanostructuring on thin film surfaces ablated with femtosecond laser pulses. *Opt. Express*, 16(20):16265–16271, Sep 2008.

[288] R. A. Ganeev, M. Baba, T. Ozaki, and H. Kuroda. Long- and short-period nanostructure formation on semiconductor surfaces at different ambient conditions. *J. Opt. Soc. Am. B*, 27(5):1077–1082, May 2010.

[289] J. Reif, F. Costache, 0. Varlamova, G. Jia, and M. Ratzke. Self-organized regular surface patterning by pulsed laser ablation. *Phys. Status Solidi (c)*, 6(3):681–686, 2009.

[290] G. Fibich and B. Ilan. Self-focusing of circularly polarized beams. *Phys. Rev. E*, 67:036622, Mar 2003.

[291] L. Ye, W. Perrie, O. J. Allegre, Y. Jin, Z. Kuang, P. J. Scully, E. Fearon, D. Eckford, S. P. Edwardson, and G. Dearden. Nuv femtosecond laser inscription of volume bragg gratings in poly(methyl)methacrylate with linear and circular polarizations. *Laser Phys.*, 23:126004, 2013.

[292] H. Zhang, M. Tang, J. McCoy, and T.-H. Her. Deposition of tungsten nanogratings induced by a single femtosecond laser beam. *Opt. Express*, 15(10):5937–5947, May 2007.

[293] R. Sugawara, S. Sekiguchi, and T. Yagi. Formation of periodic ripples through excitation of 1 micron spot using femtosecond-laser bessel beam on c-si. *Applied Surface Science*, 353:400 – 404, 2015.

[294] G. Cheng, K. Mishchik, C. Mauclair, E. Audouard, and R. Stoian. Ultrafast laser photoinscription of polarization sensitive devices in bulk silica glass. *Opt. Express*, 17(12):9515–9525, Jun 2009.

[295] Q. Zhang, H. Lin, B. Jia, L. Xu, and M. Gu. Nanogratings and nanoholes fabricated by direct femtosecond laser writing in chalcogenide glasses. *Optics Express*, 18(7):6885, 2010.

[296] K. K. Anoop, R. Fittipaldi, A. Rubano, X. Wang, D. Paparo, A. Vecchione, L. Marrucci, R. Bruzzese, and S. Amoruso. Direct femtosecond laser ablation of copper with an optical vortex beam. *Journal of Applied Physics*, 116:113102, 2014.

[297] W. C. Shen, C. W. Cheng, M. C. Yang, Y. Kozawa, and S. Sato. Fabrication of novel structures on silicon with femtosecond laser pulses. *J. Laser Micro Nanoeng*, 5(3):229–232, 2010.

[298] T. Ohno and S. Miyanishi. Study of surface plasmon chirality induced by archimedes' spiral grooves. *Opt. Express*, 14(13):6285–6290, Jun 2006.

[299] J. I. Ziegler and R. F. Haglund. Plasmonic response of nanoscale spirals. *Nanoletters*, 10:3013–3018, 2010.

[300] F. Intonti, N. Caselli, N. Lawrence, J. Trevino, D. S. Wiersma, and L. Dal Negro. Near-field distribution and propagation of scattering resonances in vogel spiral arrays of dielectric nanopillars. *New Journal of Physics*, 15(8):085023, 2013.

[301] J. Lie, C. Yang, H. Zhao, F. Lin, and Xing Z. Plasmonic focusing in spiral nanostructures under linearly polarized illumination. *Optics Express*, 22(14):16686, 2014.

[302] W.-Y. Tsai, J.-S. Huang, and C.-B. Huang. Selective trapping or rotation of isotropic dielectric microparticles by optical near field in a plasmonic archimedes spiral. *Nano Letters*, 14(2):547–552, 2014. PMID: 24392638.

[303] R. B. Davidson, J. I. Ziegler, G. Vargas, S. M. Avanesyan, Y. Gong, W. Hess, and R. F. Haglund. Efficient forward second-harmonic generation from planar archimedian nanospirals. *Nanophotonics*, 4(1):108–113, 2015.

[304] K. S. Youngworth and T. G. Brown. Focusing of high numerical aperture cylindrical-vector beams. *Opt. Express*, 7(2):77–87, Jul 2000.

[305] X.-L. Wang, J. Chen, Y. Li, J. Ding, C.-S. Guo, and H.-T. Wang. *Creation of a new vector field and focusing engineering.* Elsevier, 2014.

[306] C. L. Arnold, S. Akturk, A. Mysyrowicz, V. Jukna, A. Couairon, T. E. Itina, R. Stoian, C. Xie, J. M. Dudley, F. F Courvoisier, S. Bonanomi, O. Jedrkiewicz, and P. Di Trapani. Nonlinear bessel vortex beams for applications. *Journal of Physics B: Atomic, Molecular and Optical Physics*, 48(9):094006, 2015.

[307] M. Mikutis, T. Kudrius, G. Šlekys, D. Paipulas, and S. Juodkazis. High 90% efficiency bragg gratings formed in fused silica by femtosecond gauss-bessel laser beams. *Optical Materials Express*, 3(11):1862–1871, 2013.

[308] M. K. Bhuyan, P. K. Velpula, J. P. Colombier, T. Olivier, N. Faure, and R. Stoian. Single-shot high aspect ratio bulk nanostructuring of fused silica using chirp-controlled ultrafast laser bessel beams. *Applied Physics Letters*, 104(2), 2014.

[309] R. L. Nowack. A tale of two beams: an elementary overview of gaussian beams and bessel beams. *Studia Geophysica et Geodaetica*, 56(2):355–372, 2012.

[310] G. Cheng, A. Rudenko, C. D'Amico, T. E. Itina, J. P. Colombier, and R. Stoian. Embedded nanogratings in bulk fused silica under non-diffractive bessel ultrafast laser irradiation. *Applied Physics Letters*, 110(26):261901, 2017.

[311] A. Rudenko, J. P. Colombier, S. Höhm, A. Rosenfeld, J. Krüger, J. Bonse, and T. E. Itina. Spontaneous periodic ordering on the surface and in the bulk of dielectrics irradiated by ultrafast laser: a shared electromagnetic origin. *Scientific Reports*, 2017.

[312] G. Obara, H. Shimizu, T. Enami, E. Mazur, M. Terakawa, and M. Obara. Growth of high spatial frequency periodic ripple structures on sic crystal surfaces irradiated with successive femtosecond laser pulses. *Optics express*, 21(22):26323–26334, 2013.

[313] M. Huang, F. Zhao, Y. Cheng, N. Xu, and Z. Xu. Mechanisms of ultrafast laser-induced deep-subwavelength gratings on graphite and diamond. *Physical Review B*, 79(12):125436, 2009.

[314] A. Rudenko, J.-P. Colombier, and T. E. Itina. Graphics processing unit-based solution of nonlinear maxwell's equations for inhomogeneous dispersive media. *Int. J. Numer. Model.*, e2215:1–9, Dec 2016.

[315] S. N. Volkov, A. E. Kaplan, and K Miyazaki. Evanescent field at nanocorrugated dielectric surface. *Applied Physics Letters*, 94(4):041104, 2009.

[316] X. Shi, L. Jiang, X. Li, K. Zhang, D. Yu, Y. Yu, and Y. Lu. Temporal femtosecond pulse shaping dependence of laser-induced periodic surface structures in fused silica. *Journal of Applied Physics*, 116(3):033104, 2014.

[317] J. Bonse, S. Höhm, S. V. Kirner, A. Rosenfeld, and J. Krüger. Laser-induced periodic surface structures - a scientific evergreen. *IEEE Journal of Selected Topics in Quantum Electronics*, 23(3):9000615, 2017.

[318] H. Shimizu, S. Yada, G. Obara, and M. Terakawa. Contribution of defect on early stage of lipss formation. *Opt. Express*, 22(15):17990–17998, Jul 2014.

[319] S. P. Sharma, V. Oliveira, and R. Vilar. Morphology and structure of particles produced by femtosecond laser ablation of fused silica. *Applied Physics A*, 122(4):1–8, 2016.

[320] C.-Y. Zhang, J.-W. Yao, H.-Y. Liu, Q.-F. Dai, L.-J. Wu, S. Lan, V. A. Trofimov, and T. M. Lysak. Colorizing silicon surface with regular nanohole arrays induced by femtosecond laser pulses. *Optics letters*, 37(6):1106–1108, 2012.

[321] J. Bonse, Martin Munz, and Heinz Sturm. Structure formation on the surface of indium phosphide irradiated by femtosecond laser pulses. *Journal of Applied Physics*, 97(1):013538, 2005.

[322] E. M. Hsu, T. H. R. Crawford, H. F. Tiedje, and H. K. Haugen. Periodic surface structures on gallium phosphide after irradiation with 150 fs–7 ns laser pulses at 800 nm. *Applied Physics Letters*, 91(11):111102, 2007.

[323] T. Tomita, K. Kinoshita, S. Matsuo, and S. Hashimoto. Effect of surface roughening on femtosecond laser-induced ripple structures. *Applied Physics Letters*, 90(15):153115, 2007.

[324] D. Dufft, A. Rosenfeld, S. K. Das, R. Grunwald, and J. Bonse. Femtosecond laser-induced periodic surface structures revisited: a comparative study on zno. *Journal of Applied Physics*, 105(3):034908, 2009.

[325] D. G. Papazoglou and S. Tzortzakis. Physical mechanisms of fused silica restructuring and densification after femtosecond laser excitation. *Opt. Mater. Express*, 1(4):625–632, Aug 2011.

[326] B. Rethfeld. Free-electron generation in laser-irradiated dielectrics. *Phys. Rev. B*, 73:035101, Jan 2006.

[327] D. Du, X. Liu, G. Korn, J. Squier, and G. Mourou. LaserÂŘinduced breakdown by impact ionization in sio2 with pulse widths from 7 ns to 150 fs. *Applied Physics Letters*, 64(23):3071–3073, 1994.

[328] Y. Liu, H. Jiang, Q. Sun, Z. Wu, H. Yang, and Q. Gong. Different tendencies of breakdown threshold on pulse duration in the subpicosecond regime in fused silica. *Journal of Optics A: Pure and Applied Optics*, 7(4):198, 2005.

[329] Q. Sun, H. Asahi, Y. Nishijima, N. Murazawa, K. Ueno, and H. Misawa. Pulse duration dependent nonlinear propagation of a focused femtosecond laser pulse in fused silica. *Optics express*, 18(24):24495–24503, 2010.

[330] X. Shang, R. Zhang, and P. Ma. Analysis of avalanche mechanisms in short-pulses laser-induced damage. *Optics & Laser Technology*, 42(1):243 – 246, 2010.

[331] Y. Hayasaki, M. Isaka, A. Takita, and S. Juodkazis. Time-resolved interferometry of femtosecond-laser-induced processes under tight focusing and close-to-optical breakdown inside borosilicate glass. *Opt. Express*, 19(7):5725–5734, Mar 2011.

[332] C. Mauclair. Spatio-temporal ultrafast laser tailoring for bulk functionalization of transparent materials. *Ph.D. thesis*, 2010.

[333] A. Horn, E.W. Kreutz, and R. Poprawe. Ultrafast time-resolved photography of femtosecond laser induced modifications in bk7 glass and fused silica. *Applied Physics A*, 79(4):923–925, 2004.

[334] S. Richter, F. Zimmermann, A. Tünnermann, and S. Nolte. [invited] laser welding of glasses at high repetition rates âĂŞ fundamentals and prospects. *Optics & Laser Technology*, 83:59 – 66, 2016.

[335] B. Luther-Davies, A. V. Rode, N. R. Madsen, and E. G. Gamaly. Picosecond high-repetition-rate pulsed laser ablation of dielectrics: the effect of energy accumulation between pulses. *Optical Engineering*, 44(5):051102–051102–8, 2005.

[336] R. Weber, T. Graf, P. Berger, V. Onuseit, M. Wiedenmann, C. Freitag, and A. Feuer. Heat accumulation during pulsed laser materials processing. *Opt. Express*, 22(9):11312–11324, May 2014.

[337] J.-X. Cai, G.-Y. Jin, M. Guo, and H.-D. Yu. Thermal stress simulation of multi-pulse laser irradiate on fused silica. In *Proc. SPIE*, volume 9295, pages 92950O–92950O–5, 2014.

[338] I. Guk, G. Shandybina, and E. Yakovlev. Influence of accumulation effects on heating of silicon surface by femtosecond laser pulses. *Applied Surface Science*, 353:851 – 855, 2015.

[339] M. Lancry, J. Canning, K. Cook, M. Heili, D. R. Neuville, and B. Poumellec. Nanoscale femtosecond laser milling and control of nanoporosity in the normal and anomalous regimes of geo 2-sio 2 glasses. *Optical Materials Express*, 6(2):321–330, 2016.

[340] Y. Bellouard and M.-O. Hongler. Femtosecond-laser generation of self-organized bubble patterns in fused silica. *Optics express*, 19(7):6807–6821, 2011.

[341] B. J. Garrison, T. E. Itina, and L. V. Zhigilei. Limit of overheating and the threshold behavior in laser ablation. *Physical review E*, 68(4):041501, 2003.

[342] S. Faik, An. Tauschwitz, J. Maruhn, and I. Iosilevskiy. Lifetime of metastable states in ion-beam irradiated sio2 foils. *Physics of Extreme States of Matter*, page 105, 2011.

[343] I. Iosilevskiy, V. Gryaznov, and A. Solovév. Properties of high-temperature phase diagram and critical point parameters in silica. *arXiv preprint arXiv:1312.7592*, 2013.

[344] T. Kumada, H. Akagi, R. Itakura, T. Otobe, and A. Yokoyama. Femtosecond laser ablation dynamics of fused silica extracted from oscillation of time-resolved reflectivity. *Journal of Applied Physics*, 115(10):103504, 2014.

[345] F. Vidal, T. W. Johnston, S. Laville, O. Barthélemy, M. Chaker, B. Le Drogoff, J. Margot, and M. Sabsabi. Critical-point phase separation in laser ablation of conductors. *Physical review letters*, 86(12):2573, 2001.

[346] A. G. Lamorgese and R. Mauri. Diffuse-interface modeling of liquid-vapor phase separation in a van der waals fluid. *Physics of Fluids (1994-present)*, 21(4):044107, 2009.

[347] V. Lyakhovsky, S. Hurwitz, and O. Navon. Bubble growth in rhyolitic melts: experimental and numerical investigation. *Bulletin of volcanology*, 58(1):19–32, 1996.

[348] O. Navon, A. Chekhmir, and V. Lyakhovsky. Bubble growth in highly viscous melts: theory, experiments, and autoexplosivity of dome lavas. *Earth and Planetary Science Letters*, 160(3):763–776, 1998.

[349] William M Haynes. *CRC handbook of chemistry and physics*. CRC press, 2014.

[350] Y. Bellouard, A. Champion, B. McMillen, S. Mukherjee, R. R. Thomson, C. Pépin, P. Gillet, and Y. Cheng. Stress-state manipulation in fused silica via femtosecond laser irradiation. *Optica*, 3(12):1285–1293, 2016.

[351] V. Stankevič, G. Račiukaitis, F. Bragheri, X. Wang, E. G Gamaly, R. Osellame, and S. Juodkazis. Laser printed nano-gratings: orientation and period peculiarities. *Scientific Reports*, 7(39989):1–8, 2017.

[352] S. V. Kuzḿichev, S. A. Kukushkin, A. V. Osipov, and M. G. Shlyagin. Influence of the external mechanical load on the formation of nanopores in an optical fiber under pulsed uv light. *Physics of the Solid State*, 52(8):1645–1652, 2010.

Chapter 8

Publications

8.1 Publications in refereed journals

1. A. Rudenko, J.-P. Colombier, T. E. Itina: From random inhomogeneities to periodic nanostructures induced in bulk silica by ultrashort laser. Physical Review B, Vol. 93, 075427, 2016.

2. A. Rudenko, J.-P. Colombier, T. E. Itina: GPU-based solution of nonlinear Maxwell's equations for inhomogeneous dispersive media. Int. J. Numer. Model., e2215, 1-9, 2016.

3. A. Rudenko, J.-P. Colombier, T. E. Itina: Influence of polarization state on ultrafast laser-induced bulk nanostructuring. Journal of Laser Micro/ Nanoengineering, Vol. 11, No. 3, 2016.

4. G. Cheng, A. Rudenko, C. D'Amico, T. E. Itina, J.-P. Colombier, and R. Stoian: Embedded nanogratings in bulk fused silica under non-diffractive Bessel ultrafast laser irradiation. Appl. Phys. Letters, Vol. 110, 261901, 2017.

5. A. Rudenko, J.-P. Colombier, S. Höhm, A. Rosenfeld, J. Krüger, J. Bonse, and T. E. Itina: Spontaneous periodic ordering on the surface and in the bulk of dielectrics irradiated by ultrafast laser: a shared electromagnetic origin. Sci. Reports, DOI: 10.1038/s41598-017-12502-4, 2017.

8.2 Publications in proceedings

1. A. Rudenko, J.-P. Colombier, T. E. Itina: Femtosecond laser irradiation of dielectric materials containing randomly-arranged nanoparticles. Proc. SPIE, Vol. 9737, 97370L, 2016.

2. A. Rudenko, J.-P. Colombier, T. E. Itina: Femtosecond laser irradiation of fused silica with a nanometric inhomogeneity. PIERS Proceedings, 2015.

8.3 Participation in conferences

1. A. Rudenko, J.-P. Colombier, T. E. Itina. Femtosecond laser irradiation of fused silica with a nanometric inhomogeneity. Progress In Electromagnetics Research Symposium, 6-9 July 2015, Prague, Czech Republic. (oral talk)

2. A. Rudenko, J.-P. Colombier, T. E. Itina. Femtosecond laser irradiation of dielectric materials containing randomly-arranged nanoparticles. Photonics West LASE 2016, 13-18 February, San Francisco, USA. (oral talk)

3. A. Rudenko, J.-P. Colombier, T. E. Itina: Ultrashort laser-induced nanogratings in glass: insights from numerical modeling. International The 11^{th} Conference on High Power Laser Ablation and Directed Energy (HPLA), 4-7 April 2016, Santa Fe, New Mexico, USA. (poster)

4. A. Rudenko, J.-P. Colombier, T. E. Itina. GPU-based solution of nonlinear Maxwell's equations for inhomogeneous dispersive media. EMF 2016, 10^{th} International Symposium on Electric and Magnetic Fields, 12-14 April 2016, Lyon, France. (poster)

5. A. Rudenko, J.-P. Colombier, T. E. Itina: Numerical modeling of femtosecond laser induced nanostructuring in glass. The 17^{th} International Symposium on Laser Precision Microfabrication (LPM 2016), Book of abstracts, 23-27 May 2016, Xi'an, China. (oral talk)

6. A. Rudenko, J.-P. Colombier, T. E. Itina. On the origin of volume nanogratings created by femtosecond laser. Progress In Electromagnetics Research Symposium, 8-11 August 2016, Shanghai, China. (oral talk)

7. J.-P. Colombier, A. Rudenko, E. Bévillon, H. Zhang, T. E. Itina, and R. Stoian. Modeling 2D and 3D periodic nanostructuring of materials with ultrafast laser pulses. Photonics West LASE 2017, 27 January - 1 February, San Francisco, USA. (invited talk, co-author)

8. T. E. Itina, A. Rudenko, J.-P. Colombier, H. Ma. Ultra-short laser structuring of glasses: Predictive modeling insights. 7^{th} European Conference on Applications of Femtosecond Lasers in Materials Science, FemtoMat 2017, 20-22 March, Mauterndorf Castle, Salzburg, Austria. (invited talk, co-author)

9. A. Rudenko, T. E. Itina, K. Ladutenko, S. Makarov. Self-consistent Modeling of Photoionization-induced Field Distributions in Nanoparticles by Ultrashort Laser. Progress In Electromagnetics Research Symposium, 22-25 May 2017, Saint Petersburg, Russia. (invited oral talk)

10. A. Rudenko, J.-P. Colombier, T. E. Itina. On the thresholds of nanovoid formation in glass by femtosecond laser. Progress In Electromagnetics Research Symposium, 22-25 May 2017, Saint Petersburg, Russia. (oral talk)

11. A. Rudenko, H. Ma, R. Zakoldaev, V. P. Veiko, T. E. Itina. Ultra-short Laser Interactions for Advanced Photonic Technologies. Progress In Electromagnetics Research Symposium, 22-25 May 2017, Saint Petersburg, Russia. (oral talk, co-author)